

**Curtin Medical School**

**Faculty of Health Sciences**

**Study of Biofilm Formation by Phosphate  
Solubilising Bacteria on Rare Earth Elements  
Phosphate Minerals**

**Arya Van Alin**

ORCID iD: 0000-0002-5859-269X

**This thesis is presented for the Degree of**

**Doctor of Philosophy**

**of**

**Curtin University**

**July 2024**

## **Author's Declaration**

To the best of my knowledge and belief, this thesis contains no material previously published by any other person except where due acknowledgment has been made.

This thesis contains no material which has been accepted for the award of any other degree or diploma in any university.

Arya Van Alin

27 July 2024

## **Originality Check Report using Turnitin**

Candidate: **Arya Van Alin**

Thesis Title: **Study of Biofilm Formation by Phosphate Solubilising Bacteria on Rare Earth Elements Phosphate Minerals**

Submission ID: **2429889593**

Originality check submission date: **10 Aug 2024**

The originality check was performed using Turnitin to ensure the originality of the content and to identify any potential similarities with existing published works.

The total similarity index for the thesis is 41%. This percentage represents the proportion of the thesis content that matches existing sources in the Turnitin database.

### **Breakdown of Similarity**

19% Similarity: This portion of the similarity index corresponds to Chapter 3 of the thesis, which is based on the candidate's first published paper.

15% Similarity: This portion of the similarity index corresponds to Chapter 5 of the thesis, which is based on the candidate's second published paper.

<1% Similarity: The remaining detected similarities are less than 1% and is attributed to common phrases, section and subsection titles, parts of table and figure legends (e.g., "X-axis is \*\*\*\*" and "Y-axis is \*\*\*\*"), spelled-out abbreviations (e.g., "Time of Flight Secondary Mass Spectrometry (ToF-SIMS)"), and other common phrases (e.g., "a strategy to improve" or "changes in the chemical composition").

The supervisory team double checked the similarities and confirm significant similarities identified in Chapters 3 and 5 are expected and acceptable, as these chapters are based on the candidate's previously published works. The minor similarities (<1%) are primarily due to common academic phrases and standard terminology, which are unavoidable in scientific writing. The originality check indicates that the thesis maintains a high level of originality, with the majority of the detected similarities being attributable to the candidate's own published works and common academic phrases. No significant issues of plagiarism were identified.

**This thesis is supervised by the following supervisory team:**

**Prof Elizabeth L. J. Watkin**, Edith Cowan University, Perth, Australia

**Dr Mellissa K. Corbett**, Curtin University, Perth, Australia

**Prof Andrew Putnis**, University of Münster, Münster, Germany

**Dr Anna H. Kaksonen**, CSIRO, Perth, Australia

**Prof Jacques Eksteen**, Curtin University, Perth, Australia

**Dr Himel Nahreen Khaleque**, Edith Cowan University, Perth, Australia



## **With Heartfelt Thanks**

This thesis is dedicated to my beloved parents, who have taught me to work hard for achieving my goals, and to my amazing siblings and my lovely nieces and nephews who have always been there for me. Your unwavering support and encouragement have been my constant source of strength.

I would also like to extend my heartfelt gratitude to my supervisors, particularly Liz and Mel. The guidance, wisdom, and patience I had from the supervisory team have been invaluable throughout this journey. Your insights and encouragement have not only shaped this thesis but have also significantly contributed to my personal and academic growth.

To my friends, thank you for your unwavering support and for always being there to lift my spirits. Your companionship has made this journey much more enjoyable and manageable. The laughter, the late-night study sessions (i.e. movie nights), and the constant motivation have been indispensable.

Lastly, I wish to acknowledge everyone who has contributed to this thesis in any way. Your assistance, whether big or small, has been greatly appreciated and has helped me reach this milestone. This includes my colleagues, mentors, and anyone who provided feedback or support during this process. Thank you all for your support and encouragement.

With heartfelt thanks to all of you, this thesis stands as a testament to your belief in me and your unwavering support.

**“Nothing is better than reading and gaining more and more knowledge.”**

**Stephen Hawking**

**“The more I know, the more I realise I know nothing.”**

**(Believed to be told by) Socrates**

## **Acknowledgement**

Arya Van Alin acknowledges support through a Parker CRC for Integrated Hydrometallurgy Solutions (established and supported under the Australian Government's Cooperative Research Centres Program).

The author(s) acknowledge the Australian Research Council (ARC) for grant DP200103243.

The authors acknowledge the Curtin Health Innovation Research Institute (CHIRI), Bentley, Western Australia, for providing the confocal microscopy facilities and the John de Laeter Centre (JdLC) for provision of the scanning electron microscope, X-ray diffraction, focused ion beam SEM, and TESCAN Integrated Mineralogy Analyser.

The authors acknowledge The Institute for Geoscience Research for financial support through TIGeR Small Grants.

The authors would like to acknowledge Jeanne Edmands (CHIRI, Curtin University), Michael Nesbit (CHIRI), and Elaine Miller (JdLC, Curtin University) for their technical support with flow cytometry, light and confocal laser scanning microscopy, and electron microscopy.

## **Acknowledgement of Country**

We acknowledge that Curtin University works across hundreds of traditional lands and custodial groups in Australia, and with First Nations people around the globe. We wish to pay our deepest respects to their ancestors and members of their communities, past, present, and to their emerging leaders. Our passion and commitment to work with all Australians and peoples from across the world, including our First Nations peoples are at the core of the work we do, reflective of our institutions' values and commitment to our role as leaders in the Reconciliation space in Australia.

## Table of content

<b>Abstract</b>	<b>6</b>
<b>Chapter One Introduction</b>	<b>9</b>
Abstract	10
1. Background	11
1.1 Biohydrometallurgy and bioleaching	11
1.2 Rare Earth Elements (REE)	12
1.3 Bioleaching mechanisms	14
1.4 The significance of microorganism and microbial activity in bioleaching	18
1.5 Methods to study bioleaching and microbe-mineral interactions	22
2. Significance of the current study	25
3. Objectives and research methods	26
3.1 Objective 1 To determine the importance of biofilm formation in the bioleaching of phosphate-REE minerals.	26
3.2 Objective 2 To determine the microbial-mediated chemical and structural changes on the surface and subsurface of a mineral.	28
3.3 Objective 3 To determine the importance of complexolysis as a bioleaching mechanism for REE-phosphate minerals.	29
References	30
<b>Chapter Two Methodology development for reproducible rapid enumeration of bacterial cell using flow cytometry</b>	<b>36</b>
Abstract	37
1. Introduction	39
2. Experimental procedures	42
2.1 Microorganisms	42
2.2 Live Cell Staining with SYTO 85	43
2.3 Flow cytometry	43
2.3.1 Flow cytometer instrument	43
2.3.2 Initial settings of the flow cytometer	44
2.3.3 Evaluation of separation index	45
2.3.4 Swarm detection in response to cell concentration and flow rate	46

2.3.5 Effect of acquisition volume and EDTA on the calculate cell number	47
2.3.6 Validation of the optimised method for different bacterial genera.	47
2.3.7 Statistical analysis	48
3. Results and Discussion	48
3.1 Evaluation of Separation Index	49
3.2 Swarm detection	53
3.3 Optimising the acquisition volume and EDTA concentration	58
3.4 Evaluating the optimised settings for other Gram-positive and Gram-negative bacteria	60
4. Conclusion	63
References	65
Supplementary files	68
<b>Chapter Three Biofilm formation on the surface of monazite and xenotime during bioleaching</b>	<b>80</b>
Abstract	83
1. Introduction	84
2. Material and methods	86
2.1. Minerals and their characterisation	86
2.2. Microorganism	87
2.3. Cell enumeration by flow cytometry	87
2.4. Evaluation of biofilm formation	88
2.5. Live imaging	90
2.6. Fluorescent microscopy	91
2.7. SEM-EDS	91
2.8. Focused Ion Beam- Scanning Electron Microscopy (FIB-SEM)	91
3. Results	92
3.1. Mineral characteristics	92
3.2. Biofilm formation	93
3.3. Localization of attachment and biofilm formation to physical imperfections	98
3.4. Localization of attachment and biofilm formation to specific mineralogy or chemical composition	100

3.5. Changes on the surface and subsurface of the monazite minerals due to microbial activity	102
4. Discussion	103
5. Conclusion	108
References	110
Supplementary material	112
<b>Chapter Four Quantitative analysis of the biofilm stages and extracellular DNA production by <i>Klebsiella aerogenes</i> in bioleaching settings</b>	<b>161</b>
Abstract	162
1. Introduction	164
2. Methods	167
2.1 Microorganisms	167
2.2 Minerals:	167
2.3 CLSM settings for analysis of microbe-mineral surface interactions	167
2.4 3D modelling in NIS-Elements and Imaris	168
2.4.1 CLSM-Z-stack imaging	168
2.4.2 Computer aided modelling of the surface, microorganisms, and differently stained chemical properties of biofilm/microorganisms	169
2.5 SEM-based quantitative analysis of microbe-mineral interactions.	170
2.6 Biofilm thickness and complexity analysis	170
2.7 Statistical analysis	171
3. Results and discussion	171
3.1 Evaluating the computer aided modelling	171
3.1.1 Computer aided modelling of CLSM data	171
3.1.2 Computer aided modelling of SEM data	173
3.2 Autofluorescence of the surface before and after abiotic treatments	175
3.3 CLSM-based quantitative analysis of biofilm development	177
3.4 SEM based study of microbe-mineral surface interactions	179
3.5 Biofilm thickness	181
3.6 Changes in the biochemical properties of the extracellular polymeric substances (e-DNA in particular)	181
4. Conclusion	183

References	185
Supplementary files	189
<b>Chapter Five</b> <i>Klebsiella aerogenes</i> adhesion behaviour during biofilm formation on monazite	<b>193</b>
Abstract	195
1. Introduction	196
2. Methods	199
2.1. Minerals	199
2.2. Microorganism and Culture Conditions	200
2.3. Cell Enumeration with Flow Cytometry	200
2.4. Bacterial and eDNA Attachment Behaviour	201
2.5. Live Imaging and Evaluation of eDNA Production	203
2.6. Fluorescent Microscopy	204
2.7. Measurement of Surface Electrical Potential	204
2.8. Statistics	204
3. Results	204
3.1. Attachment Behaviour in Response to the Monazite Particle Size	204
3.2. Cell Attachment Behaviour in Response to the Nutrient Amendment and Surface Material Available for Attachment	206
3.3. Cell Attachment Behaviour in Response to the Changes in the Initial Inoculum Size	208
3.4. The Effects of the Available Area for Attachment on the Attachment Efficiency	209
3.5. eDNA Production by <i>K. aerogenes</i>	210
3.6. Role of eDNA in Early Attachment and Interaction with the Surface	213
3.7. Effects of the Surface Preconditioning with eDNA on Attachment of <i>K. aerogenes</i> Cells	215
4. Discussion	216
5. Conclusion	222
References	225
Supplementary Material	227
<b>Chapter Six</b> Complex formation (complexolysis) between rare earth elements and organic acids, a microbial bioleaching mechanism in the extraction of phosphate minerals	<b>230</b>



Abstract	231
1. Introduction	233
2. Methods	235
2.1 Microorganism	235
2.2 Minerals	235
2.3 Chemical and biological leaching	236
2.3.1 Chemical leching	236
2.3.2 Bioleaching	236
2.4 Mineralogy analysis	237
2.5 Scanning Electron Microscopy	237
2.6 Preparation of TEM foils	237
2.7 Scanning transmission electron microscope	238
2.8 FIB- Time-of-Flight Secondary Ion Mass Spectrometer microanalysis	239
2.9 IONTOF-ToF-SIMS microanalysis settings	239
3. Results and discussion	241
3.1 STEM XEDS capacity to analyse chemical changes at the immediate surface and subsurface	241
3.2 FIB-ToF-SIMS analysis of the surface and interface	250
3.3 ION-ToF-SIMS analysis of the surface and interface	253
4. Conclusion	261
References	263
Supplementary	265
<b>Chapter Seven General Discussion</b>	<b>272</b>
Future directions	277
References	278

# Abstract

Biohydrometallurgy presents a promising, cost-effective, and environmentally friendly avenue for extracting metals from low-grade ores and reprocessing metal-bearing wastes, where traditional metallurgical methods fall short economically and environmentally. Rare earth elements (REEs), which play critical roles in various green technologies like solar panels and smartphones, are of interest for biohydrometallurgy. However, only a handful of REE-bearing minerals such as monazite and xenotime, are commercially exploitable. These minerals are known as phosphate minerals; hence phosphate solubilising microorganisms (PSM) can be utilised to bioleach such minerals such and thereby extract a proportion of their REE content.

Despite the potential of bioleaching for phosphate minerals, there is a limited amount of research on the topic, particularly about the underlying mechanisms. Understanding these mechanisms could shed light on microbial-mediated (bio) chemical and physical processes like leaching, mineralisation, weathering, and remediation. This knowledge could be invaluable for enhancing biomining. Hence, this work aimed to study several key aspects:

Firstly, this research investigated microbial attachment to phosphate mineral surfaces and the subsequent formation of biofilms, as the interplay between microbial attachment and biofilm formation is pivotal in the effectiveness of bioleaching processes.

Secondly, microbial behaviour of a model PSM, *Klebsiella aerogenes*, during the early stage of biofilm formation was explored. This stage is crucial and a determining stage as it can heavily affect the further stages of biofilm development.

Thirdly, investigations of the microbial-mediated chemical and structural changes occurring on the surface and subsurface of minerals during bioleaching were performed. These changes provide insights into the overall bioleaching mechanisms, providing valuable information for enhancing strategies regarding metal recovery from ores.

Lastly, this research studied complexolysis, a previously hypothesised bioleaching strategy employed by PSM, in which the complex formation between organic acids produced by PSM and REE was studied using secondary ion mass spectrometry.

For this study, four phosphate-REE mineral samples were used, including two locally acquired ores that have a high mineral complexity, one a high-grade monazite ore (HGMO, Lynas Corp, WA, Australia), and a xenotime ore (Northern Minerals, WA, Australia), and two REE crystal containing higher purity REE-phosphates minerals, a monazite-muscovite crystal, and a xenotime crystal.

To achieve these objectives, *K. aerogenes* ATCC 13048 was used as the model PSM.

The attachment behaviour of *K. aerogenes* on monazite surfaces during the initial attachment stage of biofilm formation was particularly crucial, as it set the stage for subsequent biofilm development. Factors influencing microbial attachment, including surface properties, particle size, available attachment area, and initial inoculum size, were also investigated.

Experimental findings revealed that *K. aerogenes* swiftly attaches to monazite surfaces upon exposure to the ore. However, the ratio of planktonic to sessile cells varied significantly in response to particle size, available attachment area, and initial inoculum size. Attachment preferentially occurred on larger particles and reducing the inoculum size or increasing the

available attachment area further enhanced attachment efficiency. Notably, a portion of the inoculated cells remained in a planktonic state throughout the attachment process.

Moreover, the study examined the role of extracellular DNA (eDNA) in microbial attachment. While *K. aerogenes* exhibits lower eDNA production in response to altered surface chemical properties, the presence of eDNA impedes bacterial attachment due to repulsive interactions with bacterial cells.

Additionally, microscopic analysis using confocal laser scanning microscopy (CLSM) and scanning electron microscopy (SEM) provided insights into the stages of biofilm development on phosphate minerals. Three distinct stages were observed, starting with initial attachment, followed by surface colonisation and biofilm maturation, and concluding with dispersion. Biofilm formation primarily occurs at physical surface imperfections, such as cracks and grooves, with no discernible preference for specific mineralogical or chemical characteristics.

Time-of-Flight Secondary Ion Mass Spectrometry (ToF-SIMS) analysis of bioleached samples showed the first empirical evidence of complex formation between rare earth metals such as cerium, lanthanum and neodymium with organic acids including formic acid, acetic acid, lactic acid, oxalic acid, and several others, indicating complexolysis is another viable mechanism in bioleaching of REE-phosphate minerals.

Overall, this study underscores the potential of bioleaching with PSM for extracting REEs from phosphate minerals and highlights the intricate interplay between microbial attachment, biofilm formation, and mineral surface properties. By elucidating such interaction and shedding light to another mechanism for bioleaching, this research contributes to advancing bioleaching technologies for sustainable rare earth metal extraction and environmental remediation.

# **Chapter One**

## **Introduction**

## **Abstract**

### Background

Biohydrometallurgy is a cost-effective environmentally friendly approach to the extraction of metals from low-grade ores that cannot be processed economically by pyrometallurgical approaches. It can also be applied to the reprocessing of metal-bearing wastes. The rare earth elements (REE) have numerous applications in current and emerging green technologies such as solar panels and smartphones. Only very few REE-bearing minerals are commercially exploitable, two of them being monazite and xenotime, both being phosphate minerals. Some microorganisms can solubilise phosphate from insoluble phosphate minerals and are referred to as phosphate solubilizing microorganisms (PSM). Therefore, it is possible to use PSM for bioleaching of phosphate minerals such as monazite.

### Significance

Very few studies on the bioleaching of phosphate minerals have been performed and even less is known about the underlying mechanisms. Consideration of these potential mechanisms will provide additional information to our current understanding of microbial mediated leaching, mineralization, weathering, remediation, and other similar biogeochemical processes, and can be used to enhance the application of this process in biomining and agriculture industries.

### Objectives

The objectives of this research are to:

- Provide empirical evidence of biofilm formation and its development stages, as the most important prerequisites of contact leaching.

- Determine the specificity of early attachment of microbes to the mineral surface and subsequent biofilm formation
- Determine the microbial-mediated chemical and structural changes on the surface and subsurface of a phosphate mineral

## **1. Background**

### **1.1 Biohydrometallurgy and bioleaching**

Metals have been an essential commodity of human life since the pre-historic era, when humans learned how to smelt metal-bearing ores to extract their precious materials <sup>1</sup>. Depletion of high-grade mineral resources, high energy consumption and environmental issues of traditional mining processes, lead the mining industry to search for alternative cost-effective and environmentally friendly processes, such as biohydrometallurgy, to exploit low-grade mineral deposits <sup>2-4 5</sup>. Biohydrometallurgy is the extraction of metals from mineral ores, concentrates or waste materials in an aqueous solution using living organisms or their products <sup>5</sup>. Today, microorganisms are used for the extraction and/or recovery of metals and metalloids such as gold, copper, uranium, cobalt, zinc, nickel and rare earth elements<sup>6-12</sup> through mobilization or immobilization processes. Bioleaching is a biohydrometallurgical approach and is defined as the dissolution of minerals and mobilization of metal cations from ores through biological activities <sup>4,13,14</sup>.

#### **1.1.1 Significance of biohydrometallurgy**

Biohydrometallurgy is seen as a greener approach to the extraction of metals from low-grade ores and reprocessing of wastes including electronic waste, existing acid mine drainage,

process waters, and wastewaters <sup>2,5,9,13,15,16</sup>. Approximately 10-15% of the global copper production and 5% of the global gold production utilises biohydrometallurgy <sup>9,11,17</sup>. Bioleaching comes with its own disadvantages and bottlenecks, including but not limited to, 1) compared to smelting it is a slow process, and 2) it sometimes produces toxic chemicals such as sulfuric acid that need to be properly contained <sup>2,13</sup>.

## **1.2 Rare Earth Elements (REE)**

### **1.2.1 Importance and abundance**

The REE are 17 elements in the periodic table of elements including scandium, yttrium, and 15 elements of the lanthanide series <sup>18-20</sup>. Despite their name, these elements have a relatively high concentration in the earth crust, with, cerium the 25<sup>th</sup> most abundant element and with a concentration higher than that of copper and nickel <sup>21</sup>. However, REE tend not to become concentrated in exploitable ore deposits. Their importance and application are well discussed in a review by Balaram (2019) <sup>18</sup>. These elements have applications in many modern technologies, including, in the production of smartphones, hard drives, light-emitting diodes, magnetic resonance imaging (MRI) and fibre-optics, as well as applications in many technologies such as solar panels, wind turbines, highly efficient but less toxic rechargeable batteries, and high-strength permanent magnet alloys for magnetic refrigeration <sup>18,19</sup>. In particular, there is a very high demand in energy-efficient tools for REE due to their distinctive magnetic, phosphorescent, and catalytic properties. The price per kg for many of the REE is between \$1,000-9,000 due to the high demand but low production level <sup>19</sup>.

### **1.2.2 Abundance and ore mineralogy on the Earth's crust**

Due to their reactive nature, REE do not occur as native metals but are present in more than 250 minerals, including silicates, carbonates, oxides, and phosphates <sup>20</sup>; though, very few of



these minerals are commercially exploitable<sup>22</sup>. Those that are mined for profit include bastnäsite (carbonate-fluoride minerals), monazite (phosphate mineral), xenotime (phosphate mineral), loparite (oxide mineral) and lateritic ion-adsorption clays<sup>18,20,21</sup>. In 2010, China, as the main producer of REE (>90%), significantly reduced the REE production/export, leading to an REE crisis in the world. Although the global supply rate of REE is still higher than the global demand<sup>23</sup>, the potential for another supply crisis is possible. Since REE are becoming the cornerstone of the new green technologies, increasing the production rate by waste recycling, enhancing the current extraction processes, or using alternative extraction processes is necessary.

### 1.2.3 Bioleaching of REE

Conventional REE extraction is either using an alkaline process with concentrated sodium hydroxide or using an acidic process with concentrated sulfuric acid and high temperatures. Either way, large quantities of toxic waste containing thorium, uranium, hydrogen fluoride, and acidic wastewater<sup>24,25</sup> are generated which result in significantly higher environmental consequences compared to other metals<sup>26</sup>.

Although the commercial application of bioleaching has been limited to a few mineral ores, recent reports signify that it is possible to use bioleaching for extraction or bio-recycling of REE bearing minerals<sup>15,27-30</sup> and wastes<sup>31-35</sup>. Some of the key reports on this matter are bioleaching of REE-bearing zircon using *Acetobacter methanolicus* and *Acidithiobacillus ferrooxidans* (with a recovery yield of 60-80 %) <sup>36,37</sup>, bastnäsite bioleaching using *Actinobacteria* (1.8 mg L<sup>-1</sup> yield)<sup>30</sup>, red mud bioleaching using *Penicillium tricolor* (36-78% yield)<sup>38</sup>, and REE-bearing soil bioleaching using *Actinomycetes* (12-37% yield)<sup>39</sup>. The dissolution of REE-bearing phosphate minerals such as monazite or xenotime during

bioleaching appears to be a side effect of bacterial activity to access phosphate<sup>28,40</sup>, however, the detailed mechanism of phosphate solubilisation is not well understood for many PSM<sup>15</sup>.

#### **1.2.4 Phosphate solubilizing microorganisms**

In the case of phosphate minerals, it is shown that many microorganisms can dissolve insoluble forms of phosphate from the solid minerals of the soil and are referred to as phosphate solubilizing microorganisms (PSM). This capacity has been reported for many microorganisms and includes Gram-positive and Gram-negative bacteria, cyanobacteria, archaea, fungi, microalgae, and even protozoa, as reviewed by Kishore et al. (2015)<sup>41</sup>. These have been mostly studied due to the agricultural application of such microorganisms in soil fertilization<sup>41,42</sup>. Another application of this microbial capacity is the biomining of phosphate mineral as PSM can dissolve and use the phosphate content of such minerals as a sole source of phosphate. Nevertheless, this ability has been tested in only a few studies, mainly using PSM for REE biomining from monazite ores<sup>27-29,40,43-47</sup> or apatite minerals<sup>48-55</sup>. *Aspergillus ficuum* and *Pseudomonas aeruginosa*<sup>29</sup> were used for bioleaching of Egyptian monazite and resulted in a higher REE dissolution compared to chemical leaching<sup>29</sup>. Studies by Fathollahzadeh *et. al.* reported a significantly higher REE dissolution from monazite bioleaching using *Klebsiella aerogenes* (previously known as *Enterobacter aerogenes*) and a co-culture of *K. aerogenes* and *A. ferrooxidans*<sup>47</sup> compared to abiotic leaching<sup>28</sup>. Ceci et al. (2015, a&b) studied bioleaching of lead apatite minerals including pyromorphite, vanadinite, and mimetite using several fungi such as *Aspergillus niger* and *A. ustus* and reported a similar result (higher yield using bioleaching compared to abiotic leaching)<sup>53,54</sup>.

#### **1.3 Bioleaching mechanisms**

There are two important questions about microbial bioleaching, 1) what is the benefit of bioleaching for a microorganism? and 2) how do they do it? Answering these questions is the key to understanding the role of microorganism in the biogeochemical cycling of elements <sup>56</sup>. Understanding this processes is not only important as a fundamental microbial ecology question but is also of both environmental and industrial importance for a deeper understanding of microbial mediated leaching, mineralization, weathering, remediation, fouling, corrosion and similar processes <sup>57</sup>. Almost all our knowledge on this matter comes from numerous studies on sulfide minerals and acidophilic microorganisms.

Current explanations that answer the first question state that the released metals and other compounds from a mineral ore can be used as nutritional requirements or as a source of energy, for example in chemolithotrophic microorganisms <sup>58-60</sup>. These chemolithotrophs acquire energy from oxidation of the iron and sulfur content of the sulfide minerals and use that to fix carbon dioxide. Unlike chemolithotrophs, organotrophic microorganisms are not capable of using such mechanisms, instead they acquire their energy by consuming organic materials. However, while non-sulfidic ores such as phosphate minerals may contain no energy source for microorganisms <sup>16</sup>, they can provide access to vital nutritional requirements such as phosphate for both chemolithotrophs and organotrophs. Both groups can access the phosphate content of phosphate minerals via the breakdown of the mineral matrix, chemolithotrophs through the production of inorganic acids (sulfuric acid) and organotrophs through the production of organic acids such as oxalic or acetic acids.

The mechanisms by which microorganisms are able to mobilise metals <sup>3,4,61</sup> can broadly be categorised as (1) producing organic or inorganic acids (acidolysis); (2) oxidation and reduction reactions (redoxolysis); and (3) the excretion of complexing agents (complexolysis)

<sup>3</sup>. Microbes can use any of these mechanisms in three models of bioleaching <sup>3,4,62</sup>. Firstly, in contact leaching the microorganisms are attached to the mineral surface and leaching reactions take place in the extracellular polymeric substance (EPS) matrix at the interphase between attached cells and mineral particles. Secondly, in non-contact leaching the microorganisms are suspended in solution without having contact with the minerals and by producing lixivants, such as ferric iron and sulfuric acid they dissolve minerals and release metal(s) or other compounds. The third model is cooperative leaching model, a combination of contact and non-contact leaching. In the case of monazite as a phosphate mineral, Fathollahzadeh et. al (2018-a) proposed acidolysis, complexation of REE with organic acids and phosphate uptake by microorganisms as the driving forces of bioleaching <sup>28</sup>.

### **1.3.1 Bioleaching mechanisms for phosphate minerals**

Previous studies on monazite, an important commercially exploitable rare-earth phosphate mineral containing light REEs (La, Ce, Pr, Nd), showed that bioleaching is a potential approach for the extraction of REEs. The indigenous microbial community, acidophilic iron and sulfur oxidising bacteria, and phosphate solubilizing bacteria have been used as the bioleaching agents <sup>15,28,46,47,63</sup>.

Building upon many studies on bioleaching of sulfide minerals, Fathollahzadeh *et. al.* (2018 and 2019) proposed a conceptual model for bioleaching of phosphate minerals such as monazite <sup>15,28</sup>. However, the detailed mechanisms are different from that of the extensively studied sulfide minerals bioleaching. In the proposed model for the contact leaching of phosphate minerals, microorganisms attached to the surface of minerals produce and release organic acids into their environment. Phosphate anion and REE cations are released from phosphate minerals into the liquid phase due to the acidic attack by the released protons (H<sup>+</sup>)

(Reaction 1). This process is known as acidolysis. The released phosphate (Reaction 2) is taken up by microbial cells. Uptake of the phosphate from the environment changes the equilibrium of the chemical interaction (Reaction 2), thus more phosphate can be released and dissolved into the environment. This is one of the main forces driving bioleaching of phosphate minerals. Another major driving force of this phenomenon is hypothesised to be the interaction of the release of REE cation with the organic acid anions such as acetate, citrate, oxalate, and malate and the formation of secondary minerals (Reaction 3). This will further change the dissolution equilibrium by removing the dissolved REE cation to a certain extent.



In the proposed non-contact bioleaching model <sup>15,28</sup>, the microbial cells are not attached to the surface of the phosphate minerals. The cells release organic acids into the environment and the protons released from these organic acids attack the surface of the mineral and release the REE cation and phosphate anions. This process is very similar to chemical leaching (chemical model). However, the presence of microorganisms in the environment adds another factor (hence, biochemical model) in a sense that microorganisms take up the released phosphate and the organic acid (OA) anions released by the cells into the environment interact with the released REE cations and form REE-OA complexes <sup>15,28</sup>. As explained before, the cooperative model is a combination of contact and non-contact model, where attached cells take up phosphorus released by acid attack facilitated by organic acid-

producing suspended cells, or where suspended cells take up phosphorus released by acid attack facilitated by attached cells.

## **1.4 The significance of microorganism and microbial activity in bioleaching**

### **1.4.1 Attachment of microorganisms on the mineral surface**

Attachment of microorganism to the mineral surface is the first step of biofilm formation, and it is important to understand where this occurs on the mineral surface <sup>64</sup>. Attachment to mineral surfaces is mostly a microbial effort to find nutritional resources and is due to the high affinity of organic compounds on the microbial cell surfaces toward the mineral surface <sup>65-67</sup>. In contact bioleaching, attachment and subsequent biofilm formation enhances the leaching capacity of microorganisms by providing a unique microenvironment between the microbes and the mineral surface <sup>68</sup>. Some studies on the bioleaching of pyrite and chalcopyrite using acidophilic bacteria such as *A. ferrooxidans* showed that attachment of these bacteria and further biofilm formation on the surface of such minerals are not random and microorganisms are attracted to specific surface properties including the 3-D imperfections such as pits, cracks, and holes, or areas with certain physicochemical properties such as lower crystallinity degree, certain chemical composition, or local anodes and cathode on the surface. <sup>67-70</sup>. However, this tendency may not exist for some specific surface properties and microbes; for example, Fathollahzadeh et al. (2018-a) demonstrated that *K. aerogenes* attachment on the monazite surface showed no tendency toward specific area relevant to chemical composition <sup>28</sup>.

### **1.4.2 Biofilm**

The majority of natural microbial communities exists in a three-dimensional multicellular microbial structure known as “biofilm”. The cells in the biofilm are referred to as sessile cells, while those suspended in the aqueous phase are referred to as planktonic cells. The biofilm is defined as microbial aggregations enshrouded by a self-produced matrix of extracellular polymeric substances (EPS) <sup>71</sup>. Compared to planktonic cells, sessile cells are physiologically and behaviourally integrated and form highly structured microbial communities, thus can survive very harsh conditions. Planktonic cells are sensitive to changes in environmental conditions and can be eradicated very quickly and easily. In contrast, biofilms are a dynamic micro-ecosystem actively controlled by the microorganisms <sup>72,73</sup>. They can be either advantageous or disadvantageous, depending on their impact on humans, the environment and industry. For example, biofilms pose significant challenges in both medical settings and various industries. In hospital wards, biofilms can develop on vents, medical equipment, and surfaces, creating reservoirs of pathogens that are difficult to eradicate. These biofilms enable pathogens to persist in the environment, increasing the risk of hospital-acquired infections <sup>71,74</sup>. In industrial settings, biofilms contribute to corrosion and fouling, which can have severe economic and safety implications. Biofilms can form on metal surfaces in pipelines, water systems, and storage tanks, accelerating the corrosion process through microbial activity <sup>74</sup>. This phenomenon, known as microbiologically influenced corrosion (MIC), occurs when microorganisms in the biofilm produce corrosive substances such as acids or sulfides. These substances degrade metals, leading to structural failures, leaks, and contamination of products <sup>74</sup>. In the oil and gas industry, MIC can cause pipeline ruptures, resulting in costly repairs and environmental damage <sup>74</sup>, and similarly, in water treatment facilities, biofilm-induced corrosion can compromise the integrity of infrastructure, leading to service disruptions and increased maintenance costs.

Biofilm benefits are seen in some industries and are utilised in several biotechnological applications, including the filtration of drinking water, the degradation of wastewater and solid waste, as biocatalysis in the production of bulk and fine chemicals, as well as biofuels<sup>71</sup>. The mining industry is one of the key sectors that exploits biofilm activity and research has shown that microbial biofilms can greatly enhance bioleaching yields<sup>5,9</sup>. From a bioleaching point of view, they act as environments where microorganism can release and preserve a high concentration of organic acids and use them for biosorption, bioprecipitation, chelation, and complex formation processes<sup>68,71,74</sup>.

#### **1.4.3 Role of EPS in biofilm formation, and bioleaching (attachment and adhesion)**

In general, the self-produced matrix of extracellular polymeric substances is a means of attachment by microorganism to abiotic (e.g., mineral surface) or biotic surfaces (e.g., other microbial cells). Moreover, many of the diverse structural and functional properties of biofilm come from the EPS, as reviewed by Flemming et al. (2010 and 2016) and Hunter and Beveridge (2008)<sup>71,73,75</sup>. The quantity and quality of EPS production in planktonic and especially in sessile cells is highly dynamic, in a constant state of turnover, and responsive to the changes in the environment<sup>73</sup>. EPS can mediate the early attachment of planktonic cells to surfaces and further assists with the formation of a strong, cohesive, and three-dimensional polymer network<sup>76</sup>. It also has many ionisable functional groups (i.e., carboxyl, phosphoryl, amino and hydroxyl) and may contain organic acid contents that not only are important as a proton source for acidolysis, but also can stimulate and form complexes with the released metallic and non-metallic ions and compounds (an important functionality in a bioleaching)<sup>68,73,77</sup>. In general, EPS composition and function in planktonic and sessile cells have some similarities,



yet there are some significant differences<sup>73,76</sup>. For example, the complexation capacity of the EPS in sessile cells is significantly higher than that of planktonic cells<sup>73</sup>.

#### **1.4.4 Role of organic acids in bioleaching**

Several studies using fungi as the bioleaching microorganism and showed that organic acids produced such as citric<sup>29,38,78</sup>, oxalic<sup>29,38,53,54,78,79</sup>, and gluconic acid<sup>27,29,78</sup> had a major role in the mobilization of metals from the mineral ores or wastes. Bacteria also produce organic acids such as oxalic<sup>30,36,37</sup>, citric, lactic<sup>80</sup>, and gluconic acid<sup>32,37</sup> as essential lixivants for bioleaching. In the case of the bioleaching of phosphate minerals, production of oxalic, gluconic, citric, acetic and several other organic acids have been reported as the lixiviant agents<sup>15,28,32,40,47</sup>. The two important roles for organic acids in the bioleaching process are acidolysis, and complexolysis. The organic acids may act solely as a dissolving agent<sup>27</sup>, similar to the role of sulfuric acid in the bioleaching of sulfide minerals, (acidolysis). however, contact leaching is responsible for high bioleaching yields. The bioleaching of REE-bearing zircon with gluconic acid resulted in 60-80 % mobilization in contact experiments while non-contact bioleaching efficiency was dramatically decreased to only 4%<sup>36</sup>. Fathollahzadeh et al. (2018) showed that the leaching efficiency of REE dissolution was highest for contact bioleaching, then non-contact bioleaching and abiotic leaching, respectively<sup>28</sup>. Organic acids can also form complexes with the released metals, specifically REE, as explained by Ceci et al.<sup>53,54</sup> for fungal bioleaching of phosphate minerals and Fathollahzadeh et al.<sup>15,28,47</sup> for bacterial bioleaching of phosphate minerals. It is demonstrated that the produced REE-organic acids complexes may either precipitate or be a water-soluble salt<sup>40,53,54</sup>.

#### **1.4.5 Microbial mediated changes on the surface of minerals**

Microbes can impose many changes on the surface and subsurface of minerals through either contact and non-contact bioleaching<sup>81</sup>. Non-contact bioleaching changes are similar to those of chemical leaching using non-organic and organic acids, that is, the surface and subsurface of a mineral are changed as a result of chemical reactions. These reactions change the chemical structure of a mineral on the surface or subsurface by the mobilization of elements and compounds. Examples are the dissolution of phosphate or REE during leaching of phosphate minerals, and formation of jarosite during leaching of sulfide minerals<sup>36,66,67</sup>. The mobilization and immobilization also change the 3-D physical structure. Although chemical leaching, non-contact bioleaching, and contact bioleaching processes can impose such changes, it has been shown that the latter resulted in more extensive changes compared to that of chemical leaching or non-contact bioleaching. For example in contrast to superficial etching pits through partial dissolution of the surface of minerals through chemical leaching, contact-bioleaching of carrollite using a consortia of acidophilic bacteria resulted in the formation of deep corrosion patterns and groove- or channel-like cavities<sup>82,83</sup>, bioleaching of pyrite using *A. ferrooxidans* resulted in the formation of deep corrosion pores<sup>84</sup>, and fungal bioleaching of vanadinite resulted in deep corrosion pattern by digging holes in the mineral grain (hyphae penetration into the subsurface)<sup>54</sup>.

### **1.5 Methods to study bioleaching and microbe-mineral interactions**

There has been a great deal of research on microbe-mineral interactions during bioleaching from a range of views such as microbial, physical and chemical, utilizing a large range of methods.

Microscopy techniques are essential analytical methods for studying microbe-metal interaction. Confocal laser scanning microscopy (CLSM) or epifluorescence microscopy (EFM) were used to study the formation, structure, and function of biofilms and the EPS in microbial biofilms, for example in the bioleaching of pyrite and chalcopyrite using acidophilic bacteria such as *A. ferrooxidans* and *A. caldus* <sup>73,85-87</sup>. Staining with membrane permeable or impermeable specific fluorescent dye for particular polymers, (bio) chemical bonds, or metals, utilises these microscopy techniques to monitor the change in the polymeric composition and function of a biofilm matrix. For example, to study changes in protein, lipid, polysaccharide and extracellular DNA (eDNA) content of the EPS, or the bonding capacity and distribution pattern of the interactions between EPS or cells with metals <sup>73</sup>. McCutcheon and Southam (2018) reviewed the application of electron microscopy such as transmission electron microscopy (TEM) or scanning electron microscopy (SEM) in biofilm studies <sup>88</sup>, and when combined with analytical equipment such as energy dispersive X-ray spectroscopy (EDS), RAMAN spectroscopy, TEM and SEM provided critical information about the chemical composition of biological and mineral samples. However, there are problems with the electron microscopy of biological samples (in particular biofilms). EPS has a 97% water content, thus, subjecting such samples to chemical fixation and a vacuum environment impose extensive changes to the biofilm <sup>73,88,89</sup>. Cryo-fixation has been used as a promising approach in biofilm and EPS microscopy studies, since the cells and their biofilm polymers are snap-frozen and physically fixed, or vitrified, in space and time <sup>5,73,88</sup>. Another useful microscopy technique is atomic force microscopy (AFM) which can be used to image a surface or to determine the adhesive force between different samples, in particular between a biological sample such as biofilm with a mineral surface <sup>34,64,76,90,91</sup>. In fact, AFM is one of the few techniques available for quantitative measurement of molecular interactions during

microbial attachment to a surface. It utilises repulsive and attractive forces in order to determine the topographic, force and electrochemical properties of surface interactions. It is considered as a method with little or no destructive changes on biological samples, thus can be used for *in situ* study of biofilms <sup>92</sup>.

While microscopy is useful for visualizing biofilm behaviour and microbial-mediated changes to the surface of minerals, the changes on the physical structure and integrity of the minerals require a detailed understanding of microbe-metal interactions, covering chemical changes that have need of the combination of microscopy techniques with analytical equipment. Energy-dispersive X-ray spectroscopy (EDS) and electron energy loss spectroscopy (EELS) have been used for chemical or elemental mapping, determining the oxidation state of elements, and identifying the functional group in biological samples <sup>5,73</sup>, while Raman micro-spectroscopy has been used for non-destructive chemical characterization of wet biofilm samples <sup>5</sup>.

Secondary ion mass spectroscopy (SIMS) can provide information about the chemical composition of a surface, biofilm mapping, elemental or isotope mapping, and interaction (uptake) of isotopes with biological samples such as EPS or cells <sup>5,93-95</sup>. Focused ion beam (FIB) can be combined with electron microscopy, SIMS spectroscopy, Time of Flight (ToF) spectroscopy, and X-ray based spectroscopy to provide information about the 3-D structure of a sample (3-D tomography) and 2-D or 3-D chemical mapping of both organic and inorganic materials <sup>96-98</sup>. Utilisation of these techniques can permit the study of how a PSM such as *K. aerogenes* interact with a mineral surface, how the physical and chemical properties of the surface and subsurface changes due to microbial activity, and if the organic acids produced by PSM forms complexes with the released REE.

Microbiological analysis to study bioleaching, biofilm formation, and microbe-metal interaction can range from basic methods such as monitoring and measuring the growth of microorganism (growth rate), to more complex or sophisticated methods to study the production of particular molecules or polymers through gene expression, metabolomics, genomics, transcriptomics, proteomics or meta-OMICs analyses.

## **2. Significance of the current study**

Research in the field of bioleaching has focussed extensively on sulfide minerals. Moreover, our knowledge of microbe-mineral interactions and the mechanisms of metal mobilization is limited to a few microorganisms and minerals. Energy important minerals, in particular, phosphate minerals, have been of interest for biomining over the last few years (see [section 1.2](#)). These mineral ores are of great interest because of their rare earth elements contents (as in the case of monazite and xenotime), or other energy important metals such as vanadium (vanadinite) and lithium (lithiophilite). These metals are of significant importance for current and yet to be developed technologies due to their special physical, chemical, and electrical attributes. Due to their numerous applications in new and developing technologies, there is a high demand for these metals, which is predicted to increase further. Using conventional extraction methods means dealing with serious economic and environmental drawbacks, while biohydrometallurgical approaches as an alternative offer some advantages (see [section 1.1](#)).

When compared to the bioleaching of sulfide minerals there is little information on the bioleaching of phosphate minerals, and much less is known about the microbe-mineral interactions and metal mobilization from these minerals. Addressing the microbe-mineral interaction will provide additional information to our current understanding of microbial

mediated leaching, mineralization, weathering, remediation, fouling, corrosion, and other similar biogeochemical processes. Hence, as explained in [section 1.3](#), understanding this process is not just a matter of fundamental microbial ecology and biogeochemistry, but can also enhance the environmental and industrial application of using phosphate solubilizing microorganism in biomining or agriculture industries.

In general, microbial attachment to surfaces and possible biofilm formation are universal phenomena of microbial life <sup>99</sup>. Bacterial attachment and subsequent biofilm formation (contact bioleaching) are very important prerequisites to achieving higher bioleaching efficiency <sup>68,70</sup>. In a previous study, Fathollahzadeh *et al.* (2018-a) clearly showed that non-contact leaching is a valid model in the bioleaching of phosphate minerals<sup>28</sup>. In this study, we aim to validate contact leaching by investigating microbial attachment and formation of biofilm on the surface of monazite using advanced microscopy techniques. Moreover, we aim to investigate whether PSM use complexolysis as one of their bioleaching mechanisms.

### **3. Objectives and research methods**

#### **3.1 Objective 1**

**To determine the importance of biofilm formation in the bioleaching of phosphate-REE minerals.**

For this objective, a high-grade monazite ore (HGMO), as a rare earth bearing phosphate mineral was subjected to bioleaching by *Klebsiella aerogenes*. The following analyses were performed:

1- Biofilm formation and its stages

Confocal laser scanning microscopy (CLSM) and scanning electron microscopy (SEM) were employed to evaluate initial attachment and biofilm development over a time course experiment. Biofilm development was then studied both quantitatively and qualitatively.

## 2- Localisation of microbial colonisation and biofilm formation

It is important to understand if microorganisms have a tendency to attach to certain physical surface properties such as structural imperfections like grooves, pits, holes, cracks, and scratches. It is also important to determine if microbial colonisation is preferred around certain mineralogy or chemical composition. Understanding any preference in colonisation can be used to improve bioleaching process. CLSM, SEM and energy dispersive X-ray spectroscopy (EDS) were used for this aim.

## 3- Microbial behaviour during the early stage of the attachment

Microbial attachment at the early stage is a determining factor in the further development of a biofilm. This objective had two aims, one to determine if microorganisms produce extracellular DNA (eDNA) on REE-phosphate mineral, and if eDNA plays a role in the initial attachment. The second aim was to determine how the ratio of planktonic to sessile subpopulations changes in response to changing environmental factors such as initial cell number. eDNA production was studied by staining *K. aerogenes*' biofilm with TOTO-1, a fluorescent dye specifically targeting eDNA in live samples. The second aim required developing a fast and reliable methodology to enumerate bacterial cell number without any further processes but staining with specific fluorochromes. This research uses "attachment" and "adhesion" interchangeably to describe the act of attachment, irrespective of its mechanism or strength. However, "adsorption" is employed when referring to eDNA attachment to surfaces or its influence on the attachment of microbial cells to a surface.

4) Adopting and developing a reproducible fast method based on flow cytometry for enumeration of bacterial cells

Flow cytometry was used to assess the ratio of attached vs. planktonic cells in a time course experiment. The attachment capacity (biofilm formation capacity) of the planktonic cells after exposure to the mineral was evaluated based on the ratio of planktonic vs. sessile cells over the first 4 hours after inoculation of the media with the microorganism. The samples were stained using nucleic acids specific fluorescent dyes.

### **3.2 Objective 2**

**To determine the microbial-mediated chemical and structural changes on the surface and subsurface of a mineral.**

For this objective, the mineral surface and subsurface was investigated by exposing REE-mineral(s) to abiotic (chemical) leaching, and bioleaching. The following changes were monitored to provide information about the type and level of changes in the mineral properties due to microbial activities, and chemical speciation of the mineral compounds during bioleaching. The changes on the surface structure in terms of erosion and weathering and or forming physical imperfections such as pits, holes, cracks, scratches that have been reported in sulfide minerals were examined. Any changes in the mineral and elemental mapping of surface and subsurface of the mineral ore was studied using Scanning transmission electron microscopy (STEM) and microanalysis using high-resolution EDS (XEDS). Focused ion beam (FIB) was used to prepare the STEM samples and FIB-SEM was used to study the biofilm structure from a cross-section.



### **3.3 Objective 3**

**To determine the importance of complexolysis as a bioleaching mechanism for REE-phosphate minerals.**

Although previous studies hypothesised complex formation between REE cation and organics acid anions as one of the bioleaching mechanisms of REE-phosphate mineral employed by PSM, as yet there is no empirical evidence. Time of flight secondary ion mass spectrometry (TOF-SIMS) was used to investigate REE-OA complex formation on monazite after bioleaching by *K. aerogenes*, and to detect any potential REE-OA complex formation on the minerals surface or within the biofilm.

## References

1. Tylecote RF, Tylecote R. *A history of metallurgy*. Institute of materials London; 1992.
2. Johnson DB. Mining and Microbiology: Established, Evolving and Emerging Biotechnologies. 2008,
3. Brandl H. Microbial leaching of metals. *Biotechnology*. 2001;10:191-224.
4. Bosecker K. Bioleaching: metal solubilization by microorganisms. *FEMS Microbiology reviews*. 1997;20(3 - 4):591-604.
5. Kaksonen AH, Boxall NJ, Gumulya Y, et al. Recent progress in biohydrometallurgy and microbial characterisation. *Hydrometallurgy*. 2018;180:7-25. doi:10.1016/j.hydromet.2018.06.018
6. Kaksonen AH, Boxall NJ, Usher KM, Ucar D, Sahinkaya E. Biosolubilisation of Metals and Metalloids. In: Rene ER, Sahinkaya E, Lewis A, Lens PNL, eds. *Sustainable Heavy Metal Remediation: Volume 1: Principles and Processes*. Springer International Publishing; 2017:233-283. doi:10.1007/978-3-319-58622-9\_8
7. Morin DHR, d'Hugues P. Bioleaching of a cobalt-containing pyrite in stirred reactors: a case study from laboratory scale to industrial application. *Biomining*. Springer; 2007:35-55.
8. Puhakka JA, Kaksonen AH, Riekkola-Vanhanen M. Heap leaching of black schist. *Biomining*. Springer; 2007:139-151.
9. Brierley CL, Brierley JA. Progress in bioleaching: part B: applications of microbial processes by the minerals industries. *Applied Microbiology and Biotechnology*. 2013;97(17):7543-7552. doi:10.1007/s00253-013-5095-3
10. Schippers A, Hedrich S, Vasters J, Drobe M, Sand W, Willscher S. Biomining: Metal Recovery from Ores with Microorganisms. *Geobiotechnology I: Metal-Related Issues*. 2014;141:1-47. doi:10.1007/10\_2013\_216
11. Roberto FF. Copper Heap Bioleach Microbiology-Progress and Challenges. *Trans Tech Publ*; 2017:250-254.
12. Van Aswegen PC, Haines A, Marais H. Design and operation of a commercial bacterial oxidation plant at Fairview. *Randol Perth Gold*. 1988;88:144-147.
13. Zhuang W-Q, Fitts JP, Ajo-Franklin CM, Maes S, Alvarez-Cohen L, Hennebel T. Recovery of critical metals using biometallurgy. *Current opinion in biotechnology*. 2015;33:327-335.
14. Rawlings DE. Heavy Metal Mining Using Microbes. *Annual Review of Microbiology*. 2002;56(1):65-91. doi:10.1146/annurev.micro.56.012302.161052
15. Fathollahzadeh H, Eksteen JJ, Kaksonen AH, Watkin ELJ. Role of microorganisms in bioleaching of rare earth elements from primary and secondary resources. *Applied Microbiology and Biotechnology*. 2019;103(3):1043-1057. doi:10.1007/s00253-018-9526-z
16. Jain N, Sharma DK. Biohydrometallurgy for Nonsulfidic Minerals—A Review. *Geomicrobiology Journal*. 2004;21(3):135-144. doi:10.1080/01490450490275271
17. Watling HR. The bioleaching of sulphide minerals with emphasis on copper sulphides - A review. *Hydrometallurgy*. 2006;84(1-2):81-108. doi:10.1016/j.hydromet.2006.05.001
18. Balaram V. Rare earth elements: A review of applications, occurrence, exploration, analysis, recycling, and environmental impact. *Geoscience Frontiers*. 2019;doi:<https://doi.org/10.1016/j.gsf.2018.12.005>
19. Haxel GB, Hedrick JB, Orris GJ, Stauffer PH, Hendley li JW. *Rare earth elements: critical resources for high technology*. United States Department of the Interior, United States Geological Survey; 2002:1-4. 087-02. doi:10.3133/fs08702
20. Dostal J. Rare Earth Element Deposits of Alkaline Igneous Rocks. *Resources*. 2017;6(3)doi:10.3390/resources6030034

21. Van Gosen BS, Verplanck PL, Long KR, Gambogi J, Seal li RR. *The rare-earth elements: Vital to modern technologies and lifestyles*. United States Department of the Interior, United States Geological Survey; 2014:1-4. 2014-3078. doi:10.3133/fs20143078
22. Neary CR, Highley DE. Chapter 12 - The Economic Importance of the Rare Earth Elements. In: Henderson P, ed. *Developments in Geochemistry*. Elsevier; 1984:423-466. doi:<https://doi.org/10.1016/B978-0-444-42148-7.50017-4>
23. Klinger JM. Rare earth elements: Development, sustainability and policy issues. *The Extractive Industries and Society*. 2018;5(1):1-7. doi:<https://doi.org/10.1016/j.exis.2017.12.016>
24. Abreu RD, Morais CA. Purification of rare earth elements from monazite sulphuric acid leach liquor and the production of high-purity ceric oxide. *Minerals Engineering*. 2010;23(6):536-540. doi:<https://doi.org/10.1016/j.mineng.2010.03.010>
25. Hurst C. *China's rare earth elements industry: What can the west learn?* Institute for the Analysis of Global Security (IAGS); 2010:1-43.
26. Haque N, Hughes A, Lim S, Vernon C. Rare Earth Elements: Overview of Mining, Mineralogy, Uses, Sustainability and Environmental Impact. *Resources*. 2014;3(4)doi:10.3390/resources3040614
27. Brisson VL, Zhuang W-Q, Alvarez-Cohen L. Bioleaching of rare earth elements from monazite sand. 2016;113(2):339-348. doi:doi:10.1002/bit.25823
28. Fathollahzadeh H, Becker T, Eksteen JJ, Kaksonen AH, Watkin ELJ. Microbial contact enhances bioleaching of rare earth elements. *Bioresource Technology Reports*. 2018-a;3:102-108. doi:<https://doi.org/10.1016/j.biteb.2018.07.004>
29. Hassanien WAG, Desouky OAN, Hussien SSE. Bioleaching of some rare earth elements from Egyptian monazite using *Aspergillus ficuum* and *Pseudomonas aeruginosa*. *Walailak Journal of Science*. 2013;11(9):809-823.
30. Zhang LM, Dong HL, Liu Y, et al. Bioleaching of rare earth elements from bastnaesite-bearing rock by actinobacteria. *Chemical Geology*. 2018;483:544-557. doi:10.1016/j.chemgeo.2018.03.023
31. Marra A, Cesaro A, Rene ER, Belgiorno V, Lens PNL. Bioleaching of metals from WEEE shredding dust. *Journal of Environmental Management*. 2018;210:180-190. doi:10.1016/j.jenvman.2017.12.066
32. Reed DW, Fujita Y, Daubaras DL, Jiao Y, Thompson VS. Bioleaching of rare earth elements from waste phosphors and cracking catalysts. *Hydrometallurgy*. 2016;166:34-40. doi:<https://doi.org/10.1016/j.hydromet.2016.08.006>
33. Thompson VS, Gupta M, Jin H, et al. Techno-economic and Life Cycle Analysis for Bioleaching Rare-Earth Elements from Waste Materials. *ACS Sustainable Chemistry & Engineering*. 2018;6(2):1602-1609. doi:10.1021/acssuschemeng.7b02771
34. Keekan KK, Jalondhara JC, Abhilash. Extraction of Ce and Th from Monazite Using REE Tolerant *Aspergillus niger*. *Mineral Processing and Extractive Metallurgy Review*. 2017;38(5):312-320. doi:10.1080/08827508.2017.1350956
35. Park DM, Brewer A, Reed DW, Lammers LN, Jiao Y. Recovery of Rare Earth Elements from Low-Grade Feedstock Leachates Using Engineered Bacteria. *Environmental Science & Technology*. 2017;51(22):13471-13480. doi:10.1021/acs.est.7b02414
36. Becker S, Bullmann M, Dietze HJ, Iske U. Massenspektrographische Analyse ausgewählter chemischer Elemente bei der mikrobiellen Laugung von Zirkon. *Fresenius' Zeitschrift für analytische Chemie*. 1986;324(1):37-42. doi:10.1007/BF00469631
37. Glombitza F, Iske U, Bullmann M, Dietrich B. Bacterial leaching of zircon mineral for obtaining trace and rare earth elements(REE). 1988,
38. Qu Y, Lian B. Bioleaching of rare earth and radioactive elements from red mud using *Penicillium tricolor* RM-10. *Bioresource Technology*. 2013;136:16-23. doi:10.1016/j.biortech.2013.03.070
39. Hewedy MA, Rushdy AA, Kamal NM. Bioleaching of Rare Earth Elements and Uranium From Sinai Soil, Egypt Using Actinomycetes. *The Egyptian Journal of Hospital Medicine*. 2013;53(1):909-917. doi:DOI:10.12816/0001653

40. Corbett MK, Eksteen JJ, Niu X-Z, Croue J-P, Watkin ELJB, Engineering B. Interactions of phosphate solubilising microorganisms with natural rare-earth phosphate minerals: a study utilizing Western Australian monazite. 2017;40(6):929-942. doi:10.1007/s00449-017-1757-3
41. Kishore N, Pindi PK, Ram Reddy S. Phosphate-Solubilizing Microorganisms: A Critical Review. In: Bahadur B, Venkat Rajam M, Sahijram L, Krishnamurthy KV, eds. *Plant Biology and Biotechnology: Volume I: Plant Diversity, Organization, Function and Improvement*. Springer India; 2015:307-333. doi:10.1007/978-81-322-2286-6\_12
42. Alori ET, Glick BR, Babalola OO. Microbial Phosphorus Solubilization and Its Potential for Use in Sustainable Agriculture. *Frontiers in Microbiology*. 2017;8(971)doi:10.3389/fmicb.2017.00971
43. Shreedhar S, Devasya RP, Naregundi K, Young C-C, Bhagwath AAJAoM. Phosphate solubilizing uranium tolerant bacteria associated with monazite sand of a natural background radiation site in South-West coast of India. 2014;64(4):1683-1689. doi:10.1007/s13213-014-0812-4
44. Shin D, Kim J, Kim B-s, Jeong J, Lee J-c. Use of Phosphate Solubilizing Bacteria to Leach Rare Earth Elements from Monazite-Bearing Ore. *Minerals*. 2015;5(2):189-202. doi:10.3390/min5020189
45. Maes S, Zhuang W-Q, Rabaey K, Alvarez-Cohen L, Henebel T. Concomitant Leaching and Electrochemical Extraction of Rare Earth Elements from Monazite. *Environmental Science & Technology*. 2017;51(3):1654-1661. doi:10.1021/acs.est.6b03675
46. Corbett MK, Eksteen JJ, Niu X-Z, Watkin ELJ. Syntrophic effect of indigenous and inoculated microorganisms in the leaching of rare earth elements from Western Australian monazite. *Research in Microbiology*. 2018;169(10):558-568. doi:<https://doi.org/10.1016/j.resmic.2018.05.007>
47. Fathollahzadeh H, Hackett MJ, Khaleque HN, Eksteen JJ, Kaksonen AH, Watkin ELJ. Better together: Potential of co-culture microorganisms to enhance bioleaching of rare earth elements from monazite. *Bioresource Technology Reports*. 2018-b;3:109-118. doi:<https://doi.org/10.1016/j.biteb.2018.07.003>
48. Topolska J, Latowski D, Kaschabek S, Manecki M, Merkel BJ, Rakovan J. Pb remobilization by bacterially mediated dissolution of pyromorphite  $Pb_5(PO_4)_3Cl$  in presence of phosphate-solubilizing *Pseudomonas putida*. *Environmental Science and Pollution Research*. 2014;21(2):1079-1089. doi:10.1007/s11356-013-1968-3
49. Topolska J, Borowicz P, Manecki M, Bajda T, Kaschabek S, Merkel BJ. The effect of gluconic acid secretion by phosphate-solubilizing *Pseudomonas putida* bacteria on dissolution of pyromorphite  $Pb_5(PO_4)_3Cl$  and Pb remobilization. 2013:343-351.
50. Flis J, Manecki M, Merkel BJ, Latowski D. Bacteria mediated dissolution of pyromorphite  $Pb_5(PO_4)_3Cl$  in presence of *Pseudomonas putida* bacteria-an effect on Pb remobilization in the environment. 2010:10441.
51. Drewniak Ł, Skłodowska A, Manecki M, Bajda T. Solubilization of Pb-bearing apatite  $Pb_5(PO_4)_3Cl$  by bacteria isolated from polluted environment. *Chemosphere*. 2017;171:302-307. doi:<https://doi.org/10.1016/j.chemosphere.2016.12.056>
52. Debela F, Arocena JM, Thring RW, Whitcombe T. Organic acid-induced release of lead from pyromorphite and its relevance to reclamation of Pb-contaminated soils. *Chemosphere*. 2010;80(4):450-456. doi:<https://doi.org/10.1016/j.chemosphere.2010.04.025>
53. Ceci A, Kierans M, Hillier S, Persiani AM, Gadd GM. Fungal Bioweathering of Mimetite and a General Geomycological Model for Lead Apatite Mineral Biotransformations. *Appl Environ Microbiol*. 2015;81(15):4955-4964. doi:10.1128/AEM.00726-15
54. Ceci A, Rhee YJ, Kierans M, et al. Transformation of vanadinite  $[Pb_5(VO_4)_3Cl]$  by fungi. *Environmental Microbiology*. 2015;17(6):2018-2034. doi:10.1111/1462-2920.12612
55. Feng M-h, Ngwenya BT, Wang L, Li W, Olive V, Ellam RM. Bacterial dissolution of fluorapatite as a possible source of elevated dissolved phosphate in the environment. *Geochimica et Cosmochimica Acta*. 2011;75(19):5785-5796. doi:<https://doi.org/10.1016/j.gca.2011.07.019>
56. Gadd GM. Metals, minerals and microbes: geomicrobiology and bioremediation. 2010;156(3):609-643. doi:doi:10.1099/mic.0.037143-0

57. Ahmed E, Holmström SJM. Microbe–mineral interactions: The impact of surface attachment on mineral weathering and element selectivity by microorganisms. *Chemical Geology*. 2015;403:13-23. doi:<https://doi.org/10.1016/j.chemgeo.2015.03.009>
58. Temple KL, Colmer AR. The autotrophic oxidation of iron by a new bacterium, thiobacillus ferrooxidans. *Journal of bacteriology*. 1951;62(5):605-611. <https://www.ncbi.nlm.nih.gov/pubmed/14897836>  
<https://www.ncbi.nlm.nih.gov/pmc/PMC386175/>
59. Waksman SA, Joffe JS. Microorganisms Concerned in the Oxidation of Sulfur in the Soil: II. Thiobacillus Thiooxidans, a New Sulfur-oxidizing Organism Isolated from the Soil. *Journal of bacteriology*. 1922;7(2):239-256. <https://www.ncbi.nlm.nih.gov/pubmed/16558952>  
<https://www.ncbi.nlm.nih.gov/pmc/PMC378965/>  
<https://jb.asm.org/content/jb/7/2/239.full.pdf>
60. Natarajan KA. Chapter 3 - Microbiological Aspects of Leaching Microorganisms. In: Natarajan KA, ed. *Biotechnology of Metals*. Elsevier; 2018:29-47. doi:<https://doi.org/10.1016/B978-0-12-804022-5.00003-7>
61. Govender Y, Gericke M. Extracellular polymeric substances (EPS) from bioleaching systems and its application in bioflotation. *Minerals Engineering*. 2011;24(11):1122-1127. doi:10.1016/j.mineng.2011.02.016
62. Sand W, Gehrke T, Jozsa P-G, Schippers A. (Bio)chemistry of bacterial leaching—direct vs. indirect bioleaching. *Hydrometallurgy*. 2001;59(2):159-175. doi:[https://doi.org/10.1016/S0304-386X\(00\)00180-8](https://doi.org/10.1016/S0304-386X(00)00180-8)
63. Corbett MK, Watkin ELJ. Microbial cooperation improves bioleaching recovery rates. *Microbiology Australia*. 2018;39(1):50-52. doi:10.1071/Ma18013
64. Noël N, Florian B, Sand W. AFM & EFM study on attachment of acidophilic leaching organisms. *Hydrometallurgy*. 2010;104(3):370-375. doi:<https://doi.org/10.1016/j.hydromet.2010.02.021>
65. Little BJ, Wagner PA, Lewandowski Z. Spatial relations between bacteria and metal surfaces. *Reviews in mineralogy*. 1997;35:123-159.
66. Natarajan KA. Chapter 10 - Microbially Induced Mineral Beneficiation. In: Natarajan KA, ed. *Biotechnology of Metals*. Elsevier; 2018:243-304. doi:<https://doi.org/10.1016/B978-0-12-804022-5.00010-4>
67. Dong H. Mineral-microbe interactions: a review. *Frontiers of Earth Science in China*. 2010;4(2):127-147. doi:10.1007/s11707-010-0022-8
68. Zhang R, Bellenberg S, Neu TR, Sand W, Vera M. The Biofilm Lifestyle of Acidophilic Metal/Sulfur-Oxidizing Microorganisms. In: Rampelotto PH, ed. *Biotechnology of Extremophiles: Advances and Challenges*. Springer International Publishing; 2016:177-213. doi:10.1007/978-3-319-13521-2\_6
69. Bellenberg S, Barthen R, Boretska M, Zhang R, Sand W, Vera M. Manipulation of pyrite colonization and leaching by iron-oxidizing Acidithiobacillus species. *Appl Microbiol Biotechnol*. 2015;99(3):1435-1449. doi:10.1007/s00253-014-6180-y
70. Vera M, Schippers A, Sand WJAM, Biotechnology. Progress in bioleaching: fundamentals and mechanisms of bacterial metal sulfide oxidation-part A. 2013;97(17):7529-7541. doi:10.1007/s00253-013-4954-2
71. Flemming HC, Wingender J, Szewzyk U, Steinberg P, Rice SA, Kjelleberg S. Biofilms: an emergent form of bacterial life. *Nat Rev Microbiol*. 2016;14(9):563-575. doi:10.1038/nrmicro.2016.94
72. Stoodley P, Sauer K, Davies DG, Costerton JW. Biofilms as complex differentiated communities. *Annu Rev Microbiol*. 2002;56:187-209. doi:10.1146/annurev.micro.56.012302.160705
73. Hunter RC, Beveridge TJ. Metal–Bacteria Interactions at both the Planktonic Cell and Biofilm Levels. In: Sigel A, Sigel H, Sigel RKO, eds. *Biomineralization*. Wiley Online Books; 2008:127-165:chap 4. doi:10.1002/9780470986325.ch4

74. Dang H, Lovell CR. Microbial Surface Colonization and Biofilm Development in Marine Environments. *Microbiology and Molecular Biology Reviews*. 2016;80(1):91. doi:10.1128/MMBR.00037-15
75. Flemming HC, Wingender J. The biofilm matrix. *Nat Rev Microbiol*. 2010;8(9):623-633. doi:10.1038/nrmicro2415
76. Li Q, Sand W. Mechanical and chemical studies on EPS from *Sulfobacillus thermosulfidooxidans*: from planktonic to biofilm cells. *Colloids and Surfaces B: Biointerfaces*. 2017;153:34-40. doi:<https://doi.org/10.1016/j.colsurfb.2017.02.009>
77. Sand W, Gehrke T. Extracellular polymeric substances mediate bioleaching/biocorrosion via interfacial processes involving iron(III) ions and acidophilic bacteria. *Research in Microbiology*. 2006;157(1):49-56. doi:10.1016/j.resmic.2005.07.012
78. Gharehbagheri H, Safdari J, Roostaazad R, Rashidi A. Two-stage fungal leaching of vanadium from uranium ore residue of the leaching stage using statistical experimental design. *Annals of Nuclear Energy*. 2013;56:48-52. doi:10.1016/j.anucene.2013.01.011
79. Wei DP, Liu T, Zhang YM, Cai ZL, He JT, Xu CB. Vanadium Bioleaching Behavior by *Acidithiobacillus ferrooxidans* from a Vanadium-Bearing Shale. *Minerals*. 2018;8(1)doi:ARTN 24  
10.3390/min8010024
80. Dudeney AWL, Sbai ML. Bioleaching of Rare-Earth-Bearing Phosphogypsum. International biohydrometallurgy symposium, Vol 1; Bioleaching processes; ; 1993; Jackson Hole; WY.
81. Banfield JF, Nealson KH, Mineralogical Society of A. *Geomicrobiology : interactions between microbes and minerals / edited Jillian F. Banfield, Kenneth H. Nealson*. Washington, D.C : Mineralogical Society of America; 1997.
82. Nkulu G, Gaydardzhiev S, Mwema E, Compere P. SEM and EDS observations of carrollite bioleaching with a mixed culture of acidophilic bacteria. *Minerals Engineering*. 2015;75:70-76. doi:10.1016/j.mineng.2014.12.005
83. Yang H-y, Liu W, Chen G-b, et al. Function of microorganism and reaction pathway for carrollite dissolution during bioleaching. *Transactions of Nonferrous Metals Society of China*. 2015;25(8):2718-2754. doi:[https://doi.org/10.1016/S1003-6326\(15\)63896-1](https://doi.org/10.1016/S1003-6326(15)63896-1)
84. Liu H, Gu G, Xu Y. Surface properties of pyrite in the course of bioleaching by pure culture of *Acidithiobacillus ferrooxidans* and a mixed culture of *Acidithiobacillus ferrooxidans* and *Acidithiobacillus thiooxidans*. *Hydrometallurgy*. 2011;108(1):143-148. doi:<https://doi.org/10.1016/j.hydromet.2011.03.010>
85. Schlafer S, Meyer RL. Confocal microscopy imaging of the biofilm matrix. *Journal of Microbiological Methods*. 2017;138:50-59. doi:<https://doi.org/10.1016/j.mimet.2016.03.002>
86. Bellenberg S, Leon-Morales C-F, Sand W, Vera M. Visualization of capsular polysaccharide induction in *Acidithiobacillus ferrooxidans*. *Hydrometallurgy*. 2012;129-130:82-89. doi:<https://doi.org/10.1016/j.hydromet.2012.09.002>
87. Bellenberg S, Buetti-Dinh A, Galli V, et al. Automated Microscopic Analysis of Metal Sulfide Colonization by Acidophilic Microorganisms. *Appl Environ Microbiol*. 2018;84(20)doi:10.1128/aem.01835-18
88. McCutcheon J, Southam G. Advanced biofilm staining techniques for TEM and SEM in geomicrobiology: Implications for visualizing EPS architecture, mineral nucleation, and microfossil generation. *Chemical Geology*. 2018;498:115-127. doi:<https://doi.org/10.1016/j.chemgeo.2018.09.016>
89. Balfour-Cunningham A, Boxall NJ, Banning N, Morris C. Preservation of salt-tolerant acidophiles used for chalcopyrite bioleaching: Assessment of cryopreservation, liquid-drying and cold storage. *Minerals Engineering*. 2017;106:91-96. doi:10.1016/j.mineng.2016.09.002
90. Zhu J, Li Q, Jiao W, et al. Adhesion forces between cells of *Acidithiobacillus ferrooxidans*, *Acidithiobacillus thiooxidans* or *Leptospirillum ferrooxidans* and chalcopyrite. *Colloids and Surfaces B: Biointerfaces*. 2012;94:95-100. doi:<https://doi.org/10.1016/j.colsurfb.2012.01.022>



91. Sand W, Florian B, Noel N. Mechanisms of bioleaching and the visualization of these by combined AFM & EFM. *Biohydrometallurgy: A Meeting Point between Microbial Ecology, Metal Recovery Processes and Environmental Remediation*. 2009;71-73:297-302. doi:DOI 10.4028/[www.scientific.net/AMR.71-73.297](http://www.scientific.net/AMR.71-73.297)
92. Muller DJ, Krieg M, Alsteens D, Dufrene YF. New frontiers in atomic force microscopy: analyzing interactions from single-molecules to cells. *Curr Opin Biotechnol*. 2009;20(1):4-13. doi:10.1016/j.copbio.2009.02.005
93. Herrmann AM, Ritz K, Nunan N, et al. Nano-scale secondary ion mass spectrometry — A new analytical tool in biogeochemistry and soil ecology: A review article. *Soil Biology and Biochemistry*. 2007;39(8):1835-1850. doi:<https://doi.org/10.1016/j.soilbio.2007.03.011>
94. Behrens S, Kappler A, Obst M. Linking environmental processes to the in situ functioning of microorganisms by high-resolution secondary ion mass spectrometry (NanoSIMS) and scanning transmission X-ray microscopy (STXM). *Environmental Microbiology*. 2012;14(11):2851-2869. doi:10.1111/j.1462-2920.2012.02724.x
95. Lawrence JR, Swerhone GD, Leppard GG, et al. Scanning transmission X-ray, laser scanning, and transmission electron microscopy mapping of the exopolymeric matrix of microbial biofilms. *Appl Environ Microbiol*. 2003;69(9):5543-5554. <https://www.ncbi.nlm.nih.gov/pmc/articles/PMC194976/pdf/0559.pdf>
96. Santoro F, Zhao W, Joubert L-M, et al. Revealing the Cell–Material Interface with Nanometer Resolution by Focused Ion Beam/Scanning Electron Microscopy. *ACS Nano*. 2017;11(8):8320-8328. doi:10.1021/acsnano.7b03494
97. Rigort A, Plitzko JM. Cryo-focused-ion-beam applications in structural biology. *Archives of Biochemistry and Biophysics*. 2015;581:122-130. doi:<https://doi.org/10.1016/j.abb.2015.02.009>
98. Wirth R. Focused Ion Beam (FIB) combined with SEM and TEM: Advanced analytical tools for studies of chemical composition, microstructure and crystal structure in geomaterials on a nanometre scale. *Chemical Geology*. 2009;261(3):217-229. doi:<https://doi.org/10.1016/j.chemgeo.2008.05.019>
99. Wu S, Zhang B, Liu Y, Suo X, Li H. Influence of surface topography on bacterial adhesion: A review (Review). *Biointerphases*. 2018;13(6):060801. doi:10.1116/1.5054057

**Chapter Two**  
**Methodology development for reproducible  
rapid enumeration of bacterial cells using flow  
cytometry**



## Abstract

Flow cytometry is a widely used methodology to study both eukaryotic and prokaryotic cells. Although there is a systematic approach for the minimum information required to report flow cytometry results on eukaryotic cells, such a systematic approach has not been adopted in the flow cytometry of prokaryotes. This study presents a systematic approach to determine the optimal condition for flow cytometry of bacterial samples. *Klebsiella aerogenes* was used as the model microorganism to define optimal conditions for flow cytometry. SYTO85, a DNA specific fluorochrome was used to stain the microbial sample. The flow cytometry was conducted on an Attune NxT flow cytometer. Several parameters were tested to evaluate optimised conditions for flow cytometry. These included: side scatter (SSC) and forward scatter (FSC), separation index, swarm detection of positive events, acquisition volume, and pretreatment of microbial cells with ethylenediaminetetraacetic acid (EDTA). Finally, the impact of bacterial cell shape and wall structure on the reproducibility of the developed method was tested by using the optimised conditions on bacteria with different shapes (cocci and bacilli) and cell wall structure (Gram-positive and Gram-negative) including *Bacillus megaterium*, *Burkholderia cepacia*, *Kocuria rhizophila*, *Klebsiella pneumoniae*, and *Pseudomonas putida*. A significantly higher separation index (500 times) was determined when using SSC, compared to using FSC. Both cell concentration of the bacterial suspensions and the employed flow rate of the instrument significantly affected the accuracy of the flow cytometry. At the lower detection limit of the instrument, the background noise was detected as a false positive resulting in an inaccurate count of the true positive events. On the other hand, high concentrations of bacterial cells in the sample or using a high flow rate on the instrument can result in coincident detection of two or more true positive events as one, known as swarm detection, leading to an underestimation of the true positive events.

Moreover, the accuracy of the event counts even at optimal cell concentration was affected by the acquisition volume. Higher acquisition volumes led to an underestimation of the true positive events, because of a decline in the fluorescent intensity of the fluorochrome due to the longer time required for analysis of the sample.

The results of the reproducibility test using other microorganisms further confirmed that for all bacteria, FSC resulted in the lowest separation index while SSC provides a higher separation index regardless of bacterial shape or cell wall structure. Overall, the cell concentration calculated using flow cytometry was accurate and at the same range of the cell count as determined using plate count method.

## 1. Introduction

Enumeration of microbial cells, irrespective of the technique employed, is a fundamental practice in microbiology<sup>1</sup>. Since the beginning of modern microbiology, this simple yet significant aspect of microbiological practices has been facing many challenges, due to questions about reproducibility and speed of the employed methods whether it is a direct counting method such as counting chamber or plate count, or an indirect method like turbidometry<sup>2</sup>. One the direct counting methods is flow cytometry, a powerful technique widely employed for the rapid and precise analysis of eukaryotic cells, and microbial populations, including bacteria<sup>3</sup>. The ability to rapidly assess numerous cells at the single-cell level has notably advanced the understanding of cellular physiology, ecology, and even functional analysis<sup>4</sup>. Flow cytometry has found diverse applications in the study of microorganisms allowing the examination of microbial community structures, microbial ecology, antibiotic susceptibility, cell cycle analysis, and the study of microbial response to environmental stressors<sup>5,6</sup>.

Flow cytometry employs light scattering and fluorescence whereby a laser beam intersects cells in a fluid stream to provide detailed information regarding cell number, size, cellular complexity, presence or absence of specific metabolite or polymers such as certain proteins or polysaccharides. Scattering occurs due to cellular structural properties of a microorganism such as size or complexity, while fluorescence intensity reflects probe binding<sup>7</sup>. Flow cytometer instruments collect and measure two patterns of the scattering light, the forward scatter (FSC) which is measured along the path of the laser and is representative of the relative size of the cells or particles, and the side scatter (SSC) which is measured at 90 degrees relative to the laser direction and indicates the internal complexity of the cells<sup>8</sup>. Therefore,

FSC is used to differentiate the cells based on their size but can be of no use or problematic if the particles of interest are too small, and SSC is used to differentiate the cells based on the internal or even external complexity regardless of their size.

While flow cytometry is a powerful tool, it has challenges and limitations and faces issues such as autofluorescence, background noise, data analysis complexity, and potential biases in microbial community analysis<sup>9</sup>.

As the complexity of microbiological questions increases, there is a growing need for innovative methodologies that can overcome the limitations of conventional flow cytometry approaches and enhance the accuracy and depth of bacterial analysis. While bacterial flow cytometry has become an indispensable tool in microbiological research, ensuring the reproducibility and optimization of flow cytometry data is essential for accurate and reliable results. Challenges in standardisation, variations in instrument settings, and inconsistent sample preparation can lead to discrepancies in experimental outcomes in both eukaryotic and bacterial cells<sup>10</sup>. For example, Swarm detection is one of the main challenges in flow cytometry where multiple particles are simultaneously illuminated by the laser beam and counted as a single positive event signal<sup>11</sup>. In general, when particle size is smaller than the detection limit for flow cytometers, or if the flow rate in the cytometer is set too high, multiple particles may appear in the measurement area at the same time and register in the system as one event. This has been termed “swarm” detection and leads to an underestimation of the total event number<sup>11-13</sup>. Moreover, while analysis of the separation index of the employed settings on a flow cytometer instrument is a requirement of flow cytometry of eukaryotic cells, it has been neglected in some studies concerning flow cytometry of prokaryotic cells<sup>14-16</sup>. The significance of this parameter and how to measure it has been discussed in detail elsewhere

<sup>17,18</sup>. In brief, the separation index is a parameter that measures the separation between the stained population and the unstained population or the background noise, and is thereby used to monitor the sensitivity of the instrument and detection methodology <sup>17,18</sup>. Determining the separation index is an objective method enabling comparison of the performance of different instruments, electronics, filters, parameters, and fluorochromes in a biologically significant manner <sup>18</sup>.

The reproducibility of a flow cytometry method for analysis of bacterial populations is the bottleneck to its application or further methodology development. Some of the previously reported methodologies do not have sufficient information on numerous parameters including their sample preparation, gating and thresholding strategies, adjusted setting to provide a high enough separation index to avoid false positive detection, reasons for using FSC instead of SSC, or how swarm detection was tackled during flow cytometry analysis <sup>15,19,20</sup>. Some studies had no information on their flow cytometry settings of the bacterial populations, and hence lack reproducibility potential <sup>14,21,22</sup>. The three major neglected, overlooked or missed information in flow cytometry of bacterial samples are: 1) the separation index of the used settings to distinctively separate the background noise, that can lead to false positive detection, from true positive events; 2) the upper and lower detection limit of the used instrument; and 3) swarm detection of the positive events which leads to underestimation of the true positive events.

In this study, we present a methodology aimed at enhancing the reproducibility and optimisation of bacterial flow cytometry analysis to address several gaps in the previous studies mainly:

- 1) Separation index using different filters and different parameters, particularly gating strategies based on voltage optimisation and separation index of FSC versus SSC.
- 2) A systematic approach to determine the upper and lower detection limit of a flow cytometer instrument.
- 3) The potential occurrence of swarm detection in response to different bacterial cell concentrations or flow rates of the equipment itself.
- 4) Validation of the reproducibility of the methodology, by conducting a series of controlled experiments with various bacterial genera of different shapes (cocci and bacilli) and cell walls (Gram-positive and Gram-negative).

## **2. Experimental procedures**

### **2.1 Microorganisms**

The microorganism used in this study were *Klebsiella aerogenes* ATCC 13048, *Bacillus megaterium* DSMZ 2894, *Burkholderia cepacia* RPH WACC 135<sup>1</sup>, *Kocuria rhizophila* (formerly known *Micrococcus luteus*) ATCC 9341, *Klebsiella pneumoniae*, and *Pseudomonas putida* DSMZ 1693. All of the bacteria used in this study are culturable, hence CFU can be used as a control for flow cytometry counted cells.

All microorganisms were grown and maintained in National Botanical Research Institute's Phosphate medium (NBRIP) with the following composition: 5 g L<sup>-1</sup> MgCl<sub>2</sub>(H<sub>2</sub>O)<sub>6</sub>, 0.25 g L<sup>-1</sup> MgSO<sub>4</sub>(H<sub>2</sub>O)<sub>7</sub>, 0.2 g L<sup>-1</sup> KCl, 0.1 g L<sup>-1</sup> NH<sub>4</sub>SO<sub>4</sub>, 1 g L<sup>-1</sup> KH<sub>2</sub>PO<sub>4</sub>, 1 g L<sup>-1</sup> K<sub>2</sub>HPO<sub>4</sub>, 30 g L<sup>-1</sup> glucose, pH

---

<sup>1</sup> RPH stands for Royal Perth Hospital, with the following Western Australian culture collection reference number.

$6.2 \pm 0.4^{23}$ , and incubated at 30°C, under aerobic conditions at 100 rpm. For all tests, cultures were 18-24 h old when used for flow cytometry, meaning the microbial culture was in the log phase of the growth. Using log-phase culture ensured a minimal influence of dead cells on the flow cytometry count of the cells. Samples were diluted in sterile phosphate free NBRIP and kept on ice during sample preparation and analysis on the flow cytometer. Cell numbers in undiluted cultures were calculated using the Helber chamber method <sup>1</sup> or by measuring colony forming unit (CFU) using plate count prior to running on the flow cytometer. To keep cell number consistent in all experiments, cultures were diluted in fresh sterile NBRIP to reach  $\sim 4 \times 10^8$  cell mL<sup>-1</sup>. All dilutions were then prepared using the initial culture.

## **2.2 Live Cell Staining with SYTO 85**

Samples were stained using 5  $\mu$ L mL<sup>-1</sup> SYTO85 (5 mM, Invitrogen) for a minimum of 15 min in dark on ice. Three controls were prepared and run for each experiment: unstained NBRIP (negative media control), stained NBRIP (media and stain control), unstained bacterial sample (negative bacterial control). All samples were kept in the dark and on ice until they were processed on the flow cytometer.

## **2.3 Flow cytometry**

### **2.3.1 Flow cytometer instrument**

An Attune NxT Flow Cytometer (Invitrogen, Thermo Fisher) used in this study was equipped with four lasers (Figure S-1-A). Violet laser at 405 nm wavelength, Blue at 488 nm, Yellow at 561 nm, Red at 637 nm, with a total of 16 detection channels. It had 6 flowrates, two non-acoustic flowrates at 12.5  $\mu$ L min<sup>-1</sup> and 25  $\mu$ L min<sup>-1</sup>, and four acoustic focusing (100, 200, 500 and 1000  $\mu$ L min<sup>-1</sup>). The forward scatter was collected using photodiode detector with 488/10 nm bandpass filter. The side scatter was collected using photomultiplier tubes with default

488/10 nm bandpass filter. The 488/10 nm filter was the default setting; and hereafter this filter is referred to as baseline settings/filters. The instrument uses another side scatter filter called 488/10 nm OD2 with an optional 405/10 nm bandpass filter for detection of small particle, with a theoretical detection limit of 100 nm in size. Hereafter 488/10 nm OD2 filter is referred to as small particle detection settings/filters. Furthermore, hereafter the optional 405/10 nm filter is referred to as the violet laser filter (since it is on the 405 nm violet laser). The full schematic of the filter setting is shown in Figure S-1- A and B.

### **2.3.2 Initial settings of the flow cytometer**

For each filter “Height” “Weight” or “Area” can be used for visualization of the events of interest. In this study “Heights” (H for short) of the SSC and FCS parameters were used and abbreviated as SSC-H and FSC-H. All controls were run on the Attune NxT flow cytometer before running any test sample.

The initial experiment to gate positive stained bacterial event was tested on baseline filters. Preliminary settings were determined using stained bacteria at  $10^7$  cell mL<sup>-1</sup>. The SSC-H threshold parameter was set to minimum of 0.1 and maximum of 1000000. The voltage of yellow laser (YL-1) channel, which is used to detect SYTO85 positive events, was initially set at 500. Both SSC and FCS voltage were changed from 50 to 650 to visualise and separate SYTO85 positive events from the background. An initial voltage of 500 mV was selected for both parameters in which a distinct bacterial event was recorded (Figure 1).



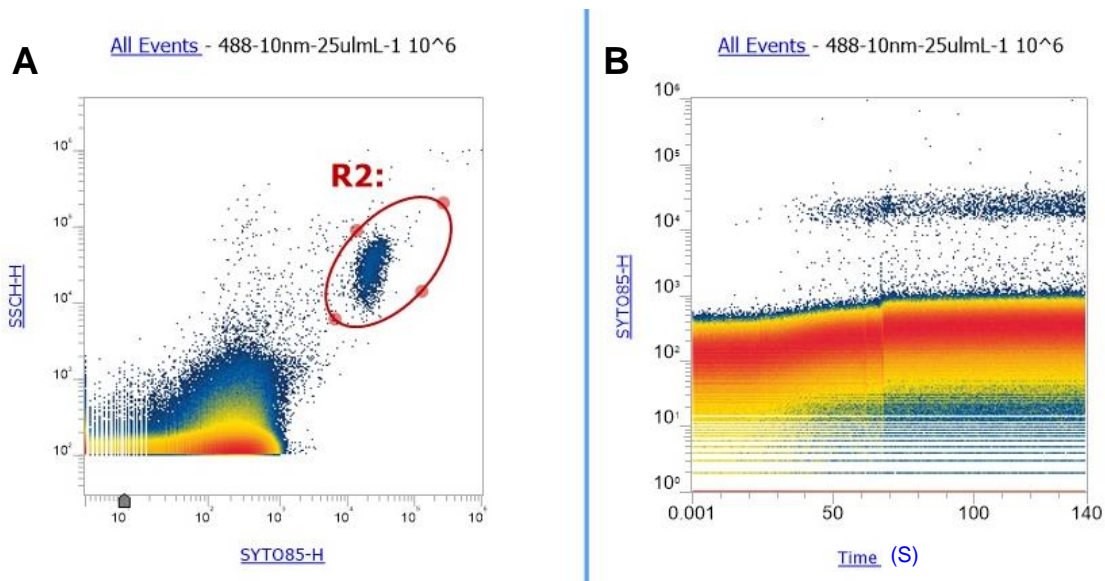


**Figure 1.** Gating of SYTO85 positive bacterial events on Attune NxT using the preliminary settings and baseline filters (488/10 nm) filter. **A)** Screenshot of all the recorded events distinctively separated as a SYTO85 positive population (R2) against the background using SSC-H and SYTO85-H. **B)** Screenshot of the time plot showing the lag phase from acquisition time, and when the flow of the SYTO85 positive events is stable.

### 2.3.3 Evaluation of separation index

The resolution of SSC or FSC parameter to distinguish bacterial events from the background was evaluated by calculating the separation index<sup>17</sup>. The separation index was calculated for SCC-H and FSC-H of the baseline filter arrangement (Figure S1) and the small particle filter arrangement (Figure S2). The separation index was also calculated for SSC-H of the violet laser, as part of the small particle filter arrangement.

An overnight *K. aerogenes* culture was diluted on a log scale to prepare cell suspensions containing cell concentrations ranging from neat ( $\sim 10^8$  cell mL<sup>-1</sup>) to  $10^2$  cell mL<sup>-1</sup>. The initial cell number was evaluated using the Helber Counting Chamber. A plate count was performed using the same cell suspensions and was used as the gold standard (control) for cell

enumeration. For the plate count standard, a 100  $\mu\text{L}$  of dilution series were lawn inoculated on nutrient agar. The plates were then incubated at 37°C for 24 h prior to cell enumeration. The flow cytometer was set to an acquisition volume of 25  $\mu\text{L}$  at a flow rate of 25  $\mu\text{L min}^{-1}$ . All SSC and FSC values were using height (H) parameter. For baseline setting filters, the voltages were evaluated from 50-650 mV at 50 mV intervals. For small particle filters, the SSC voltage was tested from 50-350 mV at 25 mV intervals but were evaluated from 50-650 mV at 50 mV intervals for the FSC laser SSC. To calculate the median of the SSC-H and FSC-H, each parameter was tested in triplicate.

The recorded cell counts using flow cytometry were reported as flow cytometry counted events (FCE) and were plotted and compared against the recorded CFU count acquired from the plate count standard method. Hereafter, the word “FCE” in the text refers to the flow cytometry counted events.

#### **2.3.4 Swarm detection in response to cell concentration and flow rate**

*A. K. aerogenes* culture ( $\sim 4.45 \pm 0.73 \times 10^8 \text{ CFU mL}^{-1}$ ) was used to prepare cell suspensions at  $10^8 \text{ cell mL}^{-1}$ . This cell concentration is considered the neat concentration and was used to prepare a log scale dilution series, to prepare cell suspensions ranging from  $10^7 - 10^2 \text{ cell mL}^{-1}$ . After staining with SYTO85, samples were run on the flow cytometer at a 25  $\mu\text{L}$  acquisition volume at flow rates of 12, 25, 100, 200, 500 and 1000  $\mu\text{L min}^{-1}$ . The cell count, and the robust standard deviation (rSD) of all filters were extracted from the meta data and the separation index was calculated for each of the tested flow rates and cell concentrations. The recorded cell counts using FCE were compared with the recorded CFU.

To evaluate the accuracy of the bacterial cell count using flow cytometer compared to the plate count method, the enumeration test using 25  $\mu\text{L min}^{-1}$  flow rate was repeated in

triplicate for all the cell suspensions. The cell concentration of the neat sample was calculated from the recorded FCE events per dilution sample using equation 2 and compared with the recorded CFU of the neat sample<sup>17</sup>.

$$\text{Cell concentration of the neat sample} = Y \times 40 \times 10^n \text{ cell mL}^{-1} \quad (2)$$

Y = FCE recorded events

40 = Converting index of the recorded *event* in 25  $\mu\text{L}$  to events in 1 mL

n = dilution factor to power of 10

### 2.3.5 Effect of acquisition volume and EDTA on the calculate cell number

Cell suspensions of *K. aerogenes* were prepared at  $10^4$  and  $10^5$  cell  $\text{mL}^{-1}$ . After staining with SYTO85, samples were run on the flow cytometer at different acquisition volumes of 10, 25, 50, 100, and 200  $\mu\text{L}$  at the non-acoustic flow rate of  $25 \mu\text{L min}^{-1}$  and the acoustic flow rate at  $100 \mu\text{L min}^{-1}$ . The recorded cell counts using FCE were compared with the recorded CFU.

The effect of EDTA concentration (0-100 mM) on the separation index and FCE recorded events was assessed using the optimised acquisition volume.

### 2.3.6 Validation of the optimised method for different bacterial genera.

The optimised flow cytometer setting was employed on both Gram-positive and Gram-negative bacteria including *Bacillus megaterium* DSMZ 2894, *Burkholderia cepacia* RPH WACC 135<sup>2</sup>, *Kocuria rhizophila* ATCC 9341, *Klebsiella pneumoniae*, and *Pseudomonas putida* DSMZ 1693.

### **2.3.7 Statistical analysis**

Attune™ NxT Software v5.3 (Invitrogen) was used for the initial flow cytometry acquisition. All flow cytometry data analysis was done using FlowJo v10.7 (BD Biosciences). The components of these plots are shown in Figure S-2. All FlowJo plots shown in this study maintain the scaling and units detailed in Figure S-2. Data preparation for statistical analysis was conducted in Microsoft Excel (2016) and GraphPad Prism v.9. The tests were conducted in a minimum of triplicate, unless otherwise specified. The data were first tested for normal distribution, and if successful, one-way analysis of variances (ANOVA) or two-way ANOVA were used for comparison with a p-value  $\leq 0.05$  considered significant. The accuracy of flow cytometry counted events was measured through comparison with the CFU count recorded for the same test. The influence of tested factors such as cell concentration, flow rates, acquisition volume and addition of EDTA were evaluated by comparing the FCE against CFU count recorded in the relevant test for accuracy. The FCEs were compared against each other to determine if, and how changing each factor affected the accuracy of the FCE. An example of a multiple comparison is provided in Figure S-14. Hereafter, the word “significant” in the text implies a statistical analysis with a p-value  $\leq 0.05$ . All of the p-values are provided in the supplementary material.

### **3. Results and Discussion**

Flow cytometry is routinely employed to enumerate eukaryotic cells, prokaryotic and small vesicles such as peroxisomes<sup>7,24,25</sup>. Some studies<sup>16,26,27</sup> used forward scatter combined with a shift in fluorescent intensity of the fluorochrome to gate bacterial event and enumerate the cell numbers. However, information regarding the gating strategy, whether they studied the possibility of swarm detection of true positive events, higher and upper limits of the bacterial

cell concentrations, and logics behind using forward scatter instead of side scatter for flow cytometry of bacterial samples were not reported or discussed adequately. Moreover, the separation index for the used setting and the resolution of these setting in isolating background noise and false positives from true positive event was the most noticeable criteria neglected or missed information in studies that used flow cytometry for bacterial population. The current study focused on a systematic approach in using flow cytometry for bacterial samples to address such gaps.

In this study, six culturable microorganisms were used. This enabled the use of CFU counts of these microorganisms as a benchmark to compare flow cytometry-detected cell numbers against CFU. Since all live-cells of these culturable microorganisms grew on agar plates, a high level of accuracy using CFU count was obtained, thereby narrowing the gap between the CFU count of the microorganisms and the flow cytometry-detected cells. Thus, considering these factors, the accuracy of the flow cytometry cell count was determined by how closely it aligned with the CFU count.

### 3.1 Evaluation of Separation Index

With the preliminary settings a distinct bacterial population (Figure 1, left panel, gate R2) was observed. The time plot (Figure 1, right panel) showed a 30 second lag from the sample acquisition until the positive population is detected by the instrument. At approximately 50-60 seconds the positive events are detected at a relatively stable pace. Therefore, it is important to always look at the time plot and only start the acquisition when the flow of events is stable. Moreover, as expected, using the control samples showed no false-positive bacterial event (Figure-2 panels O-Q).

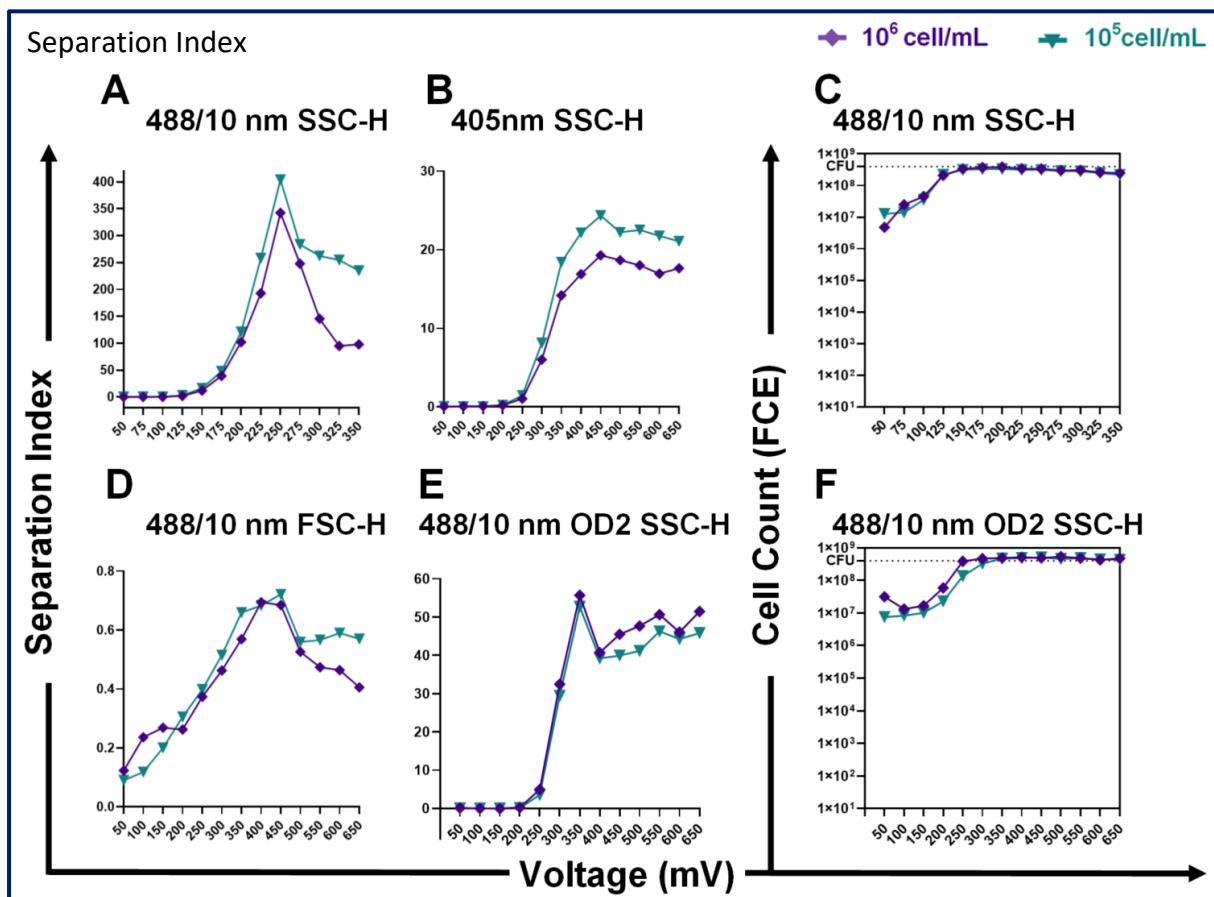
In this study, as part of the adjustment and optimisation, the optimum voltage is selected based on two factors, a higher separation index and an accurate FCE count where FCE count is comparable to the CFU count.

The maximum separation index was calculated for the SSC of the small particle filter, (Figure 2-A), at ~400 arbitrary unit using 250 mV. Using lower and higher SSC voltage resulted in a significant decline in separation index. Looking at the FCE count, SSC voltage from 150 to 300 mV recorded a relatively similar cell count, comparable to the recorded CFU. On the other hand, the separation index of the FSC parameter (Figure 2-D), of the same filter (0.7 arbitrary unit) was the lowest. The very low separation index of FSC is mainly due to bacterial size and the detection limit of the instruments. Most prokaryotic cell and viral particles are not big enough in size to be distinguished by flow cytometry, as their size range is below the detection limit of these instruments<sup>6,28</sup>. In contrast, side scatter works based on the cell complexity, hence provides a better resolution to distinguish small cells and particles. In this study, the SSC of the small particle filter was 600 times stronger than its FSC in terms of separation index, signifying that FCS is not recommended for detection of positive events.

In the next step, the separation index of the violet laser was tested. Note that, this filter is a part of the small particle detection configuration (Figure 2-B) but is using a different laser source. The highest separation index for the violet laser was ~25 and using 400 mV which is significantly lower (~95%) of what recorded for the SSC of the small particle.

The highest separation index of the SSC parameter for baseline filter was ~50 arbitrary unit (Figure 2-E), which is significantly lower than the recorded value for SSC of the small particle filter and is still much stronger (70×) than FSC. The FCE cell count (Figure 2-F) gradually improved by increasing the voltage and reached a relatively consistent number for an SSC

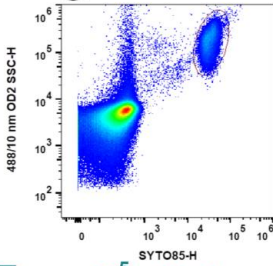
value of 250 mV and above, where the recorded FCE count was equal to the CFU number. Based on the closeness of CFU and FCE count, any voltage from 350 to 600 mV provides a similar cell count to plate count with a separation index of  $50 \pm 10$ . For the next experiments using this filter, a voltage of 550 mV was used. Since not all flow cytometry instrument are equipped with a small particle detection unit, the rest of the optimisation test was carried out for both configurations (baseline and small particle filter).



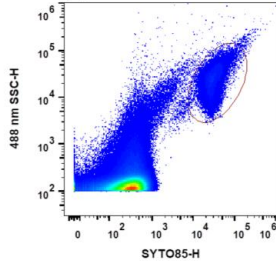
Flow cytometry plots of the stained bacterial samples

◆  $10^6$  cell/mL

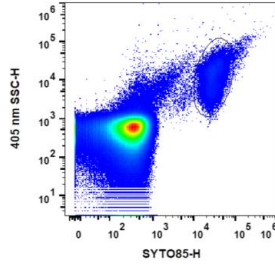
**G**



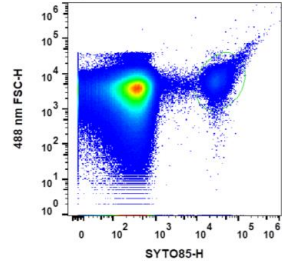
**H**



**I**

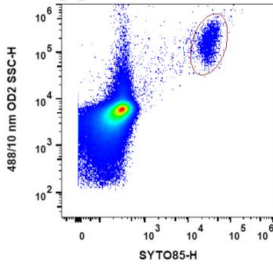


**J**

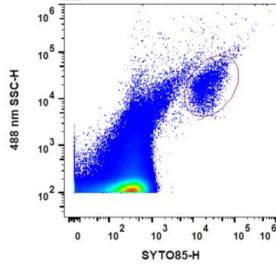


◆  $10^5$  cell/mL

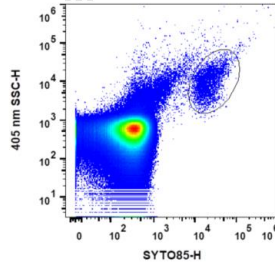
**K**



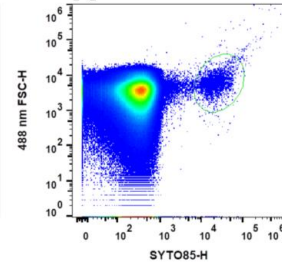
**L**



**M**

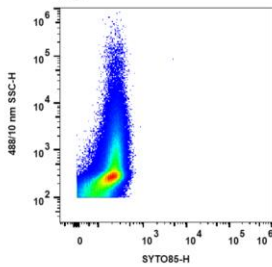


**N**

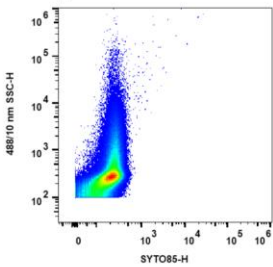


Controls

**O**



**P**



**Q**

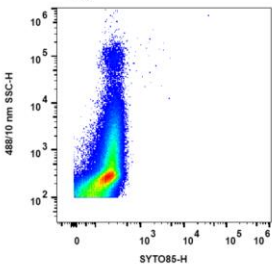


**Figure 2.** Optimisation of the voltage for baseline filter (488/10 nm OD2) and small particle filters 488/10 nm, and parameters SSC-H and FSC-H. The SSC of violet laser (405/10 nm) was also collected as part of the small particle detection system. Two cell suspension of the dilution series were tested for this step,  $10^5$  cell  $\text{mL}^{-1}$  (purple line) and  $10^6$  cell  $\text{mL}^{-1}$  (green line). The final counts of using colony forming unit (CFU) and flow cytometry counted events (FCE) were calculated back to the concentration in the neat sample. Optimal conditions are selected based on higher separation index (A, B, D and E) and accurate cell enumeration where FCE count is closest to CFU count (C and F). At these optimal conditions, the SYTO85 positive



bacterial population is well separated from the background (G-N). The control samples including sterile media control without SYTO85 (O), sterile media with SYTO85 (P) and unstained bacteria control (Q) showed false positive events.

### **3.2 Swarm detection**

In addition to separation index, the potential of swarm detection has been another important overlooked factor in bacterial flow cytometry. Swarm detection, also referred to as coincidence detection, is when an instrument is not capable of separating two or more events apart and report it as one<sup>11,29</sup>.

#### **3.2.1 Effects of cell concentration**

To evaluate occurrence of swarm detection, the calculated cell number in the neat sample using the recorded FCE count was compared to the recorded CFU counts of the original sample using both small particle (Figure 3-A) and base line (Figure 3-B) filters. The FCE count of the higher cell concentrations ( $10^8$  and  $10^7$  cell mL<sup>-1</sup>) was significantly underestimated using the small particle filter, compared to the CFU counts. At  $10^6$  cell mL<sup>-1</sup> a similar FCE count to plate count at lower flow rates (12-100  $\mu$ L min<sup>-1</sup>) was observed but there was a significant underestimation of the cell count at the higher flow rates of 200-1000  $\mu$ L min<sup>-1</sup>. At lower cell concentrations of  $10^3$ ,  $10^4$ , and  $10^5$  cell mL<sup>-1</sup>, the FCE and CFU counts were in a similar range. Moreover, the recorded rSDs (Figure 3-C and D) for these cell concentrations were relatively stable for all the tested flowrates and were significantly lower than the two highest concentrations.

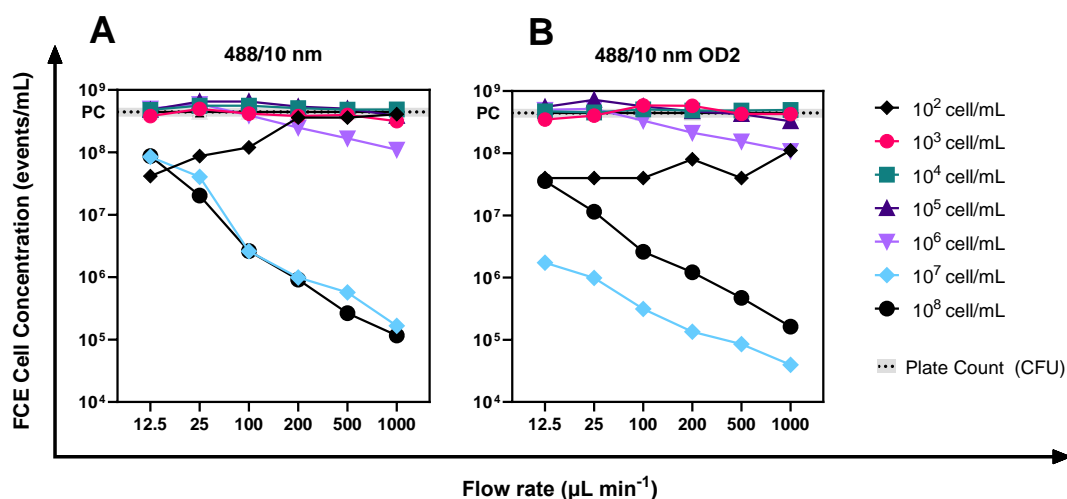


**Figure 3.** Optimisation of cell concentration and flow rate based on closeness of the FCE to CFU count and stability of the rSD values for the small particle filter (488/10 nm) **(A)** and baseline filter (488/10 nm OD2) **(B)**. Note that different cell suspensions from the dilution series were tested here and the final CFU and FCE were calculated back to the cell concentration in the neat sample.

By lowering the cell concentration to  $10^2 \text{ cell mL}^{-1}$ , it was not possible to separate the background noise from SYTO85 positive events and resulted in very low resolution between true and false positive events. At this low cell concentration, depending on the gating strategy employed, the FCE count may vary significantly. It could be lower than the CFU (underestimation), particularly when a small gating approach is adopted to minimise false positives. On the other hand, there might be an overestimation of cell numbers with a larger gating strategy to include as many potential positive events (Figure 4).

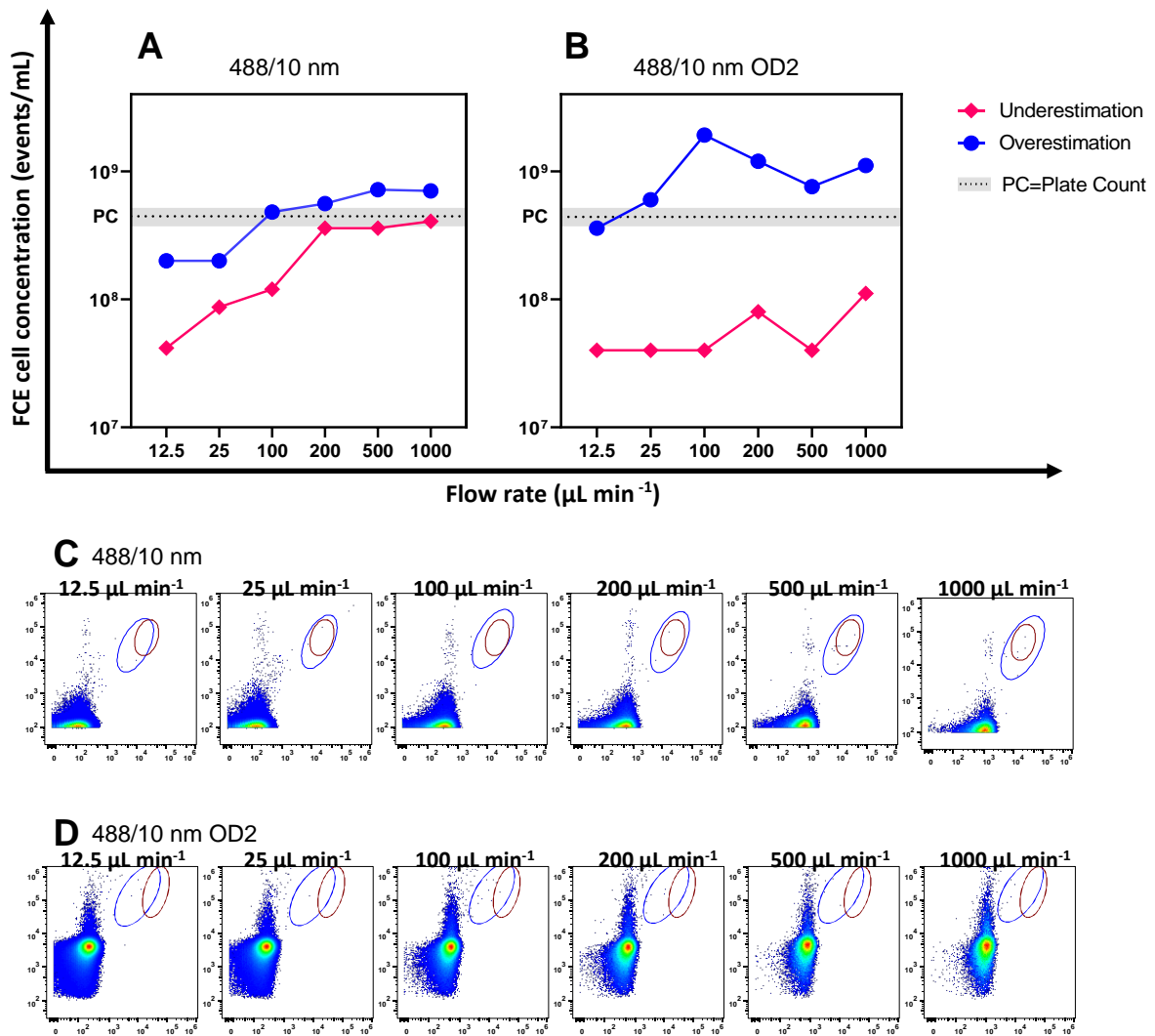


**Figure 4.** Over and underestimation of FCE count at the lower detection limit of Attune NxT using SYTO85 using  $10^2$  cell  $\text{mL}^{-1}$  suspension of the dilution series. The final CFU and FCE were calculated back to the cell concentration of the neat sample. FCE count for the small particle filter (488/10 nm) (**A**) and baseline filter (488/10 nm OD2) (**B**) at different flow rates. The flow cytometry plots are shown in **C** and **D** panels. The red oval shape is the regular size gate used for gating SYTO85 positive bacterial events at higher tested cell suspension. Blue oval shape is potential SYTO85 positive events based on their SYTO85 fluorescent intensity.

From this research, the lower detection limit of bacterial events using SYTO85 on Attune NxT is  $10^2$  cell  $\text{mL}^{-1}$  and the upper detection limit was  $10^6$  cell  $\text{mL}^{-1}$ . The lower detection limit needs to be avoided as it results in overestimation or underestimation of the positive events due to the higher interference rate of background noise with true positive bacterial events. Therefore, for samples with very low cell concentration (e.g., drinking water), it is better to concentrate the cells by centrifuging from a high sample volume. Similarly, the upper detection limit should be avoided as well. The upper detection limit is where swarm detection of the co-incident positive events occurs due to high number of bacteria in the cell suspension<sup>29,30</sup>. When a very high concentration of true positive events is passing through the instruments electronics at once, the flow cytometer detects several positive events as one, hence swarm detection, resulting in significant underestimation of the positive events. To tackle the issue, diluting the sample to the upper detection limit and lower is recommended<sup>29,30</sup>.

### **3.2.2 Effects of the flow rate**

For both small particle and baseline filters, the flow cytometry plots (Figure S3-S8) showed that increasing the flow rate from  $12.5$  to  $1000 \mu\text{L min}^{-1}$  shifted the background noise position on the x-axis (SYTO85). At cell concentrations of  $10^8$  cell  $\text{mL}^{-1}$ , the background noise was not visible for any of the tested flow rates (Figure S3-S8, panel A). At  $10^7$  cell  $\text{mL}^{-1}$  the background noise was only visible and distinguishable from the SYTO85 positive events only at lowest flow rate of  $12.5 \mu\text{L min}^{-1}$ , and was lost at higher flow rates (Figure S3-S8, panel B), while at  $10^6$  cell  $\text{mL}^{-1}$  (Figure S3-S8, panel C) it was faded from lower flow rate to higher flow rates and almost vanished at the highest flow rate of  $1000 \mu\text{L min}^{-1}$ . The loss of background noise may occur when a large number of positive events overwhelm the instrument's detector, leading to

decreased resolution as the background shifted, merging into the signal area, making it impossible for the system to differentiate between the signal and the noise. This shift of the background noise location is visible for cell suspensions below the upper detection limit. At cell concentrations of  $10^5$  cell  $\text{mL}^{-1}$  and lower (Figure S3-S8, panels D, E, F and G) the background noise shifted to the right side of x-axis with increasing flow rates, nevertheless, it was still visible and distinguishable from the SYTO85 positive events.

Using cell suspensions above the upper detection limit ( $10^6$ ,  $10^7$ ,  $10^8$  cell  $\text{mL}^{-1}$ ) also revealed that increasing the flow rates exacerbate the underestimation of the true positive events, indicating that the flow rate can also contribute to underestimation due to swarm detection. For example, there was a three-log difference (further underestimation) between the FCE count of the cell suspensions with  $10^7$  cell  $\text{mL}^{-1}$  at the highest flow rate compared to the lowest flow rate.

Finally, analysing relative stability of the rSD (Figure 5) showed that while using the cell suspension containing  $10^4$  and  $10^5$  cell  $\text{mL}^{-1}$  had the most stable rSD between all filters and parameters,  $10^3$  cell  $\text{mL}^{-1}$  cell suspension showed significant variation in the recorded rSDs between the flow rates.

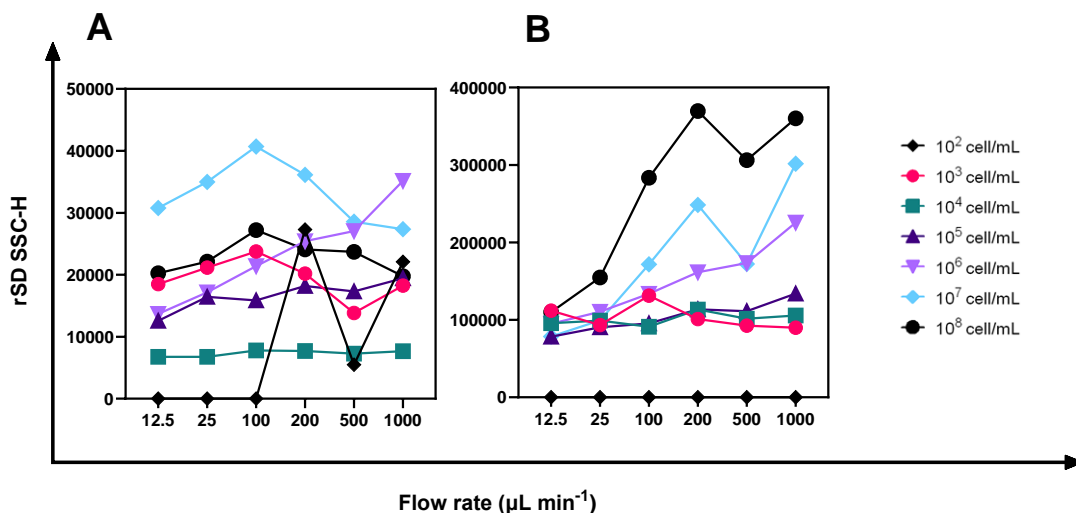


**Figure 5.** Stability of the rSD values at different cell concentrations and flow rates for the small particle filter (488/10 nm) (A) and baseline filter (488/10 nm OD2) (B).

In conclusion, using any bacterial concentrations in the suspension ranging from  $10^3$  cell  $\text{mL}^{-1}$  to  $10^6$  cell  $\text{mL}^{-1}$ , provided an accurate FCE count compared to the CFU count. However, the ideal condition was the middle range of  $10^4$  cell  $\text{mL}^{-1}$  or  $10^5$  cell  $\text{mL}^{-1}$ , ensuring the most stable rSD, minimum interference from background noise (overestimation), and avoiding underestimation due to swarm detection.

### 3.3 Optimising the acquisition volume and EDTA concentration

Studying the effects of acquisition volume, using acoustic ( $100 \mu\text{L min}^{-1}$ ) or non-acoustic ( $25 \mu\text{L min}^{-1}$ ) flow rates, and supplementation of the cell suspension with EDTA to inhibit cell aggregation may also affect the accuracy of flow cytometry. Based on previous data the effect of acquisition volume was determined with cell suspensions containing  $10^4$  and  $10^5$  cell  $\text{mL}^{-1}$ . Two flow rates were tested in these experiments,  $25 \mu\text{L min}^{-1}$  representative of non-acoustic flow rate, and  $100 \mu\text{L min}^{-1}$  to represent the acoustic flow rate. At a non-acoustic flow rate of  $25 \mu\text{L min}^{-1}$  the FCE count was comparable to CFU counts for using lower acquisition volumes of 10 to  $50 \mu\text{L}$ . However, while the FCE remained close to CFU using higher acquisition volumes for  $10^4$  cell  $\text{mL}^{-1}$  cell concentration, it declined for the higher cell concentration at  $10^5$  cell  $\text{mL}^{-1}$  (Figures 3 C). Using higher acquisition volumes means the instrument needs more time for analysis of such volumes. Longer analysis times lead to photobleaching of fluorochromes<sup>31</sup> and consequently declining the fluorescent intensity of fluorochromes.

With an acoustic flow rate of  $100 \mu\text{L min}^{-1}$ , the recorded FCE and CFU of  $10^4$  cell  $\text{mL}^{-1}$  cell concentration sample remained analogous for all the tested acquisition volumes. For the

higher cell concentration of  $10^5$  cell  $\text{mL}^{-1}$ , the FCE count declined for 200  $\mu\text{L}$  acquisition volume only. For the next step, an acquisition volume of 25  $\mu\text{L}$  was used.

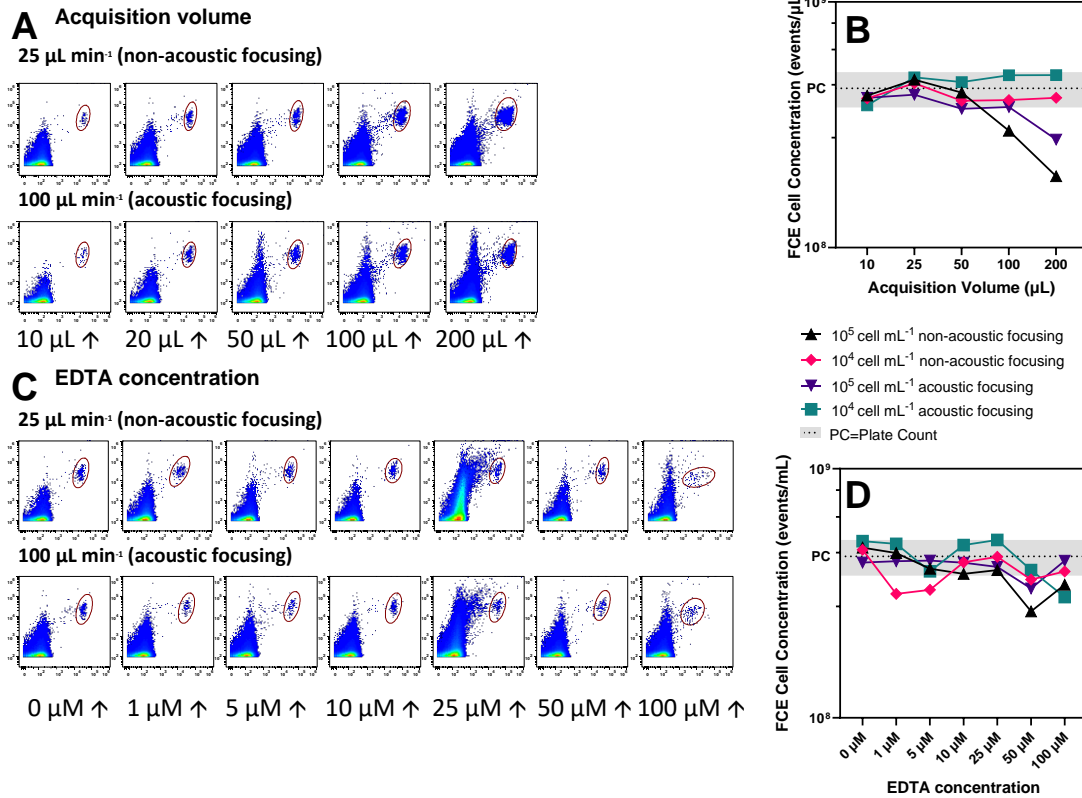


**Figure 6.** Effects of acquisition volume and EDTA supplementation on the accuracy of FCE count compared to CFU count using 25  $\mu\text{L min}^{-1}$  as the non-acoustic flow rate and 100  $\mu\text{L min}^{-1}$  as the acoustic flow rate. **A)** Flow cytometry plots of the  $10^4$  cell  $\text{mL}^{-1}$  cell suspension sample at different acquisition volume **B)** FCE count versus CFU count for each acquisition volume. **C)** Flow cytometry plots of the effects of EDTA concentrations. **D)** FCE count versus CFU count for the EDTA concentrations. Note that two different cell suspensions from the dilution series were tested here and the final CFU and FCE were calculated back to the cell concentration in the neat sample.

Previous studies suggested adding EDTA for better cell separation, inhibiting aggregate formation, or detaching adherent cells to improve flowcytometry enumeration<sup>32,33</sup>. However, treating the sample with EDTA did not result in any improvement in terms of separation index or FCE counts (Figure 6-D). However, using high concentrations of EDTA negatively affected the sample quality (Figure 6-B), decreased the separation index (data not shown), and increased the background noise. This could be due to minimal sample preparation used in this methodology development study. Most flow cytometry studies of bacterial population use centrifugation in their sample preparation. This can lead to separation of the extracellular polymeric substances (EPS) from the bacterial cells<sup>34</sup>. EPS can keep planktonic cells separated from each other and inhibit aggregation to some extent, therefore removing it can lead to creating more adherent bacterial cells<sup>35</sup>. However, at higher concentrations, EDTA adversely affected the SYTO85 intensity of the bacterial cell because EDTA adversely affects outer membrane permeability<sup>36</sup>, hence affecting bacterial cells ability to retain SYTO85 inside, or even result in cell lysis.

### **3.4 Evaluating the optimised settings for other Gram-positive and Gram-negative bacteria**

The reproducibility of the methodology was tested by employing the optimised conditions achieved for *K. aerogenes* which is a Gram-negative bacterium, for other Gram-negative and Gram-positive bacterial samples, and resulted in an accurate FCE count compared to the CFU count for all other bacteria. However, different SSC voltages were evaluated to determine if the best separation index would change for different bacteria. The best separation index for all other bacteria was 250 mV (Figure 7 A). This provided a very distinct SYTO85 positive bacterial events from the background as shown in the flow cytometry plots (Figures S 9-S14). The FSC had the lowest resolution in terms of separation index as was seen for *K. aerogenes*.



For the baseline filter arrangement any voltage from 400 mV to 550 mV provide a good separation index. The optimised voltage to achieve the best separation index was similar for a cocci-shaped bacterium *Kocuria rhizophila* (Gram-positive) and rod shape bacteria including *Bacillus megaterium* (Gram-positive), *Burkholderia cepacia* (Gram-negative), *Klebsiella aerogenes* (Gram-negative), *Klebsiella pneumoniae* (Gram-negative), and *Pseudomonas putida* (Gram-negative). The FCE count of all bacteria was comparable to that of the CFU count records determined by the plate count. Therefore, the methodology was reproducible regardless of the shape or cell-wall structure. It also demonstrated that the SSC provided the best separation index and FSC provided the lowest separation index.

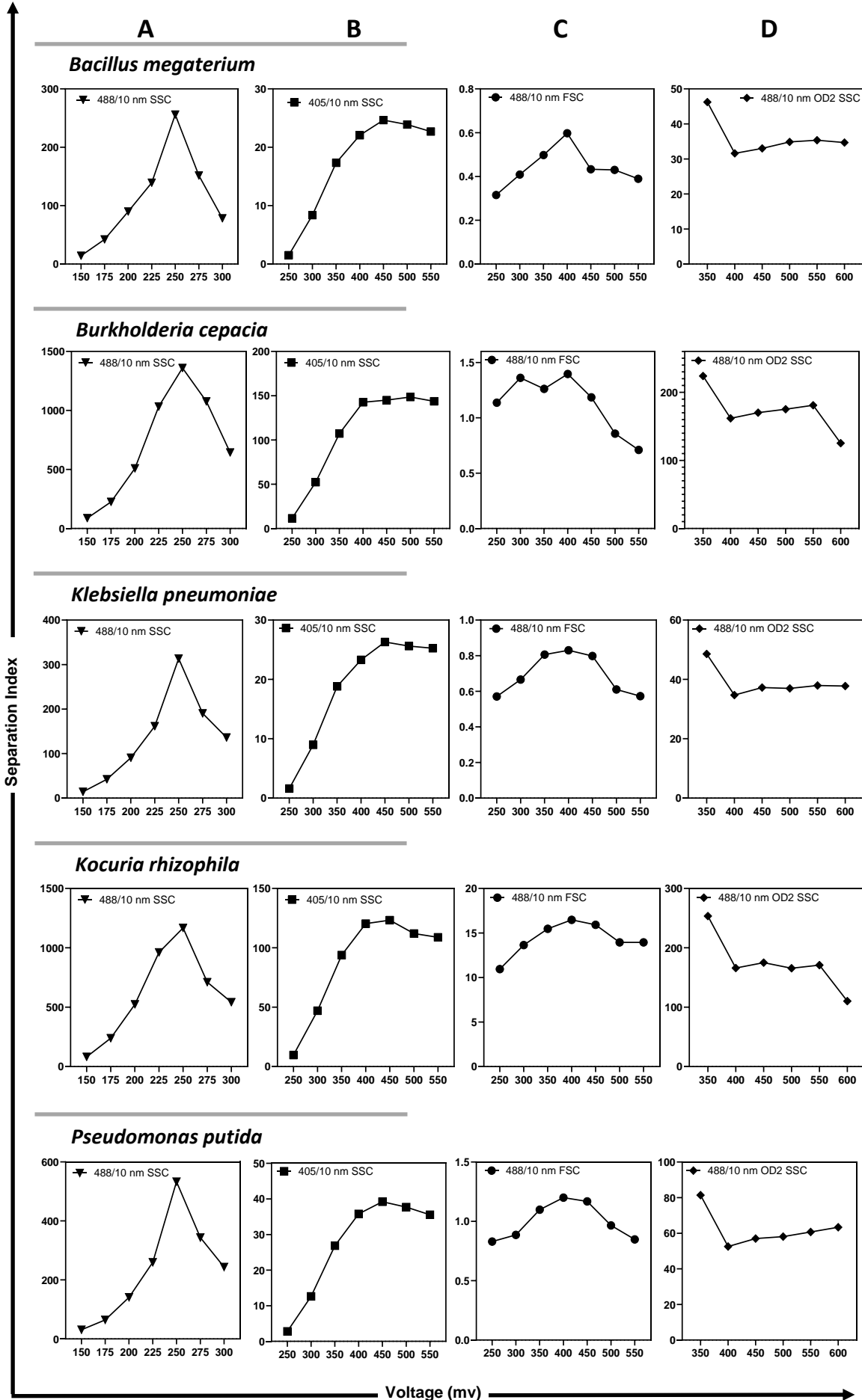


**Figure 7.** Separation index of *Bacillus megaterium*, *Burkholderia cepacia*, *Klebsiella pneumoniae*, *Kocuria rhizophila* (and *Pseudomonas putida*, using small particle filter (488/10 nm) SSC (A) violet laser (405/10 nm) SSC (B), small particle filter FSC (C) and baseline filter (488/10 OD2) SSC (D).

#### **4. Conclusion**

The accuracy of flow cytometry-based enumeration of bacterial events is notably affected by several factors including sample preparation, concentration of bacterial in the cells suspension, the instruments' filters, using SSC or FSC, and employed flow rate on the instrument. These parameters need to be optimised prior to any flow cytometry, to find the best separation index, a quantifiable parameter representative of distinguishability between true positive events from background noise. Not using optimised conditions can lead to using settings with a lower separation index, for example using FSC instead of SSC that negatively impact cellular representation. Furthermore, employing settings that would consequently lead to significant underestimation of the events of interest as a result of swarm detection is possible. Moreover, using too high acquisition volume or long acquisition time can also lead to underestimation due to photobleaching of the fluorophores. On the other hand, in samples that have lower cell concentration (at or below the lower limit) like drinking water, underground water, or using too dilute sample, there will be a higher influence of the background noise, hence the events of the interest can be significantly overestimated as a result of an incorrect gating strategy to compensate the low cell concentration. For such samples it is recommended to concentrate cells by centrifugation. Therefore, to ensure

reproducibility of flow cytometry-based study of bacterial population, it is important to systematically optimise the conditions for any fluorochromes and instrument.

### **Acknowledgment**

Arya Van Alin (AVA) acknowledges support through a Parker CRC for Integrated Hydrometallurgy Solutions (established and supported under the Australian Government's Cooperative Research Centres Program). The authors acknowledge the Australian Research Council (ARC) for grant DP200103243. The authors acknowledge the Curtin Health Innovation Research Institute (CHIRI), Bentley, Western Australia, for providing the Flow Cytometry facility. The authors would like to acknowledge Jeanne Edmands (CHIRI) for her technical support.

### **Authors' contribution**

AVA and M. Christian Tjiam (CT) designed and conducted the experiments. AVA acquired, analysed and interpreted the data, and prepared the original draft of the manuscript with critical review from CT.

AVA, Elizabeth Watkin (EW), and CT were involved in the research's conceptualisation and design. EW, Melissa K Corbett (MC), Anna H Kaksonen (AK), Andrew Putnis (AP), Jacques Eksteen (JE), Himel Nahreen Khaleque (HNK), CT and Homayoun Fathollahzadeh (HF) were involved in critical review of the data analysis and interpretation, and substantial review of the draft. AVA, EW, AP and JE were involved in funding acquisition. EW, AP, JE, AK, HNK and MC supervised the project.

All authors were involved in review & editing.

### **Competing interests**

The authors declare no competing financial or non-financial interests.

## Data availability

The authors confirm that the data supporting the findings of this study are available within the article's supplementary materials or from the corresponding author [EW] on request.

## References

1. Herbert RA. 1 Methods for Enumerating Microorganisms and Determining Biomass in Natural Environments. In: Grigorova R, Norris JR, eds. *Methods in Microbiology*. Academic Press; 1990:1-39. doi:[https://doi.org/10.1016/S0580-9517\(08\)70238-1](https://doi.org/10.1016/S0580-9517(08)70238-1)
2. Cadena-Herrera D, Esparza-De Lara JE, Ramírez-Ibañez ND, et al. Validation of three viable-cell counting methods: Manual, semi-automated, and automated. *Biotechnol Rep (Amst)*. 2015;7:9-16. doi:10.1016/j.btre.2015.04.004
3. Beal J, Farny NG, Haddock-Angelli T, et al. Robust estimation of bacterial cell count from optical density. *Communications Biology*. 2020;3(1):512. doi:10.1038/s42003-020-01127-5
4. Müller S, Nebe-von-Caron G. Functional single-cell analyses: flow cytometry and cell sorting of microbial populations and communities. *FEMS Microbiology Reviews*. 2010;34(4):554-587. doi:10.1111/j.1574-6976.2010.00214.x
5. Robinson JP, Ostafe R, Iyengar SN, Rajwa B, Fischer R. Flow Cytometry: The Next Revolution. *Cells*. 2023;12(14)doi:10.3390/cells12141875
6. Ambriz-Aviña V, Contreras-Garduño JA, Pedraza-Reyes M. Applications of flow cytometry to characterize bacterial physiological responses. *Biomed Res Int*. 2014;2014:461941. doi:10.1155/2014/461941
7. Manohar SM, Shah P, Nair A. Flow cytometry: principles, applications and recent advances. *Bioanalysis*. 2021;13(3):181-198. doi:10.4155/bio-2020-0267
8. McKinnon KM. Flow Cytometry: An Overview. *Curr Protoc Immunol*. 2018;120:5.1.1-5.1.11. doi:10.1002/cpim.40
9. Vives-Rego J, Lebaron P, Nebe-von Caron G. Current and future applications of flow cytometry in aquatic microbiology. *FEMS Microbiology Reviews*. 2000;24(4):429-448. doi:10.1111/j.1574-6976.2000.tb00549.x
10. Alexander CM, Puchalski J, Klos KS, et al. Separating stem cells by flow cytometry: reducing variability for solid tissues. *Cell Stem Cell*. 2009;5(6):579-583. doi:10.1016/j.stem.2009.11.008
11. Van Der Pol E, Van Gemert MJC, Sturk A, Nieuwland R, Van Leeuwen TG. Single vs. swarm detection of microparticles and exosomes by flow cytometry. *Journal of Thrombosis and Haemostasis*. 2012;10(5):919-930. doi:<https://doi.org/10.1111/j.1538-7836.2012.04683.x>
12. Chandler WL. Measurement of microvesicle levels in human blood using flow cytometry. *Cytometry Part B: Clinical Cytometry*. 2016;90(4):326-336. doi:<https://doi.org/10.1002/cyto.b.21343>
13. Kormelink TG, Arkesteijn GJA, Nauwelaers FA, van den Engh G, Nolte-'t Hoen ENM, Wauben MHM. Prerequisites for the analysis and sorting of extracellular vesicle subpopulations by high-resolution flow cytometry. *Cytometry Part A*. 2016;89(2):135-147. doi:<https://doi.org/10.1002/cyto.a.22644>
14. Michelutti L, Bulfoni M, Nencioni E. A novel pharmaceutical approach for the analytical validation of probiotic bacterial count by flow cytometry. *Journal of Microbiological Methods*. 2020;170:105834. doi:<https://doi.org/10.1016/j.mimet.2020.105834>

15. Servain-Viel S, Akin ML, Domenichini S, et al. A flow cytometry method for safe detection of bacterial viability. *Cytometry Part A*. 2024;105(2):146-156. doi:<https://doi.org/10.1002/cyto.a.24794>
16. Inglis TJJ, Paton TF, Kopczyk MK, Mulroney KT, Carson CF. Same-day antimicrobial susceptibility test using acoustic-enhanced flow cytometry visualized with supervised machine learning. *J Med Microbiol*. 2020;69(5):657-669. doi:10.1099/jmm.0.001092
17. de Rond L, van der Pol E, Bloemen PR, et al. A Systematic Approach to Improve Scatter Sensitivity of a Flow Cytometer for Detection of Extracellular Vesicles. *Cytometry Part A*. 2020;97(6):582-591. doi:<https://doi.org/10.1002/cyto.a.23974>
18. Bigos M. Separation Index: An Easy-to-Use Metric for Evaluation of Different Configurations on the Same Flow Cytometer. *Current Protocols in Cytometry*. 2007;40(1):1.21.21-21.21.26. doi:<https://doi.org/10.1002/0471142956.cy0121s40>
19. Brown MR, Hands CL, Coello-Garcia T, et al. A flow cytometry method for bacterial quantification and biomass estimates in activated sludge. *Journal of Microbiological Methods*. 2019;160:73-83. doi:<https://doi.org/10.1016/j.mimet.2019.03.022>
20. Lőrincz Á M, Timár CI, Marosvári KA, et al. Effect of storage on physical and functional properties of extracellular vesicles derived from neutrophilic granulocytes. *J Extracell Vesicles*. 2014;3:25465. doi:10.3402/jev.v3.25465
21. Rubio E, Zboromyrska Y, Bosch J, et al. Evaluation of flow cytometry for the detection of bacteria in biological fluids. *PLOS ONE*. 2019;14(8):e0220307. doi:10.1371/journal.pone.0220307
22. De Rosa R, Grosso S, Lorenzi G, Bruschetta G, Camporese A. Evaluation of the new Sysmex UF-5000 fluorescence flow cytometry analyser for ruling out bacterial urinary tract infection and for prediction of Gram negative bacteria in urine cultures. *Clinica Chimica Acta*. 2018;484:171-178. doi:<https://doi.org/10.1016/j.cca.2018.05.047>
23. Nautiyal CS. An efficient microbiological growth medium for screening phosphate solubilizing microorganisms. *FEMS Microbiology Letters*. 1999;170(1):265-270. doi:10.1111/j.1574-6968.1999.tb13383.x
24. Robinson JP. Overview of Flow Cytometry and Microbiology. *Curr Protoc Cytom*. 2018;84(1):e37. doi:10.1002/cpcy.37
25. Álvarez-Barrientos A, Arroyo J, Cantón R, Nombela C, Sánchez-Pérez M. Applications of Flow Cytometry to Clinical Microbiology. *Clinical Microbiology Reviews*. 2000;13(2):167-195. doi:10.1128/cmr.13.2.167
26. Chakera A, Mulroney KT, Shak HJ, McGuire AL, Eberl M, Topley N. Peritonitis in Peritoneal Dialysis patients: the case for rapid diagnosis, targeted treatment and monitoring to improve outcomes. *European Medical Journal Nephrology*. 2018;6:56-64.
27. Mulroney KT, Hall JM, McGuire AL, Inglis TJJ, Chakera A. Case Study: Applying Rapid Flow Cytometry Analysis to CAPD Effluent. *Peritoneal Dialysis International*. 2018;38(5):376-379. doi:10.3747/pdi.2017.00231
28. Leif RC. Practical flow cytometry, 3rd Edition, by Howard M. Shapiro, M.D., Wiley-Liss, Inc., New York, 1995, 542 pages, \$79.95. *Cytometry*. 1995;19(4):376-376. doi:<https://doi.org/10.1002/cyto.990190414>
29. Buntsma NC, Shahsavari M, Gąsecka A, Nieuwland R, van Leeuwen TG, van der Pol E. Preventing swarm detection in extracellular vesicle flow cytometry: a clinically applicable procedure. *Research and Practice in Thrombosis and Haemostasis*. 2023;7(4):100171. doi:<https://doi.org/10.1016/j.rpth.2023.100171>
30. van der Pol E, Welsh JA, Nieuwland R. Minimum information to report about a flow cytometry experiment on extracellular vesicles: Communication from the ISTH SSC subcommittee on vascular biology. *Journal of Thrombosis and Haemostasis*. 2022;20(1):245-251. doi:<https://doi.org/10.1111/jth.15540>
31. van den Engh G, Farmer C. Photo-bleaching and photon saturation in flow cytometry. *Cytometry*. 1992;13(7):669-677. doi:10.1002/cyto.990130702

32. Buntsma NC, Gąsecka A, Roos YBWEM, van Leeuwen TG, van der Pol E, Nieuwland R. EDTA stabilizes the concentration of platelet-derived extracellular vesicles during blood collection and handling. *Platelets*. 2022;33(5):764-771. doi:10.1080/09537104.2021.1991569
33. Lai T-Y, Cao J, Ou-Yang P, et al. Different methods of detaching adherent cells and their effects on the cell surface expression of Fas receptor and Fas ligand. *Scientific Reports*. 2022;12(1):5713. doi:10.1038/s41598-022-09605-y
34. Felz S, Al-Zuhairy S, Aarstad OA, van Loosdrecht MC, Lin YM. Extraction of Structural Extracellular Polymeric Substances from Aerobic Granular Sludge. *J Vis Exp*. 2016;(115)doi:10.3791/54534
35. Ghosh P, Mondal J, Ben-Jacob E, Levine H. Mechanically-driven phase separation in a growing bacterial colony. *Proceedings of the National Academy of Sciences*. 2015;112(17):E2166-E2173. doi:10.1073/pnas.1504948112
36. Zermeño-Cervantes LA, Martínez-Díaz SF, Venancio-Landeros AA, Cardona-Félix CS. Evaluating the efficacy of endolysins and membrane permeabilizers against *Vibrio parahaemolyticus* in marine conditions. *Research in Microbiology*. 2023;174(7):104104. doi:<https://doi.org/10.1016/j.resmic.2023.104104>

## Supplementary files

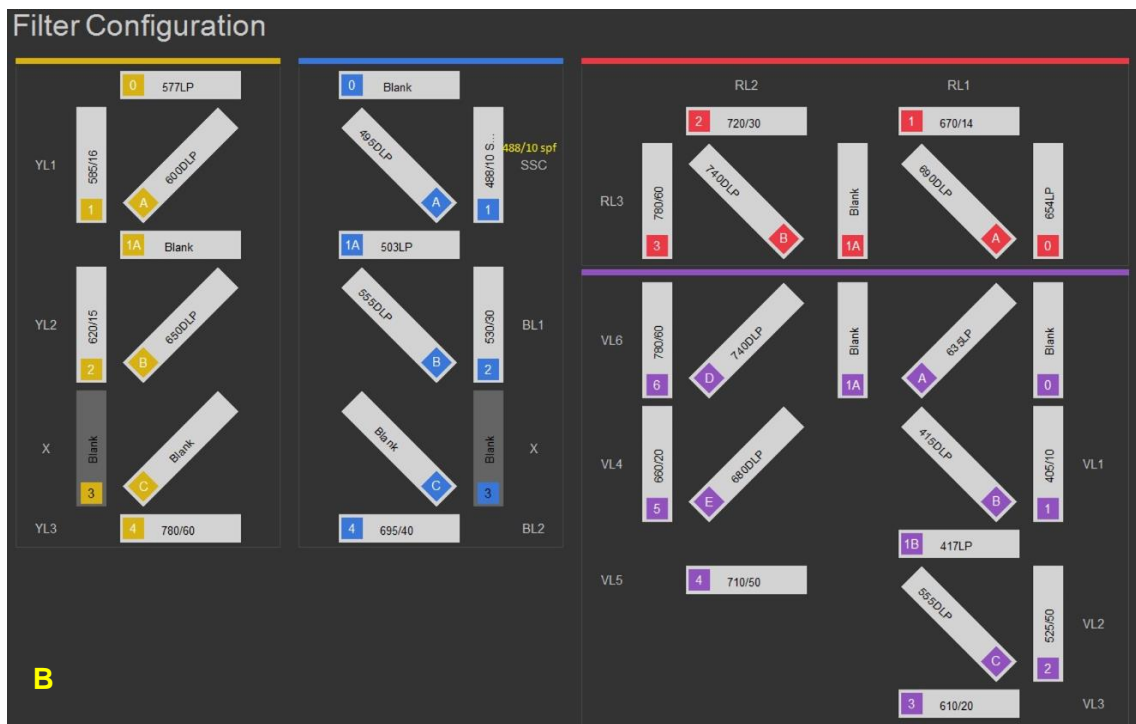
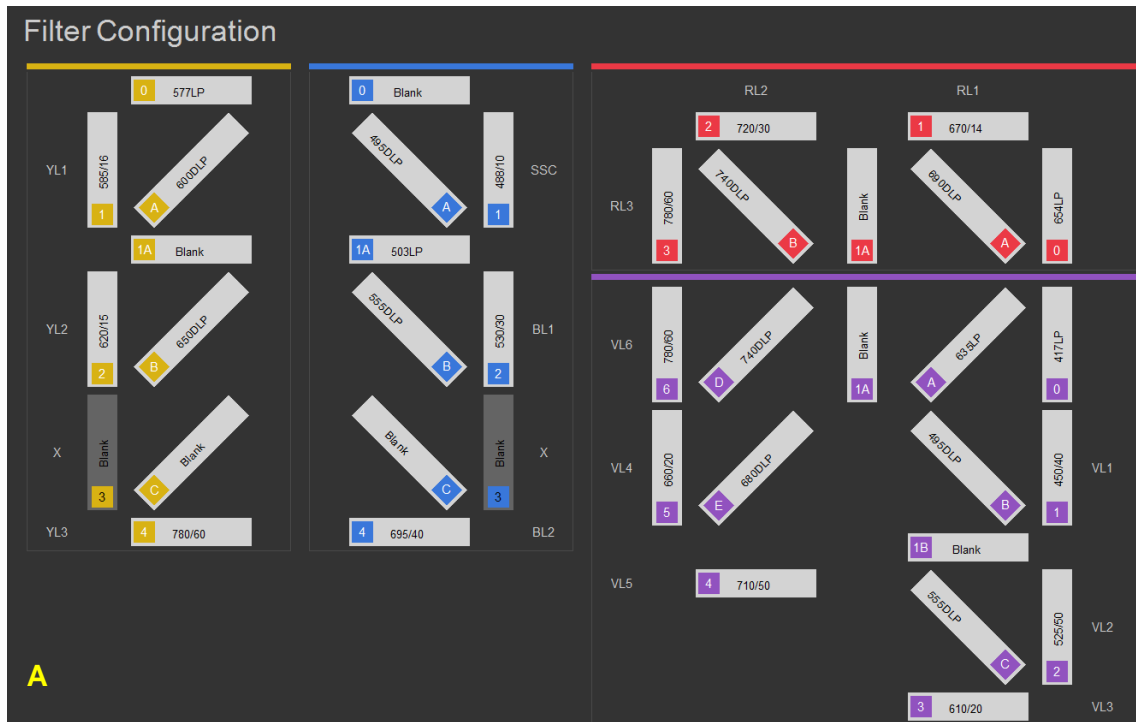


**Figure S-1. A)** Filter configuration for baseline setting. **B)** Filter configuration for small particle detection setting.



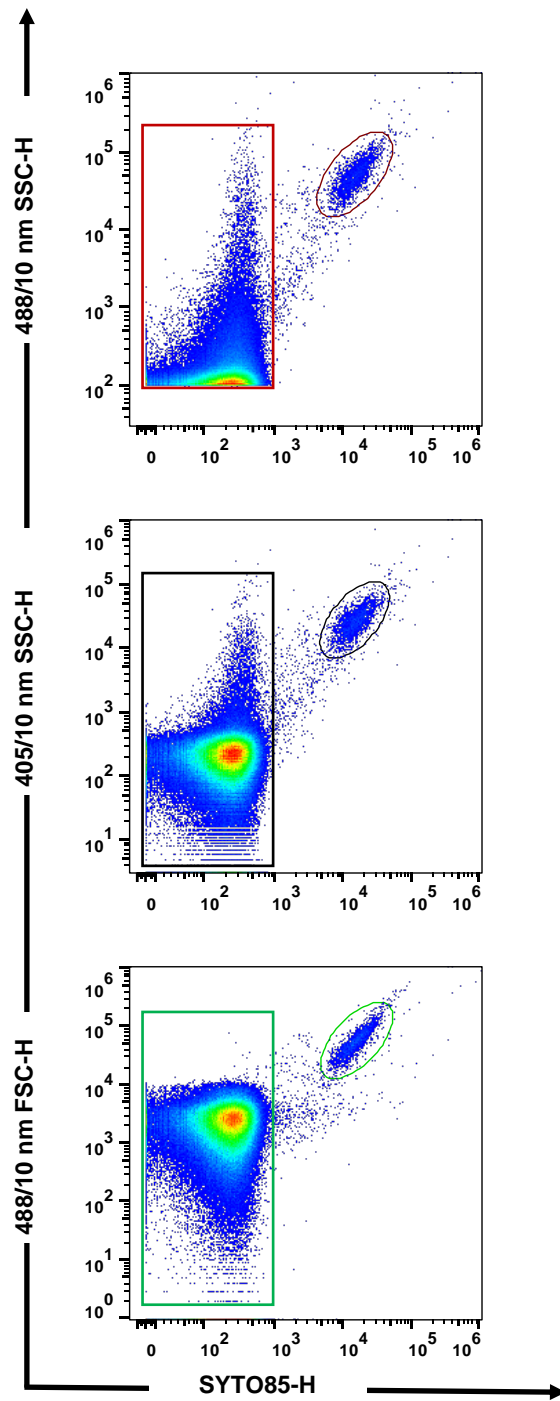


**Figure S-2** Flow cytometry plot created using FlowJo V.10. The oval gates represent SYTO85-positive events, while the square gate indicates background noise. In all flow cytometry plots in this study, the X-axis represents SYTO-85 fluorescence intensity. The Y-axis depicts the light scattering pattern, either side scatter (SSC) or forward scatter (FSC). The unit scales are arbitrary, logarithmic (base 10) and remains constant for each filter-light scattering pattern.

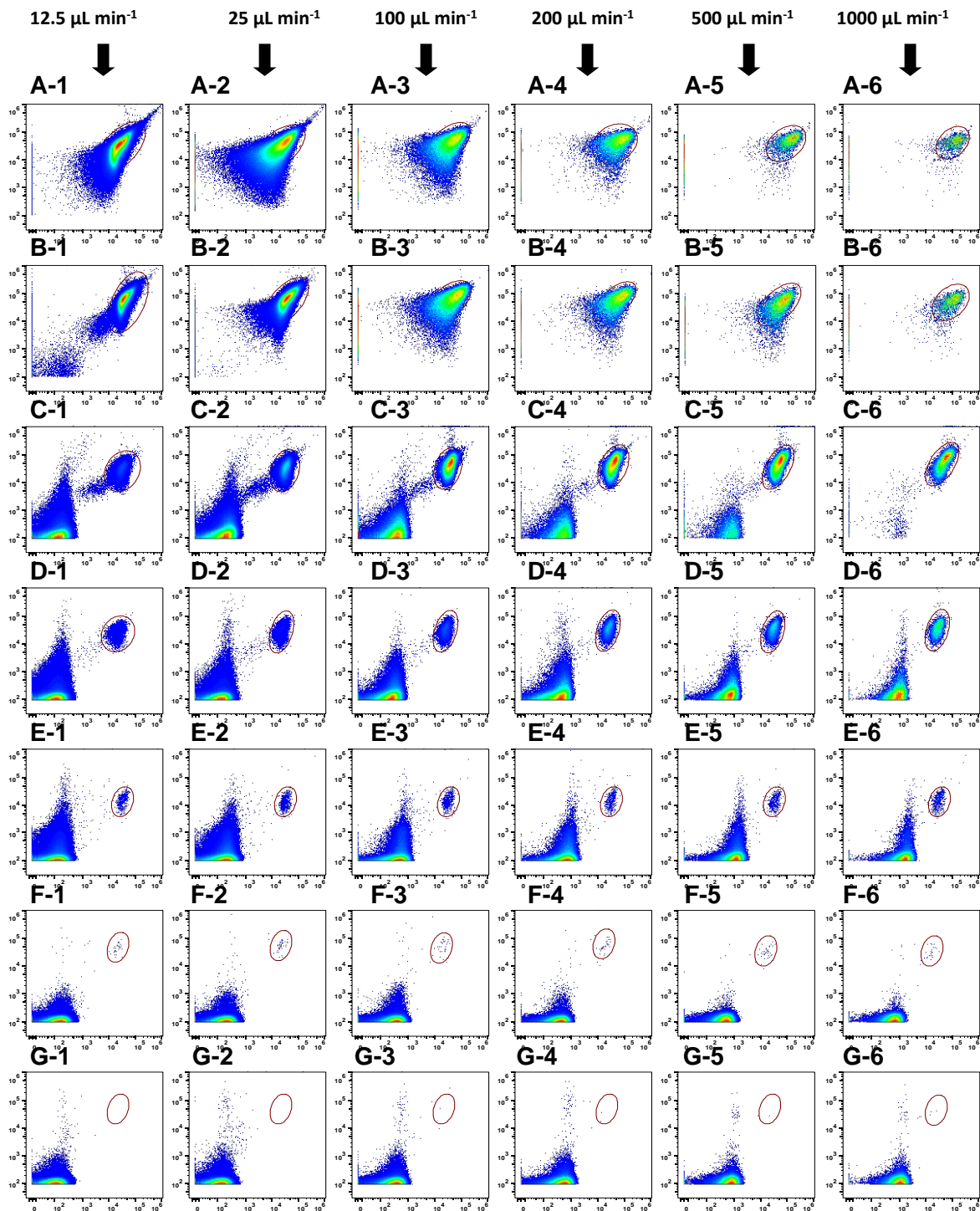


**Figure S-3** Flow cytometry plots of *K. aerogenes* using 488/10 nm filter using SSC-H and SYTO85-H. Bacterial samples were prepared in dilution series from  $10^8$  cell  $\text{mL}^{-1}$  (A)  $10^2$  cell  $\text{mL}^{-1}$  (G) and using different flow rates from  $12.5 \mu\text{L min}^{-1}$  (1) to  $1000 \mu\text{L min}^{-1}$  (6). Bacteria are stained with SYTO85. Red oval shape in the plot represents the gate where SYTO85 positive bacterial population is detected.

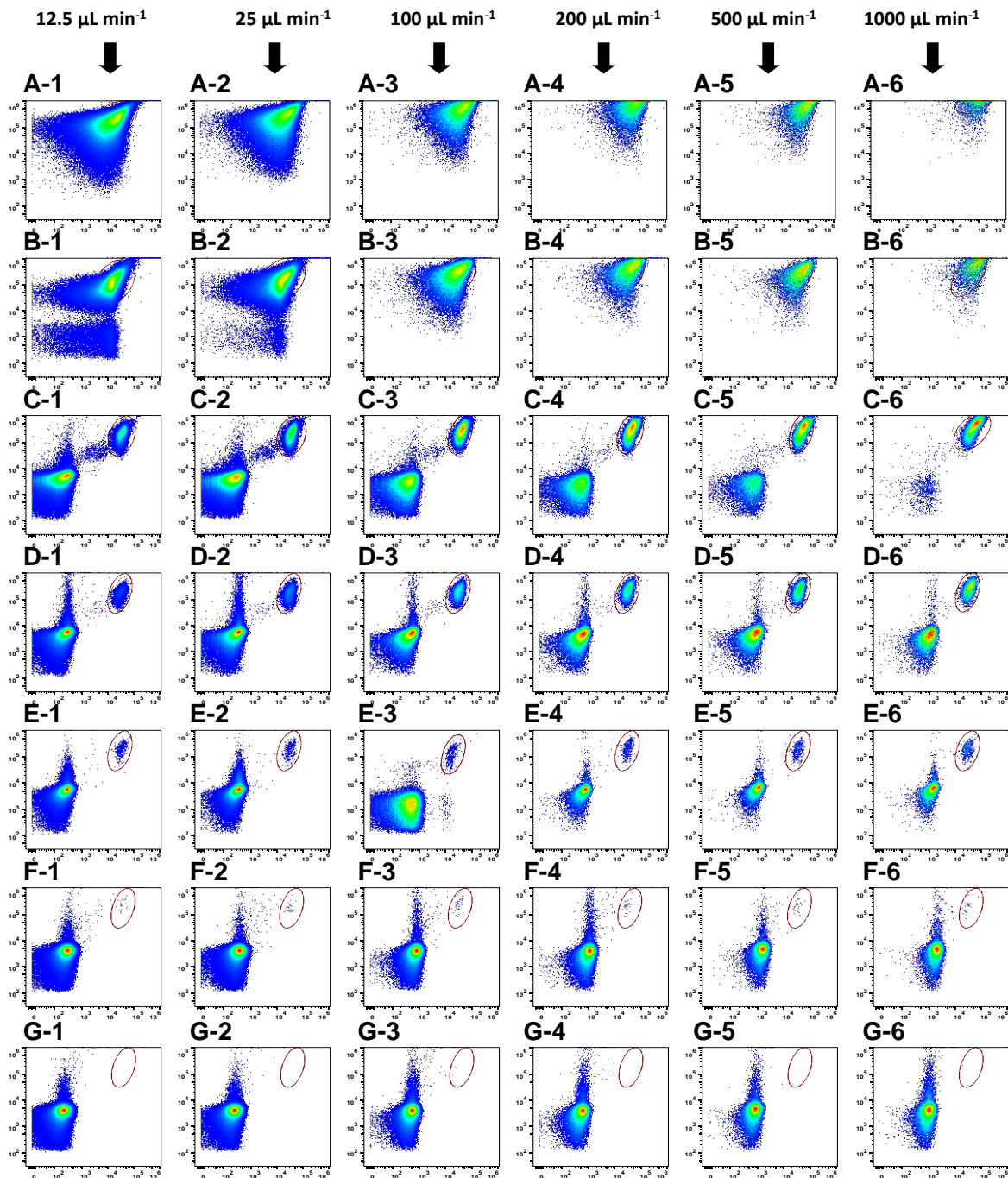


**Figure S-4** Flow cytometry plots of *K. aerogenes* using 488/10 nm OD2 filter using SSC-H and SYTO85-H. Bacterial samples were prepared in dilution series from  $10^8$  cell  $\text{mL}^{-1}$  (A)  $10^2$  cell  $\text{mL}^{-1}$  (G) and using different flow rates from  $12.5 \mu\text{L min}^{-1}$  (1) to  $1000 \mu\text{L min}^{-1}$  (6). Bacteria are stained with SYTO85. Red oval shape in the plot represents the gate where SYTO85 positive bacterial population is detected.

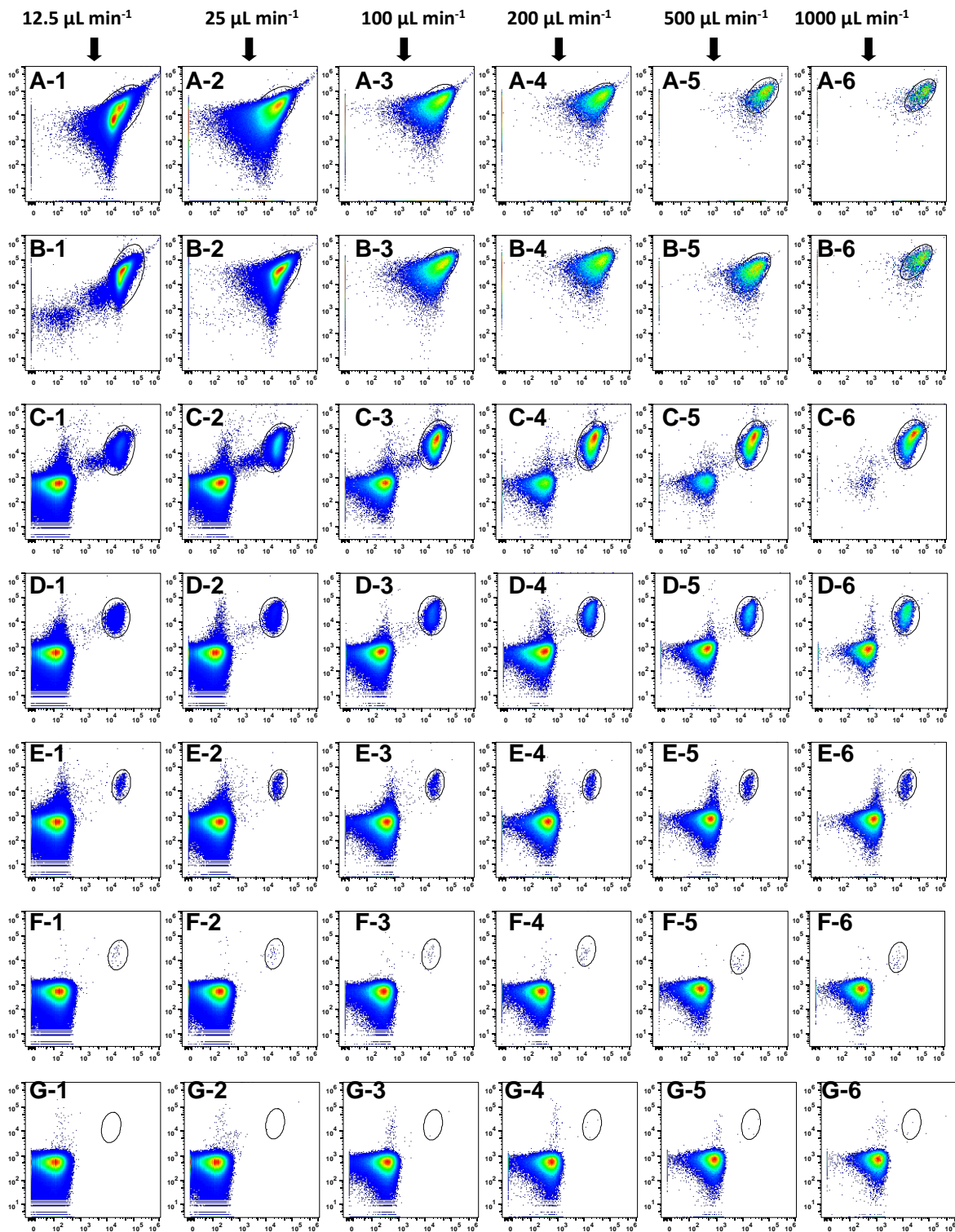


**Figure S-5** Flow cytometry plots of *K. aerogenes* on 405/10 nm filter (violet laser) using SSC-H and SYTO85-H. Bacterial samples were prepared in dilution series from  $10^8$  cell  $\text{mL}^{-1}$  (A)  $10^2$  cell  $\text{mL}^{-1}$  (G) and using different flow rates from  $12.5 \mu\text{L min}^{-1}$  (1) to  $1000 \mu\text{L min}^{-1}$  (6). Bacteria are stained with SYTO85. Red oval shape in the plot represents the gate where SYTO85 positive bacterial population is detected.

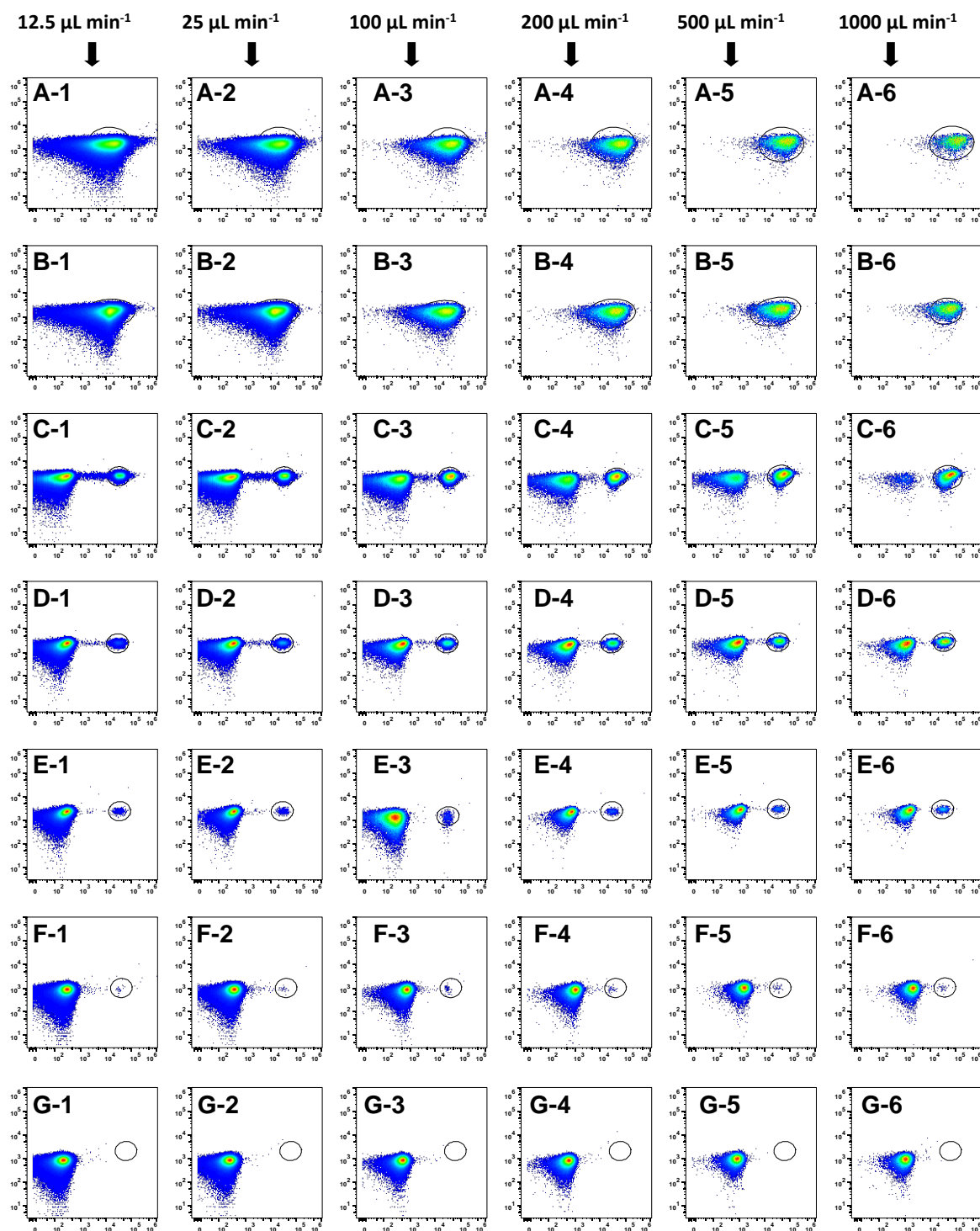


**Figure S-6** Flow cytometry plots of *K. aerogenes* on 450/40 nm filter (violet laser) using SSC-H and SYTO85-H. Bacterial samples were prepared in dilution series from  $10^8$  cell  $\text{mL}^{-1}$  (A)  $10^2$  cell  $\text{mL}^{-1}$  (G) and using different flow rates from  $12.5 \mu\text{L min}^{-1}$  (1) to  $1000 \mu\text{L min}^{-1}$  (6). Bacteria are stained with SYTO85. Red oval shape in the plot represents the gate where SYTO85 positive bacterial population is detected.



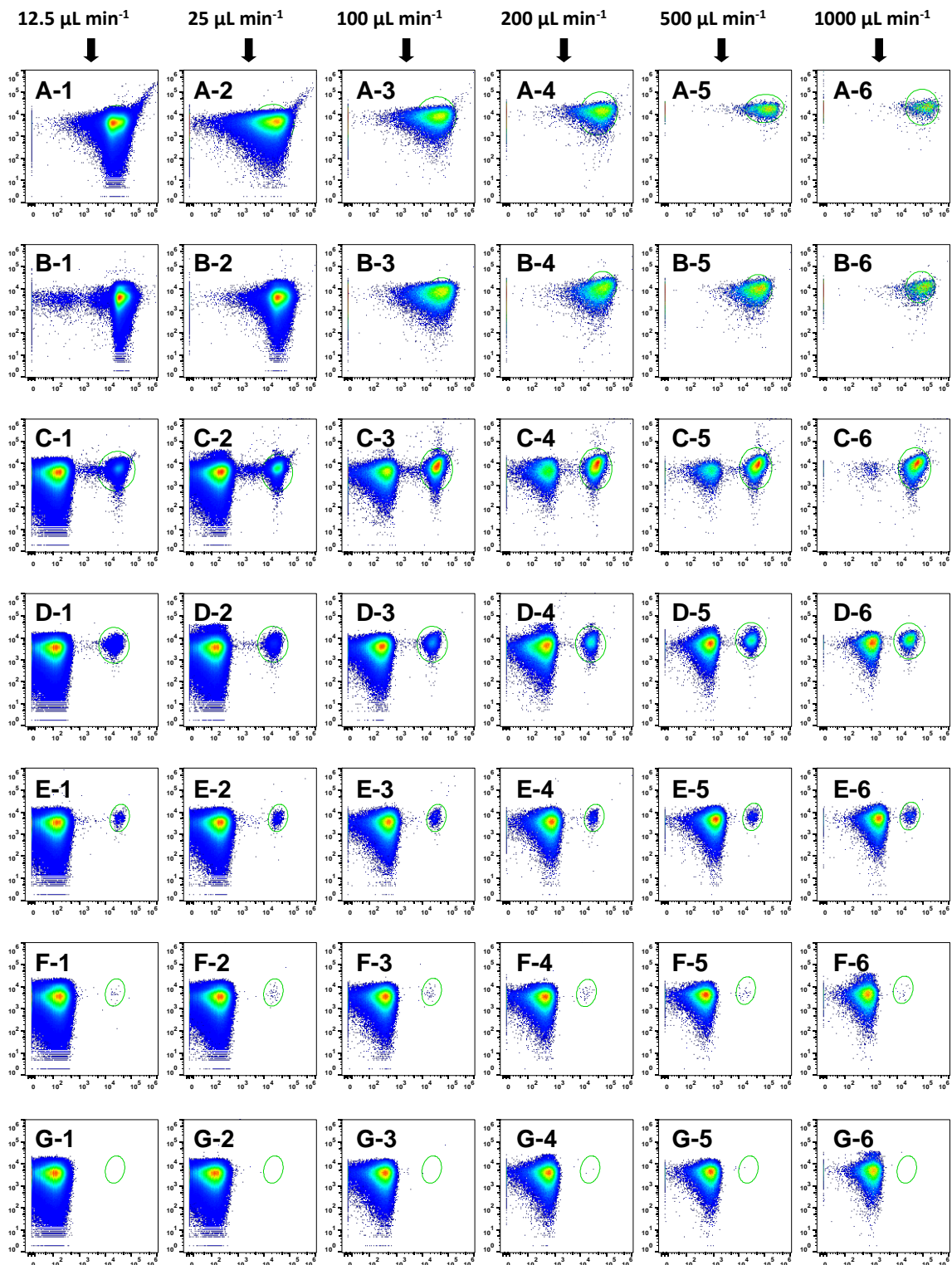


**Figure S-7** Flow cytometry plots of *K. aerogenes* on 488/10 nm using FSC-H and SYTO85-H. Bacterial samples were prepared in dilution series from  $10^8$  cell  $\text{mL}^{-1}$  (A)  $10^2$  cell  $\text{mL}^{-1}$  (G) and using different flow rates from  $12.5 \mu\text{L min}^{-1}$  (1) to  $1000 \mu\text{L min}^{-1}$  (6). Bacteria are stained with SYTO85. Red oval shape in the plot represents the gate where SYTO85 positive bacterial population is detected.

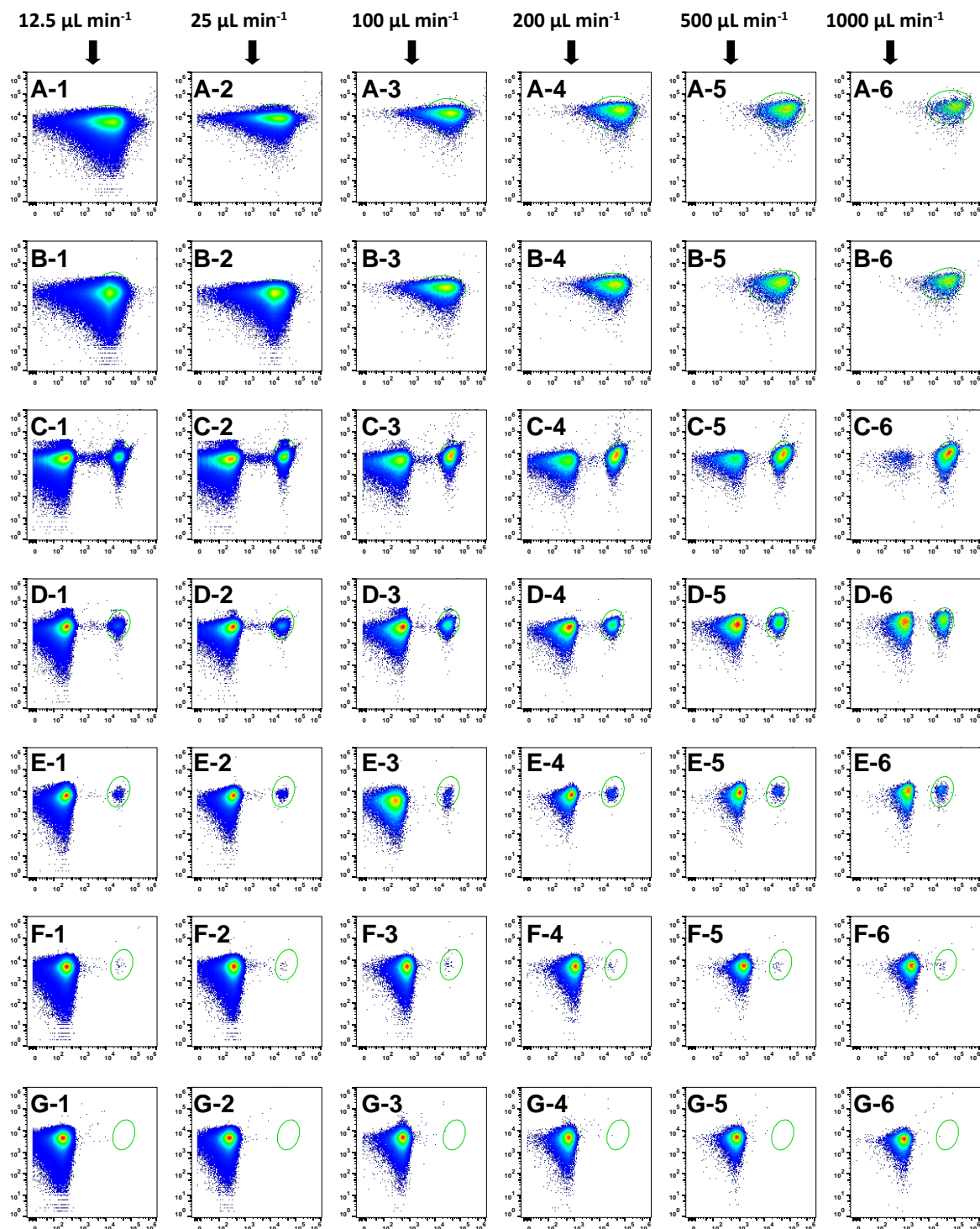


**Figure S-8** Flow cytometry plots of *K. aerogenes* on 488/10 nm OD2 using FSC-H and SYTO85-H. Bacterial samples were prepared in dilution series from  $10^8$  cell  $\text{mL}^{-1}$  (A)  $10^2$  cell  $\text{mL}^{-1}$  (G) and using different flow rates from  $12.5 \mu\text{L min}^{-1}$  (1) to  $1000 \mu\text{L min}^{-1}$ (6). Bacteria are stained with SYTO85. Red oval shape in the plot represents the gate where SYTO85 positive bacterial population is detected.

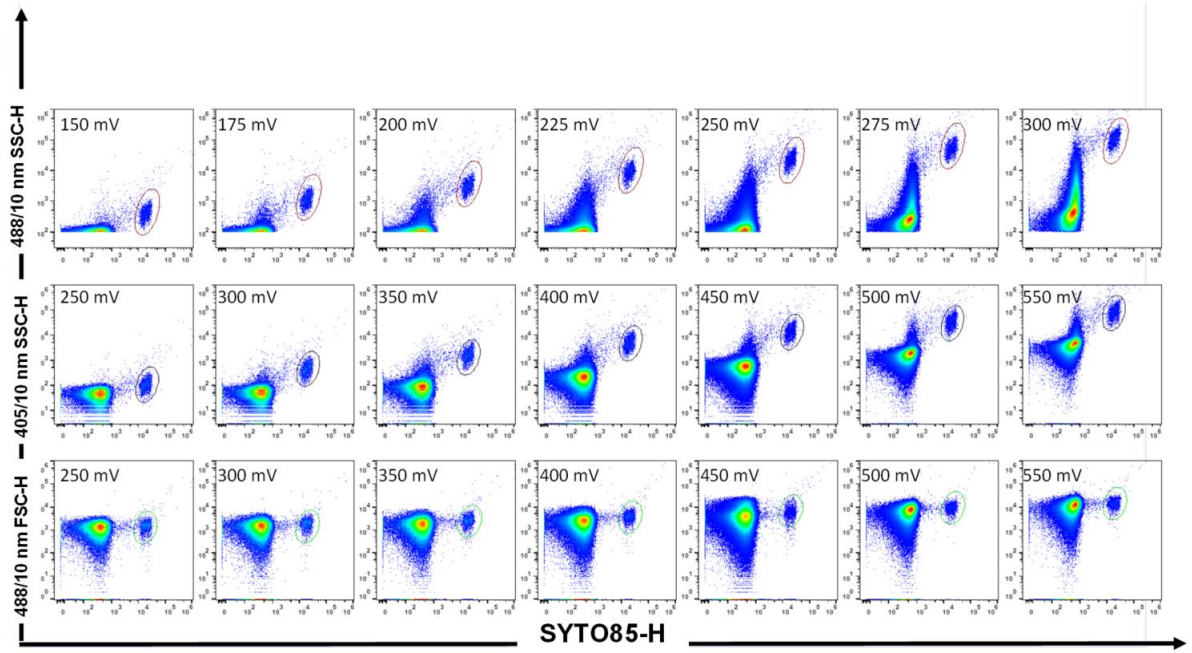


**Figure S-9.** Flow cytometry plots of *Bacillus megaterium* using small particle filter (488/10 nm) SSC and FSC and violet laser (405/10) SSC.

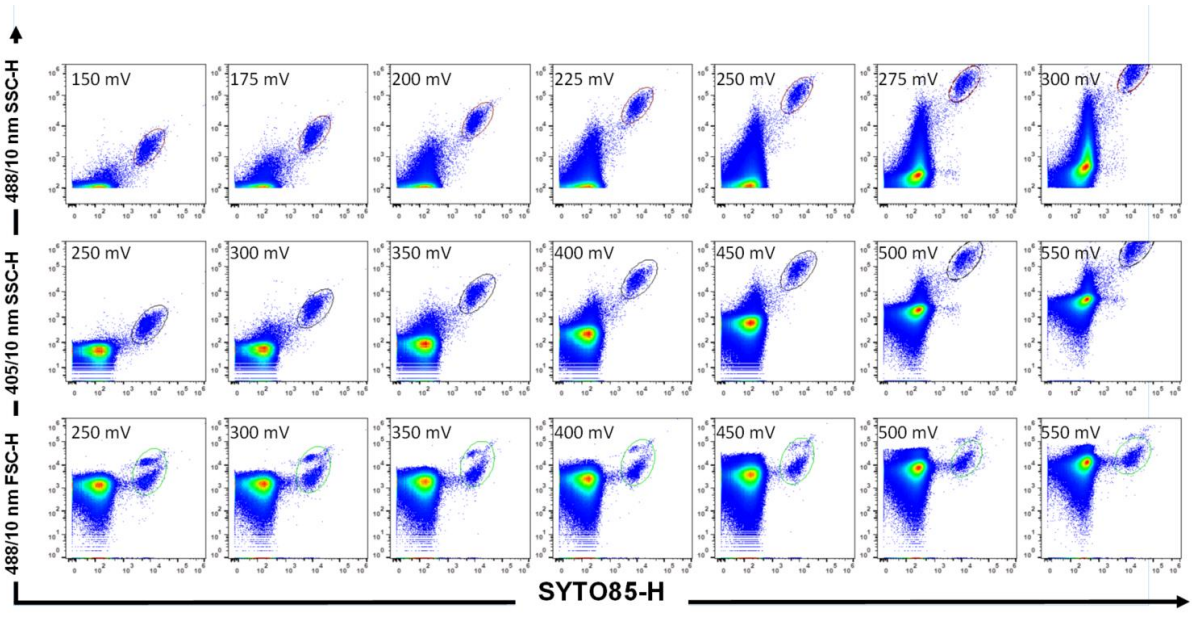


**Figure S-10.** Flow cytometry plots of *Burkholderia cepacia* using small particle filter (488/10 nm) SSC and FSC and violet laser (405/10) SSC.



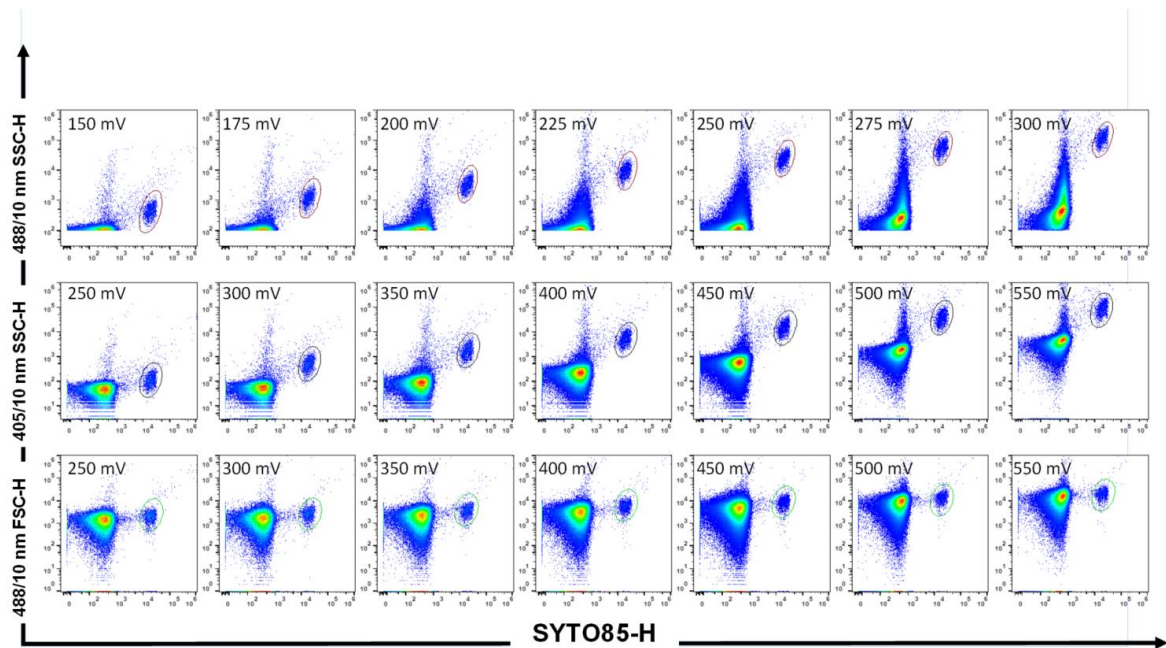


**Figure S-11.** Flow cytometry plots of *Klebsiella pneumoniae* using small particle filter (488/10 nm) SSC and FSC and violet laser (405/10) SSC.

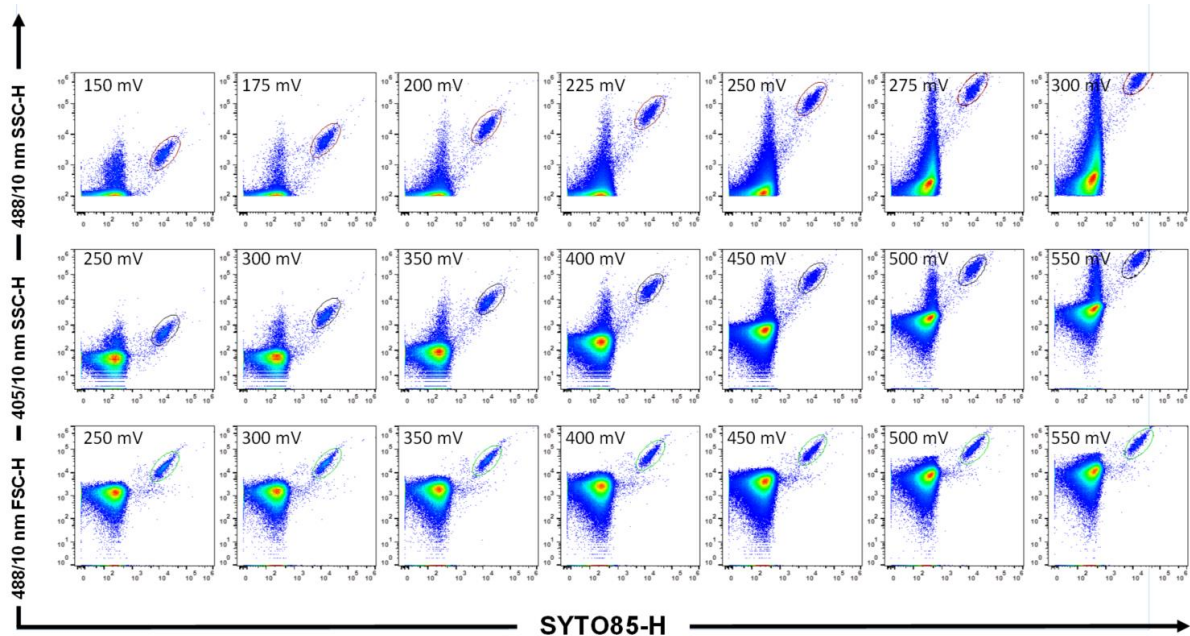


**Figure S-12.** Flow cytometry plots of *Kocuria rhizophila* using small particle filter (488/10 nm) SSC and FSC and violet laser (405/10) SSC.

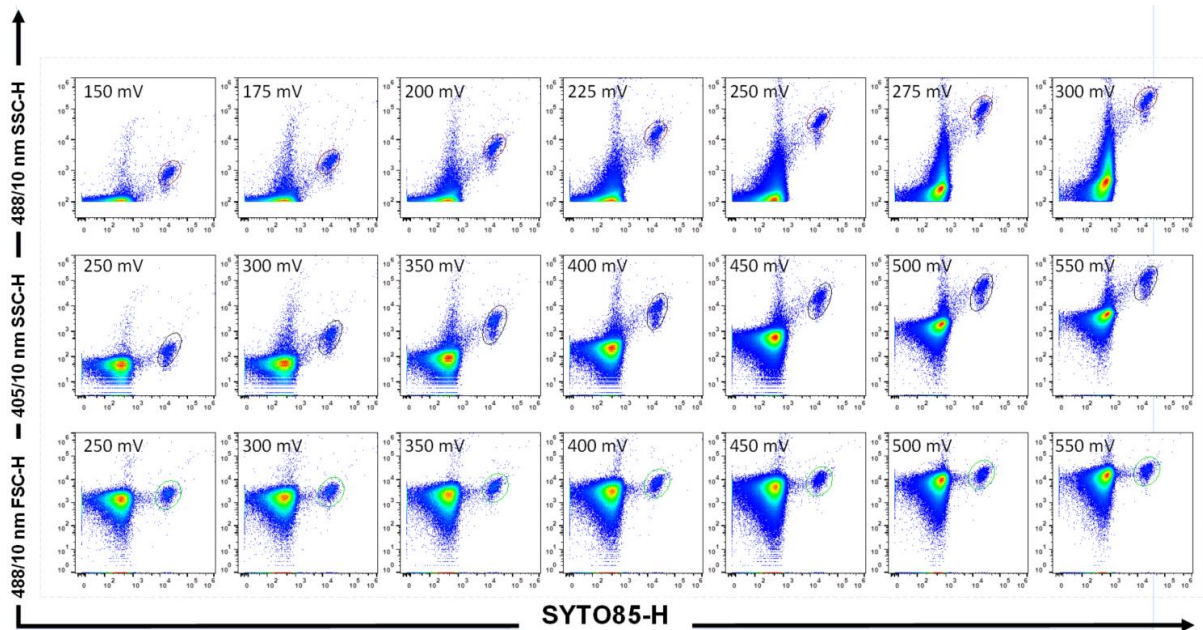


**Figure S-13.** Flow cytometry plots of *Pseudomonas putida* using small particle filter (488/10 nm) SSC and FSC and violet laser (405/10) SSC.

2way ANOVA Multiple comparisons					
Compare cell means regardless of rows and columns					
Number of families	1				
Number of comparisons per family	1128				
Alpha	0.05				
Uncorrected Fisher's LSD	Predicted (LS) mean diff.	95.00% CI of diff.	Below threshold?	Summary	Individual P Value
12.5:Plate Count vs. 12.5:10 <sup>2</sup> cell/mL	405000000	221341027 to 588658973	Yes	***	0.0004
12.5:Plate Count vs. 12.5:10 <sup>3</sup> cell/mL	97000000	-86658973 to 280658973	No	ns	0.2723
12.5:Plate Count vs. 12.5:10 <sup>4</sup> cell/mL	-28600000	-212258973 to 155058973	No	ns	0.7403
12.5:Plate Count vs. 12.5:10 <sup>5</sup> cell/mL	-108480000	-292138973 to 75178973	No	ns	0.2224
12.5:Plate Count vs. 12.5:10 <sup>6</sup> cell/mL	-55840000	-239498973 to 127818973	No	ns	0.5202
12.5:Plate Count vs. 12.5:10 <sup>7</sup> cell/mL	443259929	259600956 to 626918902	Yes	***	0.0002
12.5:Plate Count vs. 12.5:10 <sup>8</sup> cell/mL	409375000	225716027 to 593033973	Yes	***	0.0004
12.5:Plate Count vs. 25:Plate Count	0.000	-129866505 to 129866505	No	ns	>0.9999
12.5:Plate Count vs. 25:10 <sup>2</sup> cell/mL	405000000	221341027 to 588658973	Yes	***	0.0004
12.5:Plate Count vs. 25:10 <sup>3</sup> cell/mL	41000000	-142658973 to 224658973	No	ns	0.6354
12.5:Plate Count vs. 25:10 <sup>4</sup> cell/mL	-9800000	-193458973 to 173858973	No	ns	0.9094
12.5:Plate Count vs. 25:10 <sup>5</sup> cell/mL	-279800000	-463458973 to -96141027	Yes	**	0.0061
12.5:Plate Count vs. 25:10 <sup>6</sup> cell/mL	-72508000	-256166973 to 111150973	No	ns	0.4065
12.5:Plate Count vs. 25:10 <sup>7</sup> cell/mL	444011844	260352871 to 627670817	Yes	***	0.0002
12.5:Plate Count vs. 25:10 <sup>8</sup> cell/mL	433551320	249892347 to 617210293	Yes	***	0.0002
12.5:Plate Count vs. 100:Plate Count	0.000	-129866505 to 129866505	No	ns	>0.9999
12.5:Plate Count vs. 100:10 <sup>2</sup> cell/mL	405000000	221341027 to 588658973	Yes	***	0.0004
12.5:Plate Count vs. 100:10 <sup>3</sup> cell/mL	-143000000	-326658973 to 40658973	No	ns	0.1156
12.5:Plate Count vs. 100:10 <sup>4</sup> cell/mL	-63000000	-246658973 to 120658973	No	ns	0.4692
12.5:Plate Count vs. 100:10 <sup>5</sup> cell/mL	-123560000	-307218973 to 60098973	No	ns	0.1684
12.5:Plate Count vs. 100:10 <sup>6</sup> cell/mL	110316000	-73342973 to 293974973	No	ns	0.2151
12.5:Plate Count vs. 100:10 <sup>7</sup> cell/mL	444686639	261027666 to 628345612	Yes	***	0.0002
12.5:Plate Count vs. 100:10 <sup>8</sup> cell/mL	442398000	258739027 to 626056973	Yes	***	0.0002
12.5:Plate Count vs. 200:Plate Count	0.000	-129866505 to 129866505	No	ns	>0.9999
12.5:Plate Count vs. 200:10 <sup>2</sup> cell/mL	365000000	181341027 to 548658973	Yes	***	0.0010
12.5:Plate Count vs. 200:10 <sup>3</sup> cell/mL	-135000000	-318658973 to 48658973	No	ns	0.1352
12.5:Plate Count vs. 200:10 <sup>4</sup> cell/mL	-40600000	-22458973 to 143058973	No	ns	0.6387
12.5:Plate Count vs. 200:10 <sup>5</sup> cell/mL	-26960000	-210618973 to 156698973	No	ns	0.7546
12.5:Plate Count vs. 200:10 <sup>6</sup> cell/mL	231796000	48137027 to 415454973	Yes	*	0.0176
12.5:Plate Count vs. 200:10 <sup>7</sup> cell/mL	444865239	261206266 to 628524212	Yes	***	0.0002
12.5:Plate Count vs. 200:10 <sup>8</sup> cell/mL	443783048	260124074 to 627442021	Yes	***	0.0002
12.5:Plate Count vs. 500:Plate Count	0.000	-129866505 to 129866505	No	ns	>0.9999
12.5:Plate Count vs. 500:10 <sup>2</sup> cell/mL	405000000	221341027 to 588658973	Yes	***	0.0004
12.5:Plate Count vs. 500:10 <sup>3</sup> cell/mL	17000000	-166658973 to 200658973	No	ns	0.8435
12.5:Plate Count vs. 500:10 <sup>4</sup> cell/mL	-41000000	-224658973 to 142658973	No	ns	0.6354
12.5:Plate Count vs. 500:10 <sup>5</sup> cell/mL	20360000	-163298973 to 204018973	No	ns	0.8132
12.5:Plate Count vs. 500:10 <sup>6</sup> cell/mL	290212000	106553027 to 473870973	Yes	**	0.0049
12.5:Plate Count vs. 500:10 <sup>7</sup> cell/mL	444914992	261256019 to 628573965	Yes	***	0.0002
12.5:Plate Count vs. 500:10 <sup>8</sup> cell/mL	444526577	260867604 to 628185550	Yes	***	0.0002
12.5:Plate Count vs. 1000:Plate Count	0.000	-129866505 to 129866505	No	ns	>0.9999
12.5:Plate Count vs. 1000:Plate Count	0.000	-129866505 to 129866505	No	ns	>0.9999
12.5:Plate Count vs. 1000:10 <sup>2</sup> cell/mL	333888889	150229916 to 517547862	Yes	**	0.0019
12.5:Plate Count vs. 1000:10 <sup>3</sup> cell/mL	19074074	-164584899 to 202733047	No	ns	0.8248
12.5:Plate Count vs. 1000:10 <sup>4</sup> cell/mL	-50925926	-234584899 to 132733047	No	ns	0.5570
12.5:Plate Count vs. 1000:10 <sup>5</sup> cell/mL	117740741	-65918232 to 301399714	No	ns	0.1878
12.5:Plate Count vs. 1000:10 <sup>6</sup> cell/mL	335962963	152303990 to 519621936	Yes	**	0.0018
12.5:Plate Count vs. 1000:10 <sup>7</sup> cell/mL	444960555	261301582 to 628619528	Yes	***	0.0002
12.5:Plate Count vs. 1000:10 <sup>8</sup> cell/mL	444836889	261177916 to 628495862	Yes	***	0.0002

**Figure S-14.** Extract of the multiple comparison of the CFU count vs FCE count using Two Way ANOVA test. The “Summary” column shows if the calculated p value was significant.

# **Chapter Three**

## **Biofilm formation on the surface of monazite and xenotime during bioleaching**

**Notes on chapter three:**

1- Some parts of this chapter were originally submitted as the milestone two and three at Curtin University. As per Curtin University regulation, all the data from milestone one, milestone two, and milestone three, including the writing pieces can be used in the final thesis with or without any changes.

2- This chapter is published at Microbial Biotechnology Journal, Applied Microbiology International (AMI) society, Wiley.

First published: 08 June 2023

<https://doi.org/10.1111/1751-7915.14260>.

## **Biofilm formation on the surface of monazite and xenotime during bioleaching**

Arya van Alin<sup>1, 2</sup>, Melissa K Corbett<sup>1, 2</sup>, Homayoun Fathollahzadeh<sup>1,2</sup>, M. Christian Tjiam<sup>1, 3, 4</sup>, William D.A. Rickard<sup>5</sup>, Xiao Sun<sup>5</sup>, Andrew Putnis<sup>2,6</sup>, Jacques Eksteen<sup>7</sup>, Anna H Kaksonen<sup>7, 8</sup>, Elizabeth Watkin<sup>1, 2, 9\*</sup>

<sup>1</sup> Curtin Medical School, Curtin University, Western Australia, Australia

<sup>2</sup> The Institute for Geoscience Research, School of Earth and Planetary Sciences, Curtin University, Western Australia, Australia

<sup>3</sup> Wesfarmers Centre of Vaccines and Infectious Diseases, Telethon Kids Institute, Western Australia, Australia

<sup>4</sup> Centre for Child Health Research, The University of Western Australia, Western Australia, Australia

<sup>5</sup> John de Laeter Centre, Curtin University, Western Australia, Australia

<sup>6</sup> Institut für Mineralogie, University of Münster, Germany

<sup>7</sup> WA School of Mines, Minerals, Energy and Chemical Engineering, Curtin University, Western Australia, Australia

<sup>8</sup> CSIRO Land and Water, Western Australia, Australia

<sup>9</sup> School of Science, Edith Cowan University Western Australia, Australia

\*Correspondence: e.watkin@ecu.edu.au (Elizabeth Watkin).

## Abstract

Microbial attachment and biofilm formation is a ubiquitous behaviour of microorganisms and is the most crucial prerequisite of contact bioleaching. Monazite and xenotime are two commercially exploitable minerals containing rare earth elements (REEs). Bioleaching using phosphate solubilizing microorganisms is a green biotechnological approach for the extraction of REEs. In this study, microbial attachment and biofilm formation of *Klebsiella aerogenes* ATCC 13048 on the surface of these minerals were investigated using confocal laser scanning microscopy (CLSM) and scanning electron microscopy (SEM). In a batch culture system, *K. aerogenes* was able to attach and form biofilms on the surface of three phosphate minerals. The microscopy records showed three distinctive stages of biofilm development for *K. aerogenes* commencing with initial attachment to the surface occurring in the first minutes of microbial inoculation. This was followed by colonisation of the surface and formation of a mature biofilm as the second distinguishable stage, with progression to dispersion as the final stage. The biofilm had a thin-layer structure. The colonisation and biofilm formation were localised toward physical surface imperfections such as cracks, pits, grooves and dents. In comparison to monazite and xenotime crystals, a higher proportion of the surface of the high-grade monazite ore was covered by biofilm which could be due to its higher surface roughness. No selective attachment or colonisation toward specific mineralogy or chemical composition of the minerals was detected. Finally, in contrast to abiotic leaching of control samples, microbial activity resulted in extensive microbial erosion on the high-grade monazite ore.

Keywords:

Biofilm, Contact Bioleaching, *Klebsiella aerogenes*, Monazite, Phosphate Minerals, Xenotime

## 1. Introduction

The depletion of high-grade mineral resources, and high energy consumption and environmental issues of traditional mining processes have led the mining industry to search for alternative ore processing strategies <sup>1,2</sup>. Bioleaching, the dissolution of minerals and mobilization of elements from insoluble ores, concentrates or wastes through biological activity, has been used at a commercial scale for the extraction of uranium and metals such as copper, cobalt, zinc, nickel, and pre-treatment of refractory sulfidic gold ores. More recently, it has been explored for the extraction of rare earth elements (REEs) <sup>1,3,4</sup>.

The REEs are 17 elements in the periodic table of elements, including scandium, yttrium, and 15 elements of the lanthanide series, which have many applications in the current and future technologies <sup>5</sup>. Conventional pyro- and hydrometallurgical REEs extraction and refining processes use high temperatures and concentrated alkalis (sodium hydroxide) or acids (sulfuric acid). Large quantities of toxic waste containing radionuclides (thorium, uranium), hydrogen fluoride, hyperacidic, or hyperalkaline wastewater, dust and associated pollutants can be produced, which results in significant environmental consequences, greenhouse gas emissions and large carbon footprint <sup>6,7</sup>.

Previous studies on monazite, an important commercially exploitable phosphate mineral containing light REEs (La, Ce, Pr, Nd), suggest bioleaching as a potential green approach for REEs extraction <sup>8,9</sup>. Indigenous microbial communities, acidophilic iron and sulfur oxidising bacteria, and phosphate solubilizing microorganisms (PSM) were used as the bioleaching agents <sup>8,9</sup>. Amongst the tested phosphate solubilising bacteria, *Klebsiella aerogenes*, formerly known as *Enterobacter aerogenes*, had a very high phosphate dissolution efficiency from tricalcium phosphate at 43%, and the highest REE bioleaching performance from monazite at



2<sup>10</sup>. Further studies showed adding *K. aerogenes* to the native microbial community of monazite significantly promoted the REE extraction to 20 mg L<sup>-1</sup> through syntrophic effects<sup>8</sup>. In our previous studies, the changes in pH, phosphate concentration, and released REE has been reported. A 4-8 mg L<sup>-1</sup> bioleaching yield was reported for *K. aerogenes*. Furthermore, through a synergic effect, 3 days of bioleaching with *K. aerogenes* preconditioned the system for *Acidithiobacillus ferrooxidans* growth and resulted in the highest reported REE dissolution from monazite at 40 mg L<sup>-1</sup><sup>8-11</sup>. Fathollahzadeh *et al.* (2018-a) and Corbett *et al.* (2018) also reported evidence of both fungal and bacterial attachment to monazite ore. However, the process of microbial attachment and biofilm formation on the surface of these minerals is not understood.

Microbial attachment to surfaces and biofilm formation are universal phenomena of microbial life<sup>12</sup>. In a bioleaching environment, attachment and subsequent biofilm formation have been shown to be vital prerequisites of the bioleaching and result in higher bioleaching efficiency<sup>13,14</sup>. A mechanism of bioleaching monazite by phosphate solubilising microorganisms has been proposed by Fathollahzadeh *et al.* (2018-a and 2019), who suggested microbial attachment to the mineral is essential. The research demonstrated that the leaching efficiencies in the absence of microbial contact were significantly lower than when microorganisms were in contact with the mineral, signifying the importance of microbial contact in comparison to non-contact leaching<sup>4,11</sup>. Many studies have showed iron and sulfur oxidizing microorganisms are capable of colonizing the surface of sulfide minerals and form a biofilm<sup>13-15</sup>. Colonisation of a sulfide mineral surfaces by these microorganisms is favoured on and around surface areas with physical imperfection or lower degrees of crystallization. Furthermore, microbial activity resulted in more severe changes on the surface and subsurface of sulfide minerals compared to abiotic controls<sup>13-15</sup>. With detailed evidence

on the bioleaching of sulfide minerals and microbial biofilm formation on their surface, it is reasonable to hypothesise a similar mechanism of action for phosphate minerals. Nevertheless, these subjects have not been studied for phosphate minerals. In this study, microbial attachment and biofilm formation of *K. aerogenes*, localization of the biofilm formation toward physical or chemical properties of the surface, and microbial mediated changes on the surface of monazite and xenotime samples were investigated using advanced microscopy techniques.

## **2. Material and methods**

### **2.1. Minerals and their characterisation**

A high-grade monazite ore was provided by Lynas Rare Earths, Australia, and was sized into 50-200  $\mu\text{m}$ . The sample was gamma radiated at 50 kGy for 11 h (ChemCentre, Bentley, Western Australia) to inactivate any indigenous microorganisms. A monazite and a xenotime crystal were also used. The mineralogical characterization and composition analysis of these samples were undertaken by using X-ray diffraction (XRD), inductively coupled plasma mass spectrometry (ICP-MS), and TESCAN Integrated Mineralogy Analyser (TIMA)

For the XRD-phase identification, the high-grade monazite ore was micronized and front-loaded into a specimen holder, and diffraction data was collected with a Bruker D8 Discover diffractometer with Ni-filtered Cu  $K\alpha$  radiation (40 kV, 40 mA) over the range  $7 - 120^\circ 2\theta$ , with a step size of  $0.015^\circ$ . Phase identification was carried out in Bruker EVA 5.2 using the COD database. TIMA Analyses were conducted at 25 kV accelerating voltage, in dot mapping mode at an analytical resolution of 3 microns for Back-scattered Electron Detector (BSE) acquisition and 9 microns for Energy-dispersive X-ray spectroscopy (EDS) point spectroscopy

analyses. Post-processing of the acquired data was performed using TIMA software v. 2.1.1 (TESCAN, Czech Republic). The Laser Ablation ICP-MS analysis was conducted by Bureau Veritas following their guidelines (<https://www.bureauveritas.com.au/laser-ablation-icp-ms>).

## **2.2. Microorganism**

*Klebsiella aerogenes* ATCC 13048 (formerly known as *Enterobacter aerogenes* ATCC 13048) was maintained on nutrient agar (Sigma, Germany) and prior to the experiments, was transferred into 100 mL National Botanical Research Institute's Phosphate medium (NBRIP: 5 g L<sup>-1</sup> MgCl<sub>2</sub>(H<sub>2</sub>O)<sub>6</sub>, 0.25 g L<sup>-1</sup> MgSO<sub>4</sub>(H<sub>2</sub>O)<sub>7</sub>, 0.2 g L<sup>-1</sup> KCl, 0.1 g L<sup>-1</sup> NH<sub>4</sub>SO<sub>4</sub>, 1 g L<sup>-1</sup> KH<sub>2</sub>PO<sub>4</sub>, 1 g L<sup>-1</sup> K<sub>2</sub>HPO<sub>4</sub>, 30 g L<sup>-1</sup> glucose, pH 6.2±0.4)<sup>16</sup> and incubated at 30°C, under aerobic conditions at 120 rpm for 3-5 days.

## **2.3. Cell enumeration by flow cytometry**

Absolute bacterial cell numbers were determined using flow cytometry. Bacterial cells were fixed in glutaraldehyde solution (final concentration of 2%; Sigma, Germany) and assessed in log-fold dilution series in NBRIP media. Bacteria were suspended in a final volume of 1 mL of filter sterilised (0.22 µ, Millipore) NBRIP medium and stained with 5 µL of 1.67mM solution SYTO85 (Invitrogen, USA) per one millilitre of bacterial suspension for 20 minutes at room temperature, in the dark.

Samples were kept on ice in the dark before acquisition. Bacterial numbers were acquired on the four-laser configuration (405nm, 488nm, 561nm and 638nm) Attune NxT Acoustic Focusing Flow Cytometer (Invitrogen, USA). The cytometer was set to acquire 50 µL of sample at an acquisition rate of 25 µL/min. The threshold was set to the lowest SSC-H value (0.1×10<sup>3</sup>)

to determine true bacterial events from that of electronic noise, using negative controls that contained NBRIP alone, unstained bacteria in NBRIP or NBRIP with SYTO85 (Figure S-5).

A primary gate was used to identify bacteria through 488nm SSC profiles and the fluorescence signal of SYTO85. Data was exported as FCS3.0 files and analysed in FlowJo v10.7 (BD Biosciences). Bacterial SYTO85+ events were divided by the total acquisition volume to obtain the concentration of cells mL<sup>-1</sup>. This value was used to determine the volume of stock bacterial culture needed to achieve a final concentration of 1×10<sup>7</sup> cells mL<sup>-1</sup> in the test flasks.

#### **2.4. Evaluation of biofilm formation**

Confocal laser scanning microscopy (CLSM) and scanning electron microscopy (SEM) were used to monitor initial attachment and colonisation of the minerals surface, localization of biofilm formation, and microbial mediated changes on the surface of the minerals by *K. aerogenes*<sup>17</sup>.

The bioleaching setting was designed following our previous studies<sup>8,9,11</sup>. The high-grade monazite ore, monazite-muscovite crystal, and xenotime crystal (0.5-2 mm) samples were subjected to bioleaching by *K. aerogenes* in NBRIP medium using these mineral samples as the sole source of phosphate. Ore and crystal samples were fixed on pre-autoclaved standard microscope slides (glass, Westlab, Australia) using an epoxy adhesive that provides glass-like transparent curing (E6000 Multipurpose Adhesive, USA). The slides were sterilised by submerging them in 70% ethanol for 10 minutes and then exposed to UV for one hour on each side. The slides were then placed inside flasks containing 100 mL phosphate free NBRIP medium with an initial pH of 6.2±0.4 and an initial inoculum size of ~1×10<sup>7</sup> cells/mL pre-enumerated using flow cytometry. The flasks were incubated at 30°C. In previous studies a

shaking speed of 120 and 130 rpm were used<sup>8,9,11</sup>. However, 120 or 130 rpm was not enough to provide enough oxygen when the slides were used in the system. Hence, 140 rpm was used as the shaking speed. Slides were removed from the media at 4, 8, 16, 24 hours, and 2, 3, 5, 8, 11 and 14 days.

Immediately after sample collection, samples were washed with 25 mL sterile NBRIP media to remove planktonic and loosely attached cells from the surface of the samples. This step was repeated five times. A silicon cavity (Proscitech, Australia) was fixed on the slides and filled with 500  $\mu$ L of staining mixture containing Hoechst 33342 (1  $\mu$ M) and DiTO-1 (1  $\mu$ M) in phosphate and glucose-free NBRIP media, incubated in the dark at ambient temperature for a minimum of 20 minutes. The samples were washed with 25 mL sterile NBRIP medium to remove the staining solution<sup>18</sup>. These two fluorochromes were used to maximise cell visualization. Hoechst 33342 (AATBio, USA) is a membrane permeant dye that stains any DNA molecule inside and outside the cells, genomic and extracellular DNA (eDNA), respectively. DiTO-1 (AATBio, USA) is a membrane impermeant dye that only stains the DNA molecules external to the cell walls of living cells (eDNA) and the genomic DNA of the dead cells, or lives cells with compromised membrane.

The samples were air-dried at room temperature. Then 500 $\mu$ L glycerol was added to the cavity; the cover slide was then sealed with clear nail polish. The samples were kept in the dark and cold (4°C) until CLSM imaging. Chemical leaching was tested using sterile Milli-Q water and sterile NBRIP medium at three pH values (pH 6, 5, and 4) and was used as a control to study any changes in the autofluorescence of the samples. Samples were imaged using a Nikon A1+ point scanning confocal microscope with NIS elements software (Nikon Instruments, Tokyo, Japan). Hoechst 33342 was excited at 405 nm laser and detected through

450/50 filter. DiTO-1 was excited at 457 nm laser and detected through 525/50 filter. The colonisation and biofilm formation were studied using 10× and 20× objectives.

## **2.5. Live imaging**

Bioleached mineral samples were studied using live mode CLSM imaging. Bioleaching was conducted in conical flasks with phosphate free NBRIP medium at a 1% slurry of monazite as the sole phosphate source and an inoculum of  $\sim 1 \times 10^7$  cells mL<sup>-1</sup>. Samples of the high-grade monazite ore were taken at 4, 8, 16, 24 hours, and 2, 3, 5, 8, 11 and 14 days. To further evaluate the changes in the biofilm after the initial dispersion stage sampling was continued to day 70 (at days 20, 25, 30, 35, 40, 45, 50, 60, and 70). The samples were collected in microtubes and allowed to settle at room temperature for 1 minute. To remove the planktonic and unattached cells from sediments, the supernatant was discarded, 1 mL glucose and phosphate-free NBRIP medium added and microtubes mixed by gentle inversion, the ore allowed to settle, and the supernatant discarded. This was repeated five times. The staining procedure followed the same methodology as above using NBRIP with glucose to support metabolic activity of the cells. After staining, the mixture was transferred to a  $\mu$ -Slide 2 Well Glass Bottom microscope slide (ibidi, Germany).

CLSM images were collected in Z-stack mode with 3.5-7-micron intervals ( $\times 10$  and  $\times 20$  objective lenses) or  $\leq 1$  micron intervals ( $\times 40$  and  $\times 100$  objective lenses). The images were analysed in Nikon NIS elements software and were visualised in Maximum Intensity Projections mode. The 3D structure of the samples was created and recorded. In the case of high-grade monazite samples, the acquired Z-stack CLSM images were reanalysed in Imaris v 9.7 (Oxford Instruments, UK) to detect selective attachment of the cells to specific surface properties. The surface of the monazite samples was reconstructed using the “Surface” tool

and the cells were modelled using “Spots” tool to provide a better 3D view of both cells and the surface. To assess autofluorescence of the samples, abiotic leaching was conducted in NBRIP media and Milli-Q water at three different pH values: 4, 5 and 7.

## **2.6. Fluorescent microscopy**

Live fluorescent microscopy was used to study bacterial attachment 10 minutes after inoculation. *K. aerogenes* pre-stained with Hoechst 33342 was added to a high-grade monazite ore sample in 500  $\mu$ L NBRIP medium in a  $\mu$ -Slide 2 Well Glass Bottom microscope slide. Hoechst 33342 was visualised using WB: blue excitation (wide band) filter (Ex 465/15, FT 500, LP 515).

## **2.7. SEM-EDS**

After obtaining the CLSM micrographs of the immobilised monazite and xenotime samples, the same samples were used for SEM imaging and EDS analysis. Samples were subjected to carbon (10 nm) and platinum (3 nm) coating (CMCA, WA) for high resolution imaging and studied on TESCAN Clara FESEM microscope using TESCAN Essence software ((John de Laeter Centre (JdLC), Curtin University, Australia) at an operating voltage of 5 or 10 kV and beam intensity of 300 pA. Images were taken using secondary electrons (SE), or a dual detector using SE and backscattered electrons (SE/BSE). For SE an accelerating voltage of  $\geq 5$  kV and beam intensity of 300 pA were used, for EDS analyses an accelerating voltage of  $\geq 15$  kV and beam intensity of 1 nA were used, and for SE/BSE imaging either of the two setting were used.

## **2.8. Focused Ion Beam- Scanning Electron Microscopy (FIB-SEM)**

Cross-sectional analysis of the biofilm on high-grade monazite ore was conducted using a TESCAN Lyra3 FIB-SEM located at JdLC, Curtin University, which has a monoisotopic  $^{69}\text{Ga}^+$  liquid metal ion source. This dual-beam system can achieve an imaging resolution of  $<2.5$  nm (at 30 kV) for the Cobra FIB column, and 1 nm (at 30 kV) for the SEM column. A 1- $\mu\text{m}$  thick platinum (Pt) layer was deposited through electron beam and ion beam to protect the surface profile of the region to be analysed. The electron beam deposition is a non-destructive process which provides the best protection of the biofilm. Subsequently a 30 kV ion beam was employed to cross-section the region of interest by sputtering approximately 10  $\mu\text{m}$  of material away and progressively polishing the cross-section with lower currents.

### **3. Results**

#### **3.1. Mineral characteristics**

The mineral characterisation analyses of the high-grade monazite ore (Figures S-1 and S-2 and Tables S-1 to S-4) indicated that monazite was the main mineral group in this sample. Crandallite, florencite, beryl, quartz, goethite, hematite/magnetite and several other minerals were also present in this sample. Moreover, TIMA mineral mapping showed difference in the mineralogy and chemical composition between different grains of the high-grade monazite. Due to the high mineral complexity, some grains and regions were rich in elements specifically Al, Ca, Si, Fe, and REE, while others contained less or none of these elements (Figure S1 and S14).

The monazite-muscovite ore mainly consisted of two major mineral plates, the monazite plates rich in REEs-phosphate and aluminium silicate plates determined as muscovite using



TIMA analysis (Figure S3). This sample also contained florencite, hematite and several other minerals.

Xenotime crystal showed relatively homogenous mineralogy (Figure S-4), mainly containing xenotime group of minerals.

### **3.2. Biofilm formation**

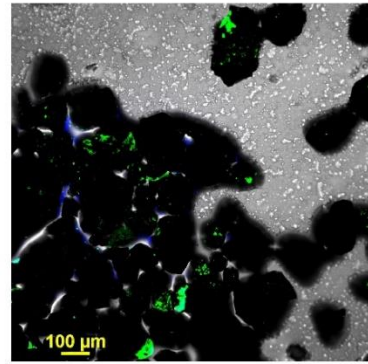
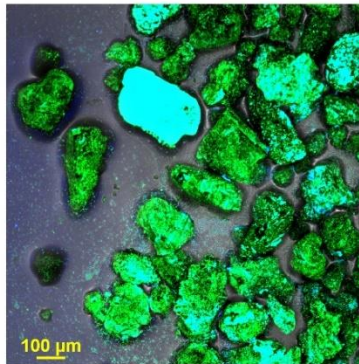
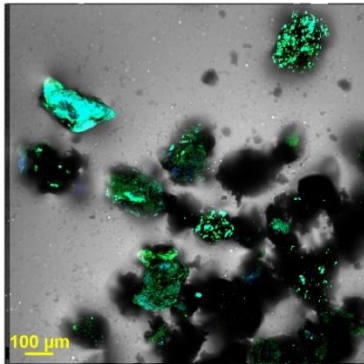
No or negligible autofluorescence due to abiotic leaching was detected using CLSM, signifying no or negligible effect of mineral autofluorescence on the recorded fluorescence of the bioleaching samples (Figure S-6). Therefore, the recorded fluorescence of the bioleaching samples was only representative of microorganisms.

**Stage 1- Attachment**

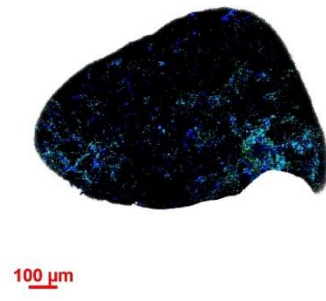
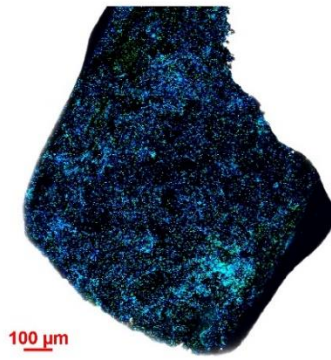
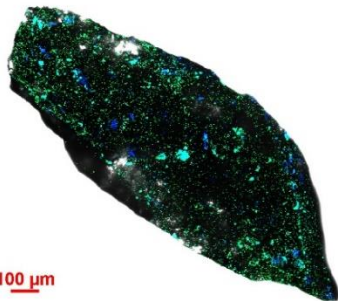
**Stage 2- mature biofilm**

**Stage 3- Dispersion**

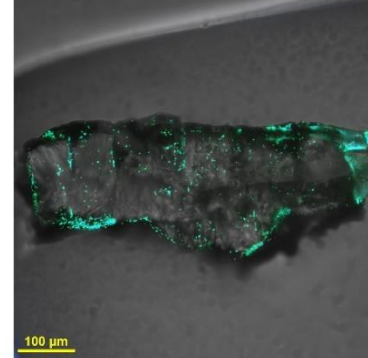
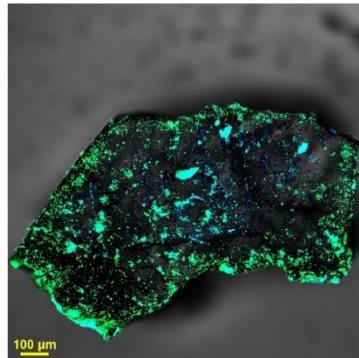
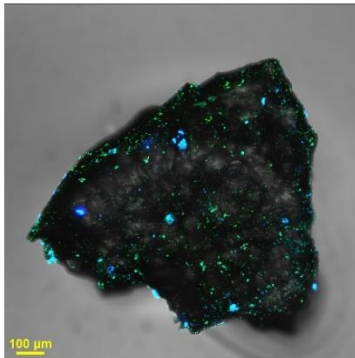
**a. high grade monazite**



**b. monazite crystal**



**c. xenotime crystal**



**d. high grade monazite**

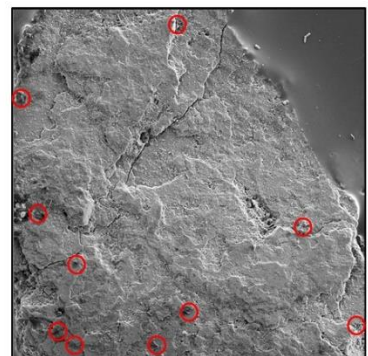
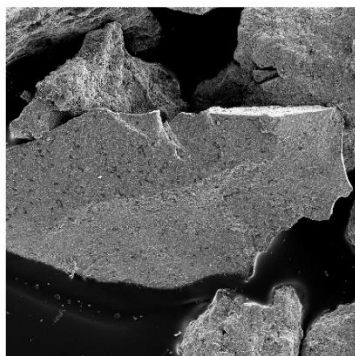
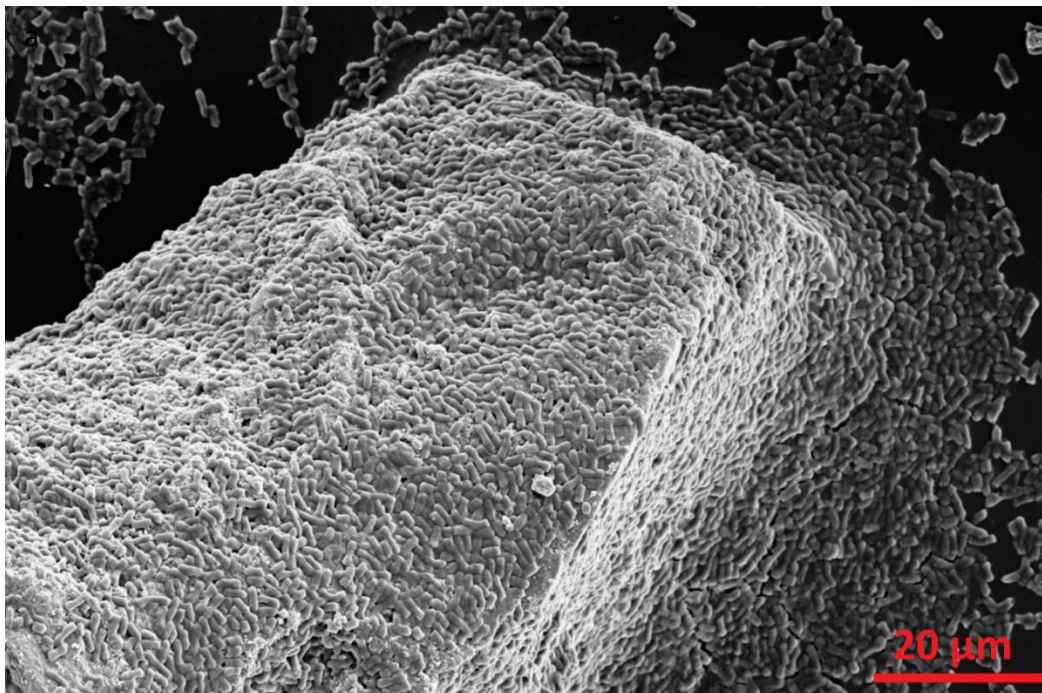


**Figure 1.** Visualisation of *Klebsiella aerogenes* biofilm on the surface of high-grade monazite ore (a and d), monazite-muscovite crystals (b) and xenotime crystals (c). CLSM images are the merged images of Hoechst 33342 (blue) and DiTO-1 (green) to maximise microbial cell visualisation and transmitted light channels. The image shows the Maximum Fluorescent Intensity of the acquired Z-stack images where blue, green or cyan colours on the surface of the ore grains (the dark grains) are representative of the microbial biofilm, the red circles in secondary electron SEM images (panel d) indicate on the small number of bacteria on the surface.

*K. aerogenes* was able to use high-grade monazite ore as the sole source of phosphate and the planktonic cell number increased from  $\sim 1 \times 10^7$  cell/mL to  $\sim 1 \times 10^9$  cell/mL in 2 to 3 days (data not shown). It was also capable of growing on both monazite and xenotime crystals. *K. aerogenes* was capable of attachment to the surface of high-grade monazite ore (Figure a & 1-d, Figure S-7 and S-10), monazite-muscovite crystals (Figure 1-b, Figure S-8), and xenotime crystals (Figure 1-c, Figure S-9). Biofilm formation and development occurred over three stages, initial attachment during the first 8 hours after inoculation, colonisation and maturation from day 1 to day 8, and dispersion at day 11 onward.

Initial attachment occurred very early after bacterial inoculation. Ten minutes after inoculation, *K. aerogenes* cells were already attached to the surface of the high-grade monazite (data not shown). The CLSM records 4 and 8 hours after bioleaching showed a high extent of attachment to some of the ore grains. This initial attachment led to the second stage of biofilm formation, the colonisation of the surfaces (16-24 h) and the formation of a mature biofilm over the following days (day 2 to day 8) (Figure S-7 and S-10).

From day 11, CLSM and SEM records indicated a reduction in the biofilm, marking the third stage, dispersion, with a significant proportion of the sessile population detaching from the biofilm as shown by a dramatic decrease of the biofilm-related fluorescence on the surface of the ore grains (Figure S-7). At day 14, while very few cells were attached to the surface for some of the ore grains, some other grains partially harboured active biofilm. Scanning electron microscopy confirmed these findings showing cell numbers attached to the surface of the ore were increasing from early attachment to colonisation and maturation stage, and then was decreasing by day 14 (Figure S-10). The live microscopy records of the high-grade monazite ore continued to 70 days after inoculation and showed signs of active re-colonisation and dispersion after the first dispersion at days 11 and 14 (Figure S-11). A similar pattern was observed for the other two mineral samples, monazite-muscovite (Figure S-8) and xenotime (Figure S-9) crystals. Moreover, the SEM and CLSM micrographs showed that the biofilm structure was a thin-layer biofilm (Figure 2, and S-12).





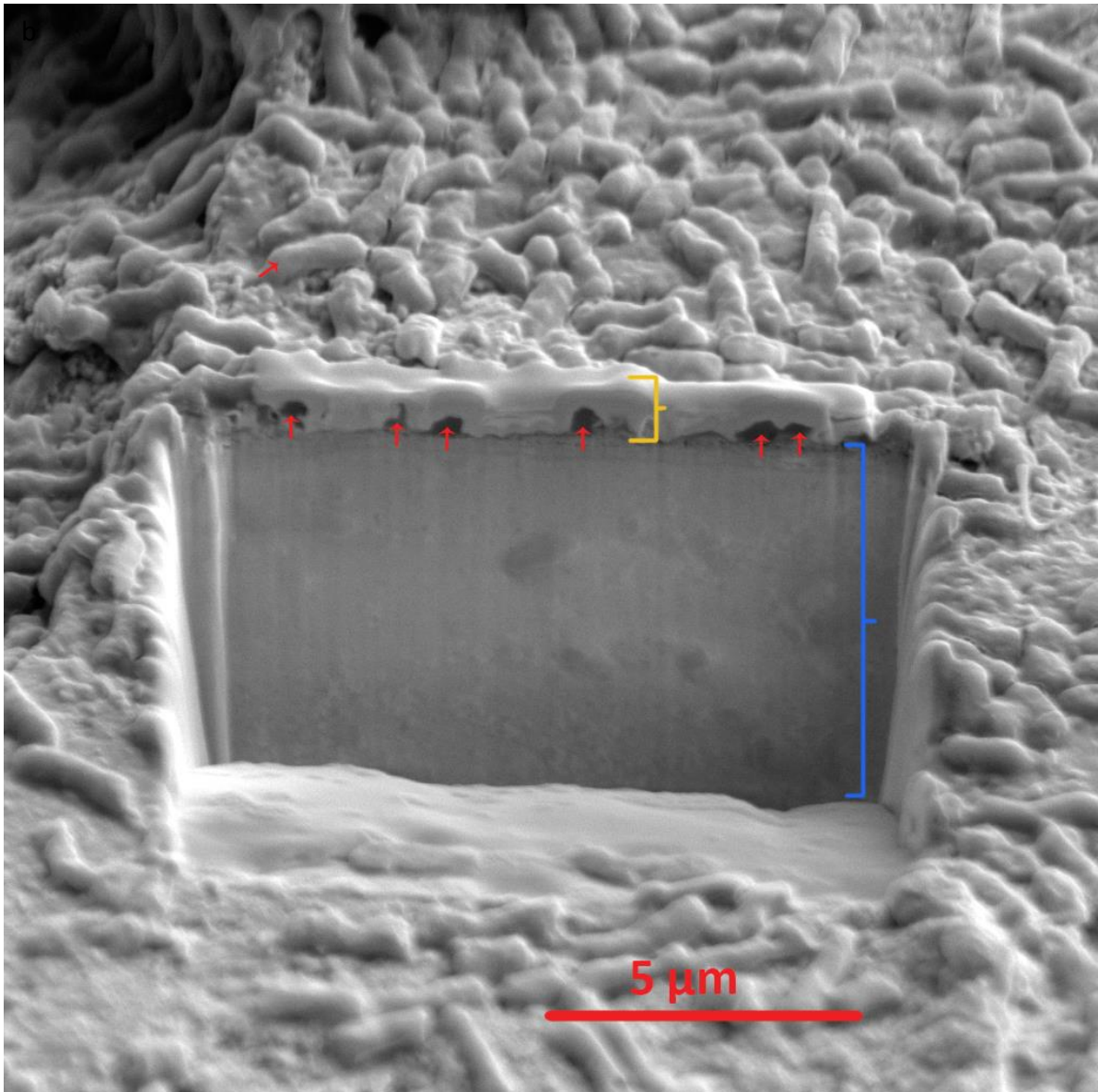


**Figure 2.** SEM micrographs of (a) high-grade monazite grain covered in *Klebsiella aerogenes* mature biofilm, and (b) a FIB cross-section as the surface of the grain revealing a ~500 nm thick biofilm on the surface of the mineral. A 1- $\mu\text{m}$  thick Pt protection layer was deposited on the region of interest before the FIB cut to keep the surface profile of the region. Red arrows indicate bacteria, yellow bracket indicate the 1- $\mu\text{m}$  thick Pt protection layer, and blue bracket shows the subsurface of high-grade monazite in the cross section.

### **3.3. Localization of attachment and biofilm formation to physical imperfections**

Attachment, further localization and the resultant formation of biofilm of *K. aerogenes* were directed toward specific areas on the minerals' surface, namely physical imperfections (cracks, grooves, dents, scratches, holes, pits, edges, etc.) on the surface of high-grade monazite ore (Figure 3-e and 3-f), monazite-muscovite (Figure 3 -c and 3-d, and Figure S-13), and xenotime crystals (Figure 3 -a and -b, and Figure S-14). SEM micrographs showed that while the reasonably flat surface of xenotime or monazite-muscovite crystals could harbour bacterial cells, the greatest intensity of biofilm formation was on and around the surface imperfections. A similar attraction and a higher density of microbial biofilm in areas with physical imperfections were also observed for high-grade monazite ore (Figure 3-e and 3-f).

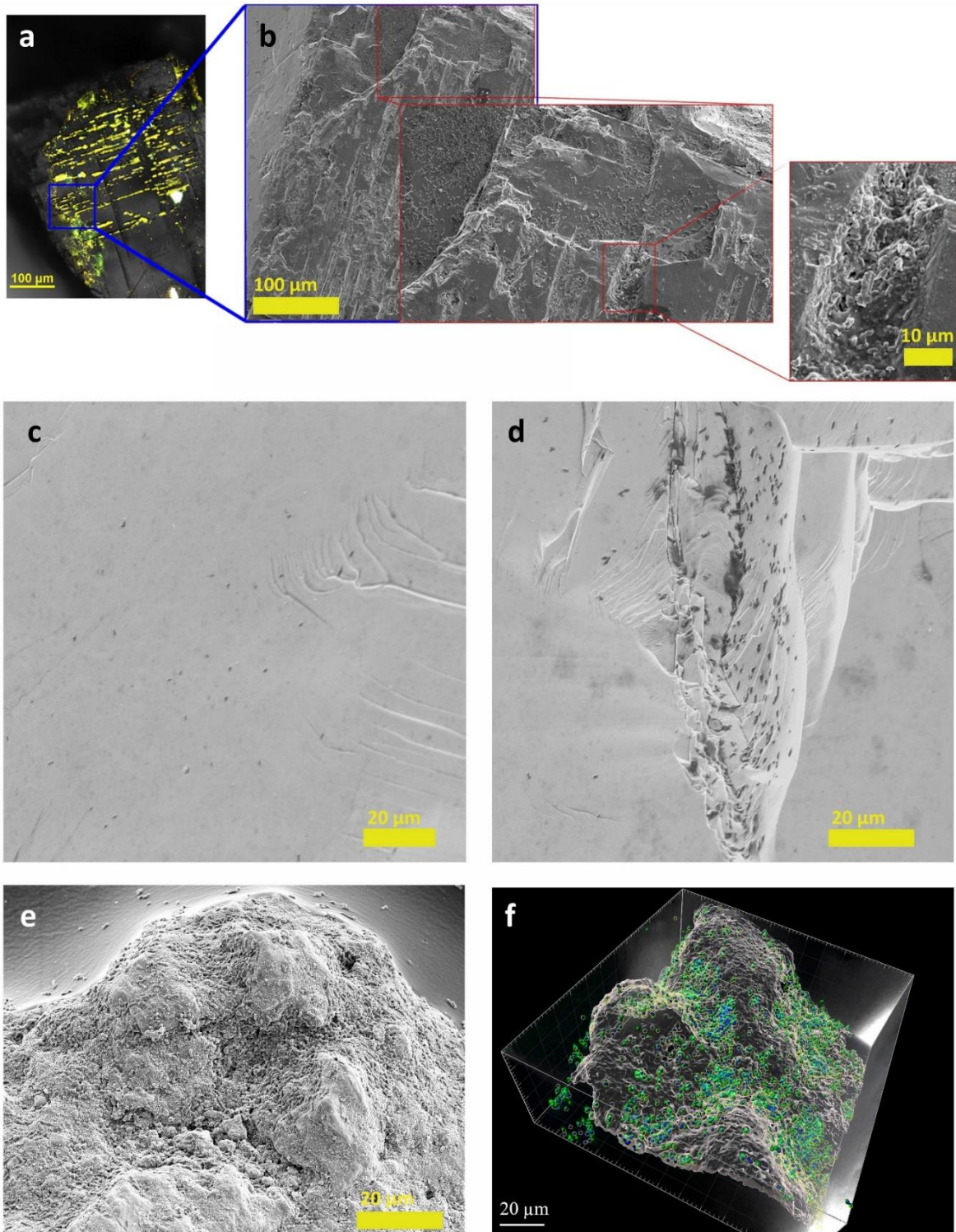


**Figure 3.** Localization of *Klebsiella aerogenes* biofilm on the surface of xenotime crystal visualised by CLSM (a) and secondary electron SEM (b), monazite-muscovite crystal visualised by SEM (c, d), and high-grade monazite ore by SEM (e) and CLSM (f). In panel “a” the golden

area is representative of bacterial biofilm. In panel “f”, the surface and the bacteria are reconstructed from CLSM Z-stack images using Imaris software. Bacteria are the blue/green spheres (blue for genomic-DNA, green for eDNA) and the surface is semi-transparent white area.

### **3.4. Localization of attachment and biofilm formation to specific mineralogy or chemical composition**

Biofilm formation was localised on and around physical imperfections; however, no specific localization based on the differences in chemical or mineral composition was observed. *K. aerogenes* developed small micro-colonies on both monazite (Figure 4-a, white regions in the SEM micrograph) and muscovite (Figure 4-a, dark regions in the SEM micrograph) plates of monazite-muscovite crystals. In the case of high-grade monazite ore, biofilm formed on all ore high-grade grains, independent of the mineral or chemical composition such as aluminium rich, iron rich or rare earth rich regions (Figure 4-c and 4-e and Figure S-15 and S-16).



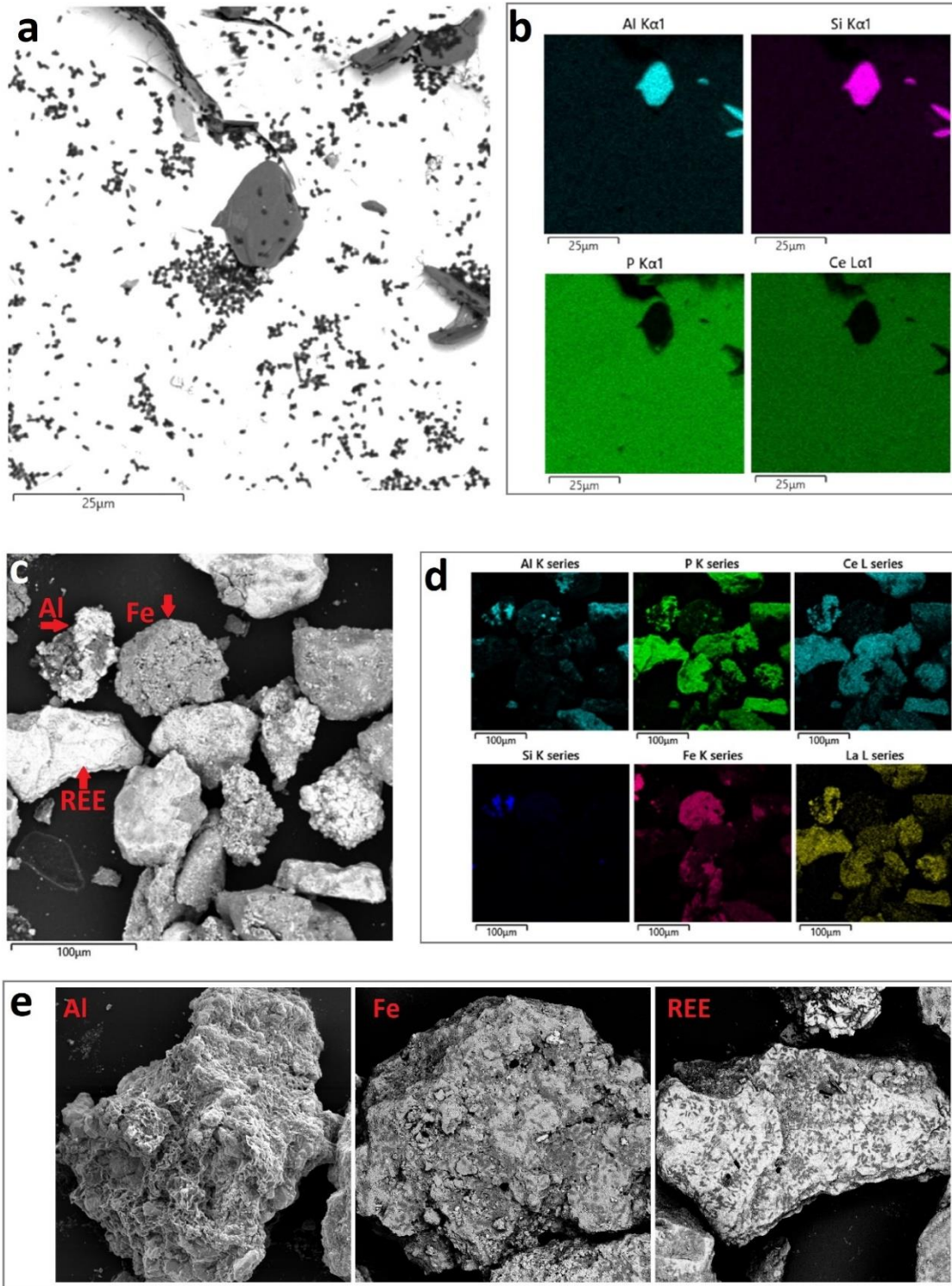


**Figure 4.** *Klebsiella aerogenes* biofilm on monazite-muscovite crystals where monazite are the white regions, and muscovite plates are the dark plates (a), and high-grade monazite ore (b). *K. aerogenes* cells are the small black/grey bacilli shapes on the surface. The SEM (SE/BSE dual detector imaging) micrographs (a, c, e) were obtained with backscattered electron imaging;

hence heavier elements depicted brighter and light elements are depicted darker. The SEM-EDS elemental map analysis shows chemical composition of different mineral plates and grains in the samples (b & d). The black regions in the SEM-EDS maps (b & d) represent absence of an element of interest and the coloured area represent the areas on the surface where the related EDS signal was detected for that specific element.

### 3.5. Changes on the surface and subsurface of the monazite minerals due to microbial activity

SEM was used to investigate changes to the mineral surface as a result of microbial activity since CLSM was not a suitable tool to study such changes in detail (data not shown). After two weeks of bacterial activity, some of the grains of high-grade monazite ore samples showed dramatic surface erosion due to microbial activity; however, such erosion patterns were not observed in abiotic control samples (Figure 5).

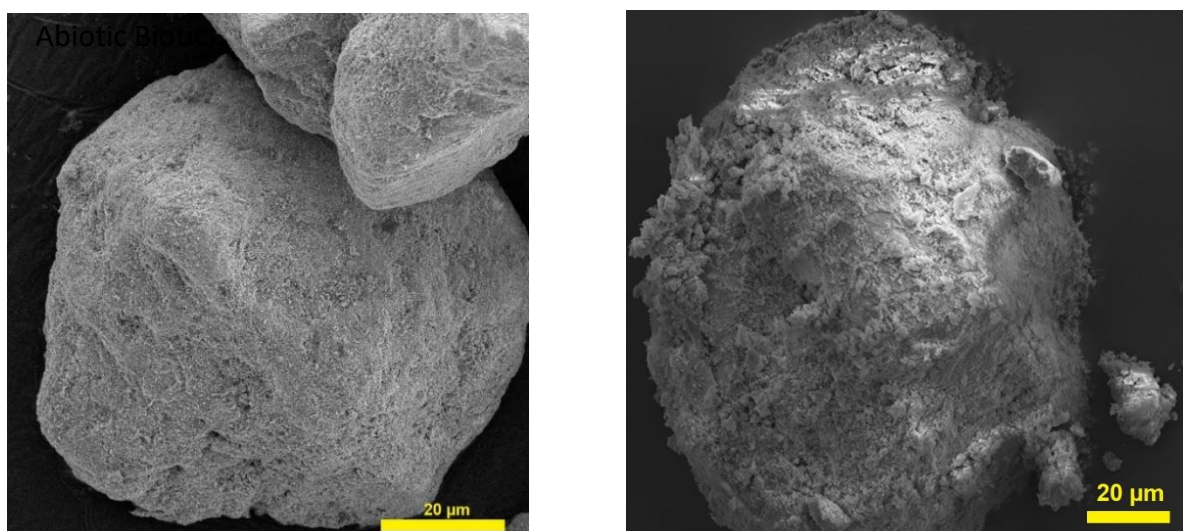


**Figure 5.** Visualisation of the surface of high-grade monazite ore monazite after 14 days of abiotic leaching (a) and bioleaching in the presence of *Klebsiella aerogenes* (b).

#### 4. Discussion

Biofilm is a universal attribute and the prevalent form of microbial life in natural ecosystems for most microorganisms, if not all <sup>19</sup>. Biofilm formation is of value in bioleaching based technology. Of the three proven mechanisms for bioleaching of sulfide minerals, contact, non-contact and cooperative models <sup>2,20,21</sup>, two mechanisms (contact and cooperative) require biofilm formation. Fathollahzadeh *et al.* (2018-a) conceptualised the bioleaching of phosphate minerals in the same three mechanisms and showed that the leaching efficiencies in the absence of contact to minerals were significantly lower than in contact with minerals, which signifies the importance of microbial contact in comparison to non-contact leaching <sup>4,11</sup>. The current study provides evidence to validate the most critical aspect of REE contact leaching, the formation of microbial biofilm on the surface of the REE minerals.

Similar to other *in vivo* or *in vitro* studies of microbial biofilm formation, the microscopy data confirmed the three main stages of biofilm formation for *K. aerogenes* on the surface of phosphate minerals. The first step in forming a biofilm involves introduction of the bacteria to a surface <sup>22,23</sup>. The initial attachment of *K. aerogenes* started very early after exposure to the high-grade monazite ore. This early phase of initial attachment is a dynamic and reversible process which is in response to nutrient availability, hydrodynamic or repulsive forces <sup>23</sup>. However, given enough time, the early attachment leads to colonisation and further development of mature biofilm, the second major distinguishable stage of biofilm development. This occurs when the cells are ready to commit to a biofilm lifestyle which requires irreversible attachment to the surface <sup>23,24</sup>. The colonisation continued further until almost the whole available surface of the high-grade monazite ore and a notable area on the

monazite or xenotime crystals were covered with bacterial biofilm which marks the maturation stage. The maturation stage favours a higher expression of factors favouring sessile state such as those associated with extracellular polymeric substances (EPS) production<sup>23,25,26</sup>. Although biofilm architecture is continuously changing as a result of the external and internal factors, it finds its most complex and stable form at the maturation stage. The SEM records of *K. aerogenes* mature biofilm demonstrated that the formed biofilm on the surface of phosphate minerals was a thin-layer structure (Figure 2). The complexity of the biofilms' 3D structure varies for different microorganisms and environmental conditions with single species-biofilm of some bacteria such as *Pseudomonas aeruginosa* capable of forming multi-layer complex structures known as the mushroom-shaped biofilm<sup>23</sup>. One reason for the simple structure of *K. aerogenes* biofilm could be due to a relatively high fluid shear force generated from shaking at 140 rpm which can affect the structure, density and attachment strength, or even metabolic activity of a biofilm<sup>27</sup>.

The final stage of a biofilm development cycle is dispersion<sup>19</sup>. Detachment is dynamic and heavily affected by the external and internal factors such as pH, temperature, and chemotaxis inside the biofilm matrix<sup>19,22</sup>. However, at some point after the maturation stages a considerable proportion of the sessile subpopulation leaves the biofilm lifestyle. For *K. aerogenes* this process was initially observed at days 11 onward when a notable decrease in the biofilm was recorded in both CLSM and SEM records in contrast to the maturation phase (days 1-8). Dispersion rarely involves the entire biofilm and occurs through passive or active mechanisms<sup>19</sup>. The fluid shear force, erosion and sloughing by fluid frictional force, and abrasion due to collisions of biofilm with floating mineral particles can lead to passive detachment of *K. aerogenes* biofilm<sup>19,22,28</sup>. Moreover, live microscopy performed between days 20 to 70 (Figure S-11) show signs of active re-colonisation and dispersion of the ore

grains after the initial dispersion observed at day 11 onward indicating an active seeding dispersal mechanism<sup>19</sup> for *K. aerogenes*.

A critical question in biofilm studies is regarding the localization of microbial biofilm. Microbial colonisation of a surface and biofilm formation are not entirely random processes and can be influenced by topography and chemical or physical properties of a surface<sup>12,14,26</sup>. In bioleaching settings, biofilm formation is predominant on the sites with higher surface roughness, physical imperfections, and surfaces with lower degrees of crystallization<sup>13,14,29</sup>. The formed biofilm on xenotime crystal (Figure 3 and S-14) shows the localization of *K. aerogenes* biofilm on and around physical imperfections of the surface (dents, grooves and cracks). The CLSM micrograph (highlighted in gold –Figure 3-a, Figure S-14) represents the biofilm and is well matched with the physical imperfections. The SEM of the same surface demonstrated the number of attached cells on the reasonably flat surfaces with minimum topographical imperfections was lower than on and around physical defect sites of the surface where some micro-colonies were formed. A similar pattern was observed for monazite-muscovite crystals, (Figure 3, and S-13). The same was also observed for high-grade monazite ore in which both SEM (Figure 3-e) and computer-aid reconstructed CLSM image (Figure 3-f) demonstrate localization of biofilm on the grooves. It is notable that the total biofilm-covered area vs. biofilm-free area on the monazite-muscovite crystals or xenotime crystals was lower than that of the high-grade monazite. This could be due to differences in the surface properties of the samples, including roughness, imperfections and crystallinity degree as the high-grade monazite ore has a higher surface roughness compared to the other two mineral samples.

Previous research on bioleaching biofilms<sup>13,26,30,31</sup> showed that *Acidithiobacillus ferrooxidans* selectively attaches and forms biofilms predominantly on and around physical and topographic imperfections sites on the surface of the minerals (such as pits, pores, holes, cavities, cracks and scratches, dents, steps and layers), crystal properties (degree of crystallization, crystal defects, grain boundaries and crystallographic orientation), and areas with different surface charge imbalances or hydrophobic/hydrophilic areas.

Easier attachment due to more favourable surface properties such as energy, charge imbalance, hydrophobicity-hydrophilicity<sup>14</sup>, and degree of crystallinity<sup>29</sup> are suggested as reasons for selective attachment and biofilm formation on and around the topographical and physical imperfections by some microorganism. Moreover, such locations on the surface provide a higher nutrient availability due to these sites being potential active dissolution regions on the surface, and also provides safety from the sheer fluid force<sup>26</sup>. Furthermore, the transitory chemotactic attraction of electrically charged microbial cells toward dissolution sites may lead to the formation of anode and cathode regions on minerals' surface, which drives the dissolution process further. In such a system, the EPS of a biofilm fills the space between the microbial cells and the surface of the mineral as the matrix interface of the leaching reaction<sup>14</sup>. The reconstructed 3D models from recorded CLSM micrograph during dispersion stage (Video S-1) shows that the developed biofilm inside some visible topographical imperfections stands still at the dispersion stage. Therefore, the topographical imperfections also provide protection against passive detachment due to weaker impacts of fluid shear forces or collisions with mineral particles floating around<sup>26,28</sup>.

Another critical question of the current study was to see if *K. aerogenes* shows selective attachment toward specific mineralogy or chemical composition on the surface. In addition

to physical properties, it has been shown that specific mineralogy or chemical composition of a surface, ionic strength, and presence of certain ions can influence the interaction, attachment, and biofilm development behaviour of microorganisms<sup>14,26</sup>. Figure 4-a and b demonstrates *K. aerogenes* attachment and micro-colony formation occurred on both mineral plates of monazite-muscovite sample, the monazite plate which is rich in REEs phosphates such as cerium (Ce) and phosphate (P) and muscovite plate rich in aluminium (Al) and silicate (Si). The same pattern was observed for the high-grade monazite sample with a much more complex mineralogy (Figure 4-c, d and e and Figures S-15 and S-16). Despite having a diverse range of minerals and chemical distribution of elements on the high-grade monazite sample, *K. aerogenes* biofilm formed on all high-grade monazite ore grains. Xenotime crystals did not show complex mineralogy and were not used for this experiment. Therefore, unlike some of the iron and sulfur oxidizing microorganisms<sup>26</sup>, *K. aerogenes* showed no selectivity toward specific chemical or mineral composition under the tested conditions. Nevertheless, this observation cannot be generalised to other phosphate minerals or phosphate solubilizing microorganisms, since the current study is the only available study addressing this aspect of biofilm formation on such minerals and using such microorganisms. Changing the surface topography, dissolution of some elements, and formation of secondary minerals can occur as a result of both biotic and abiotic leaching and has been reported for both sulfide<sup>15,26,32</sup> and phosphate minerals<sup>33</sup>. The SEM images of *K. aerogenes* activity revealed that after 14 days of bioleaching, the surface of some of the high-grade monazite ore grains subjected to the microbial activity notably changed in the form of an eroded surface, while the abiotic leaching controls with similar pH did not show drastic visible topographical changes and erosion patterns (Figure 5). Fathollahzadeh *et al.* (2018-a) reported a similar observation on MWM monazite, another sample from Lynas Corporation<sup>11</sup>.

Based on the finding of this study, it is reasonable to say in a controlled environment like bioreactor-based bioleaching, a pre-processing such as grinding and milling to fine particles can be done on ore or waste samples to increase the total available surface well as physical properties of the surface to promote microbial attachment and as a result leaching efficiency.

## **5. Conclusion**

*K. aerogenes*, as the model phosphate solubilizing microorganism, was able to colonise the surface of monazite and xenotime and form a thin-layer biofilm. Biofilm development occurred in three distinctive stages, initial attachment, maturation and dispersion. Colonisation and biofilm formation were selective toward physical imperfection such as grooves and cracks but not toward specific mineralogy or chemical composition on the surface. The selective colonisation on and around the physical imperfections could be due to easier access to nutrient on and around these dissolution sites. Such topographical imperfections provided *K. aerogenes* sessile population with protection against the fluid shear forces during initial attachment of the bacterial cells and maturation of the biofilm. The biofilm formed in the grooves and cracks were also protected from passive detachment due to weaker impacts of fluid shear forces or collisions with mineral particles.

## **Acknowledgment**

AVA acknowledges support through a Parker CRC for Integrated Hydrometallurgy Solutions (established and supported under the Australian Government's Cooperative Research Centres Program). The authors acknowledge the Australian Research Council (ARC) for grant DP200103243. The authors acknowledge the Curtin Health Innovation Research Institute (CHIRI), Bentley, Western Australia, for providing the confocal microscopy facilities and the John de Laeter Centre for provision of the scanning electron microscope, X-ray diffraction,



focused ion beam SEM, and TESCAN Integrated Mineralogy Analyser. The authors acknowledge The Institute for Geoscience Research for financial support through TIGeR Small Grants. The authors would like to acknowledge Jeanne Edmands (CHIRI), Michael Nesbit (CHIRI), and Elaine Miller (JDLC) for their technical support.

### **Authors' contribution**

AVA, designed and conducted the experiments, acquired, analysed and interpreted the data, and prepared the original draft of the manuscript.

EW, MC, AK, AP, JE, and HF were involved in the research's conceptualisation and design, critical review of the data analysis and interpretation, and substantial review of the draft. EW, AP and JE were involved in funding acquisition. EW, AP, JE, AK, and MC supervised the project. AVA and CT developed the flow cytometry methodology and data analysis. AVA, WR and XS designed, performed and analysed the focused ion beam methodology and analysis.

All authors were involved in review & editing.

### **Competing interests**

The authors declare no competing financial or non-financial interests.

### **Data availability**

The authors confirm that the data supporting the findings of this study are available within the article's supplementary materials or from the corresponding author [EW] on request.

## References

1. Brandl H. Microbial leaching of metals. *Biotechnology*. 2001;10:191-224.
2. Kaksonen AH, Boxall NJ, Gumulya Y, et al. Recent progress in biohydrometallurgy and microbial characterisation. *Hydrometallurgy*. 2018;180:7-25. doi:10.1016/j.hydromet.2018.06.018
3. Kaksonen AH, Boxall NJ, Usher KM, Ucar D, Sahinkaya E. Biosolubilisation of Metals and Metalloids. In: Rene ER, Sahinkaya E, Lewis A, Lens PNL, eds. *Sustainable Heavy Metal Remediation: Volume 1: Principles and Processes*. Springer International Publishing; 2017:233-283. doi:10.1007/978-3-319-58622-9\_8
4. Fathollahzadeh H, Eksteen JJ, Kaksonen AH, Watkin ELJ. Role of microorganisms in bioleaching of rare earth elements from primary and secondary resources. *Applied Microbiology and Biotechnology*. 2019;103(3):1043-1057. doi:10.1007/s00253-018-9526-z
5. Balaram V. Rare earth elements: A review of applications, occurrence, exploration, analysis, recycling, and environmental impact. *Geoscience Frontiers*. 2019;doi:<https://doi.org/10.1016/j.gsf.2018.12.005>
6. Haque N, Hughes A, Lim S, Vernon C. Rare Earth Elements: Overview of Mining, Mineralogy, Uses, Sustainability and Environmental Impact. *Resources*. 2014;3(4)doi:10.3390/resources3040614
7. Gwenzi W, Mangori L, Danha C, Chaukura N, Dunjana N, Sanganyado E. Sources, behaviour, and environmental and human health risks of high-technology rare earth elements as emerging contaminants. *Science of The Total Environment*. 2018;636:299-313. doi:<https://doi.org/10.1016/j.scitotenv.2018.04.235>
8. Corbett MK, Eksteen JJ, Niu X-Z, Watkin ELJ. Syntrophic effect of indigenous and inoculated microorganisms in the leaching of rare earth elements from Western Australian monazite. *Research in Microbiology*. 2018;169(10):558-568. doi:<https://doi.org/10.1016/j.resmic.2018.05.007>
9. Fathollahzadeh H, Hackett MJ, Khaleque HN, Eksteen JJ, Kaksonen AH, Watkin ELJ. Better together: Potential of co-culture microorganisms to enhance bioleaching of rare earth elements from monazite. *Bioresource Technology Reports*. 2018-b;3:109-118. doi:<https://doi.org/10.1016/j.biteb.2018.07.003>
10. Corbett MK, Eksteen JJ, Niu X-Z, Croue J-P, Watkin ELJ, Engineering B. Interactions of phosphate solubilising microorganisms with natural rare-earth phosphate minerals: a study utilizing Western Australian monazite. 2017;40(6):929-942. doi:10.1007/s00449-017-1757-3
11. Fathollahzadeh H, Becker T, Eksteen JJ, Kaksonen AH, Watkin ELJ. Microbial contact enhances bioleaching of rare earth elements. *Bioresource Technology Reports*. 2018-a;3:102-108. doi:<https://doi.org/10.1016/j.biteb.2018.07.004>
12. Wu S, Zhang B, Liu Y, Suo X, Li H. Influence of surface topography on bacterial adhesion: A review (Review). *Biointerphases*. 2018;13(6):060801. doi:10.1116/1.5054057
13. Vera M, Schippers A, Sand WJAM, Biotechnology. Progress in bioleaching: fundamentals and mechanisms of bacterial metal sulfide oxidation-part A. 2013;97(17):7529-7541. doi:10.1007/s00253-013-4954-2
14. Zhang R, Bellenberg S, Neu TR, Sand W, Vera M. The Biofilm Lifestyle of Acidophilic Metal/Sulfur-Oxidizing Microorganisms. In: Rampelotto PH, ed. *Biotechnology of Extremophiles: Advances and Challenges*. Springer International Publishing; 2016:177-213. doi:10.1007/978-3-319-13521-2\_6
15. Nkulu G, Gaydardzhiev S, Mwema E, Compere P. SEM and EDS observations of carrollite bioleaching with a mixed culture of acidophilic bacteria. *Minerals Engineering*. 2015;75:70-76. doi:10.1016/j.mineng.2014.12.005
16. Nautiyal CS. An efficient microbiological growth medium for screening phosphate solubilizing microorganisms. *FEMS Microbiology Letters*. 1999;170(1):265-270. doi:10.1111/j.1574-6968.1999.tb13383.x
17. Tuck B, Watkin E, Forsyth M, Somers A, Ghorbani M, Machuca LL. Evaluation of a novel, multi-functional inhibitor compound for prevention of biofilm formation on carbon steel in marine environments. *Scientific Reports*. 2021;11(1):15697. doi:10.1038/s41598-021-94827-9

18. Li Q, Sand W, Zhang R. Enhancement of biofilm formation on pyrite by *Sulfobacillus thermosulfidooxidans*. *Minerals*. 2016;6(3):71.
19. Rumbaugh KP, Sauer K. Biofilm dispersion. *Nature Reviews Microbiology*. 2020;doi:10.1038/s41579-020-0385-0
20. Natarajan KA. Chapter 4 - Bioleaching Mechanisms. In: Natarajan KA, ed. *Biotechnology of Metals*. Elsevier; 2018:49-80. doi:<https://doi.org/10.1016/B978-0-12-804022-5.00004-9>
21. Panda S, Akcil A, Pradhan N, Deveci H. Current scenario of chalcopyrite bioleaching: A review on the recent advances to its heap-leach technology. *Bioresource Technology*. 2015;196:694-706. doi:10.1016/j.biortech.2015.08.064
22. Donlan RM. Biofilms: microbial life on surfaces. *Emerg Infect Dis*. 2002;8(9):881-890. doi:10.3201/eid0809.020063
23. Kostakioti M, Hadjifrangiskou M, Hultgren SJ. Bacterial Biofilms: Development, Dispersal, and Therapeutic Strategies in the Dawn of the Postantibiotic Era. *Cold Spring Harbor Perspectives in Medicine*. 2013;3(4)doi:10.1101/cshperspect.a010306
24. Marshall KC, Stout R, Mitchell R. Mechanism of the Initial Events in the Sorption of Marine Bacteria to Surfaces. *Microbiology*. 1971;68(3):337-348. doi:<https://doi.org/10.1099/00221287-68-3-337>
25. Toyofuku M, Inaba T, Kiyokawa T, Obana N, Yawata Y, Nomura N. Environmental factors that shape biofilm formation. *Bioscience, Biotechnology, and Biochemistry*. 2016;80(1):7-12. doi:10.1080/09168451.2015.1058701
26. Bellenberg S, Barthen R, Boretska M, Zhang R, Sand W, Vera M. Manipulation of pyrite colonization and leaching by iron-oxidizing *Acidithiobacillus* species. *Appl Microbiol Biotechnol*. 2015;99(3):1435-1449. doi:10.1007/s00253-014-6180-y
27. Stoodley P, Sauer K, Davies DG, Costerton JW. Biofilms as complex differentiated communities. *Annu Rev Microbiol*. 2002;56:187-209. doi:10.1146/annurev.micro.56.012302.160705
28. Chiume R, Minnaar SH, Ngoma IE, Bryan CG, Harrison STL. Microbial colonisation in heaps for mineral bioleaching and the influence of irrigation rate. *Minerals Engineering*. 2012;39:156-164. doi:10.1016/j.mineng.2012.07.002
29. Sanhueza A, Ferrer IJ, Vargas T, Amils R, Sánchez C. Attachment of *Thiobacillus ferrooxidans* on synthetic pyrite of varying structural and electronic properties. *Hydrometallurgy*. 1999;51(1):115-129. doi:[https://doi.org/10.1016/S0304-386X\(98\)00079-6](https://doi.org/10.1016/S0304-386X(98)00079-6)
30. Zhang R, Bellenberg S, Castro L, Neu TR, Sand W, Vera M. Colonization and biofilm formation of the extremely acidophilic archaeon *Ferroplasma acidiphilum*. *Hydrometallurgy*. 2014;150:245-252. doi:<https://doi.org/10.1016/j.hydromet.2014.07.001>
31. Zhang RY, Neu TR, Bellenberg S, Kuhlicke U, Sand W, Vera M. Use of lectins to in situ visualize glycoconjugates of extracellular polymeric substances in acidophilic archaeal biofilms. *Microb Biotechnol*. 2015;8(3):448-461. doi:10.1111/1751-7915.12188
32. Liu H, Gu G, Xu Y. Surface properties of pyrite in the course of bioleaching by pure culture of *Acidithiobacillus ferrooxidans* and a mixed culture of *Acidithiobacillus ferrooxidans* and *Acidithiobacillus thiooxidans*. *Hydrometallurgy*. 2011;108(1):143-148. doi:<https://doi.org/10.1016/j.hydromet.2011.03.010>
33. Ceci A, Rhee YJ, Kierans M, et al. Transformation of vanadinite [Pb-5(VO<sub>4</sub>)(3)Cl] by fungi. *Environmental Microbiology*. 2015;17(6):2018-2034. doi:10.1111/1462-2920.12612

## Supplementary material

**Table S-1.** The reference chemical composition of the detected minerals in this study

Mineral	Composition	Comments
<b>Monazite group</b>	$MTO_4$	Monazite Group: Where M = REE, Th, Ca, Bi; T = P, As. Monazite-(Ce) and Cheralite were used in these Quantitative X-ray Diffraction QXRD refinements.
<b>Goethite</b>	$(Fe_x M_{1-x})O(OH)$	Goethite: Where M=Al and various other cations
<b>Quartz</b>	$SiO_2$	
<b>Kihlmanite</b>	$Ce_2TiO_2(SiO_4)(HCO_3)_2 \cdot H_2O$	Kihlmanite: Kihlmanite-(Ce) was used in these QXRD refinements. The peak identified can be overlap with other phases. Further investigation would be required for more accurate classification.
<b>Xenotime</b>	$YPO_4$	Xenotime: Xenotime-(Y) was used in these QXRD refinements.
<b>Hematite group</b>	$R_2O_3$	Hematite group: Where R=Al, $Cr^{3+}$ , $Fe^{3+}$ , $V^{3+}$ . Hematite was used in these QXRD refinements.
<b>Crandallite group</b>	$CaAl_3(PO_4)(PO_3OH)(OH)_6$	Crandallite group: Crandallite was used in these QXRD refinements. Crandallite and Florencite peaks overlap. Further investigation would be required for more accurate classification.
<b>Alunite group</b>	$AB_6(SO_4)_4(OH)_{12}$	Alunite group: Where A=Ag, Ca, $(H_3O)_2$ , $K_2$ , $Na_2$ , $(NH_4)_2$ , Pb; B=Al, $Cu^{2+}$ , $Fe^{3+}$ . Jarosite and Florencite-(Ce) were used in these QXRD refinements. Florencite and Crandallite peaks overlaps. Further investigation would be required for more accurate classification.

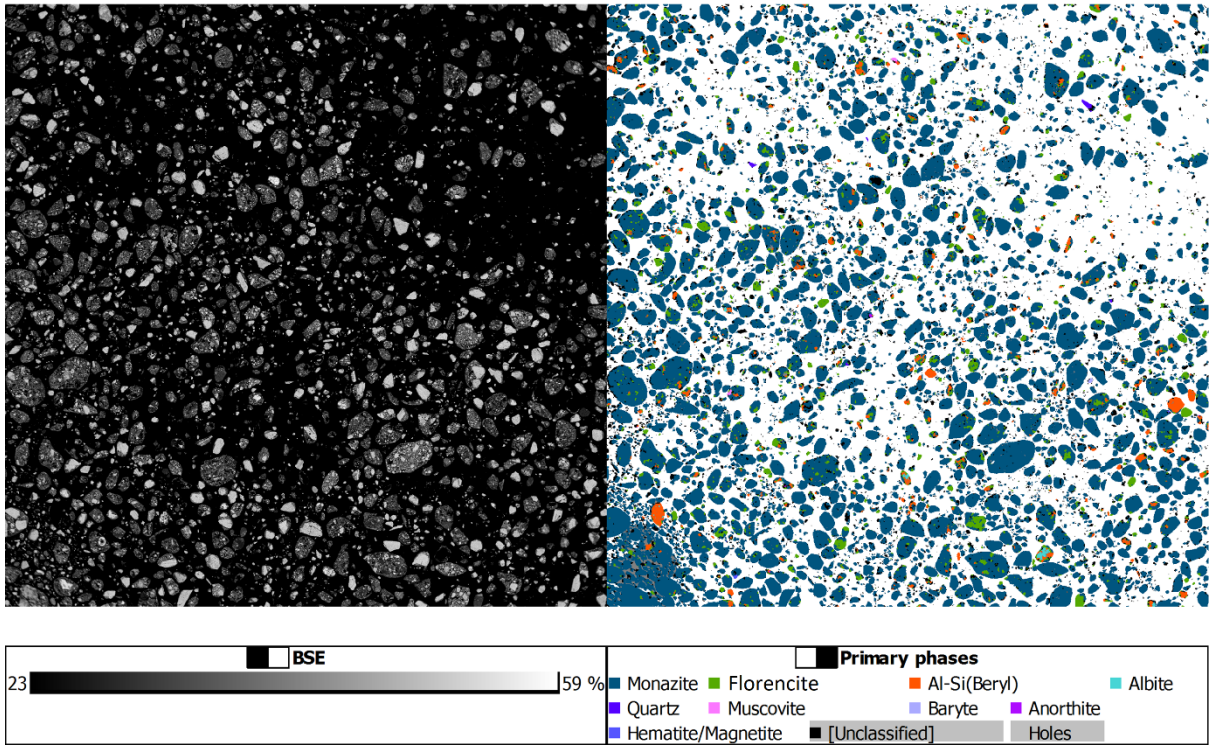


**Figure S-1.** High-grade monazite ore TESCAN Integrated Mineralogy Analyser (TIMA) mapping conducted at John de Laeter Centre, Curtin University.

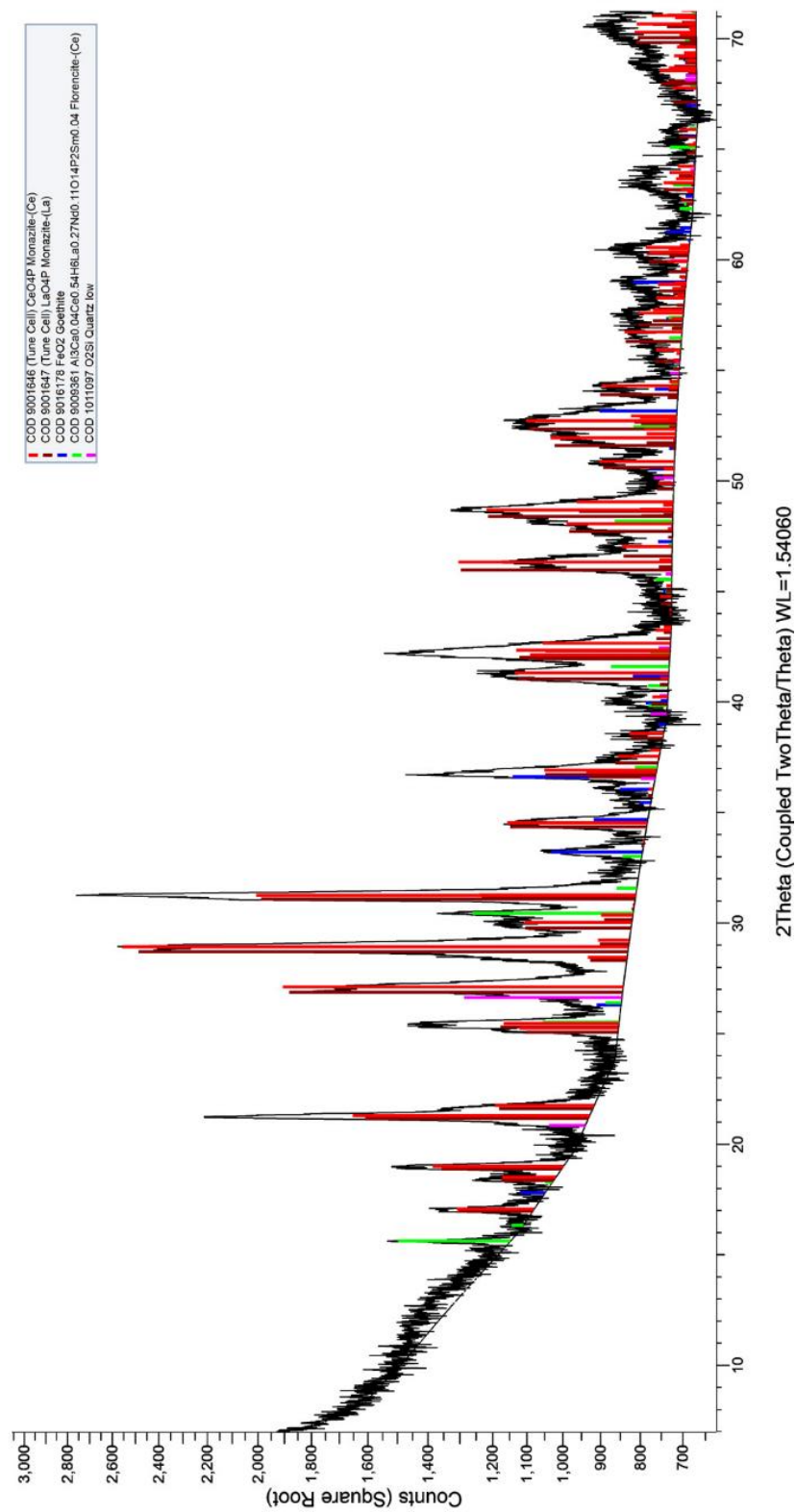


**Figure S-2.** XRD phase identification of the high-grade monazite ore conducted at John de Laeter Centre, Curtin University.

**Table S-2.** XRD and phase identification of the high-grade monazite ore conducted by John de Laeter Centre, Curtin University. The COD ID refers to the phase's identification number in the COD database (<http://www.crystallography.net/>)

Phase	COD ID	Nominal elemental composition
<b>Monazite, Ce</b>	9001646	CePO <sub>4</sub>
<b>Monazite, La</b>	9001647	LaPO <sub>4</sub>
<b>Quartz</b>	1011097	SiO <sub>2</sub>
<b>Goethite</b>	9016178	FeOOH
<b>Florencite-Ce</b>	9009361	Al <sub>3</sub> (Ce,La,Nd,Sm,Ca)(PO <sub>4</sub> ) <sub>2</sub> (OH) <sub>6</sub>

**Note:** Since crandallite group CaAl<sub>3</sub>(PO<sub>4</sub>)(PO<sub>3</sub>OH)(OH)<sub>6</sub> and florencite peaks may overlaps, another QXRD analyses was done by Bureau Veritas (Perth, WA).

**Table S-3.** Quantitative XRD results (Crystalline phases only - wt%) of high-grade monazite.  
conducted by Bureau Veritas, Perth, Australia.

Mineral	Monazite Group	Kihlmanite	Crandallite group	Alunite group	Total
	65	3	15	18	100

**Table S-4.** The inductively coupled plasma mass spectrometry, and TIMA composition analysis of high-grade monazite ore conducted by Bureau Veritas, Perth, Australia.

Elements (%)	
Al	3.9
Ca	1.8
Fe	1
K	<0.01
Mg	0.1
Mn	0.06
Na	0.1
P	8.5
Si	1.6
Ti	0.4
Y	0.18
La	11
Ce	15
Pr	2.1
Nd	7.2
Sm	0.97
S	0



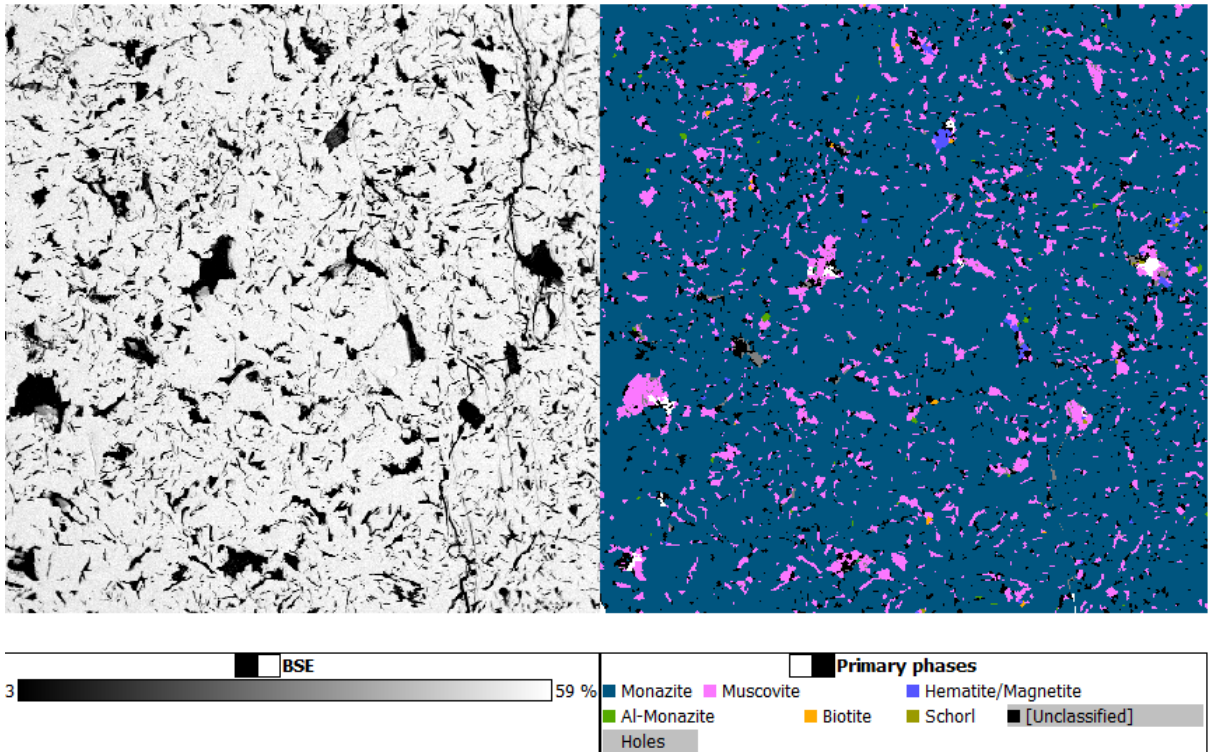


**Figure S-3.** Quantitative TIMA mineral mapping of monazite-muscovite crystals.

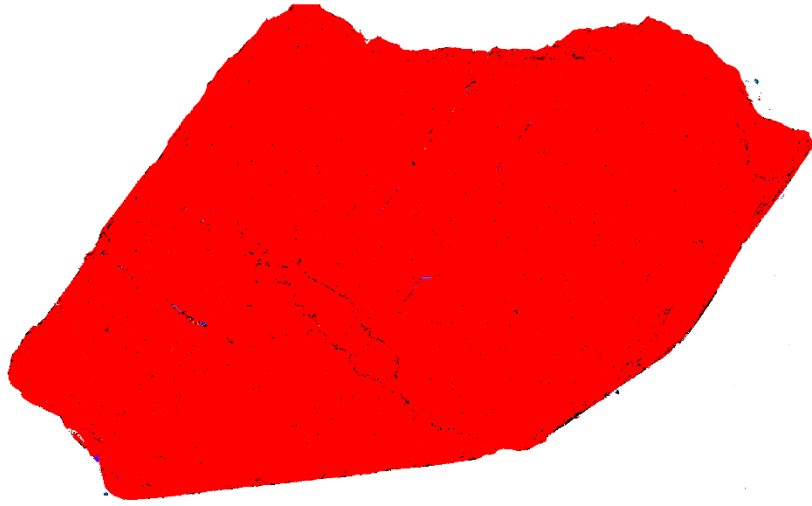
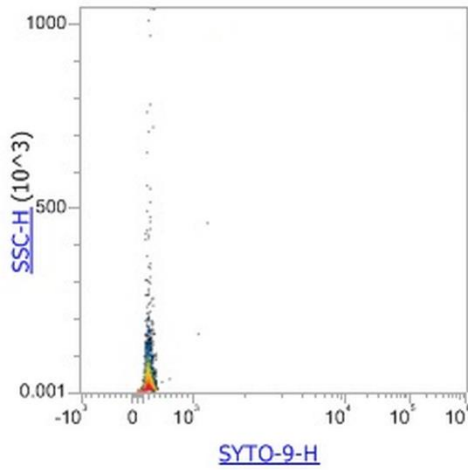
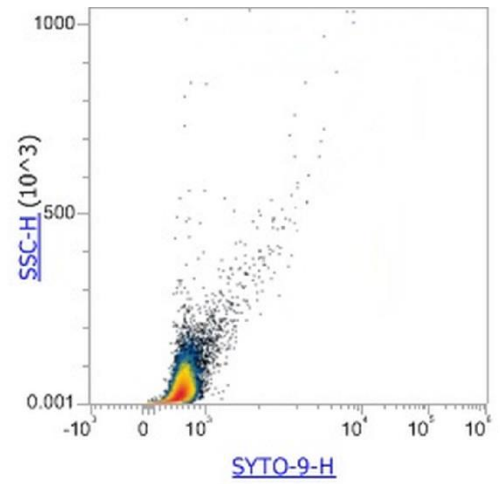


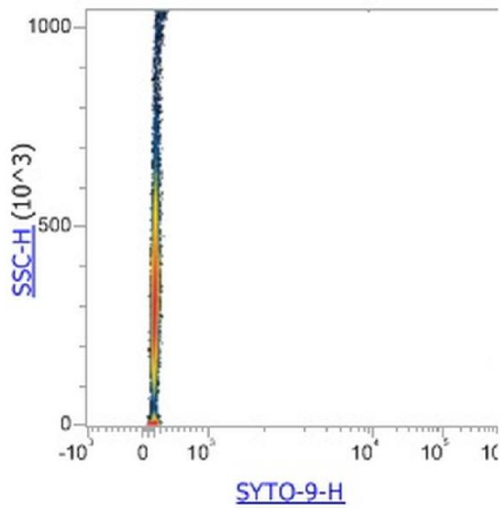
**Figure S-4.** TIMA mineral mapping of xenotime crystals.



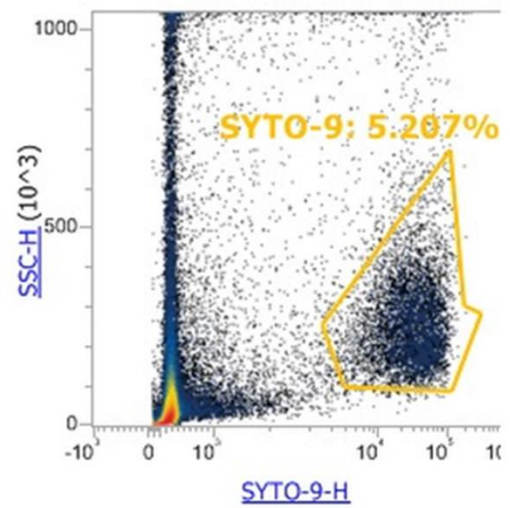
**Media**



**Media + Syto 9**



**Bacteria**



**Bacteria + Syto 9**

**Figure S-5.** The flow cytometry plots for sterile media and bacteria with and without SYTO9 as the fluorochrome for DNA.

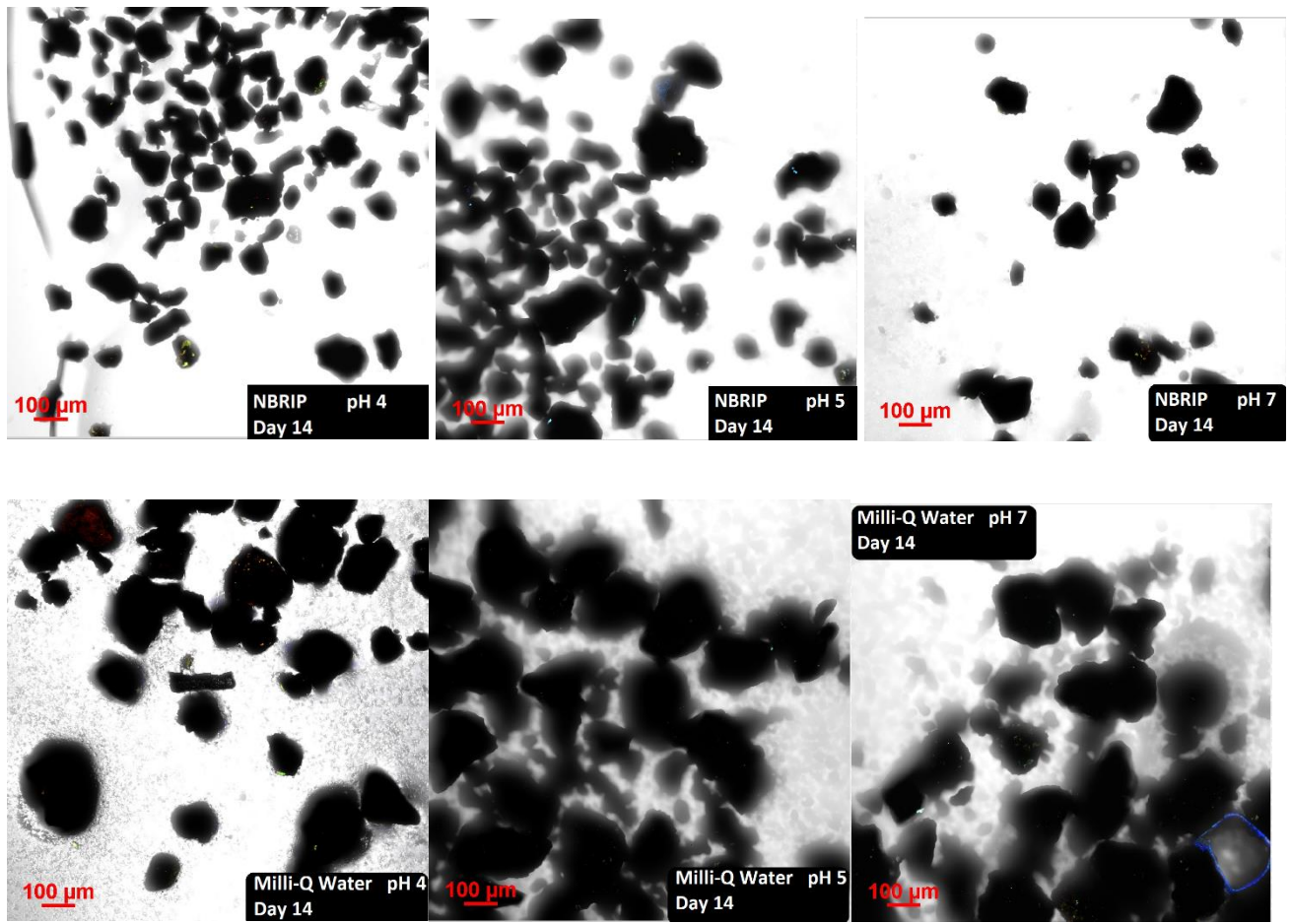
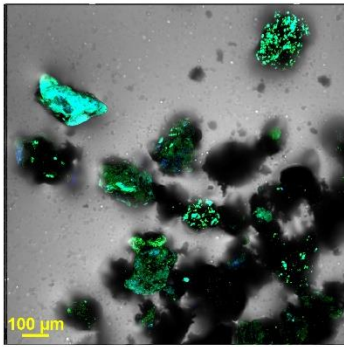


**Figure S-6.** The recorded autofluorescence of high grade monazite ore after 14 days of abiotic leaching using NBRIP and Milli-Q water at pH 4, 5 and 7.

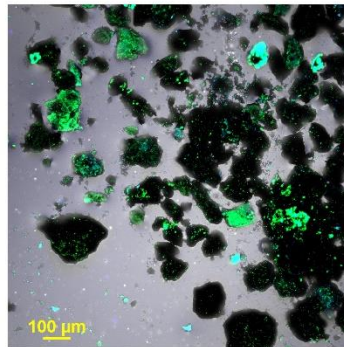


### Stage 1- Attachment

4h

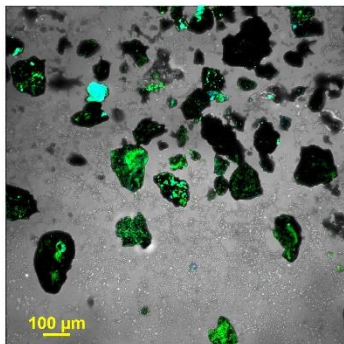


8h

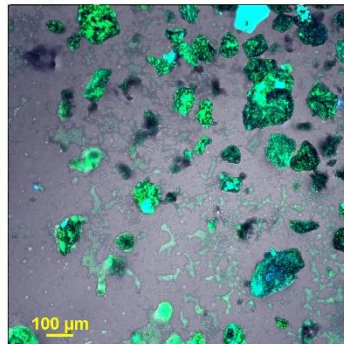


### Stage 2- Colonization and formation of mature biofilm

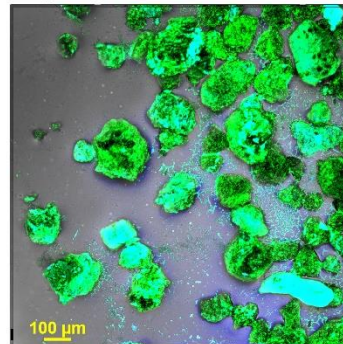
16 h



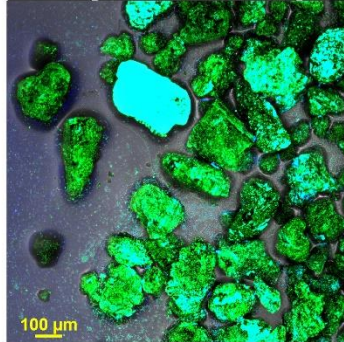
Day 1



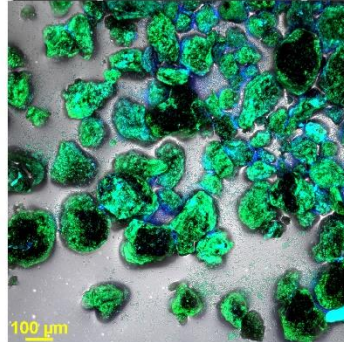
Day2



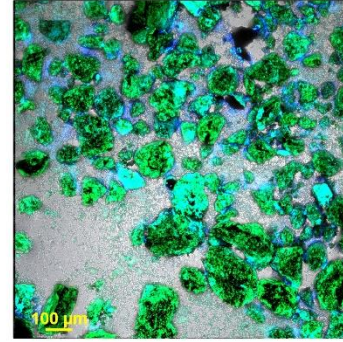
Day 3



Day 5

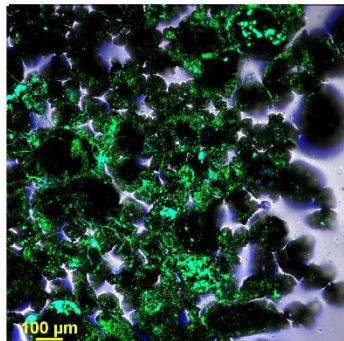


Day8



### Stage 3- Dispersion (Detachment)

Day 11



Day 14

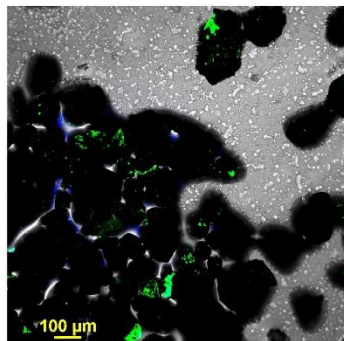
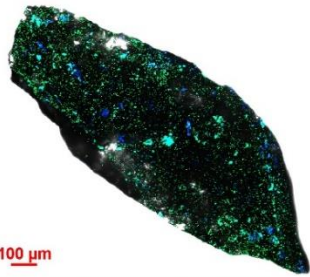


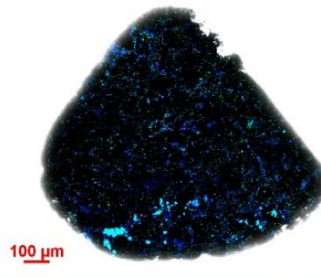
**Figure S-7.** Visualisation of *Klebsiella aerogenes* biofilm on the surface of high grade monazite ore by CLSM. Hoechst 33342 (blue) and DiTO-1 (green) were used to maximum visualisation of the bacterial cells. CLSM image is a merged image (blue, green and transmitted light channels) using the Maximum Fluorescent Intensity of the acquired Z-stack images. Blue, green or cyan colours on the surface of the mineral grains (the dark grains) are representative of the microbial biofilm. The background blue colour around the mineral grains is autofluorescent from the epoxy glue.

**Stage 1- Attachment**

4h



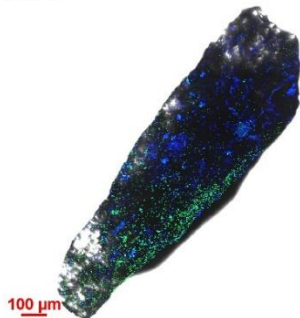
8h



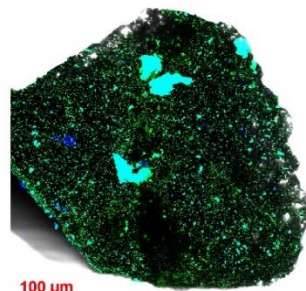
---

**Stage 2- Colonization and formation of mature biofilm**

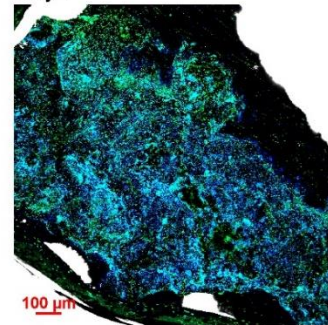
16 h



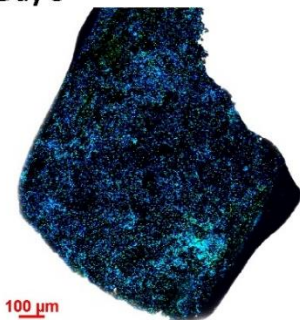
Day 1



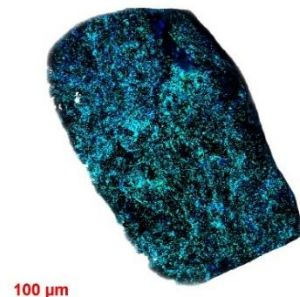
Day2



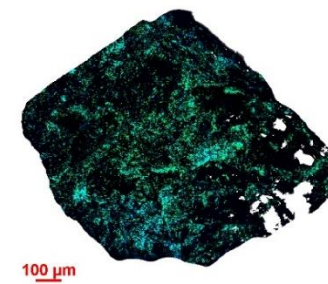
Day 3



Day 5



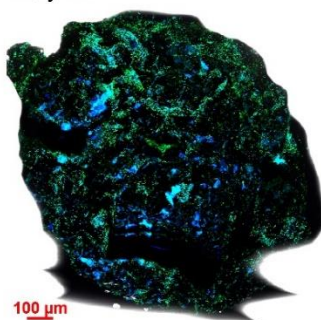
Day8



---

**Stage 3- Dispersion (Detachment)**

Day 11



Day 14

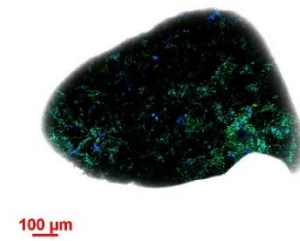
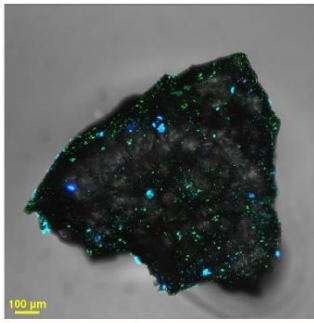


**Figure S-8.** Visualisation of *Klebsiella aerogenes* biofilm on the surface of monazite-muscovite crystals by CLSM.

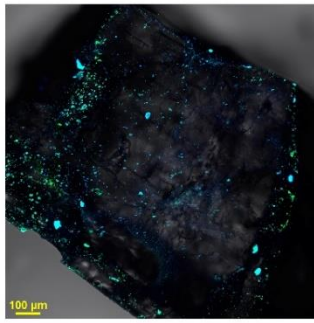


### Stage 1- Attachment

4h

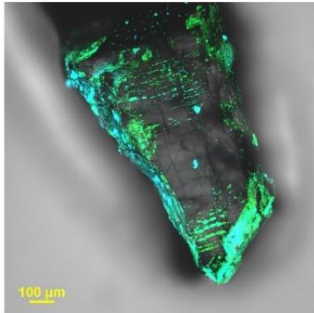


8h

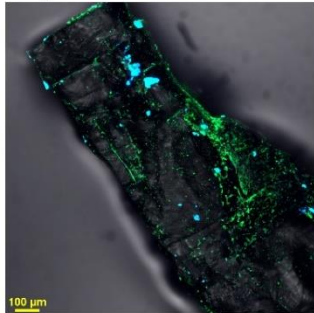


### Stage 2- Colonization and formation of mature biofilm

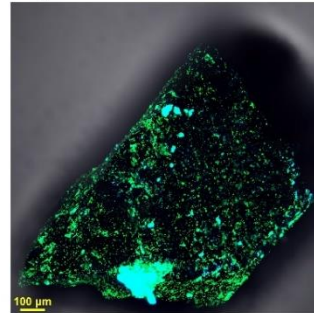
16 h



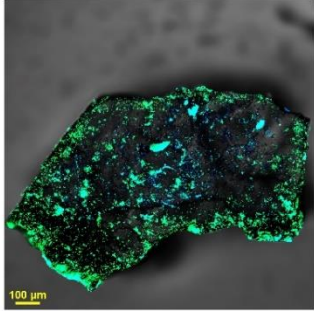
Day 1



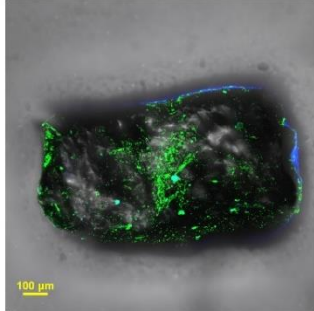
Day2



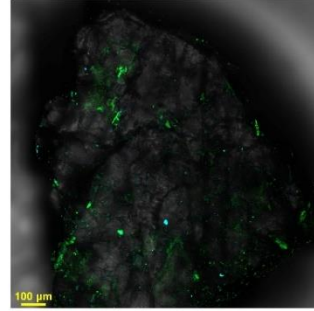
Day 3



Day 5

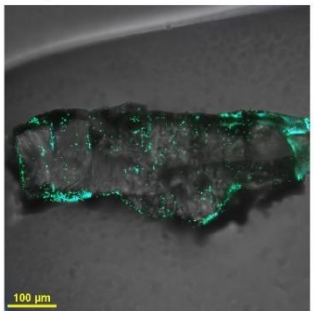


Day8



### Stage 3- Dispersion (Detachment)

Day 11



Day 14

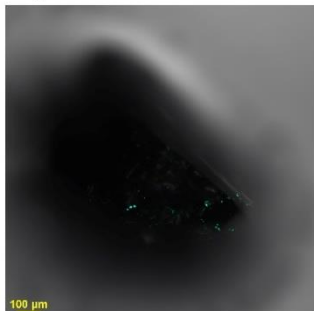
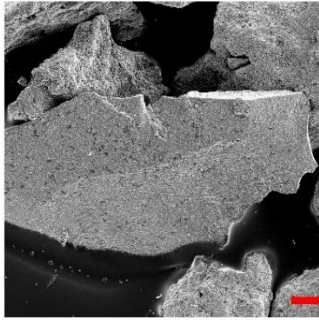


**Figure S-9.** Visualisation of *Klebsiella aerogenes* biofilm on the surface of xenotime crystals by CLSM.

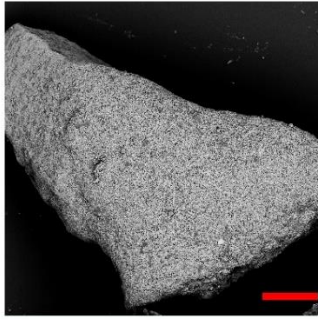


**Stage 1- Attachment**

4h



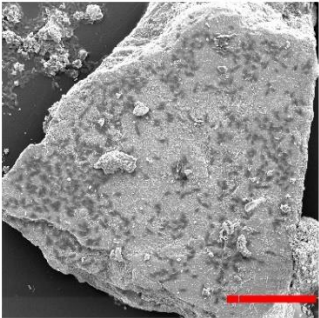
8h



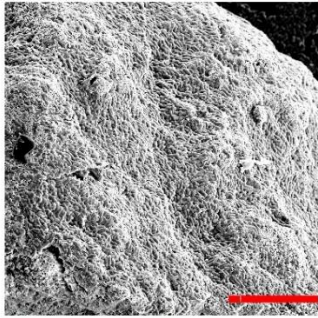
scale bar (red ribbon) 20 µm

**Stage 2- Colonization and formation of mature biofilm**

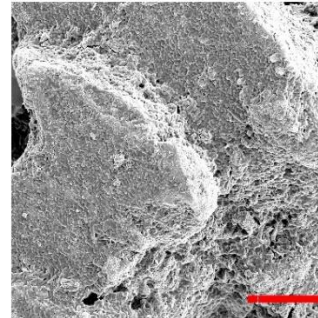
16 h



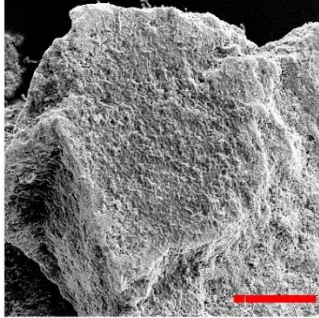
Day 1



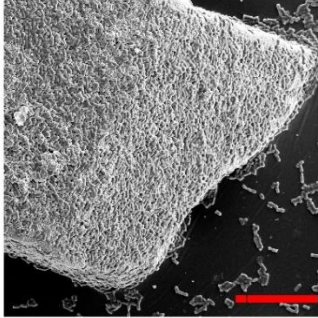
Day2



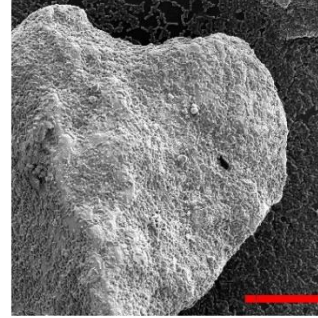
Day 3



Day 5

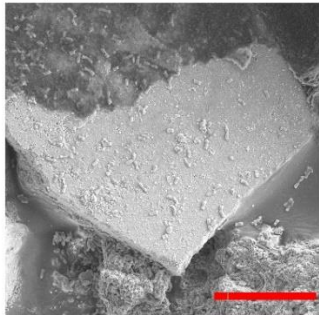


Day8



**Stage 3- Dispersion (Detachment)**

Day 11



Day 14

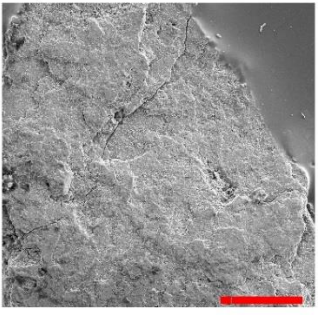


**Figure S-10.** Visualisation of *Klebsiella aerogenes* biofilm on the surface of high grade monazite ore by SEM.

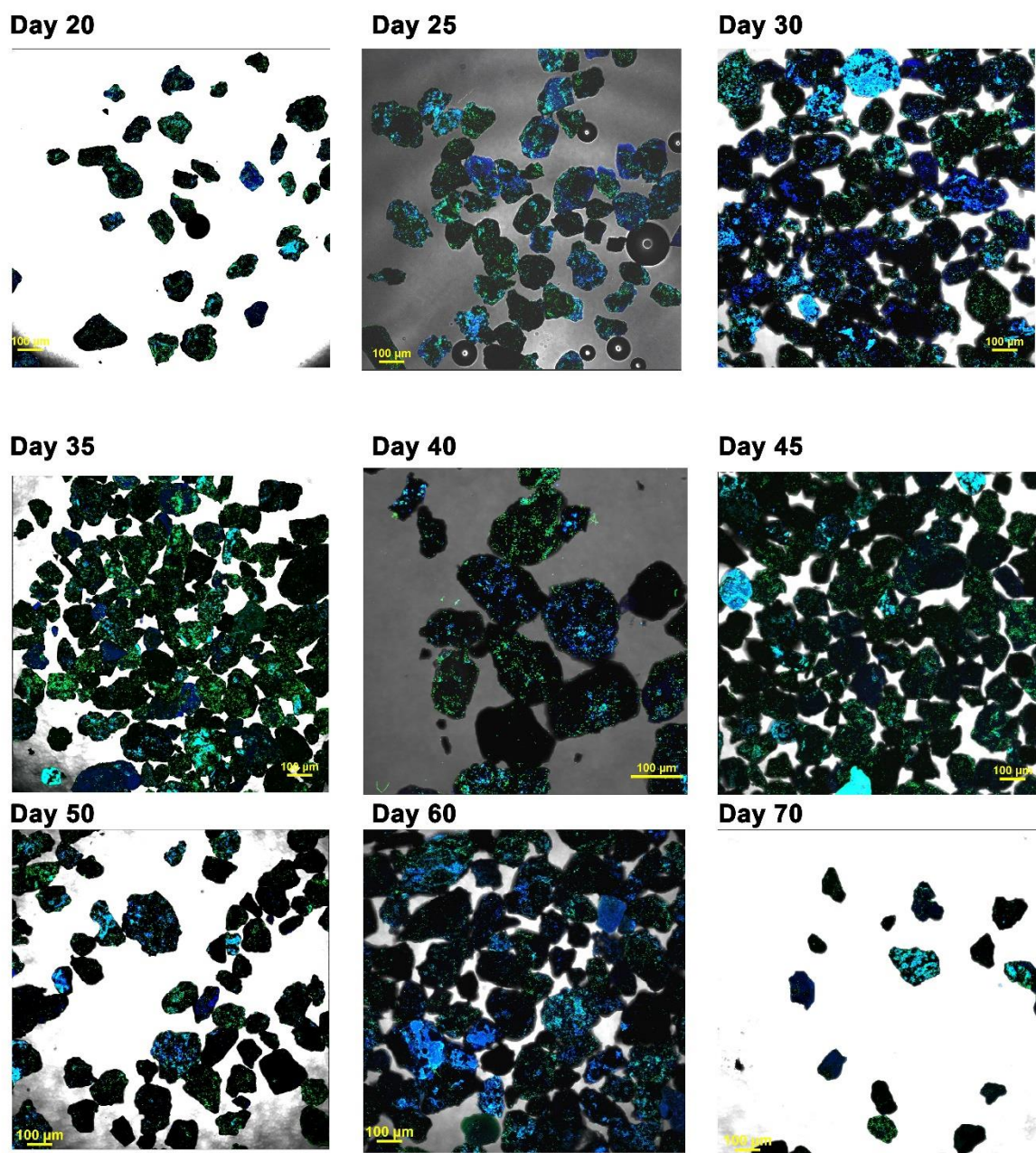
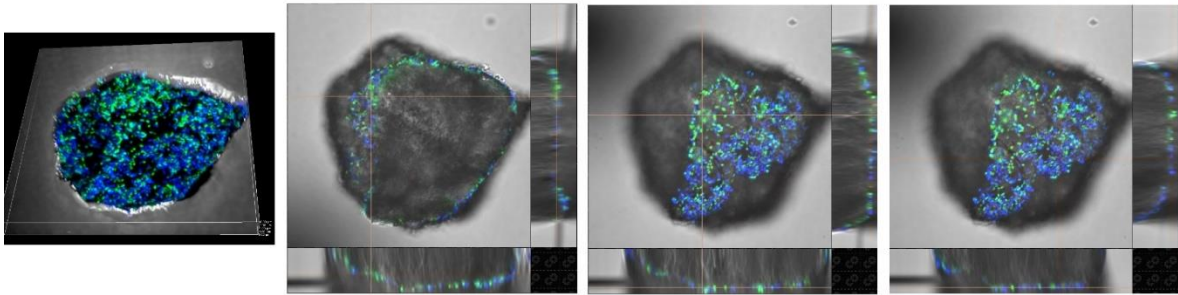


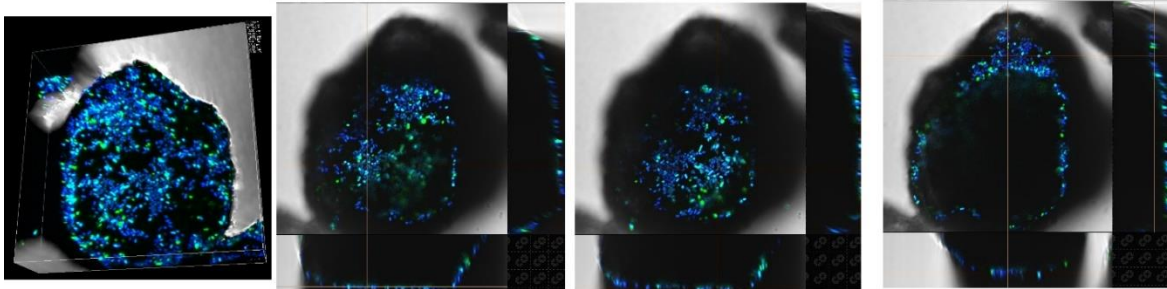
Figure S-11. Visualisation of *Klebsiella aerogenes* biofilm on the surface of high grade monazite ore, day 20-70.



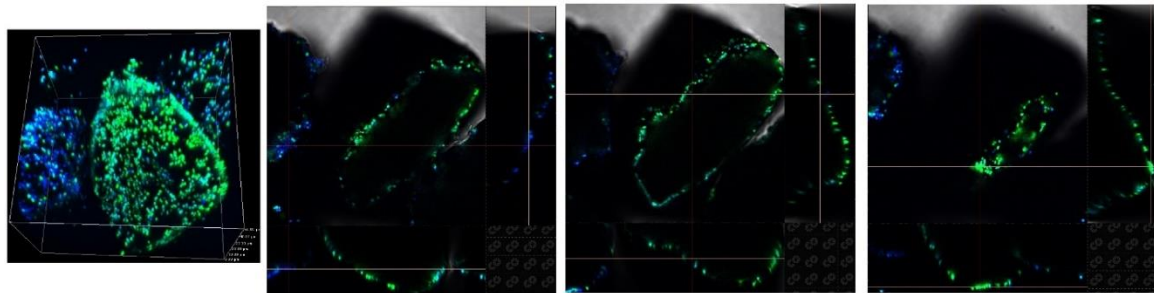
Day 2



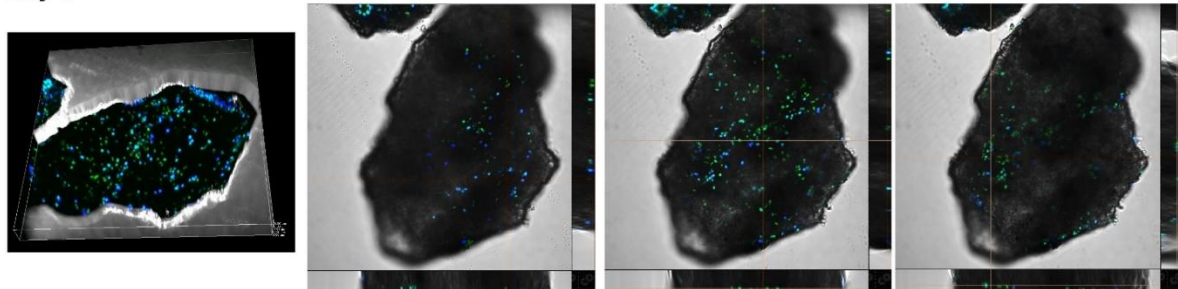
Day 3



Day 5

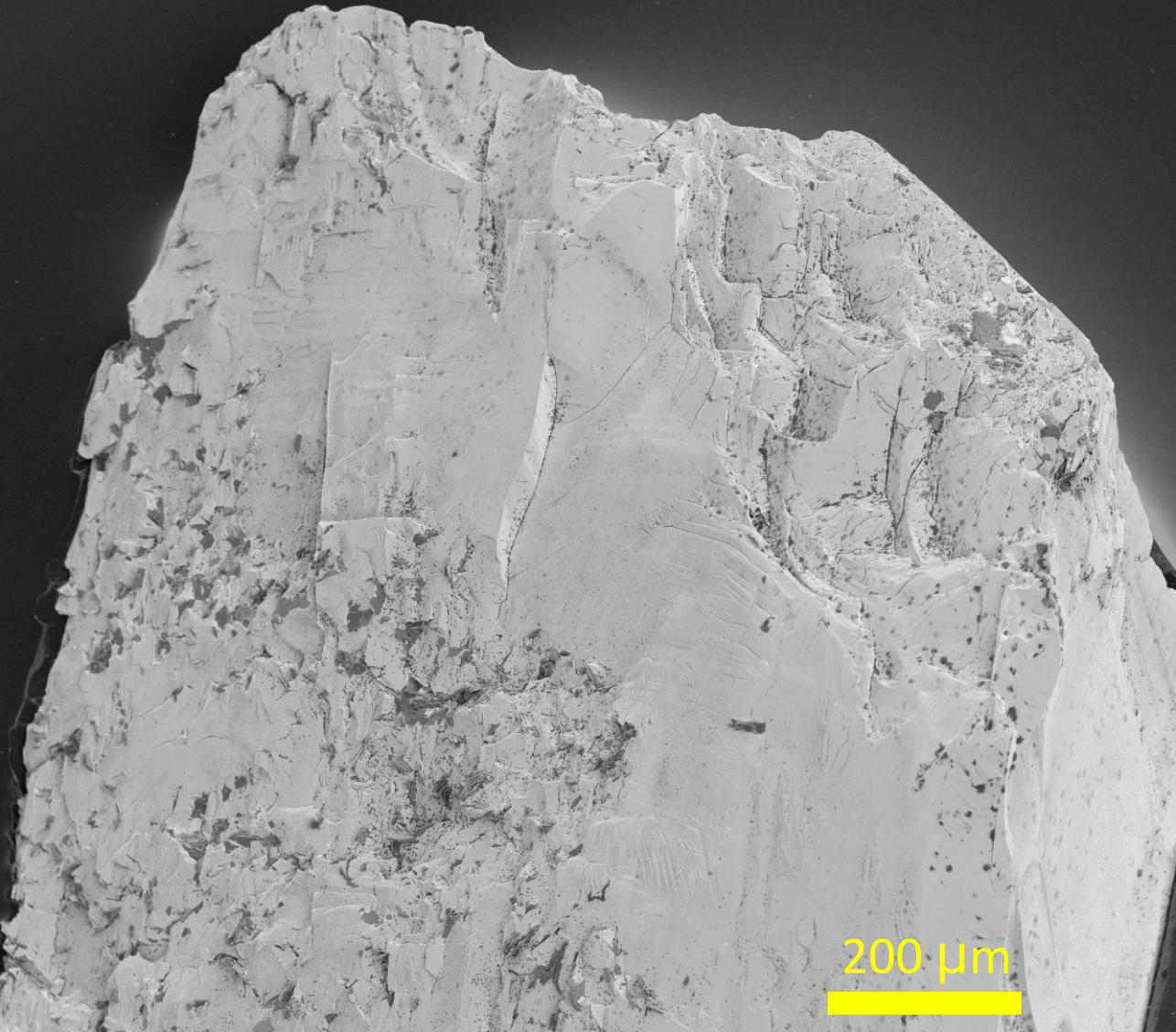


Day 8

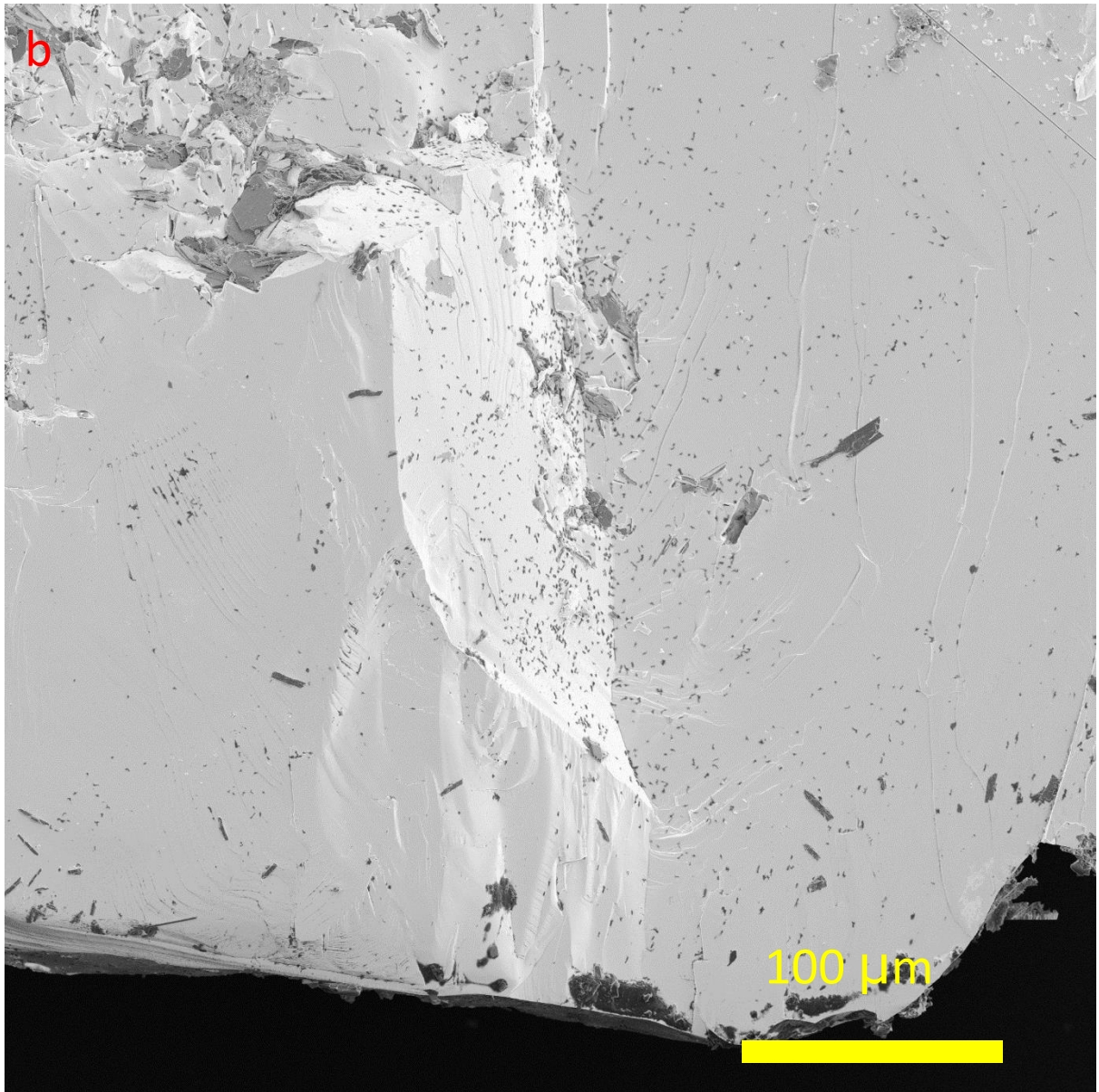


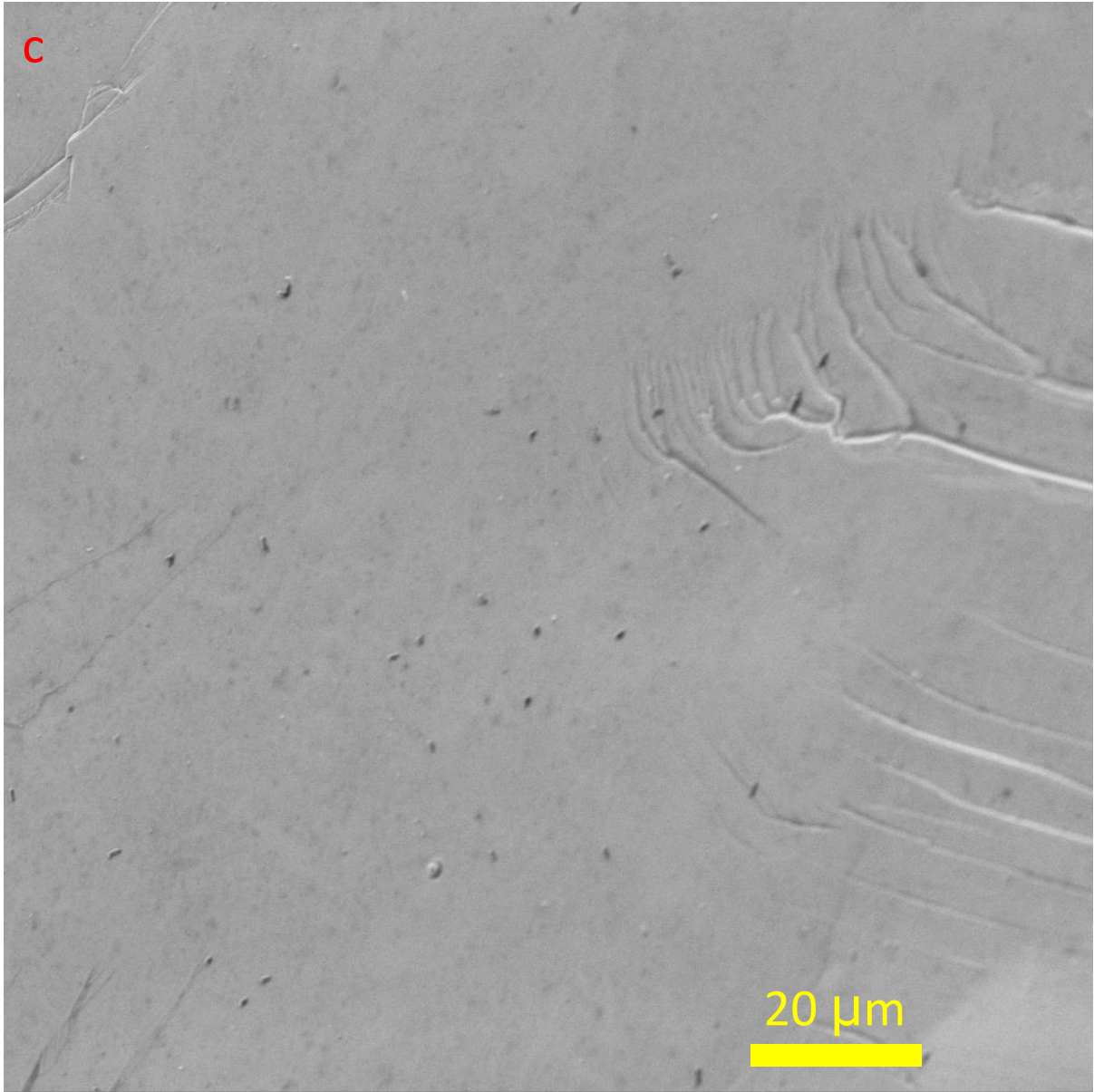
**Figure S-12.** Figure S-12. CLSM cross-section of *K. aerogenes* mature biofilms on high grade monazite ore. The blue/green shapes in the CLSM images are representative of the microbial cells.

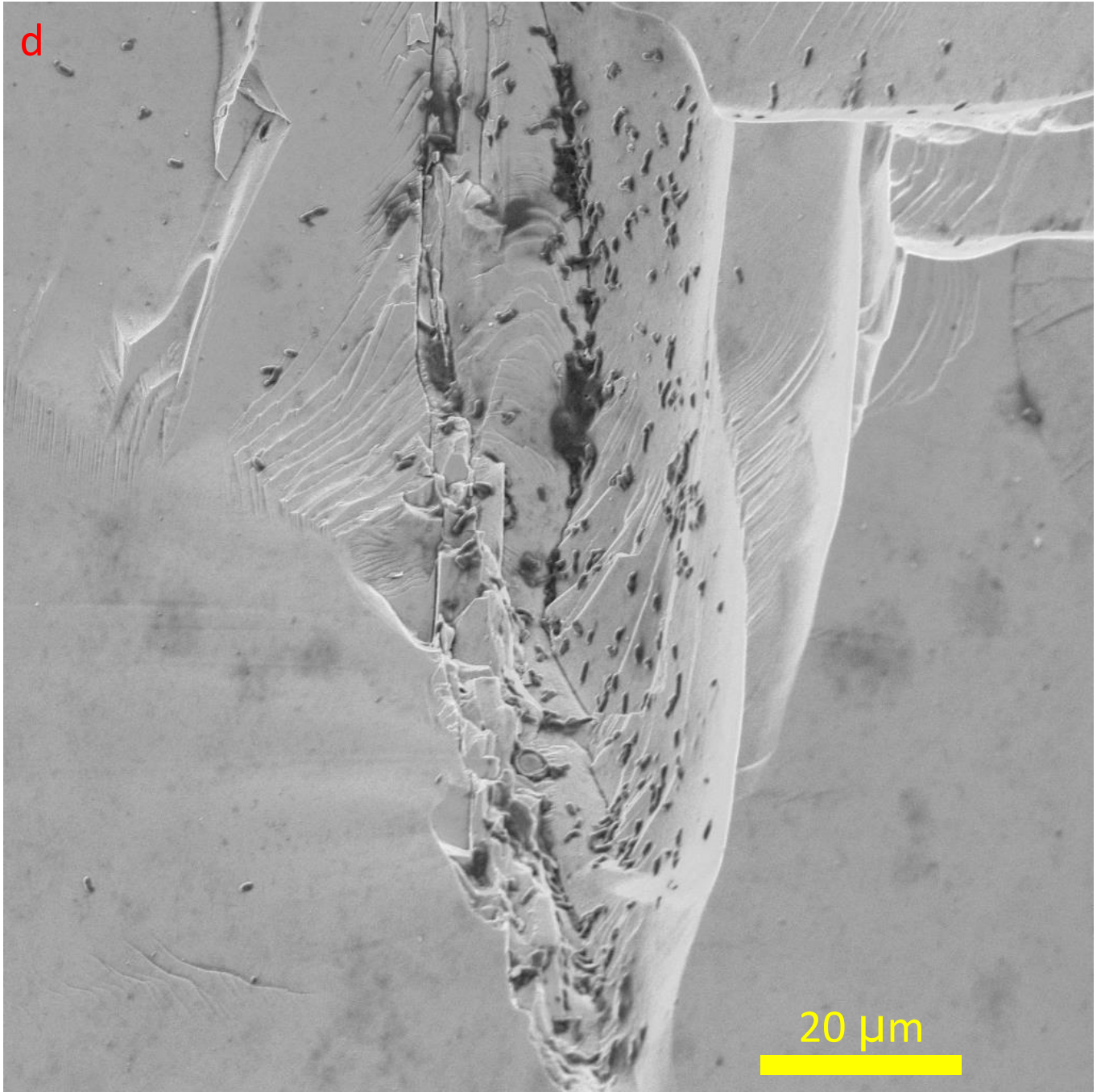
a



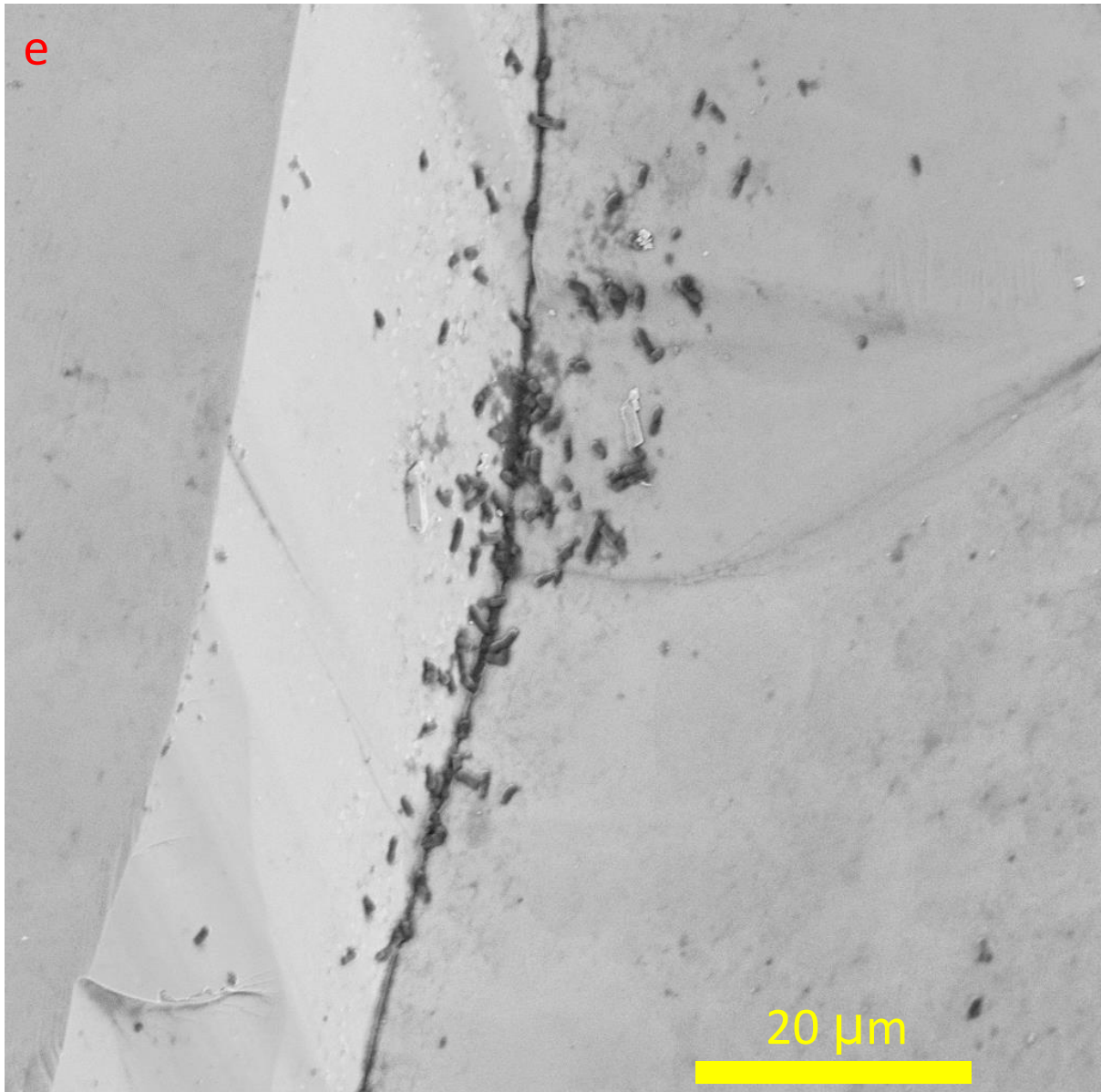




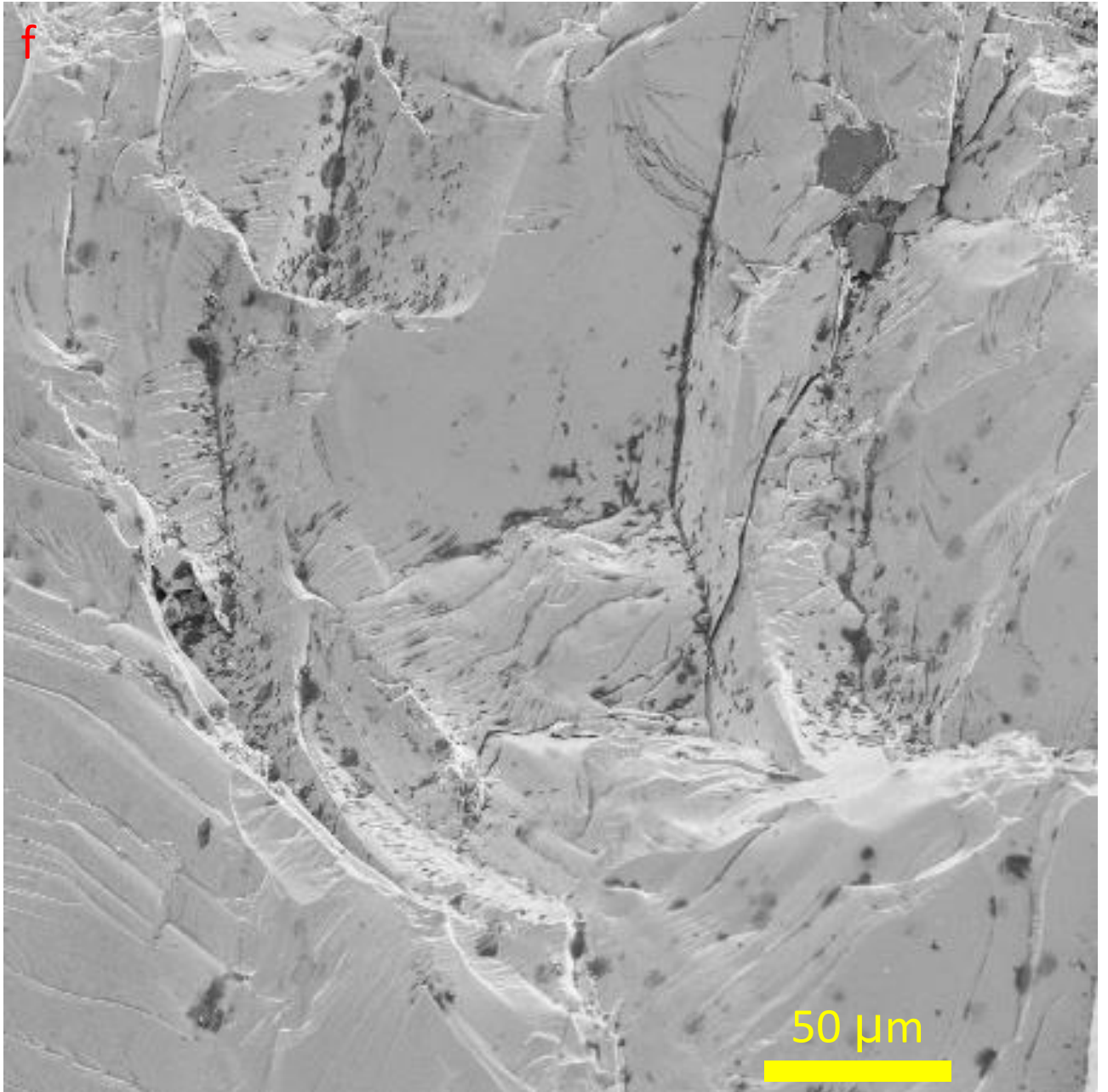


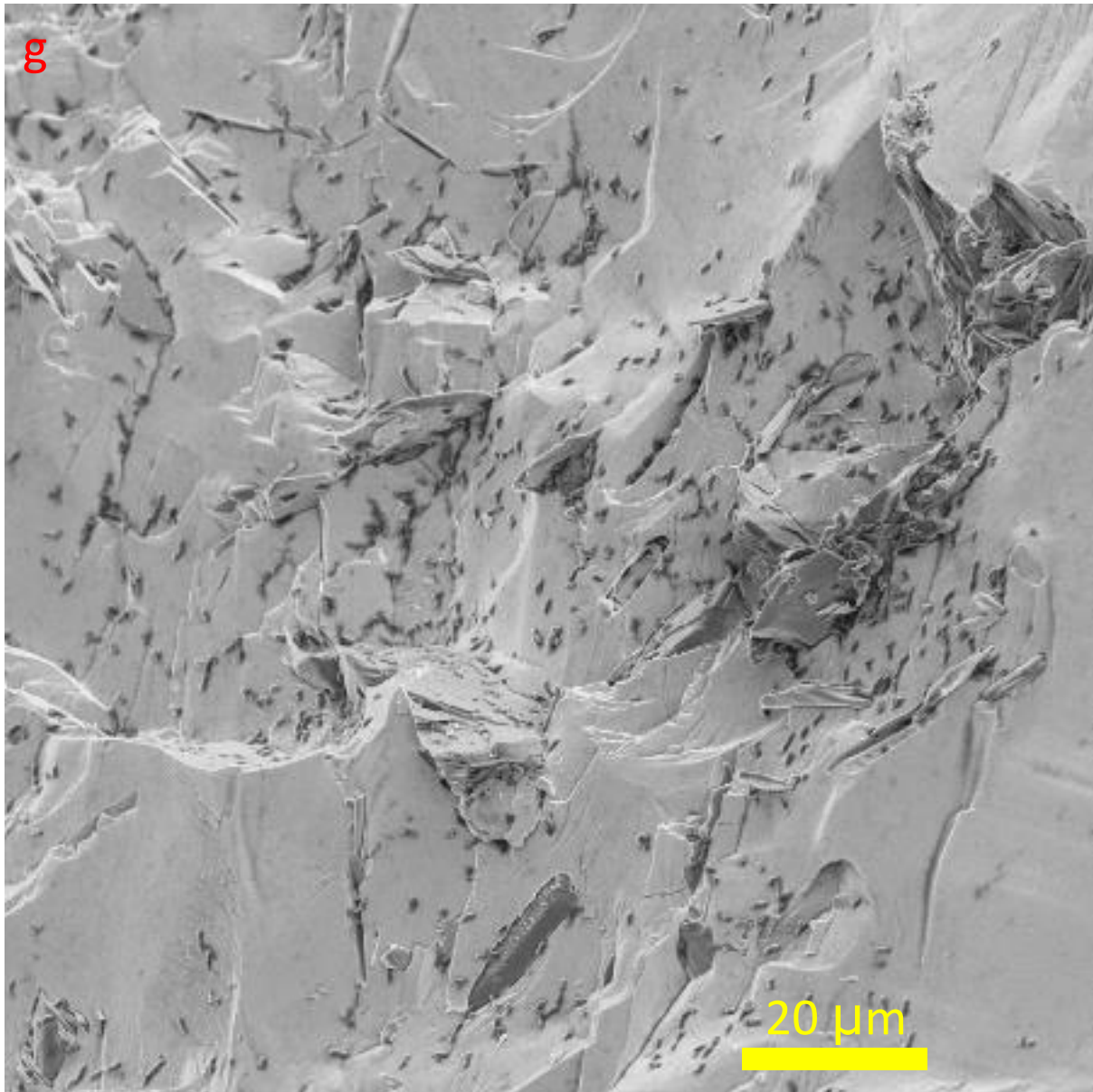






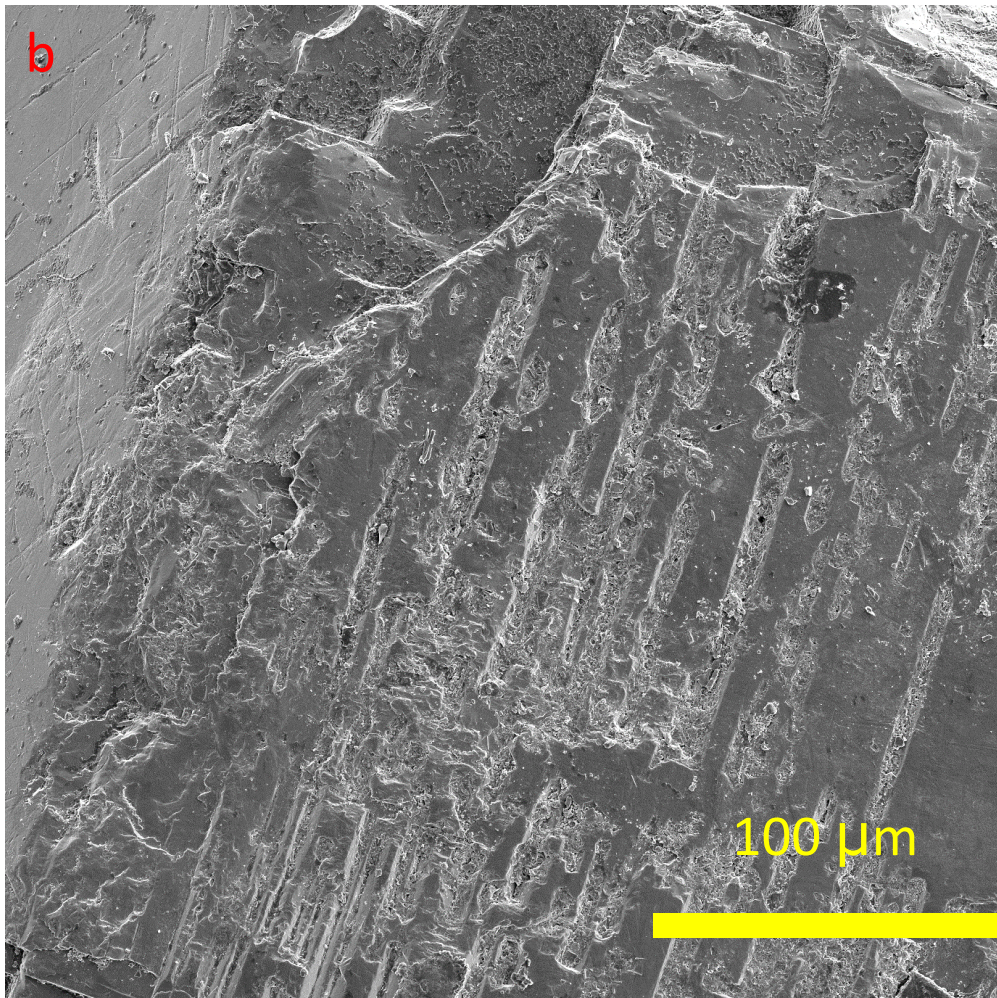
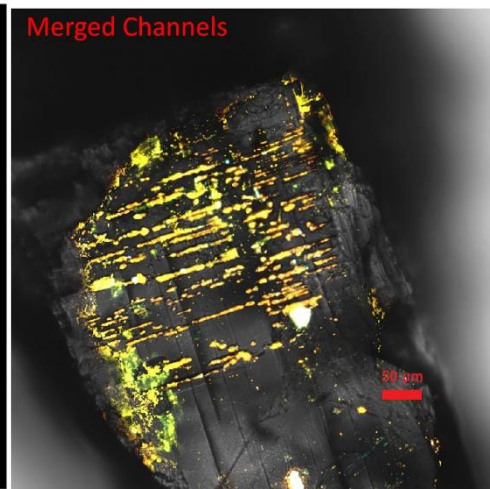
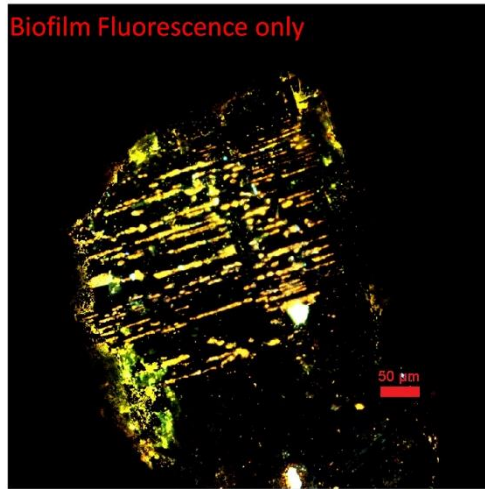




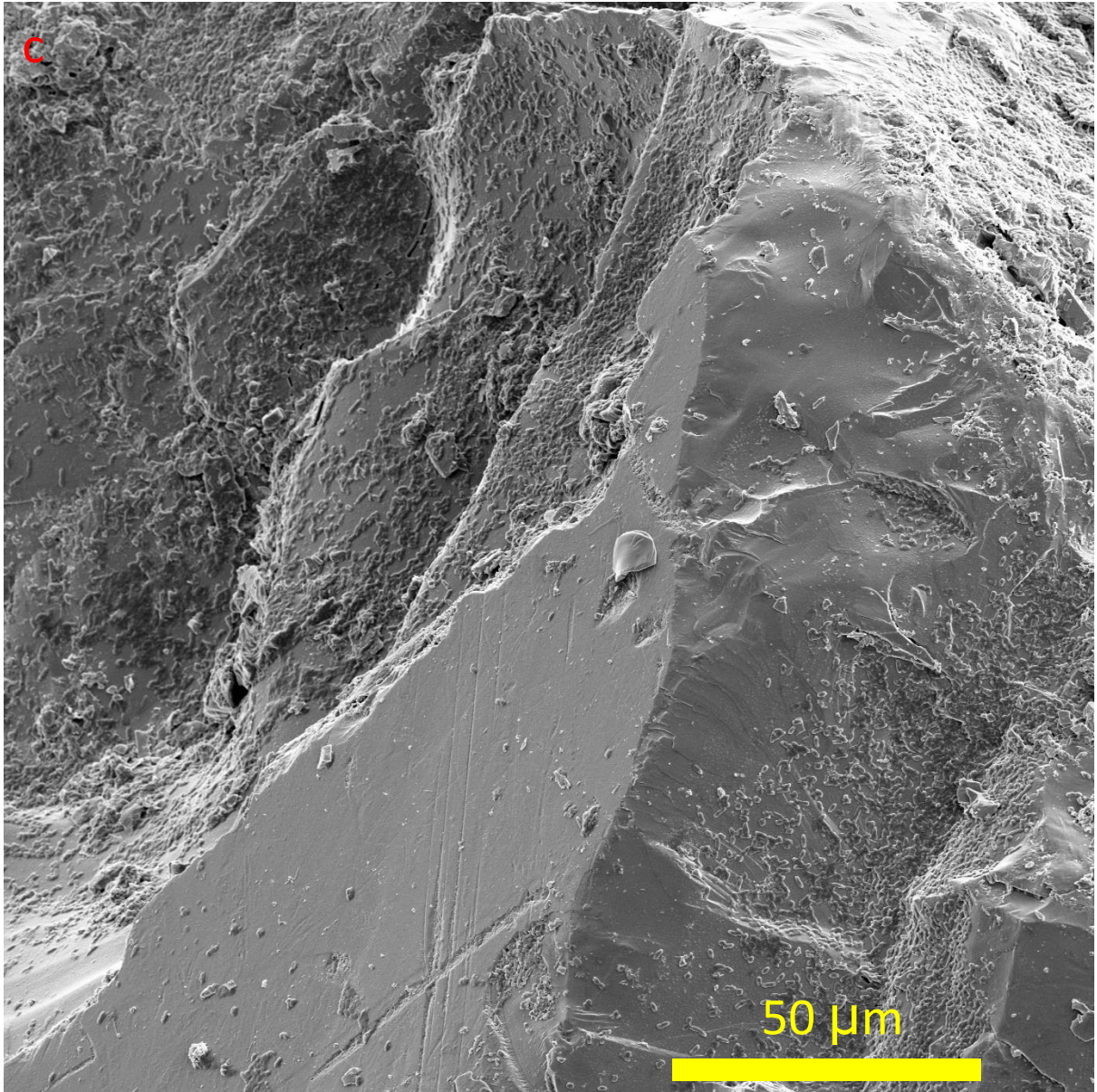


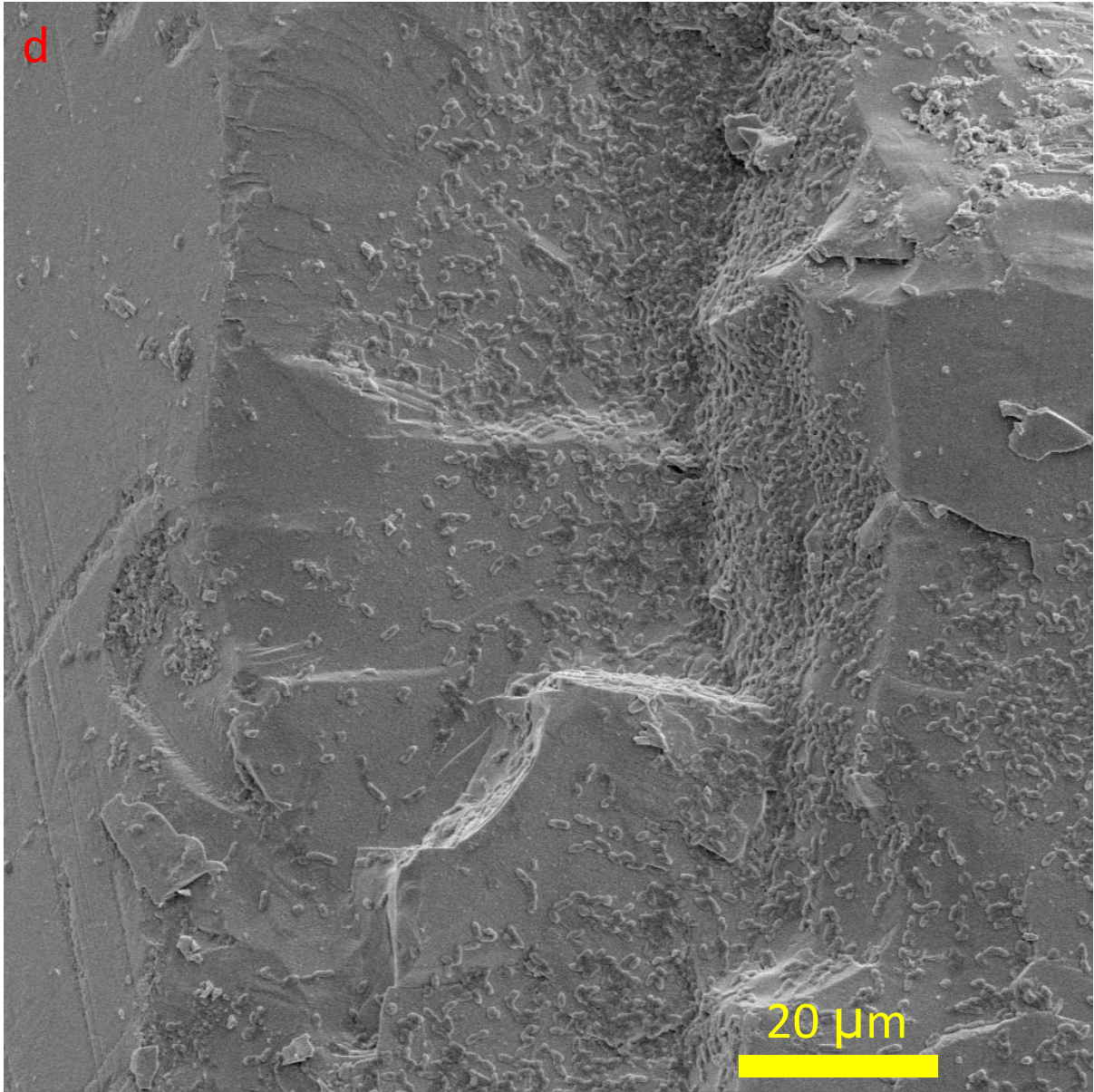
**Figure S-13.** Localization of *K. aerogenes* biofilm on and around the physical surface imperfections of monazite-muscovite crystal. (a) An overall SEM of the crystal. (b) A location on the crystal with an imperfection site (ridge) in the centre and fairly flat surfaces on the left and right of the ridge. (c) A location on the crystal with flat surface. (d-g) Other imperfection sites on the surface.



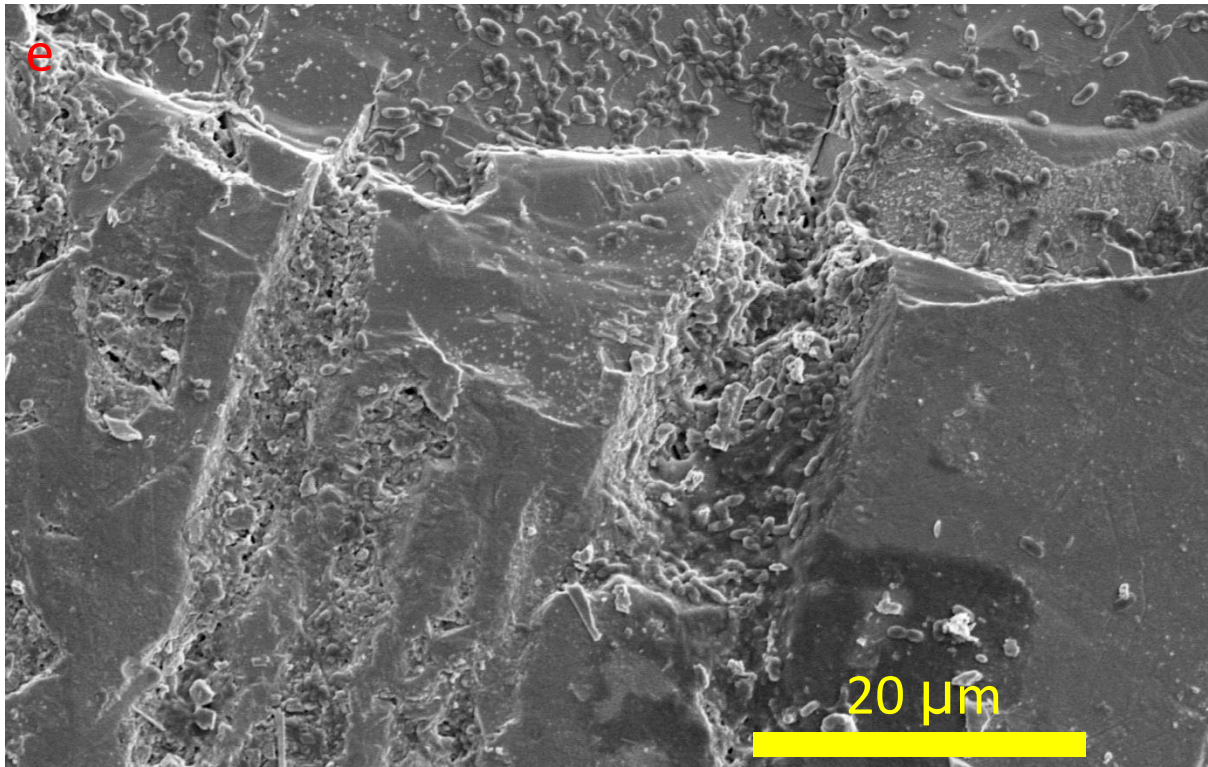






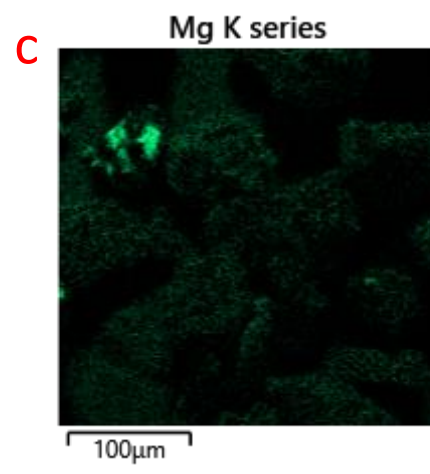
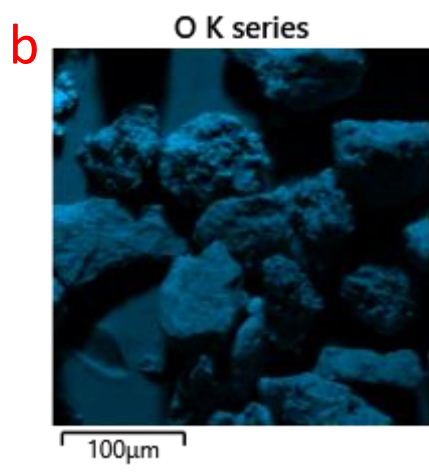
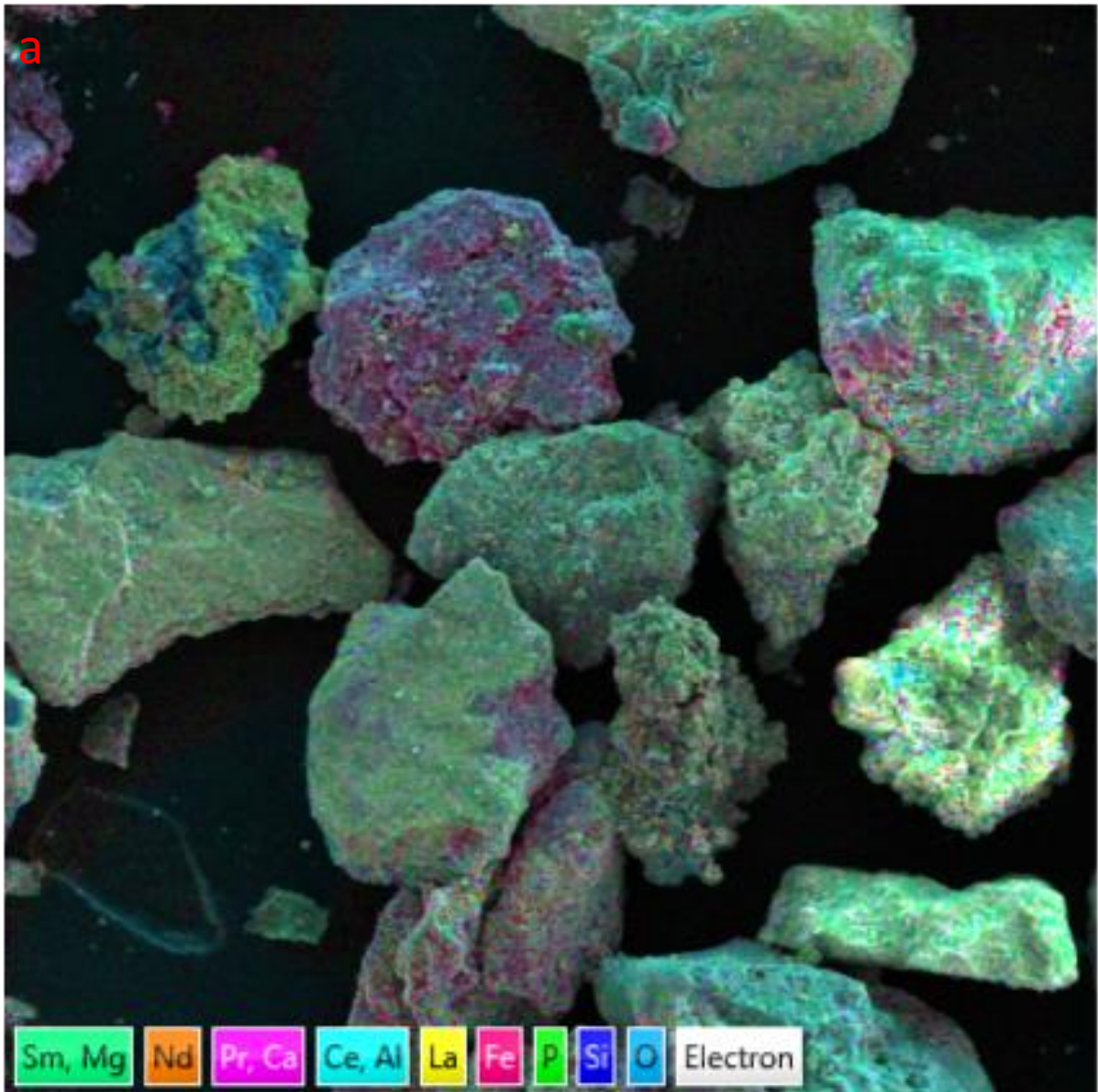




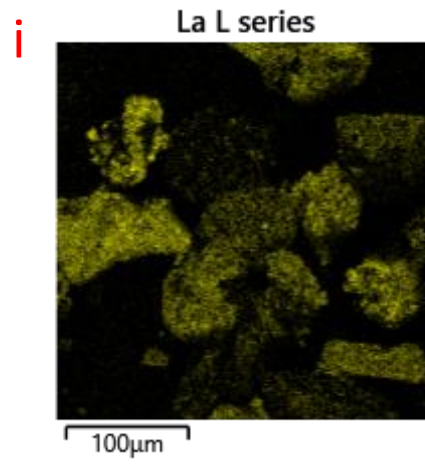
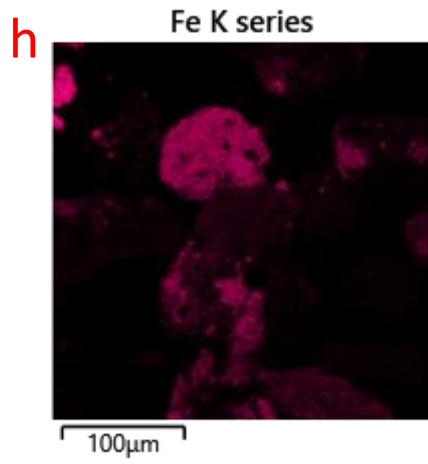
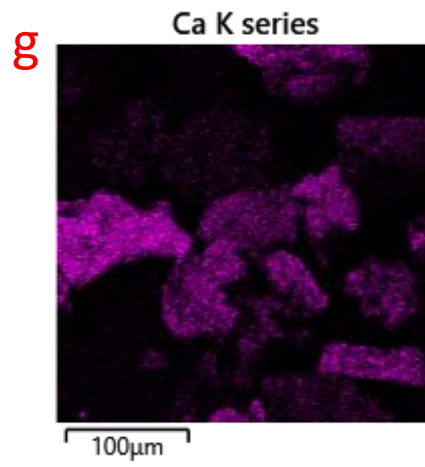
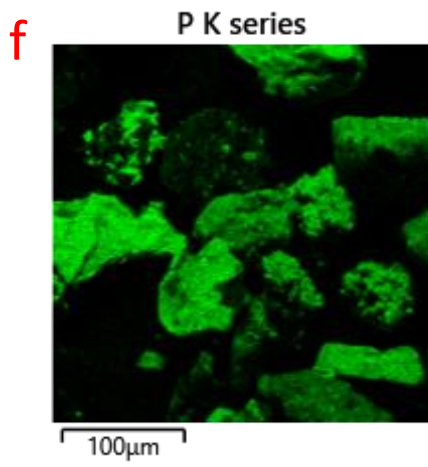
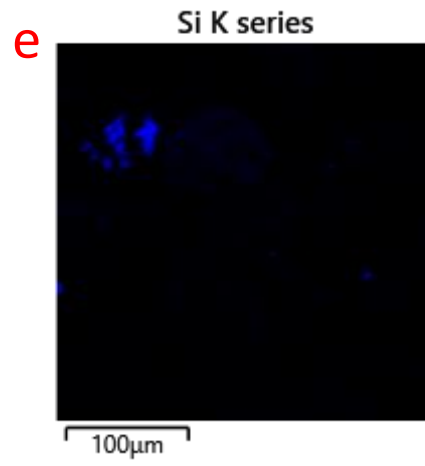
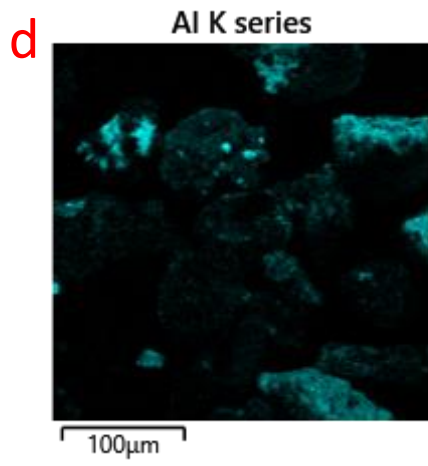


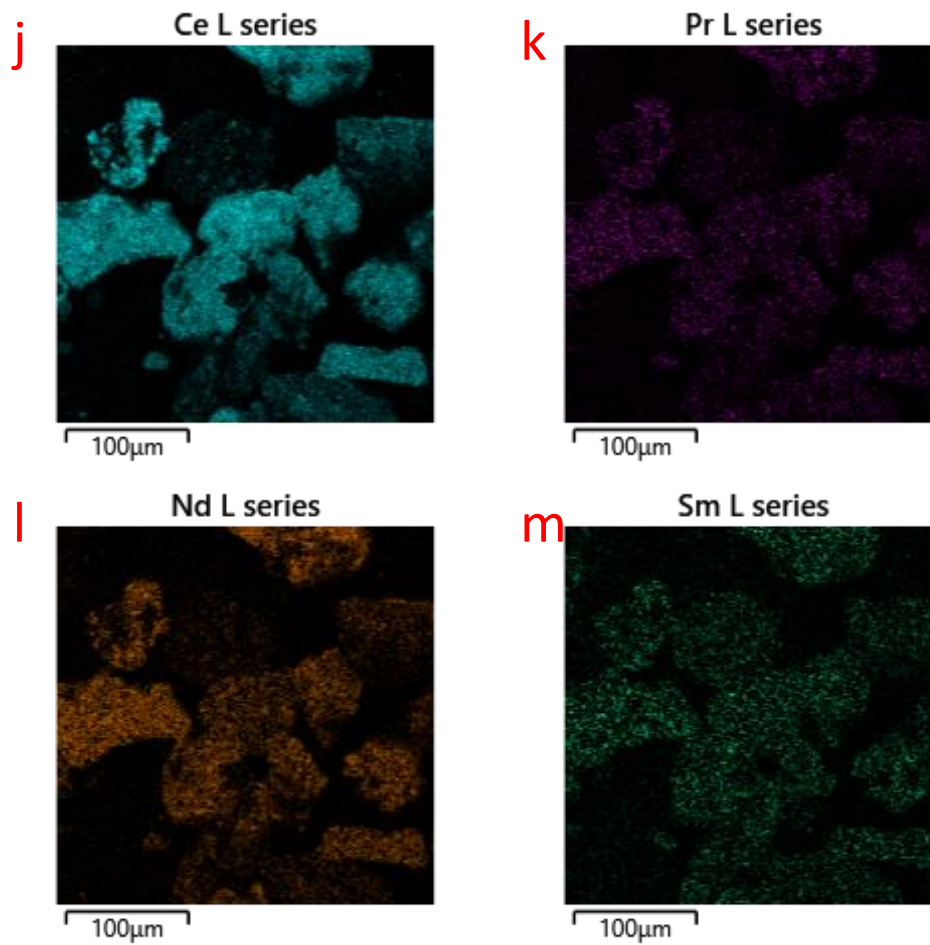
**Figure S-14.** Localization of *K. aerogenes* biofilm around the physical surface imperfections of xenotime crystal. (a) An overall CLSM image of the crystal surface in transmission light mode (physical imperfection only), fluorescence channel only, and merged image. (b-e) The SEM images of the same sample zooming on a smaller area (red box in panel-a) at different magnification.

**Video S-1.** *Klebsiella aerogenes* biofilm on the surface of high grade monazite ore monazite acquired using Z-stack imaging at maximum fluorescent intensity. The acquired Z-stack images are shown in a depth-coded rainbow coloured 3D image. The depth rainbow coloured area is representative of the biofilm and bacterial cells on the surface of the mineral. The colouring scheme represents the height of the sample where blue is closer to the top of the mineral grain and pink represent higher depth and is closer to the bottom of the mineral.

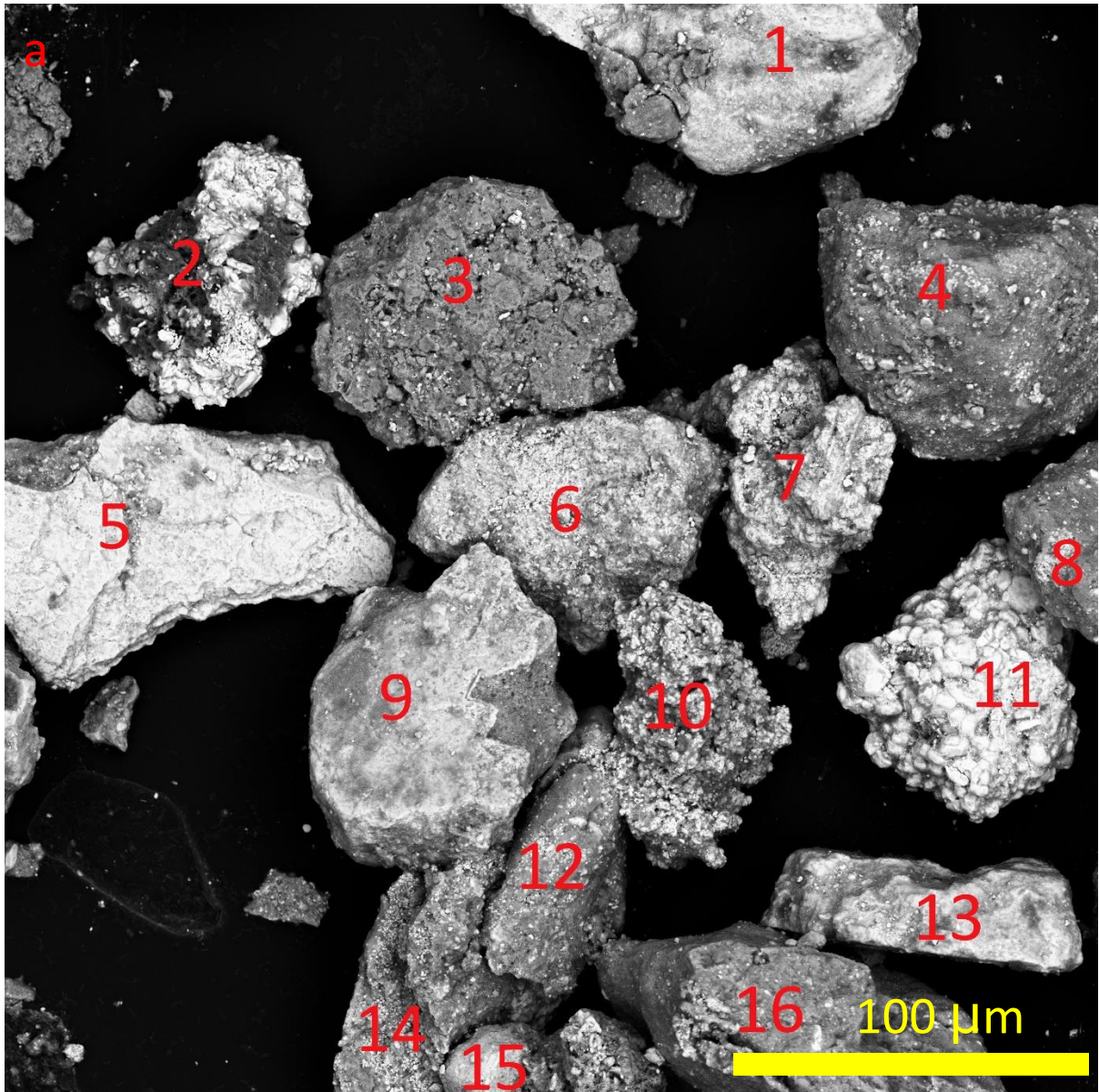




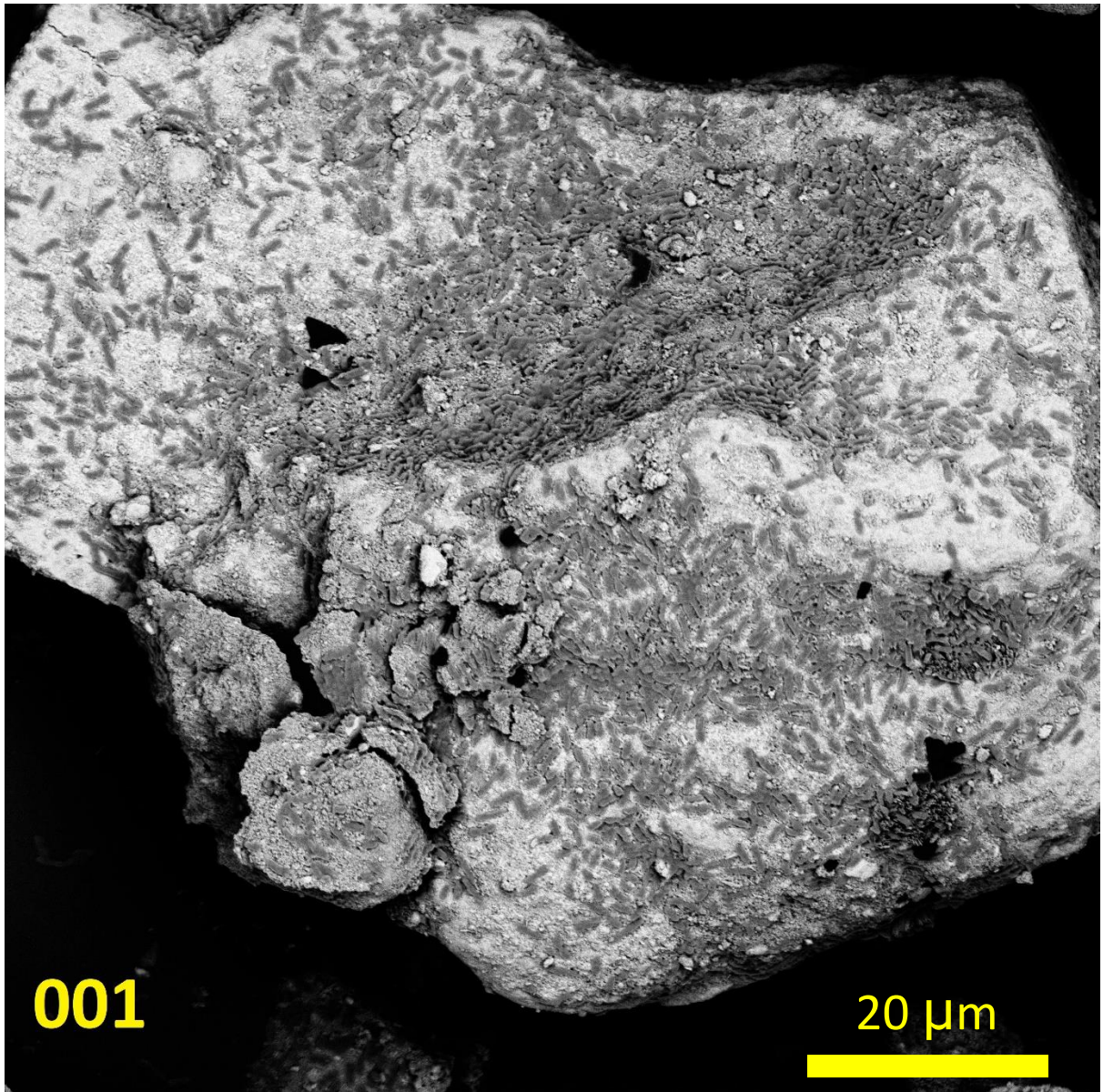


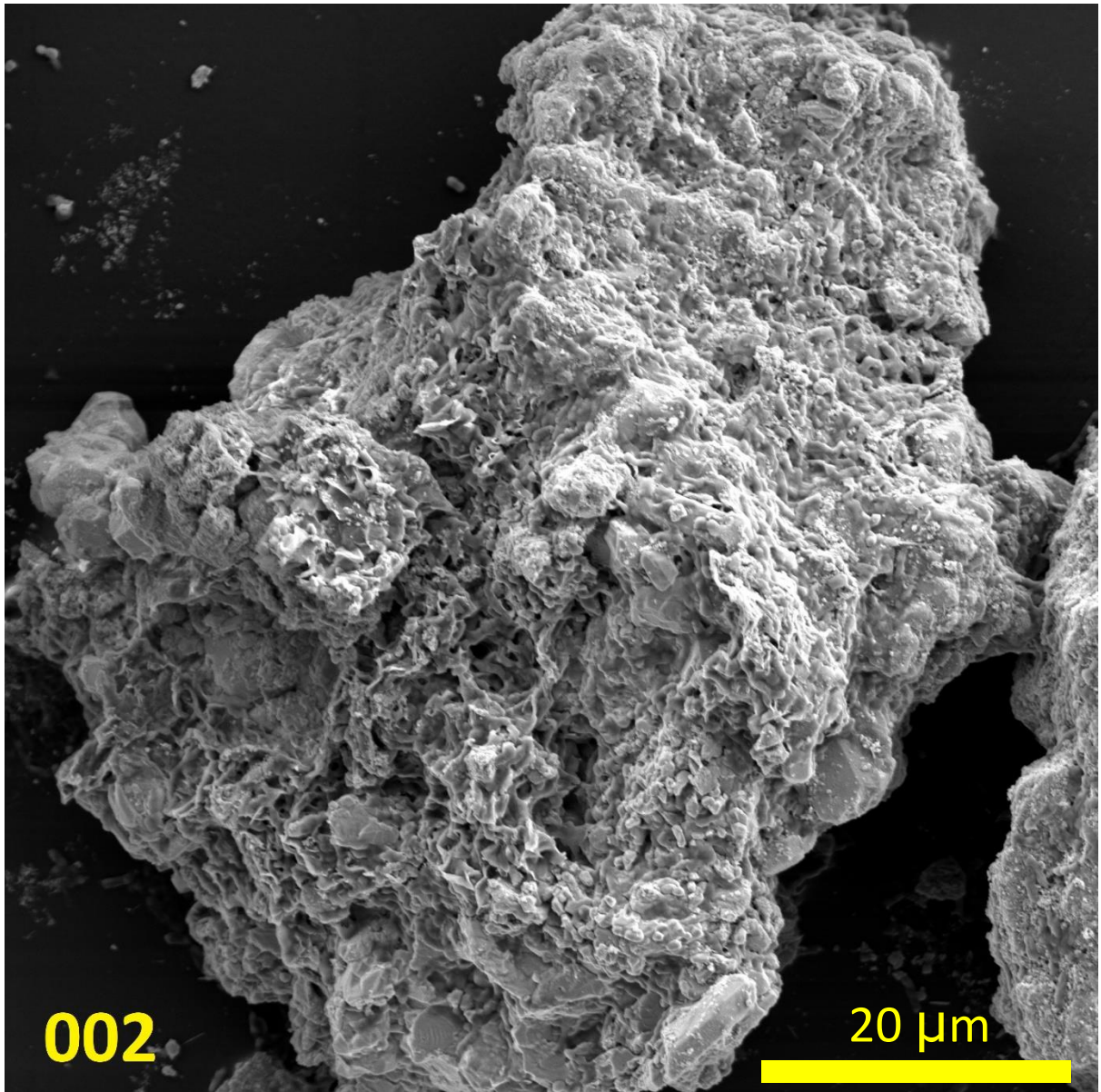


**Figure S-15.** SEM-EDS mapping of the mineral/chemical distribution and composition of high grade monazite sample. (a) The SEM overall image of the mapped area merged with the SEM-EDS elemental map. (b-m) The chemical distribution of each element in different mineral grains. The black regions in the SEM-EDS maps represent absence of an element of interest and the coloured area represent the areas on the surface where the related EDS signal was detected for that specific element.

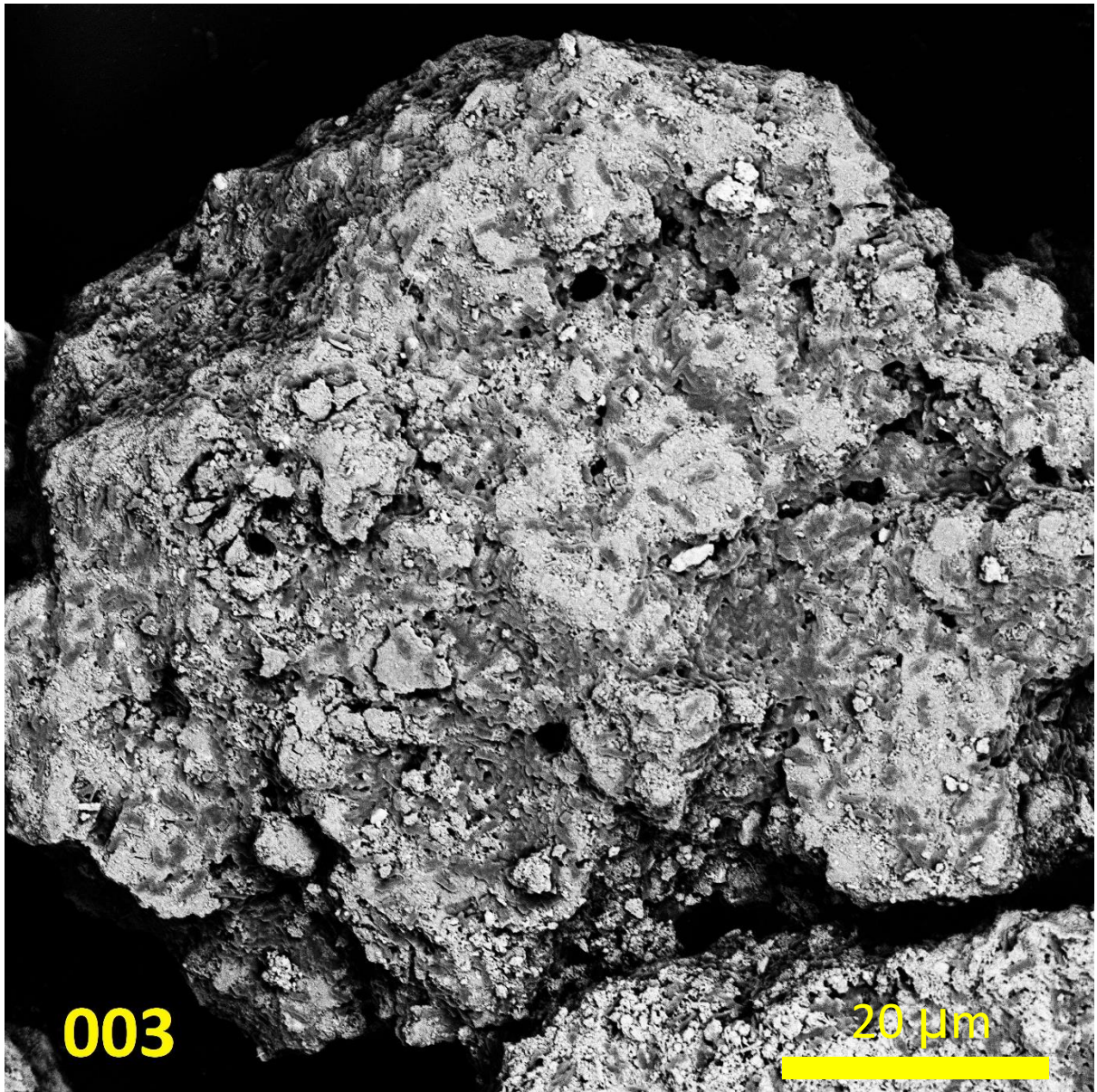




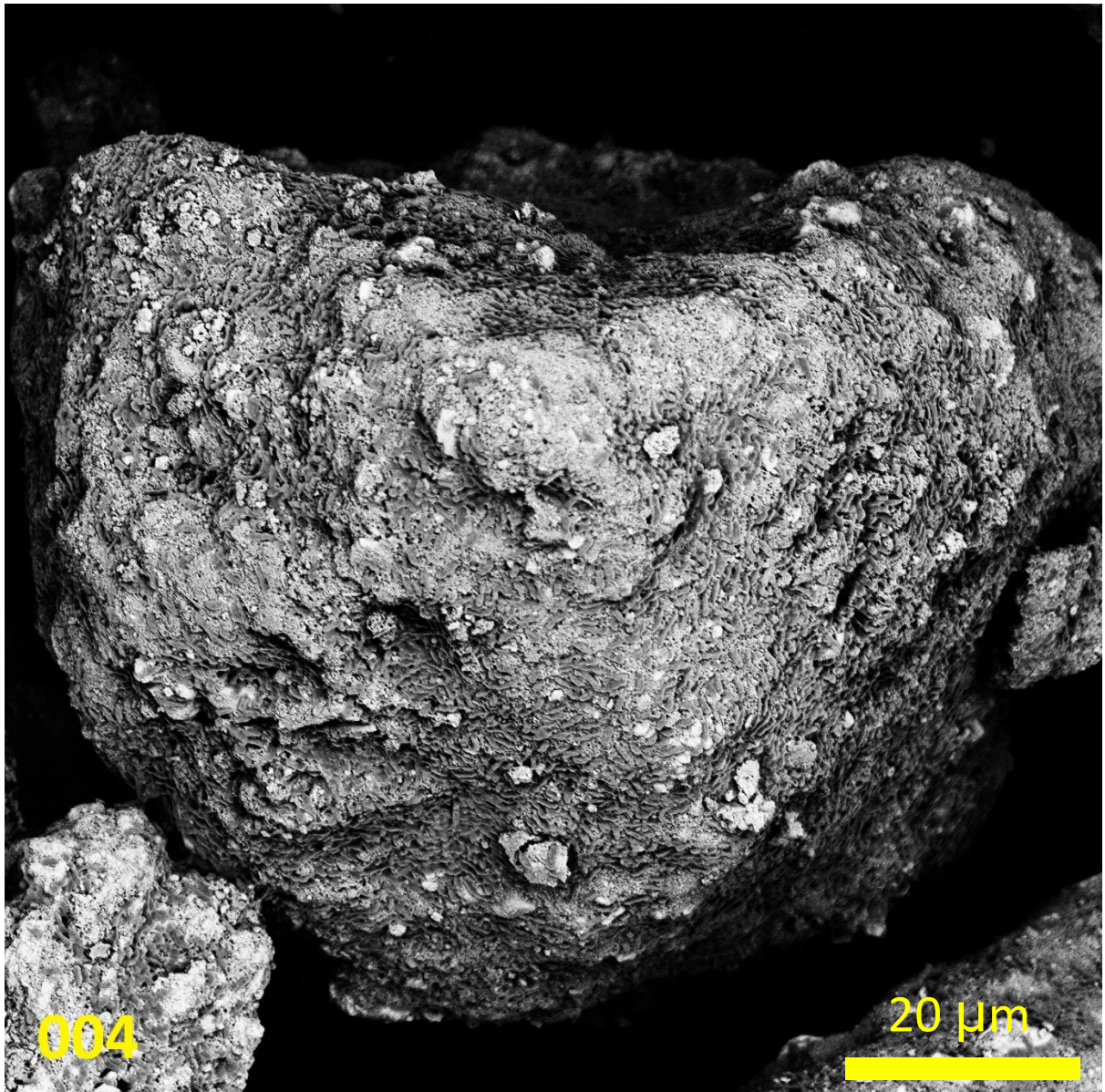


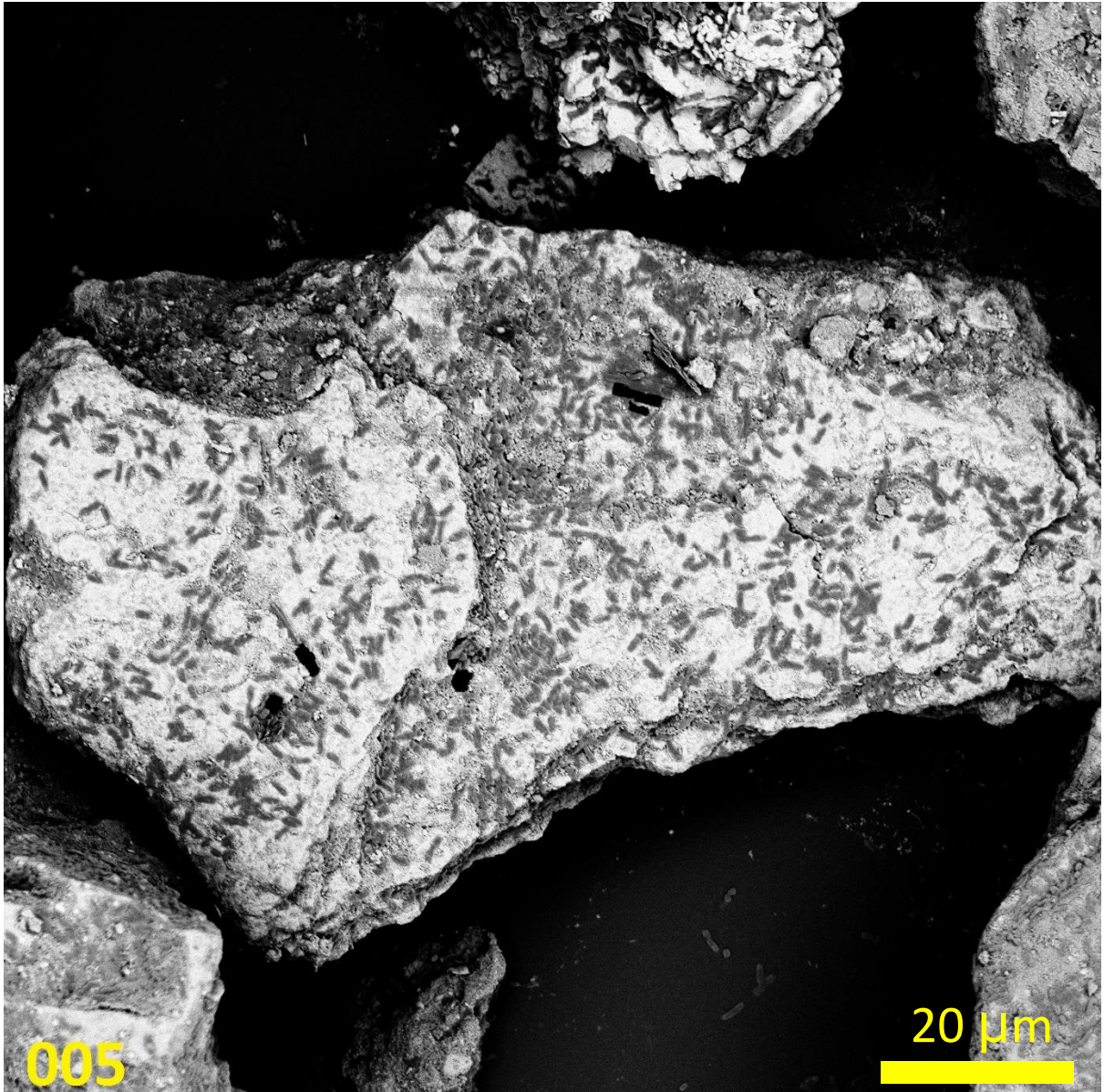




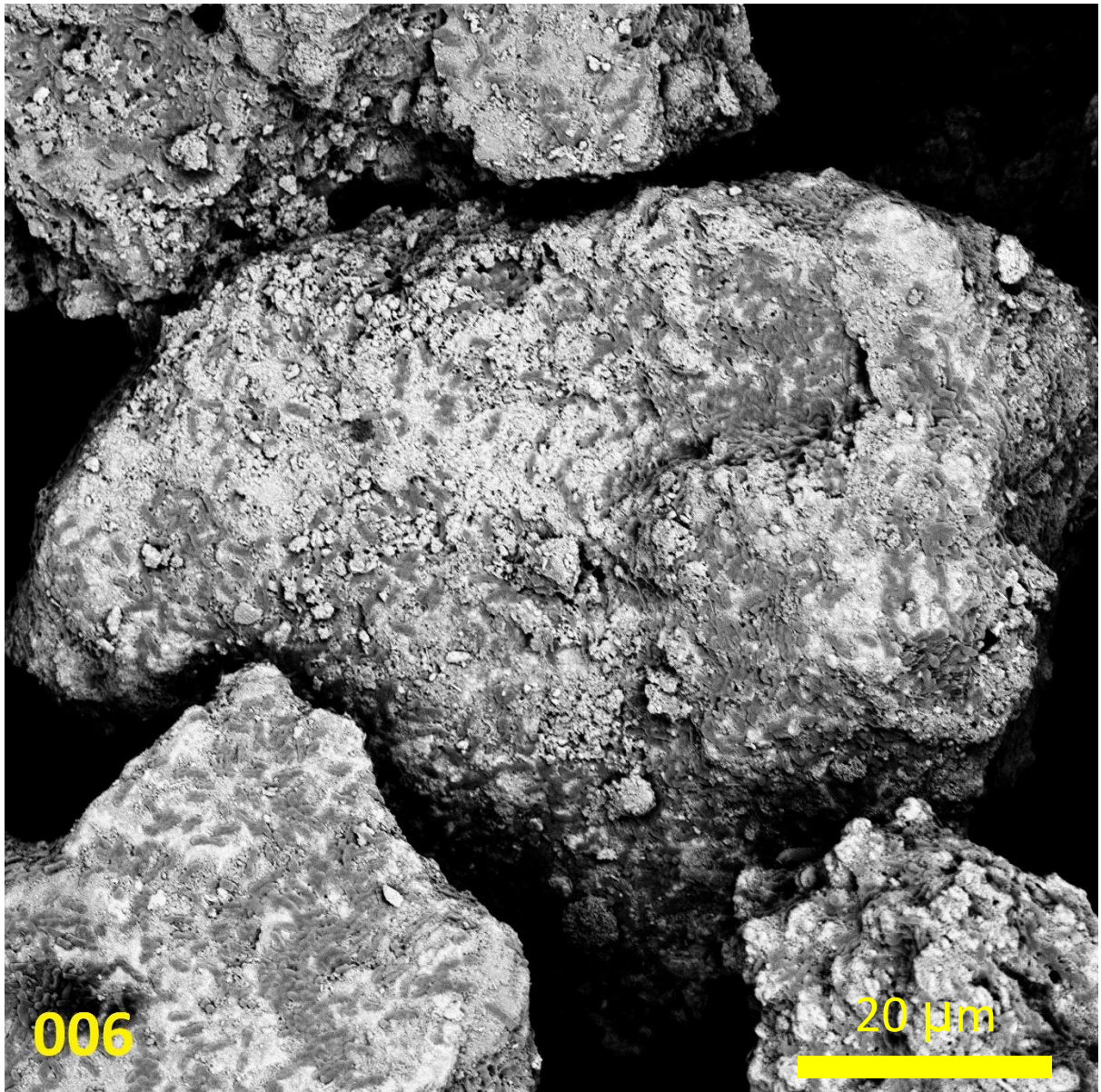




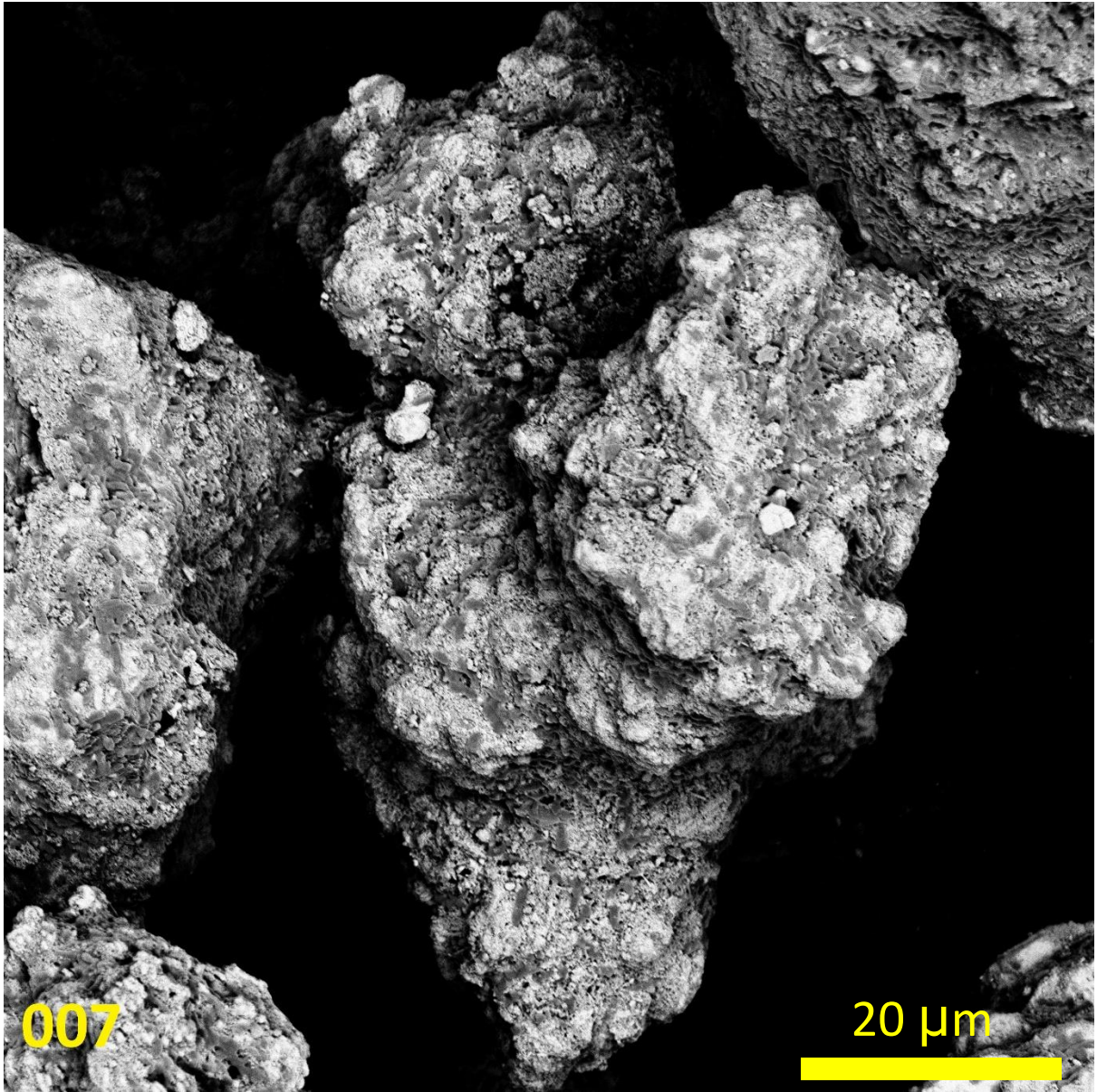


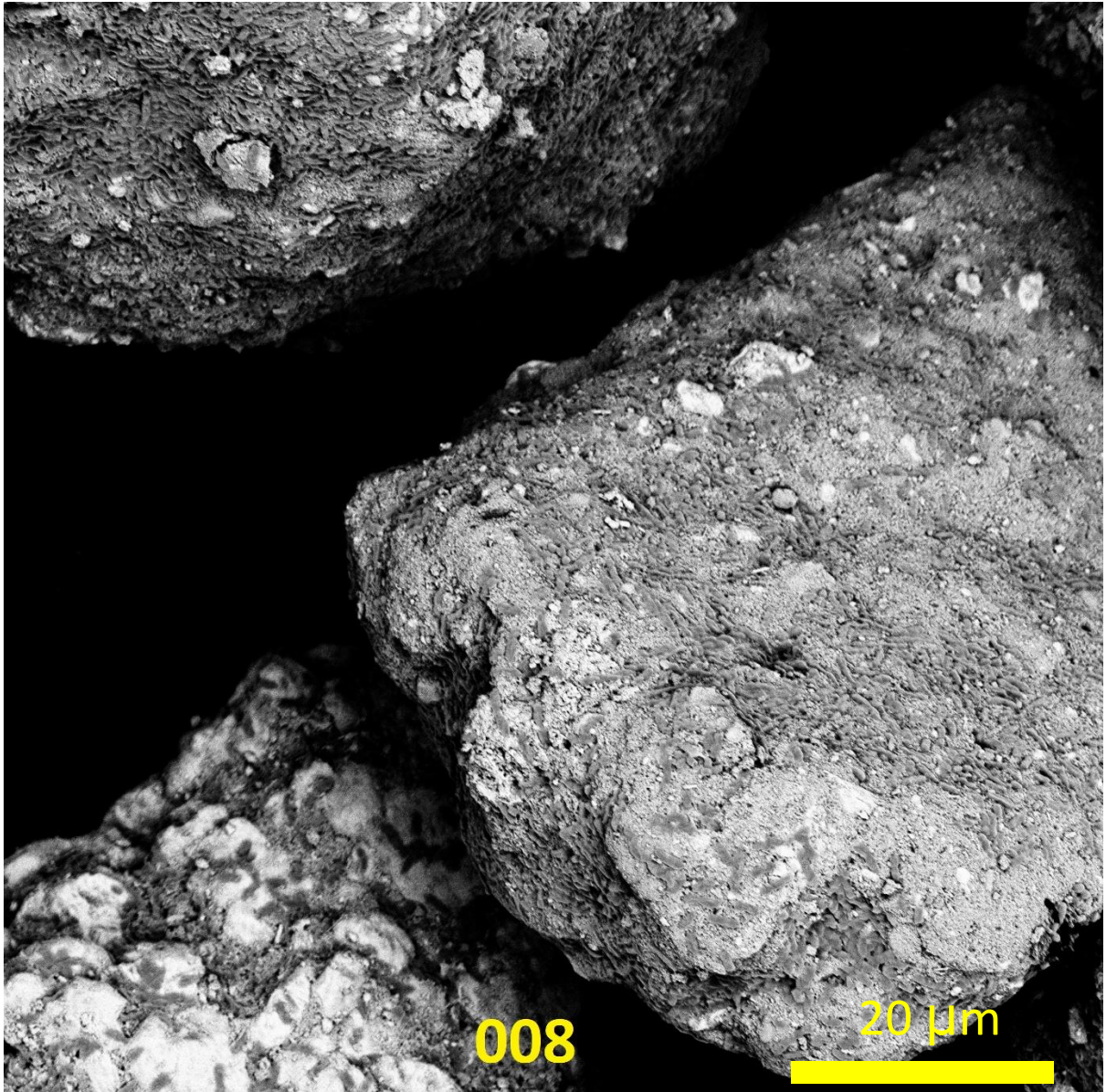




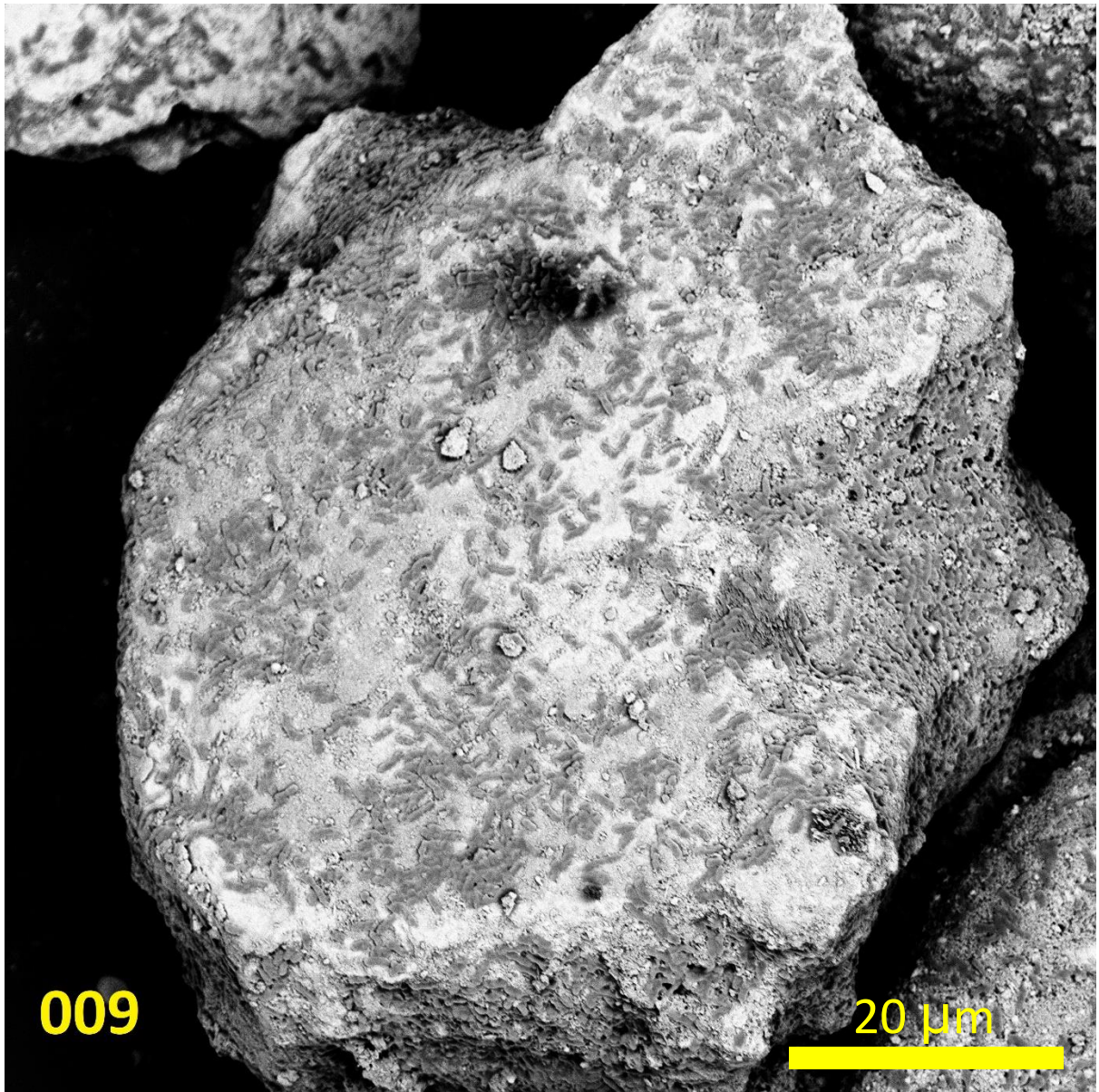


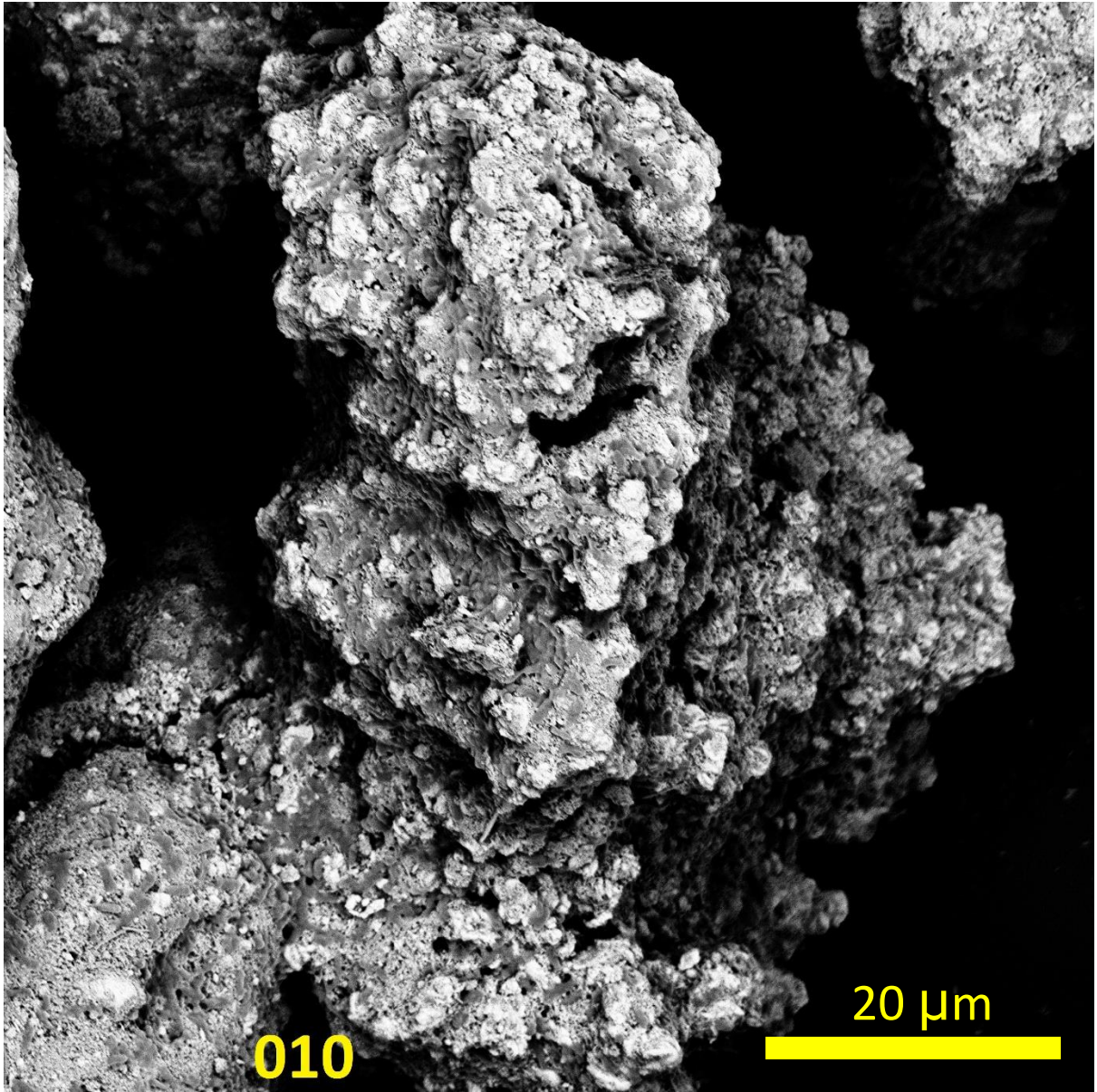




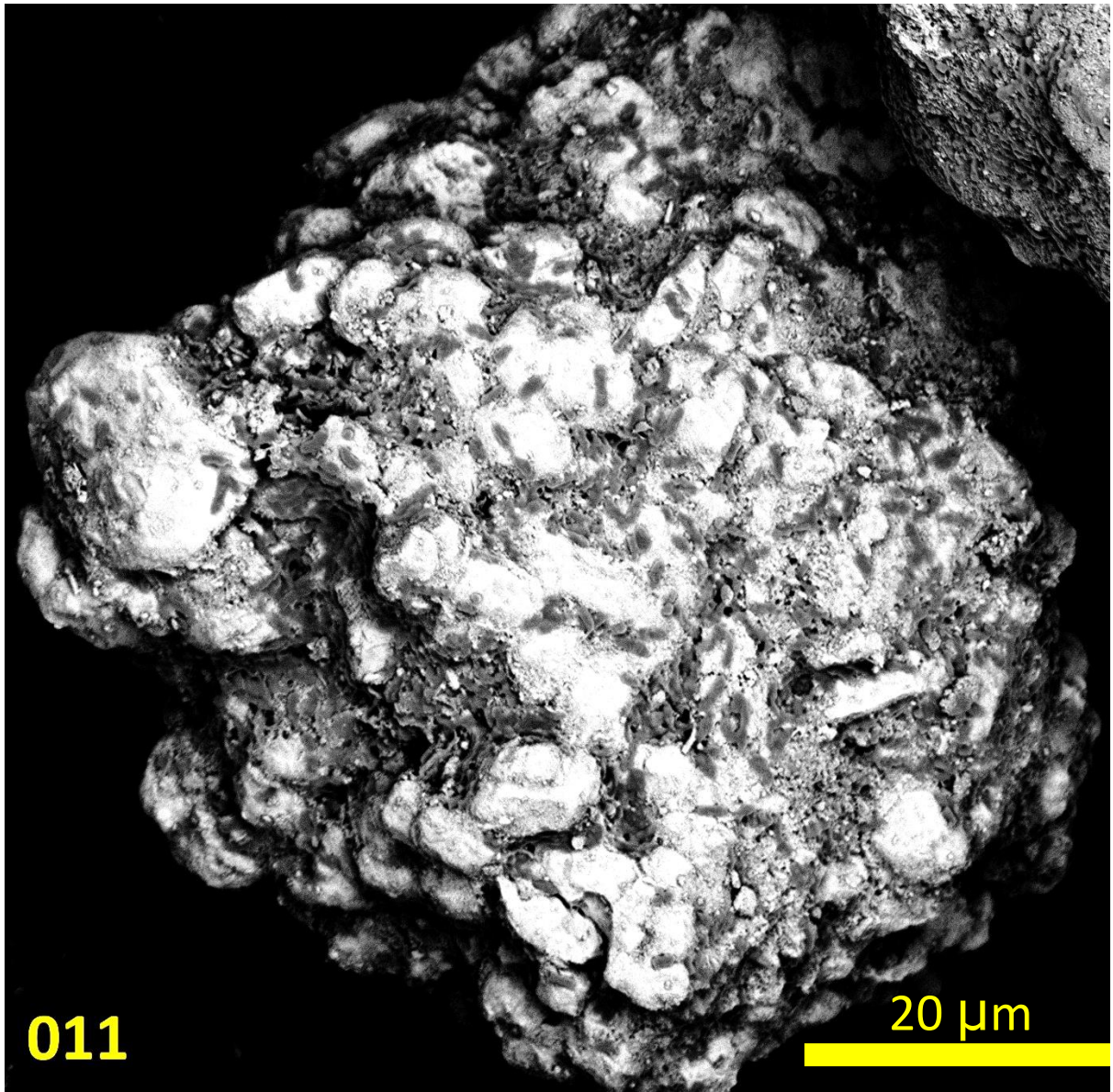


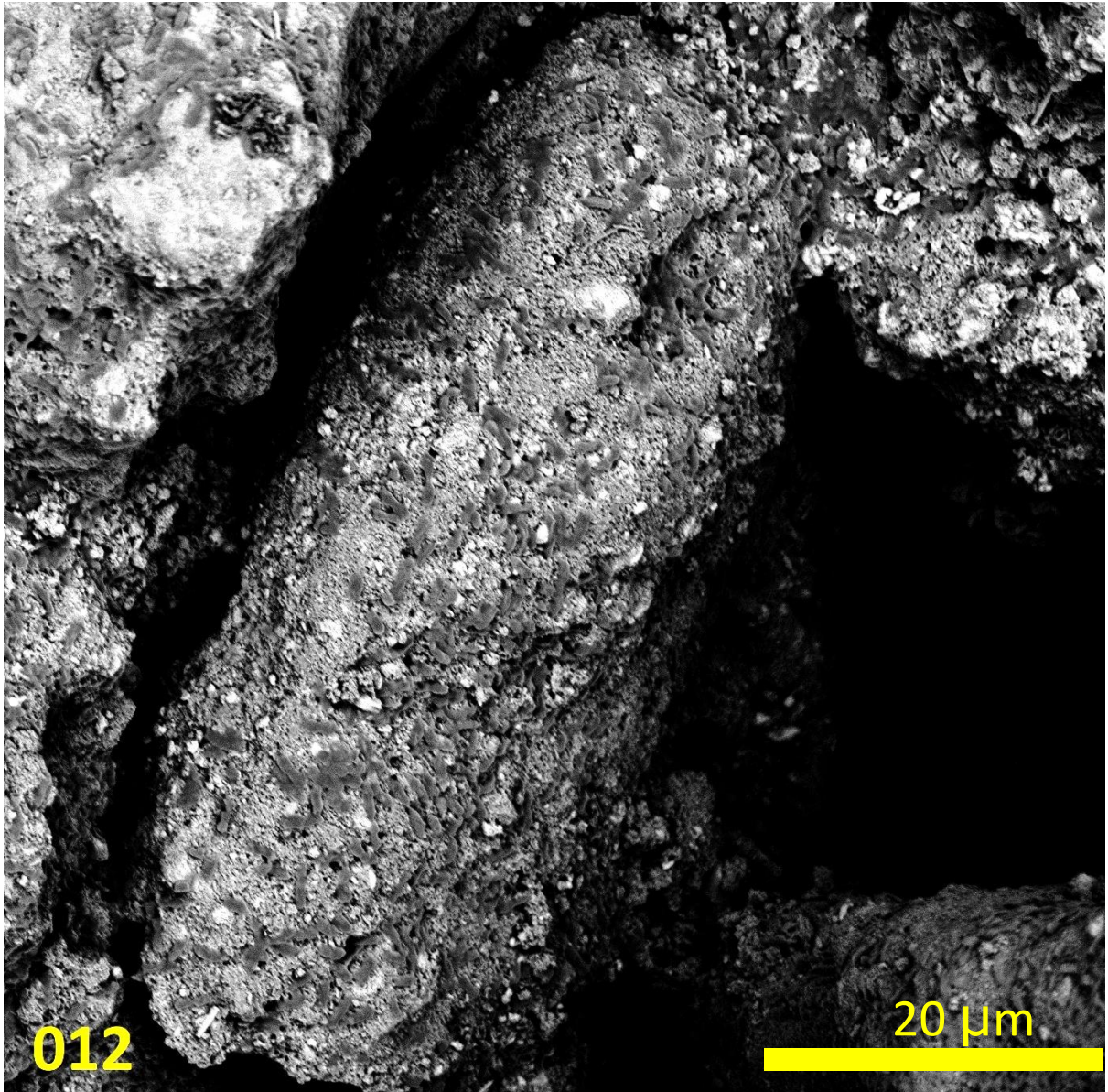




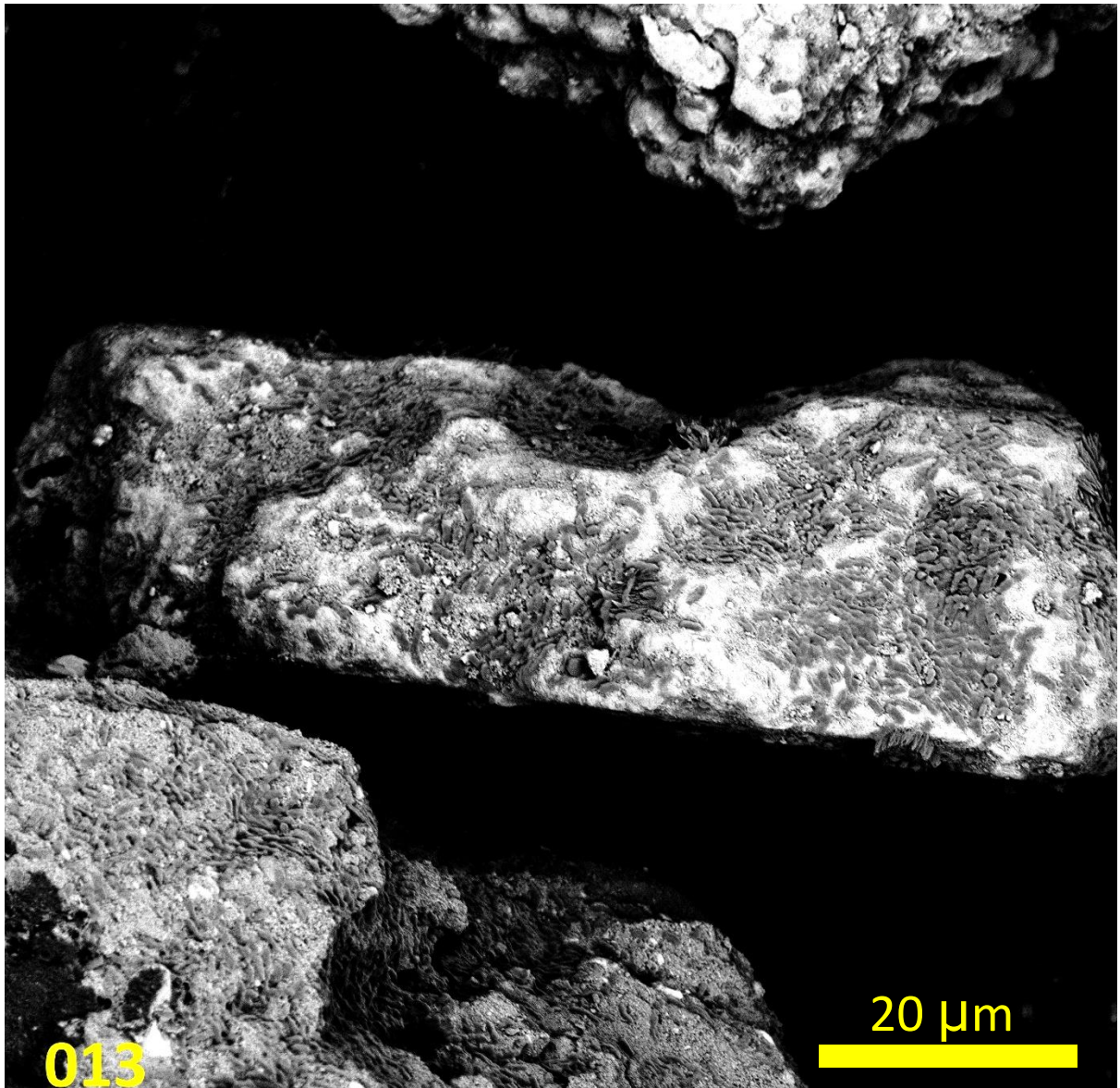


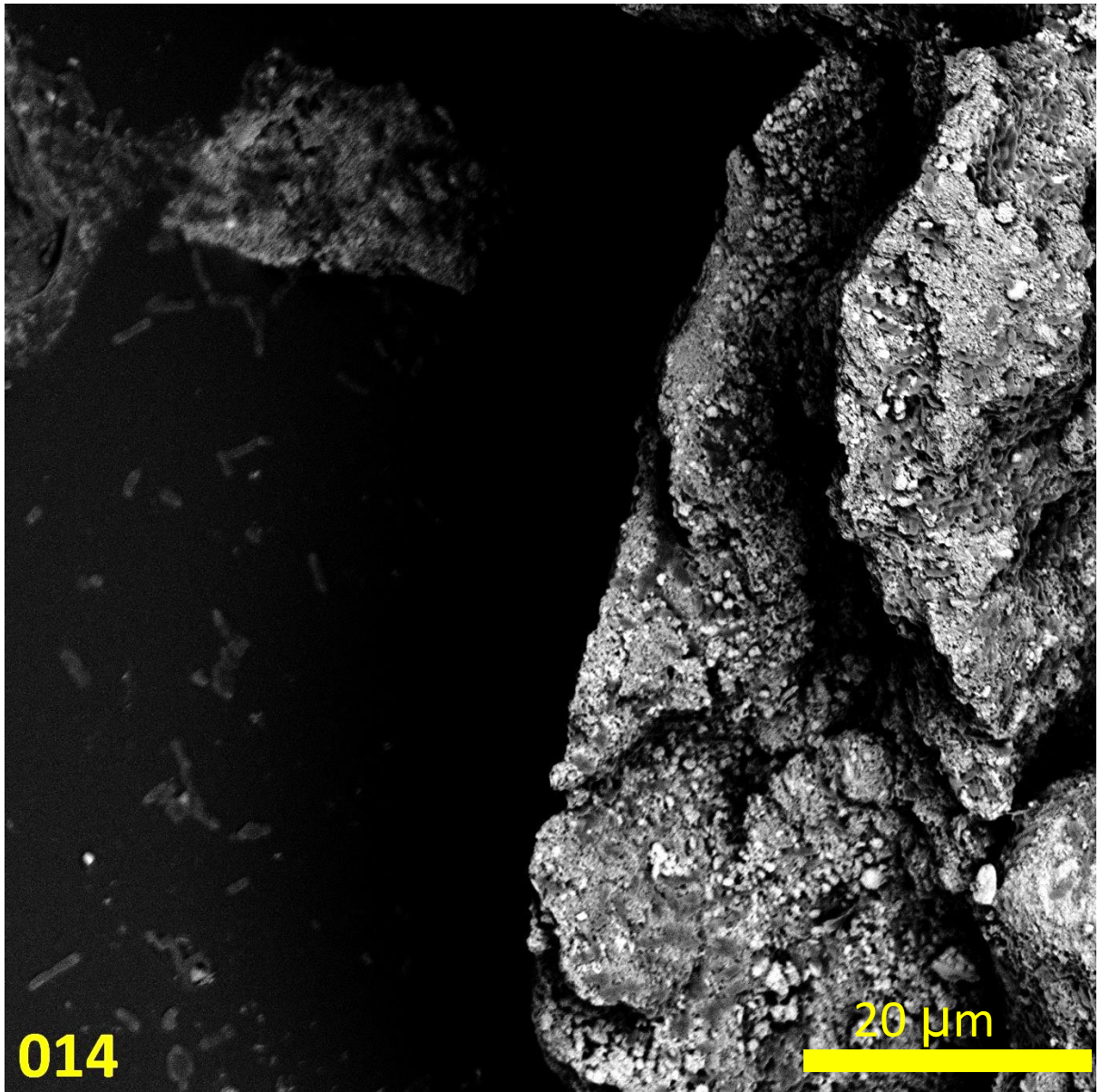




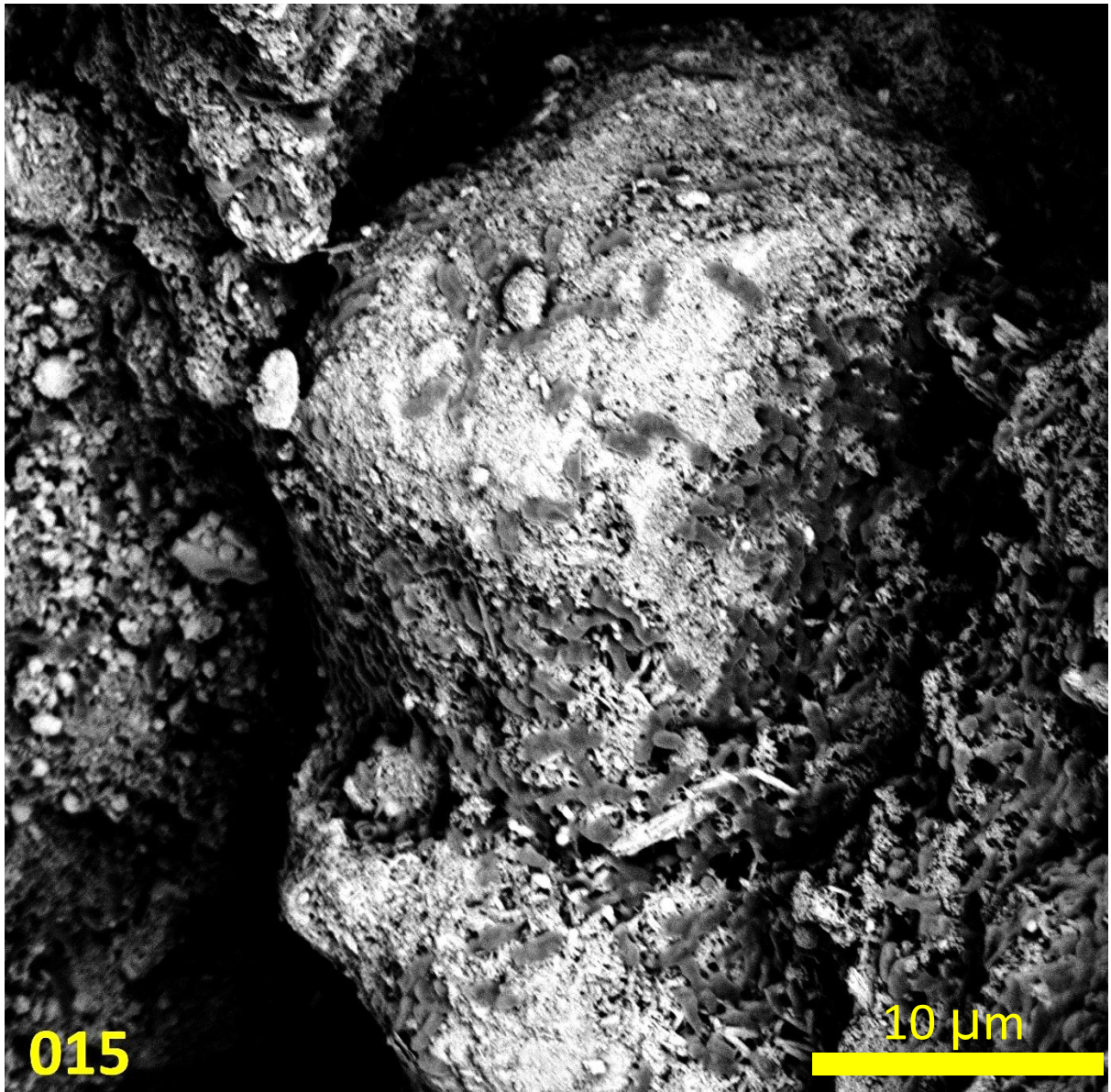












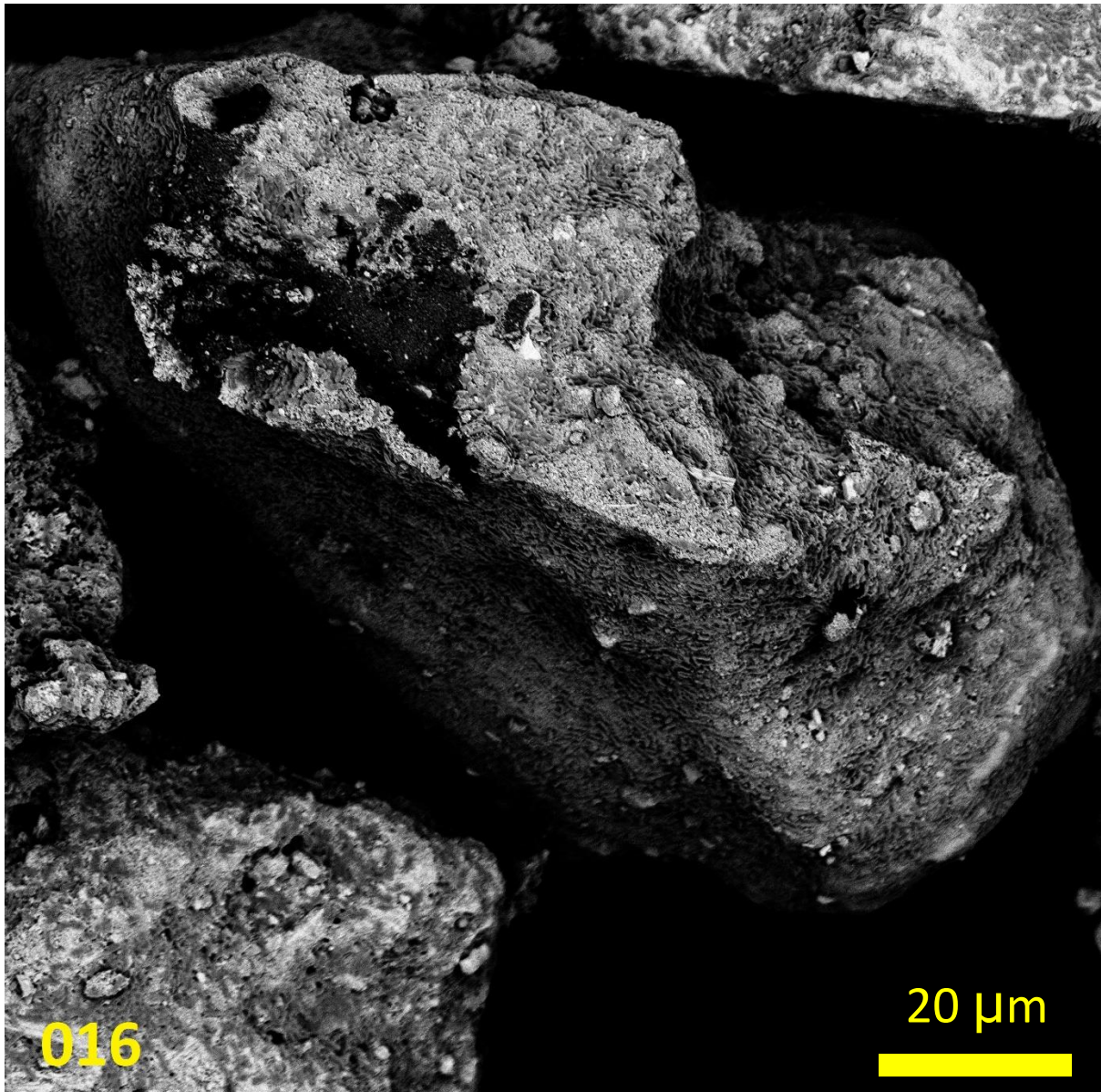


**Figure S-16.** Investigating *K. aerogenes* biofilm localization toward specific mineralogy or chemical composition. An overall backscattered electrons SEM image of the sample is provided (a) with each grain numbered for reference. The regions of the mineral surface with heavy element such as Ce or La are seen with brighter white-grey shades in the backscattered electrons SEM image and lighter element are seen darker. Another backscattered electrons SEM image of each grain was captured at higher magnifications and the referenced number of each grain (panel-a) is provided at the bottom of the image. *K. aerogenes* cells are the bacilli shaped grey features on the surface of the mineral grains.



**Chapter Four**  
**Quantitative analysis of the biofilm stages and  
extracellular DNA production by *Klebsiella*  
*aerogenes* in bioleaching settings**



## Abstract

As an important prerequisite of contact leaching, *Klebsiella aerogenes* attaches and colonises the surface of rare earth (REE) phosphate minerals like monazite to form a biofilm. Quantification of biofilm coverage at different time points or measuring the important component of biofilm like extracellular DNA (eDNA) provide a comparative approach to monitor biofilm development and quantitatively study the changes in biofilm composition or function. To study the biofilm development stages, monazite was subjected to bioleaching and imaged at different time points using confocal laser scanning microscopy and electron microscopy. The recorded images were then quantitatively analysed using image processing software Imaris (version 9 and 10) and Image (version 2). Quantitative analyses confirmed the three distinctive stages previously observed in descriptive study of the biofilm. At the initial attachment stage, attached microorganisms covered approximately 10% of the mineral surface. At the mature biofilm stage, a significantly larger area ( $\sim 70\text{-}80\%$ ,  $p \leq 0.05$ ) of the mineral surface was covered by *K. aerogenes*. Quantification of the biofilm coverage area indicates formation of the mature biofilm has two distinguishable substages, a colonisation step where approximately 50% of the mineral surface was covered by microorganisms, which further developed into a mature biofilm at which on average 80% of the surface was covered with bacterial cells for about eight days. During the last stage of the biofilm development, dispersion occurred with more than 80% of the biofilm detached from the surface. Moreover, eDNA production per  $\mu\text{m}^2$  of biofilm showed significant variation at each stage. The eDNA content of the mature biofilm was significantly higher (a twofold increase,  $p \leq 0.05$ ) compared to the initial attachment stage. While eDNA facilitates the initial attachment to the surface, a higher quantity of eDNA in the biofilm matrix is essential for the stability of the mechanical structure of the biofilm. The eDNA content significantly decreased over the dispersion

stage, which could be a contributing mechanism employed by bacteria to trigger dispersion. Furthermore, *K. aerogenes* produced significantly more eDNA on monazite which contains light REE such as cerium, lanthanum, and neodymium, compared to xenotime which contains heavy REE such as dysprosium, which could be a physiological response to the surface chemistry and mineralogy. In addition to a physiological response to different mineralogy, different levels of eDNA production in the biofilm matrix could also be a physiological response to environmental stresses such as inhibitory concentrations of harmful compounds for microorganism such as antibiotics or heavy metals. Quantitative analysis of biofilms offer a measurable means of monitoring changes in biofilm, either by attachment efficiency and coverage area, or to monitor the concentration of certain compounds or metabolites, or rate and efficiency of a function of interest. . Such quantification approaches are important to evaluate engineering processes aimed at enhancing biofilm formation or targeting biofilm eradication.

## 1. Introduction

Microorganisms are extremely diverse omnipresent biological entities on the planet. One of their ubiquitous features is the ability to produce biofilms, an enclosed multicellular matrix (aggregation) of a single species or a consortium of multi-species of microorganisms sticking to each other and/or to surfaces or interfaces<sup>1-3</sup>. A central hypothesis in microbial sciences is that biofilms are the predominant form of microbial life in almost all ecosystems with adequate amount of nutrients<sup>1</sup>. Research first performed on biofilms by Hitchman's in (1921)<sup>4</sup> of a biofilm structure suggested that attachment to a surface may benefit bacterial growth. Lloyd in (1930)<sup>5</sup> studied bacterial population adherence to the suspended particles, and Waksman *et al* (1933)<sup>6</sup>, examined marine bacteria attachment to planktonic organisms, and microbial attachment and occupation of the glass surface by ZoBell and Anderson (1936) was described as micro-organic films<sup>7</sup>. After about a century since the reports on biofilms, attachment to surface or interfaces has been accepted as another ubiquitous feature of microbial life<sup>8</sup> building upon the second central hypothesis of microbial ecology that the majority of microorganisms on the planet are in a consortia of multispecies biofilms associated with a surface<sup>1</sup>. Methods to study the attached microbial population on a surface, also known as the sessile population<sup>9</sup>, has developed greatly since then<sup>10,11</sup>; however there is still a need to adopt and develop new approaches for new or understudied surfaces or bacteria. While descriptive methodologies are important in providing fundamental information such as the morphology or complexity of a the biofilms, quantitative approaches are of high importance as they offer a mean to quantitatively measure and compare certain biofilm features of interest<sup>10</sup>.

Attachment and biofilm formation as the critical aspects of microbial bioleaching have been mainly studied for sulfide minerals<sup>12-14</sup>. It is one of the understudied subjects in bioleaching of other minerals, in particular rare earth elements (REE) bearing phosphate minerals. There is very limited data available regarding the behaviour of either the planktonic or sessile populations within these systems. Previous studies on the bioleaching of monazite<sup>15,16</sup>, as one of the main REE-phosphate minerals, reported that the bioleaching rate was higher when microorganisms were in contact with the mineral surface than with suspended cells<sup>15</sup>. The authors hypothesised that the sessile subpopulation had a critical role in bioleaching, mainly through organic acid production (acidolysis) and complex formation between released rare earth cations and organic acid residues<sup>15,17</sup>. In the proposed mechanisms, the extracellular polymeric substances (EPS) was depicted as the matrix where acidolysis and complex formation occurred<sup>17</sup>. Nevertheless, there was not enough information regarding the sessile subpopulation. Moreover, the methodology used to study this subpopulation was limited to electron microscopy and atomic force microscopy. There was not enough information regarding how a biofilm develops on REE-phosphate minerals, what is the efficiency of attachment, what percentage of the total available area for attachment on the mineral surface is covered in biofilm at each stage, and whether and how biofilm composition changes over time or on different phosphate minerals. This chapter focuses on quantitative analysis of biofilm development by *K. aerogenes* on Australian monazite and xenotime minerals, two important REE-phosphate minerals<sup>18</sup>.

Light microscopy has always been one of the main tools in microbial studies. Confocal laser scanning microscope (CLSM) has been proven as one of most advanced light-based microscopes to study biofilm<sup>19,20</sup> with one of the main applications of CLSM in studying the microbe-mineral surface interaction is to monitor microbial attachment and colonisation of

the surface in a descriptive and/or semi-quantitative approach<sup>10</sup>. By using specific fluorochromes for certain biochemical compounds, for example DNA, proteins, or cell wall components such as cellulose, CLSM and other fluorescent based microscopy techniques allow monitoring of the microbial cells' activities. For example, many studies used various fluorescent based microscopy techniques to monitor different stages of the biofilm formation or changes within the biofilm matrix<sup>18,21,22</sup>. Changes in the attachment intensity has been used to identify different stages of microbial biofilm development over a time course. CLSM can be used to create a 3D structure of the biofilm and its morphology by recording several images from the same location (fixed on X and Y axis) at different height on the Z-axis, which is referred to Z-stacks. In addition to morphology of the biofilm, the Z-stacks can provide valuable information regarding biofilm complexity such as cellular arrangement, orientation, or specific functionality such as formation of water channels inside biofilms<sup>23,24</sup>. However, the main bottleneck in using CLSM to study microbe-mineral interaction, is the inability to detect microbially imposed chemical changes on the mineral. Electron microscopy on the other hand is highly capable of enabling such studies and in addition to CLSM, scanning electron microscopy (SEM) has been widely employed for the analysis of microbial biofilms<sup>10,25</sup>. Although CLSM images and SEM micrographs primarily contains descriptive information about the biofilm, the recorded images from both methods can be processed and used for quantitative analysis<sup>10</sup>. In chapter 3, we provided empirical evidence to address the biofilm formation and its stages in bioleaching of phosphate minerals. This chapter focuses on the further processing of the data used in Chapter 3, providing a quantitative analysis of the biofilm and its stages, and investigates whether the observed changes or stages are statistically significant.

## **2. Methods**

### **2.1 Microorganisms**

*Klebsiella aerogenes* ATCC 13048 was used for bioleaching experiments and grown on National Botanical Research Institute's Phosphate medium (NBRIP) as described by Van Alin *et. al.* (2022- a and b). Cells were enumerated using flow cytometry with an Attune NxT flow cytometer as described in chapter three. For all bioleaching tests the media were inoculated with *K. aerogenes* to reach a final cell number of  $1 \times 10^7$  cell mL<sup>-1</sup>. For bioleaching experiments, microorganisms were grown in phosphate deficient media.

### **2.2 Minerals:**

Two ores acquired from Australian mines, one a high-grade monazite ore (HGMO, Lynas Corp, WA, Australia) and a xenotime ore (Northern Minerals, WA, Australia) were used as the mineral of choice. Mineral characteristics and composition determined by X-ray diffraction (XRD) and inductively coupled plasma mass spectrometry (ICP-MS) for these samples have been published by Van Alin *et. al.* (2022 a and b).

### **2.3 CLSM settings for analysis of microbe-mineral surface interactions**

CLSM imaging was conducted using Nikon A1+ point scanning confocal microscope with 405 nm, 488 nm, 561 nm, 640 nm laser units, and a motorised XYZ stage. NIS-Elements software (V4.4, Nikon Instruments) and Imaris (V9 and V10, Oxford Instruments) were used for CLSM imaging analysis. Hoechst 33342 (AATBio) and DiTO-1 (AATBio) were used for staining as published in (Van Alin et al 2022). Hoechst 33342 was excited at 405 nm laser and detected through 450/50 filter. DiTO-1 was excited at 457 nm laser and detected through 525/50 filter. For autofluorescence the excitation/emissions at 561/595 nm and 650/700 nm were also collected.



To study the attachment of microorganisms and biofilm formation to the mineral surface, samples were stained with fluorochromes that target polymeric nucleic acids, polysaccharides, lipids, proteins and other metabolites. Nucleic acid content inside and outside the microbial cell was targeted by staining using two fluorochromes, Hoechst 33342 (1  $\mu$ M) and DiTO-1 (1  $\mu$ M) following Van Alin et al (2022-a). Hoechst 33342 stains genomic DNA (gDNA) inside the cells and other DNA polymers that are produced for or trapped inside the extracellular polymeric matrix around microbial cells referred to as extracellular DNA (eDNA). In contrast, DiTO-1 is a membrane-impermeable dye, hence attaches to eDNA molecules of healthy living cells (their cell wall and cell membrane is intact).

## **2.4 3D modelling in NIS-Elements and Imaris**

### **2.4.1 CLSM-Z-stack imaging**

For 3D modelling, CLSM imaging was done in Z-stack mode, at 1-3  $\mu$ m height interval when low magnification imaging was employed using 10  $\times$  or 20  $\times$  objective lenses. This setting was used to quantify the biofilm covered area as it provided a very large analysis region (1 mm  $\times$  1 mm at 100-300  $\mu$ m high). Covering a large area for analysis allowed for a more accurate measurements of the biofilm instead of averaging a small area on the surface of multiple particles through the acquisition and analysis of multiple images.

At higher magnifications using 40  $\times$  - 100  $\times$  objective lenses a height interval of 0.5  $\mu$ m was used for Z-stack recording. The Z-stack were used to create either a 2D Maximum (fluorescence) Intensity Profile (MIP) image, or a 3D model which allow illustration of the surface topography and some of the physical properties including grooves. This setting was used for the analysis based on cell number, permitting calculation (percentage) of eDNA producing cells. The Z-stack were converted to a 3D model in NIS-Elements (Ar and C packages)

and Imaris (V9 and V10) to create a virtual 3d model of the surface resembling the same size, shape and to some extent the topographical features of the surface.

#### **2.4.2 Computer aided modelling of the surface, microorganisms, and differently stained chemical properties of biofilm/microorganisms**

The Z-stack were converted to 3D models in NIS-Elements using 3D tool at MIP. On Imaris, the Z-stack are automatically converted into 3D model at MIP. In Imaris, the mineral surface was recreated using “Surface” tool utilising the background noise and/or the samples’ autofluorescence recorded on 561/595 nm and 650/700 nm filters. Using the same methodology, the g-DNA or e-DNA signal were used to create another surface representing the area covered with biofilm using the specific signal acquired on 450/50 and 525/50 channels. Given that biofilm formation and coverage were not uniform processes, Z-stack CLSM images covering extensive areas of the sample (1000  $\mu\text{m}$   $\times$  1000  $\mu\text{m}$   $\times$  300  $\mu\text{m}$ ) were modelled and utilised for quantifying biofilm coverage. This method enabled the definition of the entire surface area of each particle in the field of view in its 3D form, ensuring that the biofilm’s heterogeneity did not impact the quantification. The measured area and the percentage of the biofilm covered area against the total available surface was used to quantitatively compare the changes in the intensity of *K. aerogenes* attachment at different stages.

Additionally, microbial cells were 3D modelled in Imaris using “Spot” tool. This tool created representative objects (spherical or oval shaped) per each individual signal acquired from each cell inside the biofilm, allowing relatively accurate counts of an event of interest, e.g., number of the cells attached to the surface. The gDNA of each bacterium stained with Hoechst 33348 (Figure 2-C) was represented as a blue sphere in the 3D model, and the eDNA

signals which only produced by cells that were also stained with DiTO-1 were represented in green. The produced 3D models were used to differentiate the cells that produce eDNA (yellow arrow) from those that did not (red arrow). For quantitative analysis, the number of recreated spheres for each signal was extracted from the metadata and used to calculate and compare the percentage of the cells that produced eDNA at a given stage of the biofilm formation.

### **2.5 SEM-based quantitative analysis of microbe-mineral interactions.**

After CLSM imaging, the samples were airdried, then moved to a desiccator for dehumidification. The samples then coated with carbon and platinum prior to SEM analysis. SEM imaging was conducted with a TESCAN Clara FESEM microscope using TESCAN Essence software (John de Laeter Centre [JdLC], Curtin University) at 5 kV operating voltage and 300 pA beam intensity. Changes in the bacterial attachment intensity to a surface was calculated on ImageJ software (<https://imagej.net>, Version 2) by measuring the surface area covered by microbial cells against the total surface area. The three image processing steps for quantification of these regions are shown in Figure 2.

### **2.6 Biofilm thickness and complexity analysis**

Quantitative analysis of the biofilm thickness was tested using cross section analysis by both CLSM and FIB-SEM. For CLSM based analysis, the cross-section requires Z-stack imaging. The thickness of the biofilm was measured across the samples, averaging a minimum of 20 locations per sample.

FIB-SEM analysis was done using a TESCAN LYRA3 GM (TESCAN instruments, JDLC, Curtin University) instrument. It was employed to make cross-sections of the region of interest, or to prepare TEM lamellas. Prior to any FIB analysis a 1- $\mu\text{m}$  thick platinum protection layer was

deposited on the region of interest, to minimise curtaining effects and protect the mineral surface and microbial biofilm from the ion beam <sup>26</sup>. A high current (10nA) focused ion beam was used to mill a trench and expose the cross-section under the protection layer. Subsequently low currents (1nA, 300pA) ion beams were used to polish the cross-section and minimise the surface damage and roughness. High resolution (nm scale) images acquired with tilt corrected SEM ensure measurements were in the direction orthogonal to sample surface. The cross sections were analysed using SEM and the lamellas were analysed using TEM.

## **2.7 Statistical analysis**

When relevant, data preparation for statistical analysis was done in Microsoft Excel (2016) and GraphPad Prism v.9 from a minimum of two replica. Depending on the data, T-test, One-way ANOVA or Two-way ANOVA were used for comparison and a p-value of  $\leq 0.05$  was considered significant. Hereafter, the word “significant” in the text implies a statistical analysis with a P-value  $\leq 0.05$ .

## **3. Results and discussion**

### **3.1 Evaluating the computer aided modelling**

#### **3.1.1 Computer aided modelling of CLSM data**

Evaluating the 3D models created in NIS-Elements and Imaris showed that although both provide 3D- MIP images (Figure 2-A and B), only Imaris was capable of recreating accurate 3D models of microbial cells (representing the biofilm, Figure 1, panels C-H), mineral surface (Figure 1-I), or a combined image (Figure 1-K and L)).

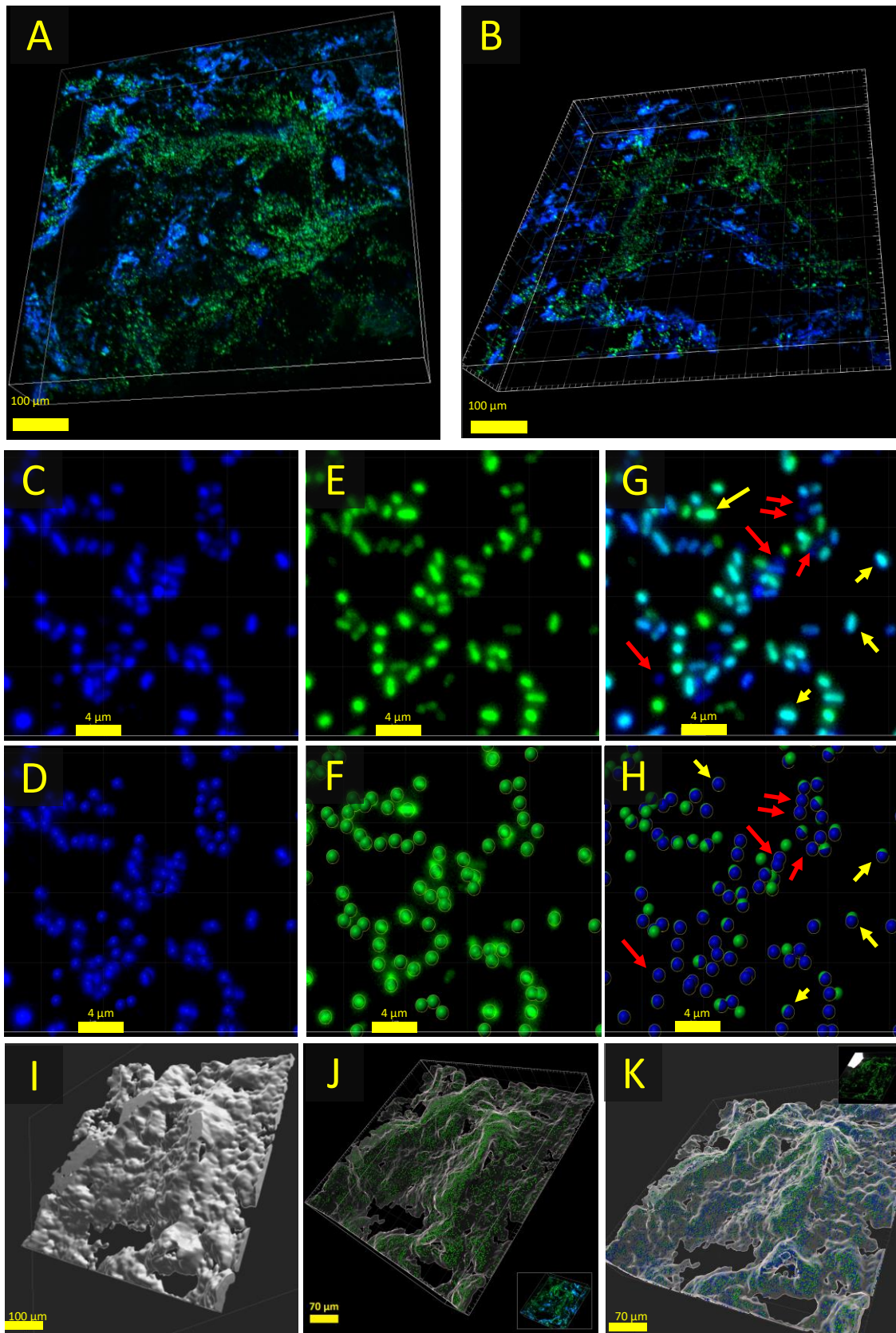


**Figure 1.** A) Biofilm's Maximum Intensity Profile (MIP) model was created using NIS-Elements software, and B) Imaris. C) Hoechst 33348 stained bacteria produced the fluorescent signal

for genomic DNA (g-DNA). **D)** Each g-DNA signal from a bacterial cell was modelled as a blue sphere. **E)** DiTO-1 specifically targeted and produced a fluorescent signal for extracellular DNA (e-DNA). **F)** The e-DNA signal from a bacterial cell was modelled as a green sphere. **G)** MIP image of merged g-DNA (blue) and e-DNA (green) signals. **H)** The final model where blue spheres represent cells (red arrow) without e-DNA production, while half blue-half green spheres represent e-DNA producing cells (yellow arrow). **I)** Imaris “surface” tool recreated the mineral surface, shown from a bottom perspective. **J)** Merged models of e-DNA producing bacterial cells on the surface, using the e-DNA signal. **K)** Merged models of the mineral surface and bacterial cells producing g-DNA and e-DNA on the surface.

The recreated mineral surface (Figure 1-I) offered a detailed view of the topography and facilitated the measurement of the total surface area of each mineral particle. The same method was employed using g-DNA or e-DNA signals to create a surface representing the biofilm-covered area, enabling the calculation of the biofilm coverage percentage on the mineral surface. Using higher magnification during imaging with 40× - 100× objective lenses provided clear images of each bacterial cell (Figure 1, panels C-H), making it possible to distinguish the specific signal of Hoechst 33348 (for g-DNA) and DiTO-1 (for e-DNA) for each cell. The recreation of bacterial cells using distinct g-DNA and eDNA signals into circles allowed enumeration of cells in Imaris, as well as distinguishing eDNA-producing cells (Figure 1-yellow arrow) from non-producing cells (Figure 1-red arrow). Then, these values were used for a quantitative comparison of the percentage of cells producing eDNA at each biofilm formation stage.

### **3.1.2 Computer aided modelling of SEM data**

By utilising the three image processing stages (Figure 2, A, B and C) in ImageJ, the final image was ready for a quantitative analysis. The surface shape area was automatically computed



(Figure 2-D, black region), with enclosed shapes within this space representing bacterial cells (Figure 2-D, yellow region). A comparison of these two regions' areas revealed the percentage of mineral surface covered by bacterial cells at each biofilm development stage

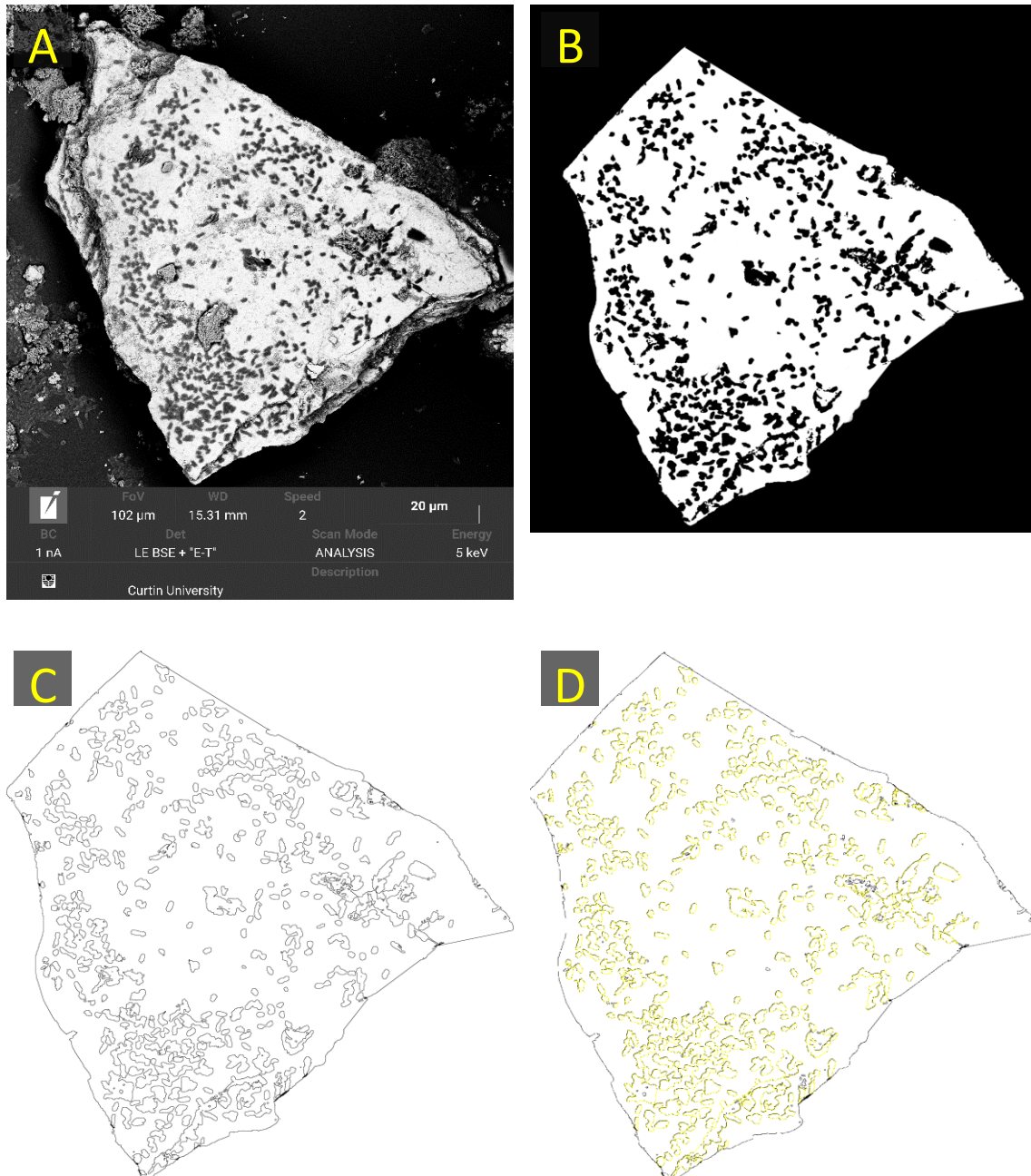


**Figure 2.** Image processing steps used on SEM acquired images using ImageJ software. **A)** the original SEM image, with dark grey rod-shaped spots on the mineral particle indicative of

bacteria. **B)** Converting the region of interest into a high-contrast image. Mineral particle is the white region, and the black spots represent bacteria. **C)** Conversion of the high-contrast image into a line image. Bacterial cells are the enclosed small shape area inside the borders of the mineral particle. **D)** The microbial representative shapes are selected (yellow) and used to measure the area occupied on each particle.

### **3.2 Autofluorescence of the surface before and after abiotic treatments**

To study the interaction of microorganisms with a surface it was important to ensure the surface did not have an autofluorescence, and if it did, the autofluorescence should not interfere with the studied parameters. This is important for both descriptive and quantitative analyses. In quantitative analysis, such interfering autofluorescence signals would lead to false creation of bacterial cells that do not exist on the surface, resulting in the wrong measurement of an event of interest. The tested minerals in this study had negligible autofluorescence when assayed through excitation/emissions at 561/595 nm (Figure 3-A) and 650/700 nm (data not shown) channels. Therefore, 561/595 nm and 650/700 nm filters were not used to study the biofilm, instead the recorded signals from these two channels were used to model the entire surface of the mineral grains in its 3D shape, with detailed surface topography (Figure 1-I). No autofluorescence was recorded on 450/50 and 525/50 filters (Figure 3-B), hence they were used for studying the biofilm using two DNA-based fluorophores, Hoechst and DiTO-1 respectively, as there was no interference between the samples natural autofluorescence and biofilm study (Figure 3-C).

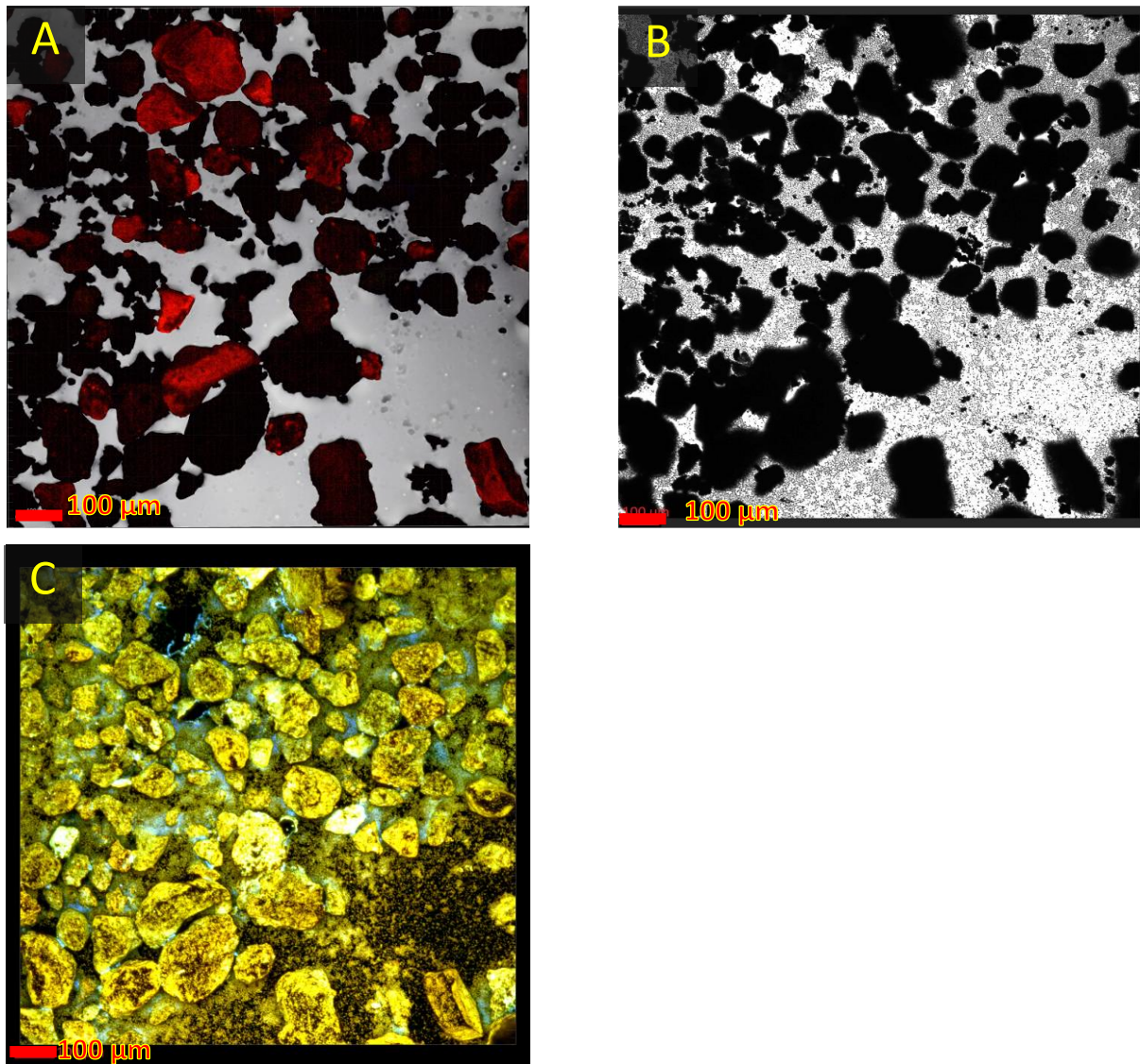


**Figure 3.** High-grade monazite ore samples glued to a glass slid. **A)** Autofluorescence of the sample before bioleaching shows signal at 561/595 nm excitation/emission channels. **B)** The same sample was imaged after bioleaching but before staining on 450/50 and 525/50 filters and showed no autofluorescence interference. **C)** Imaging the sample after staining bacterial DNA with Hoechst and DiTO-1. The golden spots represent the microbial biofilm. Scale bar = 100 µm.

### 3.3 CLSM-based quantitative analysis of biofilm development

In chapter 3 a descriptive analysis of microbe-mineral interactions in a bioleaching setting was provided, specifically using *K. aerogenes* and HGMO, and three distinctive stages for *K. aerogenes* biofilm formation were shown (Figure 4). At initial attachment (Figure 4-A) *K. aerogenes* were attached to a small proportion ( $11.8 \pm 4.4$  %) of the total available surface (Figure 4-D and E). As mentioned in the previous chapter, second stage is when a mature biofilm is formed (Figure 4-B). Quantitative analysis indicates two substages during forming mature biofilm. The second stage started with bacteria colonising significantly more surface area (Figure 4-D and E) compared to the initial stage. Approximately 16 h after microbial exposure to HGMO, 50 % of the mineral surface was colonised by *K. aerogenes*. Subsequently, there was a further transition toward forming a mature biofilm where bacteria covered a significantly larger proportion ( $71.3 \pm 8.7$  %) of the total available area of the mineral surface for about eight days. At the third stage microbial cells detached from the surface (Figure 4-C) resulting in a significantly smaller area of mineral surface being covered by a biofilm ( $13.8 \pm 10.2$  %).

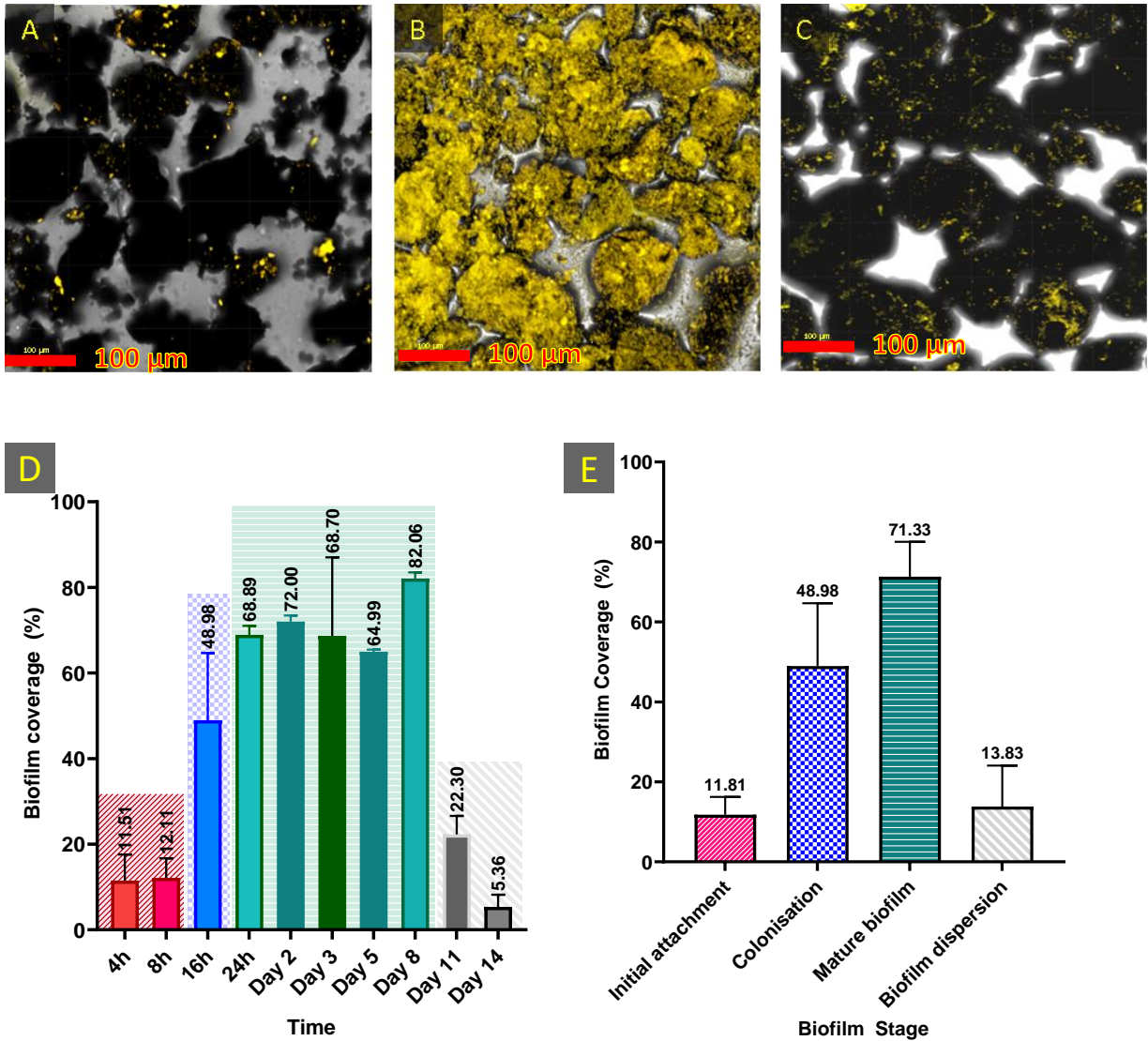


**Figure 4.** Descriptive and quantitative analysis of *Klebsiella aerogenes* biofilm development on high-grade monazite ore over a time-course experiment. MIP image of the biofilm at **A**) Initial attachment stage **B**) Mature biofilm stage with two substages, colonisation (16 h) and forming mature biofilm (day 1-8, image is from day 3) **C**) Biofilm dispersion stage at day 11 and 14 (image is from day 11). The golden-colour area on the surface is representative of the biofilm. **D**) Biofilm coverage in percentage of the total available area for attachment on the high-grade monazite ore grains. **E**) Average surface covered by the biofilm at different development stages. Scale bar = 100  $\mu\text{m}$



Both descriptive and quantitative analyses are fundamental in studying the efficiency of enhancing strategies on biofilm formation in particular for studying beneficial biofilms <sup>27</sup>. Descriptive analysis provides a visualised approach to how biofilms respond to a treatment or strategy in terms of morphology and complexity, and it provides a basic perspective on the relative thickness and coverage efficiency. On the other hand, quantitative analysis offers a measurable approach where the thickness, attachment efficiency, surface coverage efficiency or other measurable feature can be compared before and after a treatment or environmental change <sup>27</sup>. This is also important for studies on eradication of harmful biofilms such biofilm formed by pathogens or corrosive and undesirable microbial biofilms <sup>28,29</sup>.

#### **3.4 SEM based study of microbe-mineral surface interactions**

Quantitative analysis of the biofilm development on monazite with *K. aerogenes* using high-resolution SEM imaging confirmed the same pattern (Figure 5). An initial attachment with only ~3% of the available mineral surface covered by microbial cells. It was followed by the second stage, development into forming mature biofilm with two substages, colonisation (covering ~30 % of the surface) and then mature biofilm (covering ~80% of the surface). And the final stage, dispersion, at which about 95% of the biofilm was detached from the surface.



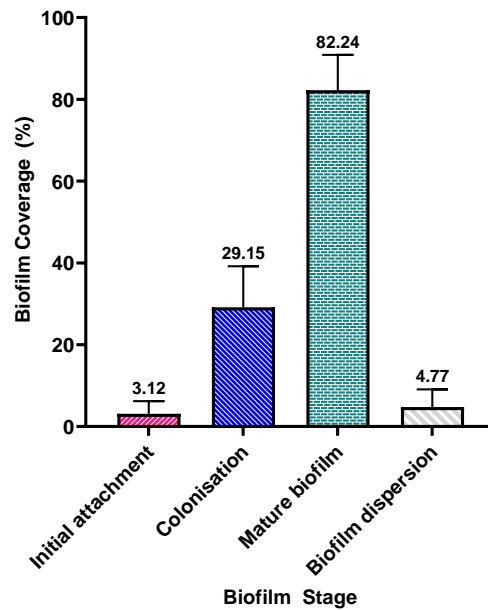


**Figure 5.** Quantitative analysis of scanning electron microscopy data, detailing *Klebsiella aerogenes* biofilm coverage on high-grade monazite ore at different stages of biofilm development.

The reason for the difference between the measured values by CLSM and SEM, in terms of the percentage of the covered surface by bacteria, was most likely due to the different measurement mechanisms employed by these instruments. With SEM analysis, only the main body of the cells were considered in calculation because the extracellular polymeric substance of the microorganism was not easily detectable by SEM. To visualise the EPS, several tedious fixation, staining and dehydration are usually required <sup>25,30</sup>, which was avoided in this study by altering the protocol to have minimal processing. In this study the samples were air dried, followed by dehumidification and coating. On the other hand, CLSM analysis involved both main body of the bacterial cells by recording the g-DNA signals as well

as the EPS through e-DNA signal. Hence, some difference was expected between the values measured by SEM and CLSM. Regardless, the general pattern was the same.

### **3.5 Biofilm thickness**

The biofilm thickness was recorded at  $0.98 \pm 0.24 \mu\text{m}$  from CLSM imaging of the live cells, and  $0.50 \pm 0.20 \mu\text{m}$  using FIB-SEM or TEM imaging of air-dried biofilm. The lower value for SEM was due to shrinking cell size after air-drying and dehumidification processes for SEM preparation. Compared to 10-500  $\mu\text{m}$  biofilm produced by other bacteria such as *Pseudomonas* spp<sup>31</sup>, or biofilms formed in industrial scale bioreactors<sup>32</sup> and environmental biofilm<sup>33</sup>, this was not considered a thick biofilm. Hence, it is not structurally thick enough to form complex organisational structures such as water channels within the biofilm<sup>23,24</sup>.

### **3.6 Changes in the biochemical properties of the extracellular polymeric substances (e-DNA in particular)**

Changes in the biochemical properties of the microbial populations was recorded in terms of e-DNA during the three stages of the biofilm formation (Figure 6), and as a physiological response to different mineralogy. Although descriptive analysis showed that *K. aerogenes* produced e-DNA at all three stages of its biofilm development on monazite<sup>18,34</sup>, it failed to capture the difference in terms of quantity. Analysing the average fluorescent intensity per  $\mu\text{m}^2$  of the biofilm mass revealed *K. aerogenes* produced significantly more e-DNA when the biofilm is at the mature stage. The recorded fluorescent intensity for e-DNA gradually increased from  $\sim 80$ -90 arbitrary unit per  $\mu\text{m}^2$  during initial attachment and colonisation, to  $\sim 180$  arbitrary unit at the mature stage.

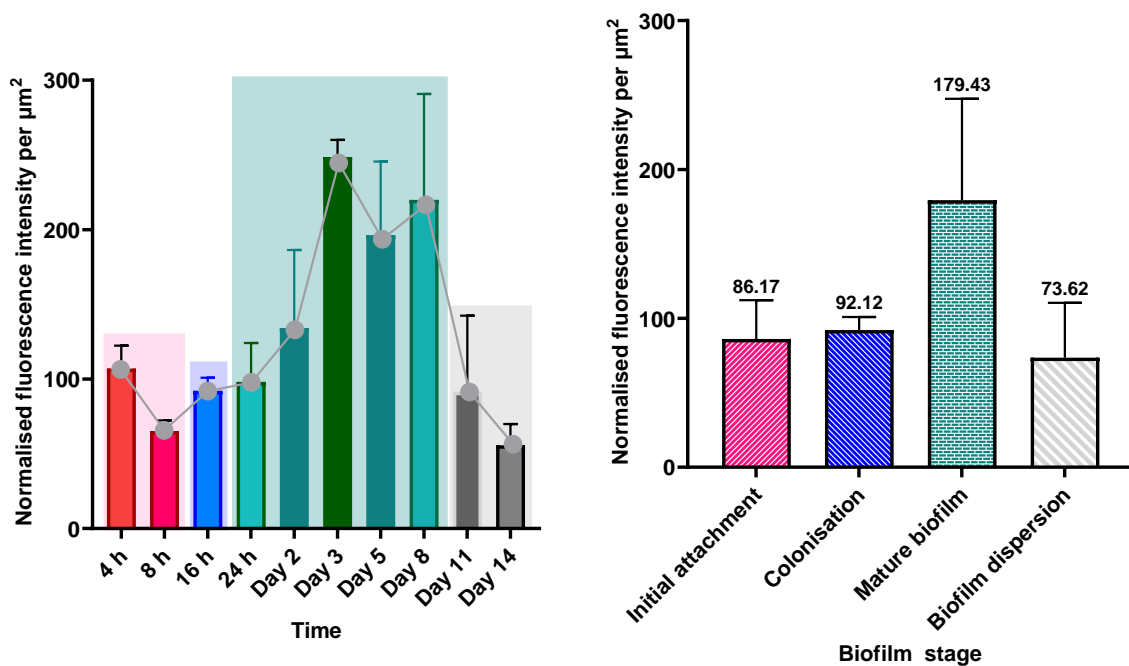


**Figure 6.** Changes in the e-DNA fluorescence intensity in *K. aerogenes* biofilm at different time points (A) and Stages (B) of the biofilm development. The fluorescence intensity was normalised per  $\mu\text{m}^2$ .

As discussed in our previous study (chapter 5), during the initial attachment phase, the e-DNA content of the EPS around the main body of the planktonic cells facilitated *K. aerogenes* attachment to the monazite<sup>34</sup>. The two-fold increase in e-DNA content of *K. aerogenes* during the mature biofilm stage (from day 2 to day 8) indicated that there was another important role for e-DNA in *K. aerogenes* biofilm on monazite. Previous studies have discussed the significant roles of e-DNA content in biofilm<sup>35</sup> with the most important role of this increased eDNA content in mature biofilm attributed to providing a better mechanical stability of the biofilm structure<sup>36,37</sup>. As mentioned in previous chapter, *K. aerogenes* biofilm formed on a very strong sheer force produced due to shaking at 140 rpm.

On the other hand, some studies reported that removing e-DNA from biofilms reduced the structural stability and resulted in eradication of the biofilm over time<sup>37-39</sup>, confirming the

important role of e-DNA in improving the structural stability of the biofilm. Additionally, it can also explain the sharp decrease in e-DNA content of the biofilm at dispersion stage where biofilm detaches from the surface. Not only biofilms with reduced e-DNA content are more prone to detachment due to shear force of the liquids around them<sup>37,40</sup>, but it is also shown that active removal of e-DNA is a strategy employed by some bacteria such as *Pseudomonas aeruginosa* to trigger dispersion of the biofilm<sup>41</sup>.

Quantitative analysis of *K. aerogenes* cells on monazite and xenotime ores showed that on average  $77.8 \pm 10.0$  % of the cells produced e-DNA when forming a biofilm on HGMO, however it was significantly less on xenotime with an average of  $39.9 \pm 3.2$  % cells. The lower e-DNA production on xenotime could be a physiological response to exposure to surfaces with different chemical composition<sup>42</sup>. Changing the e-DNA content in biofilm is also a physiologic response to toxic compounds for microorganisms such as antibiotics or heavy metals<sup>41,43</sup>. Xenotime contains heavy rare earths such as dysprosium whereas monazite mainly contains light rare earths such as lanthanum, cerium and neodymium, with both groups known to have toxic effects on microorganisms<sup>44,45</sup>. However, their toxicity level and the microbial response to different REEs has not been studied in *Klebsiella* genus or similar bacteria to the best of our knowledge.

#### **4. Conclusion**

Quantitative and qualitative studies of biofilms both have their own significance. One approach answers question regarding morphology and complexity, while the other provides a comparable measurement to evaluate the effects of different conditions or treatments. The quantitative study of *K. aerogenes* biofilm formation on monazite confirms the previously observed stages in our descriptive analysis. However, it showed that the maturity stage can

be divided into two sub-stages based on the significant difference in the percentage of the surface covered by biofilm. Development of mature biofilm by *K. aerogenes* started with a *K. aerogenes*' cells colonising mineral surface. At this point the coverage efficiency increased significantly compared to the initial attachment stage but the eDNA content is still at a similar level per  $\mu\text{m}^2$ . But over time it led to formation of a mature biofilm, covering about 80% of the mineral surface with a much higher e-DNA content per  $\mu\text{m}^2$ . The quantification of changes of e-DNA in the biofilms also showed significant variation at each stage. Quantitative analysis of biofilms opens new avenues in identifying potential targets for enhancing biofilm formation in some biotechnological applications such as bioleaching, or to eradicate them in some other ecosystems like biofilms that contain pathogens.

### **Acknowledgment**

AVA acknowledges support through a Parker CRC for Integrated Hydrometallurgy Solutions (established and supported under the Australian Government's Cooperative Research Centres Program). The authors acknowledge the Australian Research Council (ARC) for grant DP200103243. The authors acknowledge the Curtin Health Innovation Research Institute (CHIRI), Bentley, Western Australia, for providing the confocal microscopy facilities and the processing software, and the John de Laeter Centre for provision of the scanning electron microscope, focused ion beam SEM, TEM, and the image analysis facilities. The authors acknowledge The Institute for Geoscience Research for financial support through TIGeR Small Grants. The authors would like to acknowledge Jeanne Edmands (CHIRI), Michael Nesbit (CHIRI), and Elaine Miller (JDLC) for their technical support.

### **Authors' contribution**

AVA, designed and conducted the experiments, acquired, analysed and interpreted the data, and prepared the original draft of the manuscript. AVA, WR and XS designed, performed and analysed the focused ion beam methodology and analysis. AVA, and AD designed and analysed TEM samples. EW, MC, AK, AP, JE, HNK, and HF were involved in the research's conceptualisation and design, critical review of the data analysis and interpretation, and substantial review of the draft. EW, AP and JE were involved in funding acquisition. EW, AP, JE, AK, MC and HNK supervised the project. All authors were involved in review & editing.

### Competing interests

The authors declare no competing financial or non-financial interests.

### Data availability

The authors confirm that the data supporting the findings of this study are from the corresponding author [EW] on request.

### References

1. Costerton JW, Lewandowski Z, Caldwell DE, Korber DR, Lappin-Scott HM. Microbial biofilms. *Annu Rev Microbiol.* 1995;49:711-745. doi:10.1146/annurev.mi.49.100195.003431
2. Sauer K, Stoodley P, Goeres DM, et al. The biofilm life cycle: expanding the conceptual model of biofilm formation. *Nature Reviews Microbiology.* 2022;20(10):608-620. doi:10.1038/s41579-022-00767-0
3. Flemming H-C, van Hullebusch ED, Neu TR, et al. The biofilm matrix: multitasking in a shared space. *Nature Reviews Microbiology.* 2022;doi:10.1038/s41579-022-00791-0
4. Hitchens AP. Advantages of Culture Mediums Containing Small Percentages of Agar. *The Journal of Infectious Diseases.* 1921;29(4):390-407. [www.jstor.org/stable/30082437](http://www.jstor.org/stable/30082437)
5. Lloyd B. Bacteria of the Clyde Sea Area: A Quantitative Investigation. *Journal of the Marine Biological Association of the United Kingdom.* 1930;16(3):879-907. doi:10.1017/S0025315400073124
6. Waksman SA, Reuszer HW, Carey CL, Hotchkiss M, Renn CE. Studies on the Biology and Chemistry of the Gulf of Maine. III. Bacteriological Investigations of the Sea Water and Marine Bottoms. *Biological Bulletin.* 1933;64(2):183-205. doi:10.2307/1537228
7. Zobell CE, Anderson DQ. Observations on the Multiplication of Bacteria in Different Volumes of Stored Sea Water and the Influence of Oxygen Tension and Solid Surfaces. *Biological Bulletin.* 1936;71(2):324-342. doi:10.2307/1537438



8. Wu S, Zhang B, Liu Y, Suo X, Li H. Influence of surface topography on bacterial adhesion: A review (Review). *Biointerphases*. 2018;13(6):060801. doi:10.1116/1.5054057
9. Marshall KC. Planktonic Versus Sessile Life of Prokaryotes. In: Dworkin M, Falkow S, Rosenberg E, Schleifer K-H, Stackebrandt E, eds. *The Prokaryotes: Volume 2: Ecophysiology and Biochemistry*. Springer New York; 2006:3-15. doi:10.1007/0-387-30742-7\_1
10. Wilson C, Lukowicz R, Merchant S, et al. Quantitative and Qualitative Assessment Methods for Biofilm Growth: A Mini-review. *Res Rev J Eng Technol*. 2017;6(4),
11. Azeredo J, Azevedo NF, Briandet R, et al. Critical review on biofilm methods. *Critical Reviews in Microbiology*. 2017;43(3):313-351. doi:10.1080/1040841X.2016.1208146
12. Olson GJ, Brierley JA, Brierley CL. Bioleaching review part B: Progress in bioleaching: applications of microbial processes by the minerals industries. *Applied Microbiology and Biotechnology*. 2003;63(3):249-257. doi:10.1007/s00253-003-1404-6
13. Rohwerder T, Gehrke T, Kinzler K, Sand W. Bioleaching review part A: Progress in bioleaching: fundamentals and mechanisms of bacterial metal sulfide oxidation. *Applied Microbiology and Biotechnology*. 2003;63(3):239-248. doi:10.1007/s00253-003-1448-7
14. Dong H. Mineral-microbe interactions: a review. *Frontiers of Earth Science in China*. 2010;4(2):127-147. doi:10.1007/s11707-010-0022-8
15. Fathollahzadeh H, Becker T, Eksteen JJ, Kaksonen AH, Watkin ELJ. Microbial contact enhances bioleaching of rare earth elements. *Bioresource Technology Reports*. 2018-a;3:102-108. doi:<https://doi.org/10.1016/j.biteb.2018.07.004>
16. Corbett MK, Eksteen JJ, Niu X-Z, Watkin ELJ. Syntrophic effect of indigenous and inoculated microorganisms in the leaching of rare earth elements from Western Australian monazite. *Research in Microbiology*. 2018;169(10):558-568. doi:<https://doi.org/10.1016/j.resmic.2018.05.007>
17. Fathollahzadeh H, Eksteen JJ, Kaksonen AH, Watkin ELJ. Role of microorganisms in bioleaching of rare earth elements from primary and secondary resources. *Applied Microbiology and Biotechnology*. 2019;103(3):1043-1057. doi:10.1007/s00253-018-9526-z
18. van Alin A, Corbett MK, Fathollahzadeh H, et al. Biofilm formation on the surface of monazite and xenotime during bioleaching. *Microbial Biotechnology*. 2023;16(9):1790-1802. doi:<https://doi.org/10.1111/1751-7915.14260>
19. van Hoogstraten SWG, Kuik C, Arts JJC, Cillero-Pastor B. Molecular imaging of bacterial biofilms—a systematic review. *Critical Reviews in Microbiology*. 1-22. doi:10.1080/1040841X.2023.2223704
20. Cleaver L, Garnett JA. How to study biofilms: technological advancements in clinical biofilm research. *Front Cell Infect Microbiol*. 2023;13:1335389. doi:10.3389/fcimb.2023.1335389
21. Schlafer S, Meyer RL. Confocal microscopy imaging of the biofilm matrix. *Journal of Microbiological Methods*. 2017;138:50-59. doi:<https://doi.org/10.1016/j.mimet.2016.03.002>
22. Zhang R, Bellenberg S, Castro L, Neu TR, Sand W, Vera M. Colonization and biofilm formation of the extremely acidophilic archaeon *Ferroplasma acidiphilum*. *Hydrometallurgy*. 2014;150:245-252. doi:<https://doi.org/10.1016/j.hydromet.2014.07.001>
23. Wilking JN, Zaburdaev V, De Volder M, Losick R, Brenner MP, Weitz DA. Liquid transport facilitated by channels in *Bacillus subtilis* biofilms. *Proceedings of the National Academy of Sciences*. 2013;110(3):848-852. doi:10.1073/pnas.1216376110
24. Quan K, Hou J, Zhang Z, et al. Water in bacterial biofilms: pores and channels, storage and transport functions. *Critical Reviews in Microbiology*. 2022;48(3):283-302. doi:10.1080/1040841X.2021.1962802
25. McCutcheon J, Southam G. Advanced biofilm staining techniques for TEM and SEM in geomicrobiology: Implications for visualizing EPS architecture, mineral nucleation, and microfossil generation. *Chemical Geology*. 2018;498:115-127. doi:<https://doi.org/10.1016/j.chemgeo.2018.09.016>
26. Fager C, Röding M, Olsson A, et al. Optimization of FIB–SEM Tomography and Reconstruction for Soft, Porous, and Poorly Conducting Materials. *Microscopy and Microanalysis*. 2020;26(4):837-845. doi:10.1017/S1431927620001592

27. Mukhi M, Vishwanathan AS. Beneficial Biofilms: a Minireview of Strategies To Enhance Biofilm Formation for Biotechnological Applications. *Appl Environ Microbiol.* 2022;88(3):e0199421. doi:10.1128/aem.01994-21
28. Vyas N, Sammons RL, Addison O, Dehghani H, Walmsley AD. A quantitative method to measure biofilm removal efficiency from complex biomaterial surfaces using SEM and image analysis. *Scientific Reports.* 2016;6(1):32694. doi:10.1038/srep32694
29. Torkzadeh H, Cates EL. Biofilm growth under continuous UVC irradiation: Quantitative effects of growth conditions and growth time on intensity response parameters. *Water Research.* 2021;206:117747. doi:<https://doi.org/10.1016/j.watres.2021.117747>
30. Priester JH, Horst AM, Van De Werfhorst LC, Saleta JL, Mertes LAK, Holden PA. Enhanced visualization of microbial biofilms by staining and environmental scanning electron microscopy. *Journal of Microbiological Methods.* 2007;68(3):577-587. doi:<https://doi.org/10.1016/j.mimet.2006.10.018>
31. Peyton BM. Effects of shear stress and substrate loading rate on *Pseudomonas aeruginosa* biofilm thickness and density. *Water Research.* 1996;30(1):29-36. doi:[https://doi.org/10.1016/0043-1354\(95\)00110-7](https://doi.org/10.1016/0043-1354(95)00110-7)
32. Wang X, Chen S, Bi X, et al. Morphological image analysis of biofilm evolution with quantitative analysis in a moving bed biofilm reactor. *Science of The Total Environment.* 2023;856:159199. doi:<https://doi.org/10.1016/j.scitotenv.2022.159199>
33. Pereira J, Pang S, Borsje C, Sleutels T, Hamelers B, ter Heijne A. Real-time monitoring of biofilm thickness allows for determination of acetate limitations in bio-anodes. *Bioresource Technology Reports.* 2022;18:101028. doi:<https://doi.org/10.1016/j.biteb.2022.101028>
34. Van Alin A, Corbett MK, Fathollahzadeh H, et al. *Klebsiella aerogenes* Adhesion Behaviour during Biofilm Formation on Monazite. *Microorganisms.* 2023;11(5). doi:10.3390/microorganisms11051331
35. Groizeleau J, Rybtke M, Andersen JB, et al. The anti-cancerous drug doxorubicin decreases the c-di-GMP content in *Pseudomonas aeruginosa* but promotes biofilm formation. *Microbiology.* 2016;162(10):1797-1807. doi:<https://doi.org/10.1099/mic.0.000354>
36. Panlilio H, Rice CV. The role of extracellular DNA in the formation, architecture, stability, and treatment of bacterial biofilms. *Biotechnology and Bioengineering.* 2021;118(6):2129-2141. doi:<https://doi.org/10.1002/bit.27760>
37. Secchi E, Savorana G, Vitale A, Eberl L, Stocker R, Rusconi R. The structural role of bacterial eDNA in the formation of biofilm streamers. *Proceedings of the National Academy of Sciences.* 2022;119(12):e2113723119. doi:10.1073/pnas.2113723119
38. Yang Y, Li M, Zheng X, Ma H, Nerenberg R, Chai H. Extracellular DNA plays a key role in the structural stability of sulfide-based denitrifying biofilms. *Science of The Total Environment.* 2022;838:155822. doi:<https://doi.org/10.1016/j.scitotenv.2022.155822>
39. Schlafer S, Meyer RL, Dige I, Regina VR. Extracellular DNA Contributes to Dental Biofilm Stability. *Caries Research.* 2017;51(4):436-442. doi:10.1159/000477447
40. Okshevsky M, Regina VR, Meyer RL. Extracellular DNA as a target for biofilm control. *Current Opinion in Biotechnology.* 2015;33:73-80. doi:<https://doi.org/10.1016/j.copbio.2014.12.002>
41. Cherny KE, Sauer K. *Pseudomonas aeruginosa* Requires the DNA-Specific Endonuclease EndA To Degrade Extracellular Genomic DNA To Disperse from the Biofilm. *Journal of bacteriology.* 2019;201(18):e00059-00019. doi:10.1128/JB.00059-19
42. Zhang R, Bellenberg S, Neu TR, Sand W, Vera M. The Biofilm Lifestyle of Acidophilic Metal/Sulfur-Oxidizing Microorganisms. In: Rampelotto PH, ed. *Biotechnology of Extremophiles: Advances and Challenges.* Springer International Publishing; 2016:177-213. doi:10.1007/978-3-319-13521-2\_6
43. Brackman G, Breyne K, De Rycke R, et al. The Quorum Sensing Inhibitor Hamamelitannin Increases Antibiotic Susceptibility of *Staphylococcus aureus* Biofilms by Affecting Peptidoglycan Biosynthesis and eDNA Release. *Scientific Reports.* 2016;6(1):20321. doi:10.1038/srep20321
44. Malhotra N, Hsu HS, Liang ST, et al. An Updated Review of Toxicity Effect of the Rare Earth Elements (REEs) on Aquatic Organisms. *Animals (Basel).* 2020;10(9)doi:10.3390/ani10091663

45. Kurvet I, Juganson K, Vija H, et al. Toxicity of Nine (Doped) Rare Earth Metal Oxides and Respective Individual Metals to Aquatic Microorganisms *Vibrio fischeri* and *Tetrahymena thermophila*. *Materials*. 2017;10(7). doi:10.3390/ma10070754

## Supplementary files

### Statistical analysis of biofilm coverage measurement using CLSM

Tukey's multiple comparisons test	Mean Diff.	95.00% CI of diff.	Below threshold?	Summary	Adjusted P Value
4h vs. 8h	-0.6050	-33.16 to 31.95	No	ns	>0.9999
4h vs. 16h	-37.47	-70.02 to -4.919	Yes	*	0.0213
4h vs. 24h	-57.38	-89.93 to -24.83	Yes	***	0.0009
4h vs. Day 2	-60.49	-93.04 to -27.94	Yes	***	0.0006
4h vs. Day 3	-57.20	-89.75 to -24.64	Yes	***	0.0009
4h vs. Day 5	-53.48	-86.03 to -20.93	Yes	**	0.0016
4h vs. Day 8	-70.56	-103.1 to -38.00	Yes	***	0.0002
4h vs. Day 11	-10.80	-43.35 to 21.76	No	ns	0.9290
4h vs. Day 14	6.145	-26.41 to 38.70	No	ns	0.9980
8h vs. 16h	-36.87	-69.42 to -4.314	Yes	*	0.0236
8h vs. 24h	-56.78	-89.33 to -24.22	Yes	**	0.0010
8h vs. Day 2	-59.89	-92.44 to -27.33	Yes	***	0.0006
8h vs. Day 3	-56.59	-89.14 to -24.04	Yes	**	0.0010
8h vs. Day 5	-52.88	-85.43 to -20.32	Yes	**	0.0018
8h vs. Day 8	-69.95	-102.5 to -37.40	Yes	***	0.0002
8h vs. Day 11	-10.19	-42.74 to 22.36	No	ns	0.9476
8h vs. Day 14	6.750	-25.80 to 39.30	No	ns	0.9961
16h vs. 24h	-19.91	-52.46 to 12.64	No	ns	0.4006
16h vs. Day 2	-23.02	-55.57 to 9.531	No	ns	0.2519
16h vs. Day 3	-19.73	-52.28 to 12.83	No	ns	0.4110
16h vs. Day 5	-16.01	-48.56 to 16.54	No	ns	0.6453
16h vs. Day 8	-33.09	-65.64 to -0.5335	Yes	*	0.0456
16h vs. Day 11	26.68	-5.876 to 69.23	No	ns	0.1382
16h vs. Day 14	43.62	11.06 to 76.17	Yes	**	0.0076
24h vs. Day 2	-3.110	-35.66 to 29.44	No	ns	>0.9999
24h vs. Day 3	0.1850	-32.37 to 32.74	No	ns	>0.9999
24h vs. Day 5	3.900	-28.65 to 36.45	No	ns	>0.9999
24h vs. Day 8	-13.18	-45.73 to 19.38	No	ns	0.8218
24h vs. Day 11	46.59	14.03 to 79.14	Yes	**	0.0047
24h vs. Day 14	63.53	30.97 to 96.08	Yes	***	0.0004
Day 2 vs. Day 3	3.295	-29.26 to 35.85	No	ns	>0.9999
Day 2 vs. Day 5	7.010	-25.54 to 39.56	No	ns	0.9949
Day 2 vs. Day 8	-10.07	-42.62 to 22.49	No	ns	0.9511
Day 2 vs. Day 11	49.70	17.14 to 82.25	Yes	**	0.0029
Day 2 vs. Day 14	66.64	34.08 to 99.19	Yes	***	0.0003
Day 3 vs. Day 5	3.715	-28.84 to 36.27	No	ns	>0.9999
Day 3 vs. Day 8	-13.36	-45.91 to 19.19	No	ns	0.8115
Day 3 vs. Day 11	46.40	13.85 to 78.95	Yes	**	0.0048
Day 3 vs. Day 14	63.34	30.79 to 95.89	Yes	***	0.0004
Day 5 vs. Day 8	-17.08	-49.63 to 15.48	No	ns	0.5749
Day 5 vs. Day 11	42.69	10.13 to 75.24	Yes	**	0.0088
Day 5 vs. Day 14	59.63	27.07 to 92.18	Yes	***	0.0007
Day 8 vs. Day 11	59.76	27.21 to 92.31	Yes	***	0.0007
Day 8 vs. Day 14	76.70	44.15 to 109.3	Yes	****	<0.0001
Day 11 vs. Day 14	16.94	-15.61 to 49.49	No	ns	0.5838

Test details	Mean 1	Mean 2	Mean Diff.	SE of diff.	q	DF
4h vs. 8h	11.51	12.11	-0.6050	8.223	0.1041	10
4h vs. 16h	11.51	48.98	-37.47	8.223	6.444	10
4h vs. 24h	11.51	68.89	-57.38	8.223	9.869	10
4h vs. Day 2	11.51	72.00	-60.49	8.223	10.40	10
4h vs. Day 3	11.51	68.70	-57.20	8.223	9.837	10
4h vs. Day 5	11.51	64.99	-53.48	8.223	9.198	10
4h vs. Day 8	11.51	82.06	-70.56	8.223	12.13	10
4h vs. Day 11	11.51	22.30	-10.80	8.223	1.857	10
4h vs. Day 14	11.51	5.360	6.145	8.223	1.057	10
8h vs. 16h	12.11	48.98	-36.87	8.223	6.340	10
8h vs. 24h	12.11	68.89	-56.78	8.223	9.764	10
8h vs. Day 2	12.11	72.00	-59.89	8.223	10.30	10
8h vs. Day 3	12.11	68.70	-56.59	8.223	9.733	10
8h vs. Day 5	12.11	64.99	-52.88	8.223	9.094	10
8h vs. Day 8	12.11	82.06	-69.95	8.223	12.03	10
8h vs. Day 11	12.11	22.30	-10.19	8.223	1.753	10
8h vs. Day 14	12.11	5.360	6.750	8.223	1.161	10
16h vs. 24h	48.98	68.89	-19.91	8.223	3.424	10
16h vs. Day 2	48.98	72.00	-23.02	8.223	3.959	10
16h vs. Day 3	48.98	68.70	-19.73	8.223	3.392	10
16h vs. Day 5	48.98	64.99	-16.01	8.223	2.753	10
16h vs. Day 8	48.98	82.06	-33.09	8.223	5.690	10
16h vs. Day 11	48.98	22.30	26.68	8.223	4.588	10
16h vs. Day 14	48.98	5.360	43.62	8.223	7.501	10
24h vs. Day 2	68.89	72.00	-3.110	8.223	0.5349	10
24h vs. Day 3	68.89	68.70	0.1850	8.223	0.03182	10
24h vs. Day 5	68.89	64.99	3.900	8.223	0.6707	10
24h vs. Day 8	68.89	82.06	-13.18	8.223	2.266	10
24h vs. Day 11	68.89	22.30	46.59	8.223	8.012	10
24h vs. Day 14	68.89	5.360	63.53	8.223	10.93	10
Day 2 vs. Day 3	72.00	68.70	3.295	8.223	0.5667	10
Day 2 vs. Day 5	72.00	64.99	7.010	8.223	1.206	10
Day 2 vs. Day 8	72.00	82.06	-10.07	8.223	1.731	10
Day 2 vs. Day 11	72.00	22.30	49.70	8.223	8.547	10
Day 2 vs. Day 14	72.00	5.360	66.64	8.223	11.46	10
Day 3 vs. Day 5	68.70	64.99	3.715	8.223	0.6389	10
Day 3 vs. Day 8	68.70	82.06	-13.36	8.223	2.298	10
Day 3 vs. Day 11	68.70	22.30	46.40	8.223	7.980	10
Day 3 vs. Day 14	68.70	5.360	63.34	8.223	10.89	10
Day 5 vs. Day 8	64.99	82.06	-17.08	8.223	2.937	10
Day 5 vs. Day 11	64.99	22.30	42.69	8.223	7.341	10
Day 5 vs. Day 14	64.99	5.360	59.63	8.223	10.25	10
Day 8 vs. Day 11	82.06	22.30	59.76	8.223	10.28	10
Day 8 vs. Day 14	82.06	5.360	76.70	8.223	13.19	10
Day 11 vs. Day 14	22.30	5.360	16.94	8.223	2.913	10

## Statistical analysis of biofilm coverage measurement using SEM

Tukey's multiple comparisons test	Mean Diff.	95.00% CI of diff.	Below threshold?	Summary	Adjusted P Value
Initial attachment vs. Colonisation	-26.03	-38.93 to -13.12	Yes	***	0.0002
Initial attachment vs. Mature biofilm	-79.12	-92.03 to -66.22	Yes	****	<0.0001
Initial attachment vs. Biofilm dispersion	-1.652	-14.56 to 11.25	No	ns	0.9826
Colonisation vs. Mature biofilm	-53.09	-66.00 to -40.19	Yes	****	<0.0001
Colonisation vs. Biofilm dispersion	24.37	11.47 to 37.28	Yes	***	0.0003
Mature biofilm vs. Biofilm dispersion	77.47	64.56 to 90.37	Yes	****	<0.0001

Test details	Mean 1	Mean 2	Mean Diff.	SE of diff.	q	DF
Initial attachment vs. Colonisation	3.119	29.15	-26.03	4.511	8.160	16
Initial attachment vs. Mature biofilm	3.119	82.24	-79.12	4.511	24.81	16
Initial attachment vs. Biofilm dispersion	3.119	4.771	-1.652	4.511	0.5181	16
Colonisation vs. Mature biofilm	29.15	82.24	-53.09	4.511	16.65	16
Colonisation vs. Biofilm dispersion	29.15	4.771	24.37	4.511	7.642	16
Mature biofilm vs. Biofilm dispersion	82.24	4.771	77.47	4.511	24.29	16



## Statistical analysis of eDNA production

Tukey's multiple comparisons test	Mean Diff.	95.00% CI of diff.	Below threshold?	Summary	Adjusted P Value
Initial attachment vs. Colonisation	-6.0	-142 to 130	No	ns	0.9993
Initial attachment vs. Mature biofilm	-93	-186 to -0.62	Yes	*	0.0482
Initial attachment vs. Biofilm dispersion	13	-98 to 123	No	ns	0.9878
Colonisation vs. Mature biofilm	-87	-209 to 34	No	ns	0.2083
Colonisation vs. Biofilm dispersion	19	-117 to 154	No	ns	0.9791
Mature biofilm vs. Biofilm dispersion	106	13 to 198	Yes	*	0.0225

Test details	Mean 1	Mean 2	Mean Diff.	SE of diff.	q	DF
Initial attachment vs. Colonisation	86	92	-6.0	47	0.18	16
Initial attachment vs. Mature biofilm	86	179	-93	32	4.1	16
Initial attachment vs. Biofilm dispersion	86	74	13	39	0.46	16
Colonisation vs. Mature biofilm	92	179	-87	42	2.9	16
Colonisation vs. Biofilm dispersion	92	74	19	47	0.55	16
Mature biofilm vs. Biofilm dispersion	179	74	106	32	4.6	16

**Chapter Five**  
***Klebsiella aerogenes* adhesion behaviour during  
biofilm formation on monazite**

**Notes on chapter five:**

1- Some parts of this chapter were originally submitted as the milestone two and three at Curtin University. As per Curtin University regulation, all the data from milestone one, milestone two, and milestone three, including the writing pieces can be used in the final thesis with or without any changes.

2- This chapter is published at Microorganisms Journal, MDPI.

First published: 18 May 2023

Doi: <https://doi.org/10.3390/microorganisms11051331>.

## Abstract

The adsorption behaviour of micro-organisms during the initial attachment stage of biofilm formation affects subsequent stages. The available area for attachment and the chemophysical properties of a surface affect microbial attachment performance. This study focused on the initial attachment behaviour of *Klebsiella aerogenes* on monazite by measuring the ratio of planktonic against sessile subpopulations (P:S ratio), and the potential role of extracellular DNA (eDNA). eDNA production, effects of physicochemical properties of the surface, particle size, total available area for attachment, and the initial inoculation size on the attachment behaviour were tested. *K. aerogenes* attached to monazite immediately after exposure to the ore; however, the P:S ratio significantly ( $p = 0.05$ ) changed in response to the particle size, available area, and inoculation size. Attachment occurred preferentially on larger-sized ( $\sim 50 \mu\text{m}$ ) particles, and either decreasing the inoculation size or increasing the available area further promoted attachment. Nevertheless, a portion of the inoculated cells always remained in a planktonic state. *K. aerogenes* produced lower eDNA in response to the changed surface chemical properties when monazite was replaced by xenotime. Using pure eDNA to cover the monazite surface significantly ( $p \leq 0.05$ ) hindered bacterial attachment due to the repulsive interaction between the eDNA layer and bacteria.

**Keywords:** biofilm; *Klebsiella aerogenes*; monazite; extracellular DNA (eDNA); surface attachment

## 1. Introduction

In each ecosystem, micro-organisms live in two distinctive subpopulations: free-living or planktonic cells and sessile or biofilm-forming cells <sup>1</sup>. Biofilms are a universal feature of microbial life and, from a human point of view, can be both detrimental and advantageous depending on the circumstances <sup>2</sup>. Biofilms can pose a great health risk by causing more severe symptoms in patients and can lead to significantly higher resistance to antimicrobials <sup>3,4</sup>. In the oil and gas industry, biofilms have been documented as causing biofouling and corrosion. In contrast, biofilms are advantageous for industries benefiting from biotechnological processes such as bioleaching, biofuel cells, bioremediation, and biofertilisers <sup>5</sup>. Prevention or promotion of biofilm formation and development requires detailed understanding of the underlying mechanisms as well as the intrinsic and extrinsic factors affecting the effectiveness of attachment. Adherence to a surface is one of the main capacities of the sessile subpopulation; regardless, attachment to a solid surface is not a requirement to form a biofilm <sup>6,7</sup>. In surface-attached biofilms, only the bottom layer of the cells are directly attached to a substratum <sup>6</sup>. However, in non-surface biofilm, microbial cells are attached to each other and form flocs of biofilm. Some bacteria, such as *Pseudomonas aeruginosa*, establish chronic infections by forming biofilm flocs <sup>8,9</sup> and in natural environments, marine particles gel and form clumps during cyanobacteria and microalgal blooms <sup>9</sup> which are some examples of non-surface-attached biofilms. Micro-organisms are capable of attaching to any surface in general, both biotic such as micro-organisms and abiotic such as minerals, with the ability to attach or detach from a surface in response to the environmental conditions <sup>2</sup>. These cycles of attachment and detachment can promote either planktonic or biofilm lifestyle over the other. Each of these populations has a functional role in the ecosystem, and changes in the planktonic to sessile (P:S) ratio in any ecosystem can

change the microbial functions in that ecosystem <sup>5,10</sup>. This simple yet significant feature of microbial life can be employed to engineer microbial functions to demote or promote certain activities, such as bioleaching, bioremediation, biodegradation, bioconversion, or antimicrobial resistance.

Bioleaching has attracted enormous interest in the mining industry in recent decades <sup>11</sup> and despite the numerous studies on the significance of planktonic and biofilm subpopulations in bioleaching of sulfide minerals, the translation of this research for promoting or demoting either of these subpopulations to whole processes is still in its infancy. In the bioleaching of rare earth elements (REE) bearing phosphate minerals, very limited data is available regarding the behaviour of either the planktonic or sessile populations within these systems. Previous studies on the bioleaching of monazite <sup>12,13</sup> refer to microbial attachment, and van Alin et al. (2023) is the only study addressing biofilm formation on monazite and xenotime. Fathollahzadeh et al. (2018) reported that the bioleaching rate is higher when microorganisms are in contact with the mineral surface <sup>12</sup>. Our previous studies have shown that *K. aerogenes* biofilm formation occurs in three characteristic stages <sup>14</sup>. Initial attachment occurred during the first 4–8 h of microbial exposure to the ore surface (1), followed by (2) colonisation of the surface, with a mature biofilm maintained for several days, and (3) finally, cells detached from the ore surface, marking the last stage, biofilm dispersion <sup>14</sup>. Physical imperfections of REE-phosphate ore surfaces enhanced microbial attachment and, as a result, biofilm formation by *K. aerogenes*. However, in contrast, the mineralogy or chemical composition of the ores' surface neither promoted nor demoted microbial attachment or biofilm formation <sup>14</sup>.

As the initial attachment can be critical in determining the progression to biofilm development, promoting a higher sessile or a planktonic lifestyle <sup>2,5</sup> can strongly influence the



bioleaching process. Extrinsic factors, such as the chemophysical condition of a surface, environmental conditions, the size and shape of the available particles, and the total number of the planktonic cells per given space of attachment, can all contribute to the successful attachment and colonisation of a surface<sup>2</sup>. Additionally, intrinsic factors, such as extracellular appendages or the composition of extracellular polymeric substances (EPS) produced by microbes, can change the attachment behaviour<sup>2,15,16</sup>. EPS is known to play a critical role in mediating the initial adhesion of planktonic cells to surfaces, aiding in the stability of the biofilm structure, and providing safety from environmental stresses<sup>15-17</sup>. In bioleaching, EPS increases the interface reaction in favour of leaching<sup>18</sup>. EPS also plays another critical role by providing a microenvironment where some of the bioleaching processes, such as dissolution or complexation, occur, hence acting as a micro-biochemical reactor<sup>19,20</sup>. The detailed role of EPS as a microenvironment for bioleaching is described elsewhere<sup>20,21</sup>. In brief, a 50–100 nm space between the outer membrane of micro-organisms and the surface layer of metal-containing ores is filled with EPS. This EPS matrix acts as a biochemical bridge connecting the surface of the substratum and microbes, where micro-organisms release or store the biochemical agents for bioleaching, such as organic/inorganic acids, metal reducing/oxidising enzymes, chemical shuttles capable of reducing or oxidising metals or some other elements, such as sulfur, and bio-chemical shuttles capable of complex formation with the dissolved metals<sup>21,22</sup>. Extracellular DNA (eDNA) is one of the main components of EPS and is involved in many of its functions, such as initial attachment and the integrity and stability of the biofilm structure<sup>17,23,24</sup>. The presence of eDNA can play critical roles in the attachment of micro-organisms to sulfide minerals<sup>25</sup> or metallic surfaces<sup>26</sup> and largely influences microbial behaviour at the surface of the ore<sup>24,27,28</sup>. Whether eDNA promotes the microbial attachment, for example, *Shewanella chilikensis* attachment to steel<sup>26</sup>, or demotes it, as in *Caulobacter*

*crescentus* attachment to polystyrene and polyvinylchloride <sup>28</sup>, seems to be specific to each type of micro-organism and surface.

In our previous studies on monazite, the changes in pH, phosphate concentration, and released REE were tested using different phosphate solubilizing micro-organisms <sup>13,29</sup>, and *K. aerogenes* had the highest phosphate dissolution rate and REE bioleaching performance from monazite <sup>30</sup>. We also explained the role of planktonic and sessile subpopulations of *K. aerogenes* during the bioleaching of monazite <sup>12,31</sup> and biofilm formation <sup>14</sup>. The effect of differences in chemical and physical properties of the monazite ore surface on *K. aerogenes* attachment and biofilm formation has been discussed by van Alin et al. (2023). The current study aims to shed light on the very first stage of *K. aerogenes* biofilm formation on monazite surfaces. The effects of both the physical and chemical properties of the ores' surfaces on attracting or deflecting either planktonic or sessile populations were studied. Moreover, eDNA production, its role, and the mechanism of action in *K. aerogenes* attachment were studied.

## **2. Methods**

### **2.1. Minerals**

A high-grade monazite ore (Mt Weld Mine, Laverton, Western Australia) and xenotime beneficiation concentrate (mineral beneficiation is a process by which valuable constituents of an ore are concentrated by means of a physical separation process; the sample was donated by Louis de Klerk, Northern Minerals, WA, Australia) were sterilised by gamma irradiation at 50 kGy for 11 h (ChemCentre, Bentley, Western Australia) to inactivate indigenous micro-organisms. Monazite has high concentrations of light rare earth metals and xenotime has a high concentration of heavy rare earth metals (Tables S1–S3), as determined

by X-ray diffraction (XRD), and inductively coupled plasma mass spectrometry (ICP-MS). The main minerals in the high-grade monazite were monazite in the form of (Ce, La, Pr, Nd, Sm)PO<sub>4</sub> and florencite Al<sub>3</sub>(Ce, La, Nd, Sm, Ca)(PO<sub>4</sub>)<sub>2</sub>(OH)<sub>6</sub>, and main minerals in the xenotime beneficiation concentrate were quartz (SiO<sub>2</sub>) and aluminosilicate minerals (Al<sub>2</sub>SiO<sub>5</sub>), and xenotime (Y, Dy, ER, Yb, Gd)PO<sub>4</sub>.

## **2.2. Microorganism and Culture Conditions**

All biological experiments were performed using *Klebsiella aerogenes* ATCC 13048. The National Botanical Research Institute's phosphate medium (NBRIP (g L<sup>-1</sup>): 5 MgCl<sub>2</sub>(H<sub>2</sub>O)<sub>6</sub>, 0.25 MgSO<sub>4</sub>(H<sub>2</sub>O)<sub>7</sub>, 0.2 KCl, 0.1 NH<sub>4</sub>SO<sub>4</sub>, 2 KH<sub>2</sub>PO<sub>4</sub>, 30 glucose, pH 6.2 ± 0.4) was used as the growth medium. The cultures were incubated at 30 °C and 120 rpm.

## **2.3. Cell Enumeration with Flow Cytometry**

A flow cytometry assay for enumerating bacteria was used in this study, as previously described <sup>14</sup>, with some modifications. Bacterial samples were fixed in 2% glutaraldehyde solution (Sigma, Roedermark, Germany) and assessed in a log-fold dilution series. First 100 µL of the fixed bacterial sample was stained with 1 µL of SYTO 85 (5 mM; Invitrogen, Waltham, MA, USA) for 20 min at room temperature in the dark. Then bacteria were suspended in a final volume of 1 mL of 0.22 µM filter-sterile NBRIP medium and kept on ice in the dark before acquisition on a 4-laser (405 nm, 488 nm, 561 nm and 640 nm) Attune NxT Acoustic Focusing Flow Cytometer (Invitrogen, USA) equipped with side-scatter filters on BL-1 (488 nm) and VL-1 (405 nm) detectors, to aid in small particle discrimination. The cytometer was set to acquire a volume of 50 µL at a flow rate of 25 µL min<sup>-1</sup> and was set to trigger at an SSC-H threshold value of 0.1 × 10<sup>3</sup>. True bacterial events were discriminated from electronic noise using negative controls that contained NBRIP only or NBRIP and SYTO 85 in the absence of bacteria.

A primary gate was used to identify bacterial events through 405 nm and 488 nm SSC profiles, followed by SYTO 85 fluorescence. The concentration of bacteria in each sample was derived by dividing the number of SYTO 85<sup>+</sup> events by the acquisition volume. Data was exported from the Attune NxT software as FCS3.0 files and analysed in FlowJo v10.7 (BD Biosciences, Franklin Lakes, NJ, USA).

## **2.4. Bacterial and eDNA Attachment Behaviour**

Bacterial and eDNA attachment behaviour were studied using monazite and *K. aerogenes* cells and/or DNA.

### **2.4.1. Effects of the Inoculum Size and Available Surface Area for Attachment on Bacterial Adsorption Behaviour**

The bacterial adsorption to the mineral surfaces was studied in terms of the ratio of planktonic cells against sessile (attached) cell subpopulations. The number of the planktonic cells of *K. aerogenes* was determined using flow cytometry at different experimental settings. The number of the attached cells was calculated by deducting the enumerated planktonic cells from the initial inoculum size ( $1 \times 10^7$  cell mL<sup>-1</sup>) and used to calculate the planktonic:sessile population ratio (P:S ratio).

The microbial attachment to a surface was dependent on two variables: the initial number of bacteria and the initial available surface area for attachment. The effects of changing any of these two variables on the attachment behaviour were studied (1) using various inoculation sizes ( $1 \times 10^6$ ,  $1 \times 10^7$ ,  $5 \times 10^7$  cell mL<sup>-1</sup>) with a fixed available area for attachment (1% monazite slurry), and (2) changing the total available area for attachment in terms of monazite slurry percentage (0.5, 1, 2, 5, and 10%) with a fixed inoculation size of  $1 \times 10^7$  cells mL<sup>-1</sup>. Samples were taken at 1, 10, 30, 60, 120, 180, and 240 min and immediately fixed with

glutaraldehyde (final concentration of 2%) and refrigerated until analysis. This experiment was performed in triplicate. The attachment performance of cells on glass surfaces was studied in conical flasks using phosphate-deficient NBRIP and NBRIP amended with dissolved phosphate. These samples were also used as the growth controls. Since phosphate is essential for microbial growth, the sample with no phosphate did not support growth of *K. aerogenes*. The control sample with phosphate, allowed for growth and cell division. The effects of microbial growth (cell division) was determined by comparing the cell number of these two samples. Attachment to monazite was tested by adding 1% monazite to the flask using phosphate-free NBRIP medium.

#### **2.4.2. Effects of the Surface Chemical Properties on Bacterial Adsorption Behaviour**

DNA was extracted from a 10 mL aliquot of a pure culture of *K. aerogenes* grown in NBRIB media after harvesting cells by centrifugation at 10,000× *g*. The supernatant was discarded, and the cell pellet was used for DNA extraction using DNeasy Kit (Qiagen, Hilden, Germany), following the manufacturer's procedure. The DNA quantity was measured using Qubit kit (Invitrogen, USA), following the manufacturer's guidelines. The extracted DNA was used as a pure source of *K. aerogenes* eDNA to evaluate its attachment of eDNA and its impact on bacterial attachment.

The eDNA attachment on monazite surfaces was assessed at concentrations of 5, 25, 50, and 100 ng mL<sup>-1</sup> in glass flasks containing NBRIP medium in the absence of bacterial cells. The attachment of eDNA to glass flask surfaces was used as the control, also in the absence of bacterial cells. The effects of attached eDNA on *K. aerogenes* adsorption behaviour were studied using monazite ore with and without preconditioning with eDNA. In the absence of bacteria, monazite surface was initially exposed to various concentrations (0, 5, 25, 50 and 100 ng) of eDNA for 60 min. Then, *K. aerogenes* was added to the flasks at an initial cell

number of  $1 \times 10^7$  cell  $\text{mL}^{-1}$  and the flasks were incubated at 30 °C and 120 rpm for four hours. Samples were taken at 1, 10, 30, 60, 120, 180, and 240 min and immediately fixed with glutaraldehyde (final concentration of 2%) and refrigerated until enumeration of the planktonic population. The experiment was performed in triplicate.

## **2.5. Live Imaging and Evaluation of eDNA Production**

To visualise the eDNA production during all three stages of biofilm formation, confocal laser scanning microscopy (CLSM) was performed with live bacteria attached to monazite minerals. Genomic DNA was stained with Hoechst 33342 (AATBio, Sunnyvale, CA, USA) and eDNA was stained with DiTO-1 (AATBio, USA), a highly specific fluorochrome dye that stains DNA external to the cell walls of living cells, i.e., eDNA. Samples were taken from bioleaching experiments conducted in conical flasks (phosphate-free NBRIP medium, 1% slurry of monazite,  $10^7$  cells  $\text{mL}^{-1}$  inoculum size) with monazite grains extracted at 4, 8, 16, 24 h, and 2, 3, 5, 8, 11, 14 days after inoculation. The samples (1 mL) were collected in microtubes and allowed to settle at room temperature for 1 min. The supernatant containing the planktonic subpopulation was discarded, and the solids were gently washed with sterile NBRIP medium to remove any remaining planktonic or loosely attached cells from the minerals. Samples were stained with the two fluorochromes ( $1 \mu\text{L mL}^{-1}$ ) for 20 min and then, transferred to a  $\mu$ -Slide 2 Well Glass Bottom microscope slide (ibidi, Gräfelfing, Germany). CLSM images were collected in Z-stack mode with 3.5–7 micron intervals ( $\times 10$  and  $\times 20$  objectives) or  $\leq 1$  micron intervals ( $\times 40$  and  $\times 100$  objectives). The images are shown in Maximum Intensity Projections mode or Maximum Intensity Projections in 3D. To further visualise eDNA production, the acquired Z-stack CLSM images were reanalysed in IMARIS v 9.7 (Oxford Instruments, Oxford, UK). The surface of monazite samples was reconstructed using the “Surface” tool, and the



cells were modelled using “Spots” tool following IMARIS v 9.7 user guidelines to provide a better 3D view of both cells and the surface.

## **2.6. Fluorescent Microscopy**

In order to study bacterial behaviour during the first minutes (1–10 min) of *K. aerogenes* contact with high-grade monazite ore, images from bacterial attachment were recorded using Olympus BX51 upright microscope. Pre-stained cells with Hoechst 33342 (1  $\mu\text{L mL}^{-1}$ , 20 min) were added to 10 mg of each mineral sample in microtubes at  $10^7$  cells  $\text{mL}^{-1}$ , gently mixed, and immediately studied using WB: blue excitation (wide band) filter (Ex 465/15, FT 500, LP 515).

## **2.7. Measurement of Surface Electrical Potential**

A ZS ZEN3600 Zetasizer (Dispersion Technology Software v5.10, 2008, Malvern, UK) and low-volume plastic disposable cuvettes (ZEN112, Malvern, UK) were used to measure the surface electrical potential <sup>32</sup>.

## **2.8. Statistics**

Data preparation for statistical analysis was conducted in Microsoft Excel (2016) and GraphPad Prism v.9. Two-way ANOVA was used for comparison, and a  $p$ -value  $< 0.05$  was considered significant. The statistical analysis, including calculated  $p$ -values, is provided as supplementary material.

## **3. Results**

### **3.1. Attachment Behaviour in Response to the Monazite Particle Size**

*K. aerogenes* attachment to monazite occurred immediately after adding the microbial culture to the system (Figure 1). Depending on the particle size, the microbial behaviour was different. *K. aerogenes* cells were mainly gathered around small (approximately  $\leq 10 \mu\text{m}$ ) and

mid-size ( $\sim 20 \mu\text{m}$ ) monazite particles while they were attached to the surface of larger monazite particles ( $\sim 50 \mu\text{m}$ ) (Figure 1).

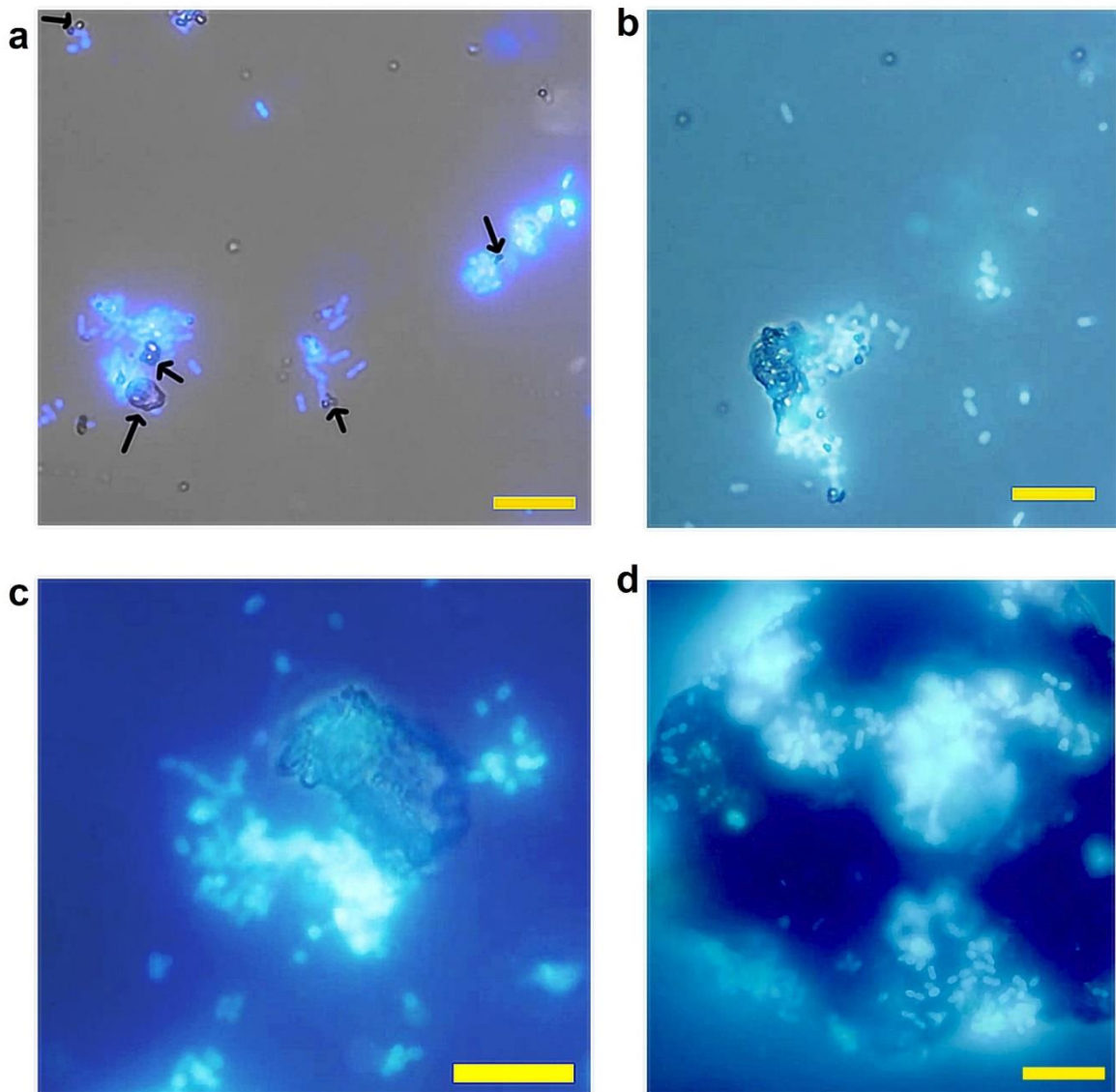


**Figure 1.** Epifluorescence microscope images of *Klebsiella aerogenes* on high grade monazite ore over the first 10 min after inoculation. (a) Bacterial cells gathering around small particles of approximately  $\leq 10 \mu\text{m}$ , (b, c) partially attached and partially gathered around larger ore particles of  $\sim 10\text{--}20 \mu\text{m}$  (d) and bacterial cells mainly attached to the surface of larger particles ( $\geq 50 \mu\text{m}$ ). Black arrows point to the small particles. Black arrows point to the small particles. Scale bar  $20 \mu\text{m}$ .

### 3.2. Cell Attachment Behaviour in Response to the Nutrient Amendment and Surface

#### Material Available for Attachment

In control samples (no monazite), glass was provided as the only available surface for attachment. The absence (phosphate ( $\text{PO}_4$ ) deficient control) or presence (dissolved  $\text{PO}_4$  control) of phosphate did not cause a significant change in the attachment of the bacteria on glass with an inoculation size of  $1 \times 10^7$  cell  $\text{mL}^{-1}$  ( $p \geq 0.05$ , Figure 2a). Moreover, there were no significant changes in the cell number ( $p \geq 0.05$ ), signifying no or very slow reproduction rate for the *K. aerogenes* during the first 4 h of inoculation. Bacteria rapidly and consistently attached themselves to the glass over the first 30 min. The P:S ratio of the two control samples decreased from 9:1 (~10% attachment efficiency) in the first minute to approximately 1:1 (~50% attachment efficiency) after 30 min. Then, the attachment efficiency gradually decreased to 40% (P:S ratio of 1.5:1) by two hours and remained relatively stable until the end of the experiment (4 h). In the presence of monazite (1% slurry,  $1 \times 10^7$  cell  $\text{mL}^{-1}$ ), the attachment efficiency was relatively higher than the glass controls and improved to ~60% of the initial inoculated cells (a P:S ratio of ~1:1.5) after 30 min, compared to ~50% efficiency of the control samples. The planktonic subpopulation continued to decrease to ~25% of the initial inoculum size (a P:S ratio of ~1:3) by the end of the experiment (Figure 2a).

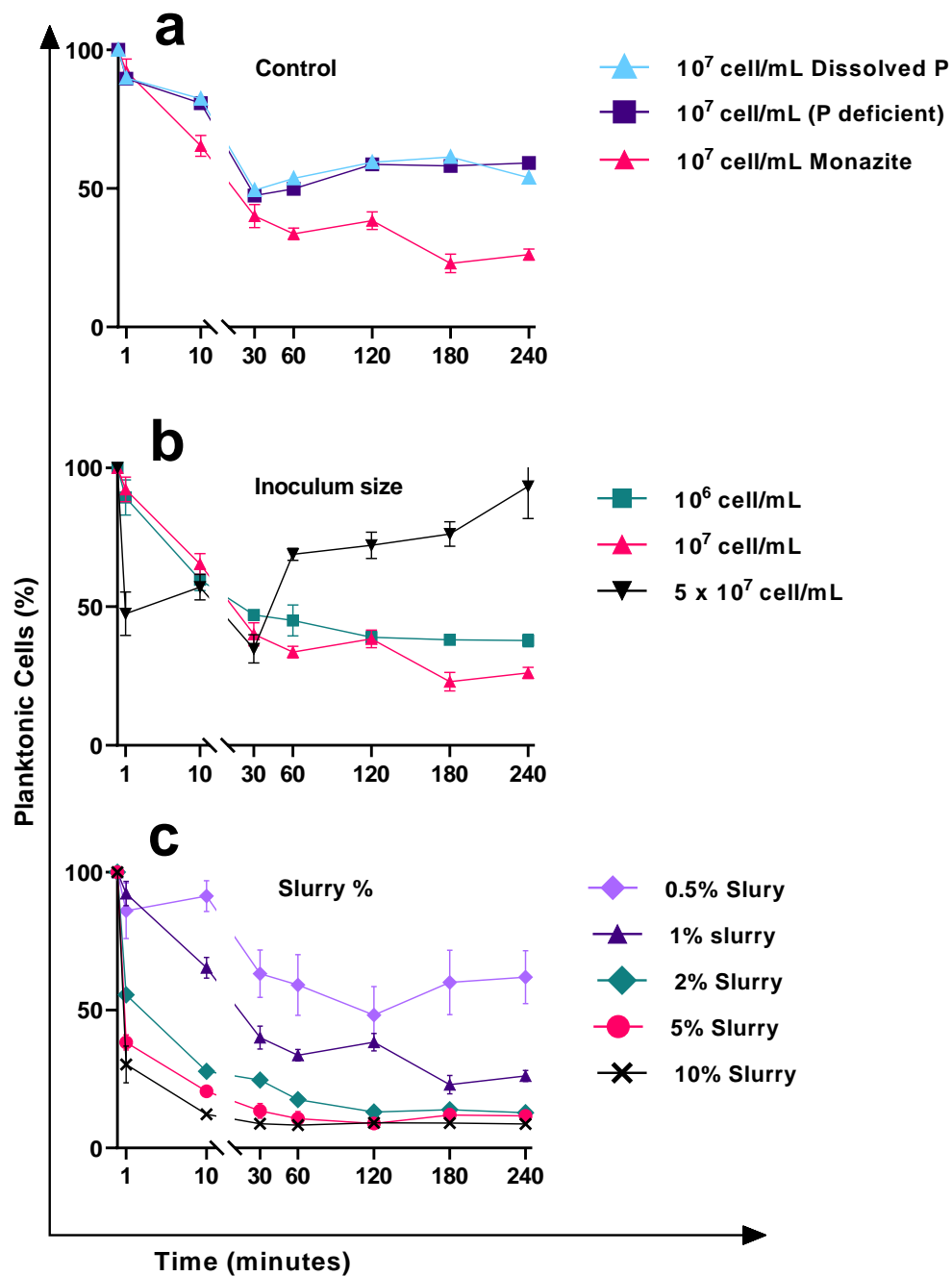


**Figure 2.** The percentage of planktonic *Klebsiella aerogenes* during the early attachment phase of biofilm formation on glass and high-grade monazite ore. (a) Attachment to glass surface in NBRIP medium at an initial inoculum size of  $1 \times 10^7$  cell  $\text{mL}^{-1}$ , with (dissolved P) or without (P deficient) phosphate in the medium, and to both glass and monazite using 1% slurry monazite as the only source of phosphate and (b) with varying initial inoculum sizes

with 1% slurry of monazite, and (c) with varying amounts of monazite at a fixed initial inoculum size of  $1 \times 10^7$  cell mL<sup>-1</sup>. The depicted data are bacterial cells enumerated by flow cytometry.

### 3.3. Cell Attachment Behaviour in Response to the Changes in the Initial Inoculum Size

In the presence of a fixed amount of monazite (1% slurry), varying the cell numbers significantly changed the efficiency of the attachment ( $p \leq 0.05$ ) (Figure 2b). The attachment behaviour of *K. aerogenes* to monazite at a lower inoculum size of  $1 \times 10^6$  cell mL<sup>-1</sup> was fairly similar to that of the  $1 \times 10^7$  cell mL<sup>-1</sup>, but at a slightly lower efficiency. At the very first minute of exposure to monazite, the number of attached cells with an initial  $1 \times 10^6$  cell mL<sup>-1</sup> was similar to when  $1 \times 10^7$  cell mL<sup>-1</sup> was used (P:S ratio of 9:1). The attachment efficacy improved over time, from approximately 10% to 60%. In contrast, increasing the inoculum size to  $5 \times 10^7$  cell mL<sup>-1</sup> changed the attachment behaviour of *K. aerogenes*. The planktonic subpopulation decreased to half within the very first minute of exposure to monazite, resulting in a P:S ratio of 1:1 compared to 9:1 (10% attachment ratio) for the other samples (Figure 2b, black line). The attachment efficiency fluctuated to ~40% at 10 min and then 60% after 30 min. However, the attachment behaviour of the bacteria changed after this time point. Two hours after exposure to monazite, the attachment efficacy of both  $1 \times 10^6$  and  $1 \times 10^7$  cell mL<sup>-1</sup> inoculum sizes improved to ~60%, an increased P:S ratio of 1:1.5 (Figure 2b, red and green lines). It remained unchanged to the end of the experiment for the lower inoculum size, while it continued to improve for the initial inoculum size of  $1 \times 10^7$  cell mL<sup>-1</sup> (75% attachment efficiency, an enhanced P:S ratio of 1:3 after 4 h). In contrast to these two groups, the attachment behaviour of *K. aerogenes* at a higher initial inoculum size of  $5 \times 10^7$  cell mL<sup>-1</sup> drastically changed after 30 min. The attachment behaviour reversed and largely decreased

from ~66% (a P:S ratio of 1:2), to ~25% (a P:S ratio of 3:1) at 60 min. This sharp drop continued to ~7% (a P:S ratio of 13:1) by the end of the experiment.

### **3.4. The Effects of the Available Area for Attachment on the Attachment Efficiency**

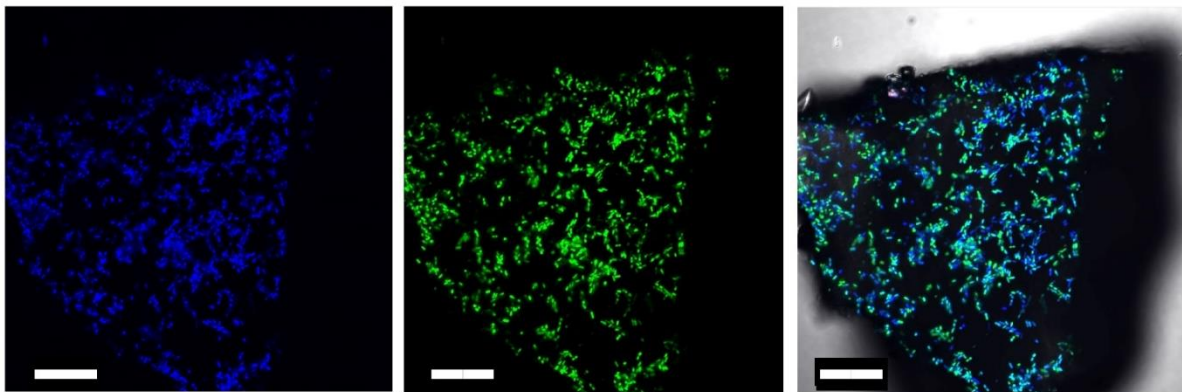
The inoculum size is not the only influencing factor changing the attachment efficiency. In the presence of monazite, at a constant inoculum size of  $1 \times 10^7$  cells mL<sup>-1</sup>, varying the available area for attachment in terms of changing the slurry percentage of monazite resulted in different attachment behaviours (Figure 2c). While the general pattern was a continuous decrease in the planktonic subpopulation, the attachment efficiency was significantly different ( $p \leq 0.05$ ). Attachment behaviour of the bacteria using higher amounts of monazite (2, 5, and 10%, slurry, Figure 2c) was fairly similar; sharp attachment efficiency was observed during the very first minute of exposure to monazite, which was significantly higher than what was observed for 1% slurry ( $p \leq 0.05$ ). The attachment efficiency of samples with  $\geq 1\%$  monazite slurry significantly improved over time ( $p \leq 0.05$ ) and stabilised at a P:S ratio of ~1:3, approximately 75% attachment efficiency 3 h after inoculation. Increasing the slurry to 2, 5, and 10 percent significantly improved the attachment efficiency in terms of both attachment efficiency (P:S ratio) and time ( $p \leq 0.05$ ). For 2% and 5% slurry, approximately 87% and 89% attachment efficiency were achieved after 2 h, and using 10% slurry, 91% attachment efficiency was recorded just an hour after inoculation. In contrast, halving the available monazite (0.5% slurry), resulted in lower attachment efficiency with gradual improvement to a P:S ratio of 1:1 (50% attachment efficiency) two hours after inoculation, followed by a reversal of the attachment behaviour in favour of the planktonic subpopulation, where the attachment efficiency dropped to 40% by the end of the experiment.



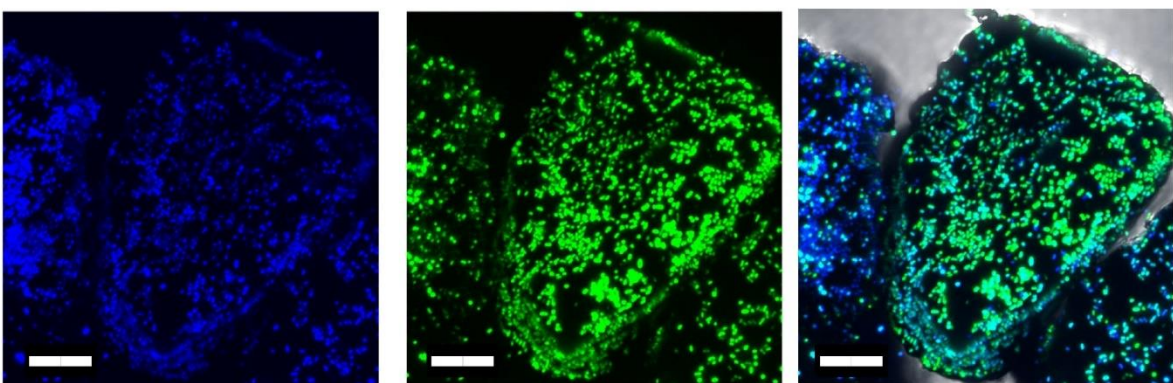
### **3.5. eDNA Production by *K. aerogenes***

The CLSM live imaging of *K. aerogenes* biofilm demonstrates eDNA production in all three stages of biofilm development (Figure 3); however, not all cells were involved in the production of eDNA. Moreover, the reconstructed models showed that eDNA production differed between different mineral grains. A major proportion of cells attached to some of the mineral grains produced eDNA (blue-green spheres), while for the other grains, very limited eDNA production was detected (blue-only spheres, Figure 4). Therefore, different mineralogy could explain the different patterns of eDNA production. Since CLSM is not capable of determining the mineral composition of different grains in the sample, another phosphate mineral (xenotime) was used to test this hypothesis. The CLSM images clearly showed that eDNA production by *K. aerogenes* cells was different on xenotime (Figure 5). The bacteria produced much less eDNA on xenotime compared to high-grade monazite.

### Stage 1- Initial attachment



### Stage 2- Formation of mature biofilm



### Stage 3- Dispersion (Detachment)

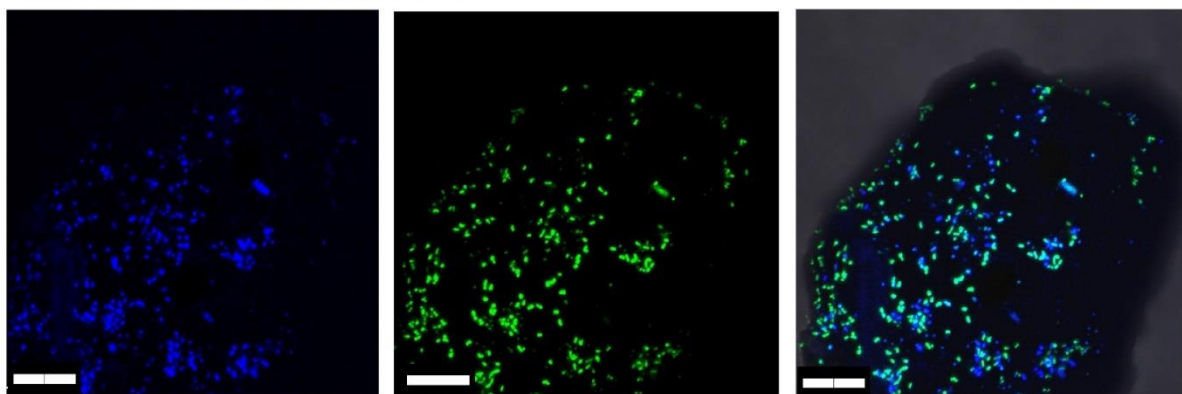


**Figure 3.** Confocal laser scanning microscopy (CLSM) images of *Klebsiella aerogenes* on the surface of high-grade monazite ore show eDNA (green fluorescent dye) presence at the three stages of biofilm development. Scale bar = 10  $\mu\text{m}$

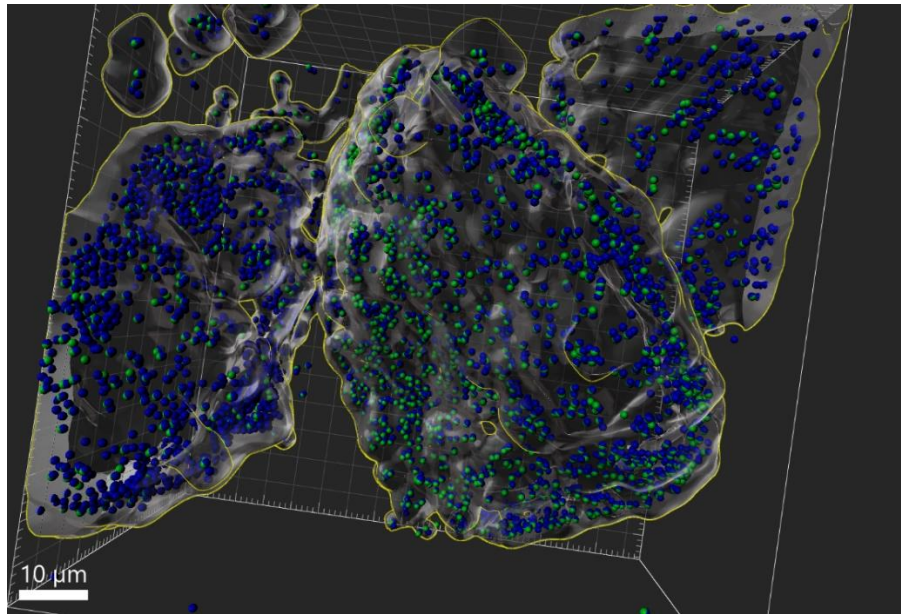


**Figure 4.** Three-dimensional model of *Klebsiella aerogenes* attachment to the surface of high-grade monazite ore reconstructed using CLSM Z-stack images in IMARIS software (v4). Genomic DNA identification was obtained using Hoechst 33324. In the reconstructed 3D models, cells that were positive for Hoechst 33324 were depicted as a blue sphere. eDNA production was studied using DiTO-1, an eDNA-specific stain (shown in green). Each sphere represents a single bacterial cell. Cells with a positive signal for eDNA were depicted as blue-green spheres against blue-only spheres, which represent no eDNA production.

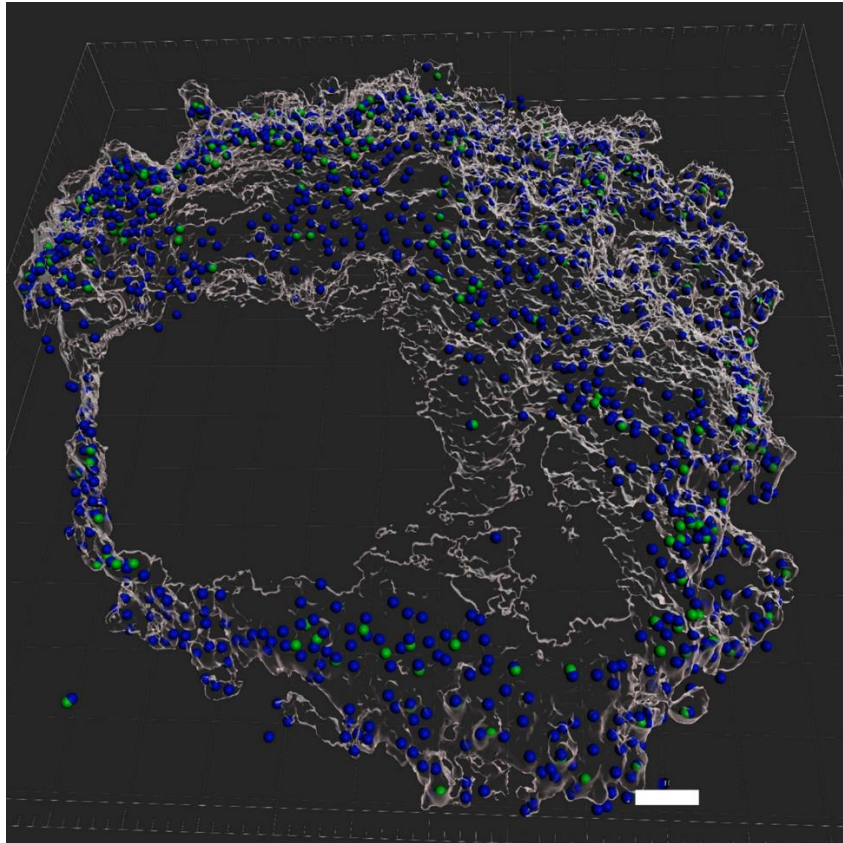


**Figure 5.** The 3D model of *Klebsiella aerogenes* attachment to xenotime surface reconstructed in IMARIS software (v 9.7). Scale bar: 10  $\mu\text{M}$ . For info on green and blue spheres, please see the caption for Figure 4.

### **3.6. Role of eDNA in Early Attachment and Interaction with the Surface**

The eDNA interaction with the surface of minerals was tested using DNA extracted from *K. aerogenes*. In the control sample, where no bacteria were present, the DNA extracted from *K. aerogenes* adhered to the glass surface (Figure 6). By adding monazite to the system, significantly higher attachment was recorded for all tested eDNA concentrations (5–100  $\text{ng mL}^{-1}$ ). eDNA attachment to the glass surface followed a relatively similar pattern (Figure 6), with an improved attachment rate to the glass surface in the beginning followed by a gradual detachment of the adsorbed eDNA, reaching a relatively stable value. In contrast, in the presence of 1% monazite slurry, the general pattern of eDNA adsorption to the surface was a

sharp adsorption rate to the surface over the first 60 min of exposure, followed by continuous attachment until a major proportion (~90–95%) of eDNA was attached to the surface. Using 100 ng mL<sup>-1</sup> eDNA, the eDNA progressively adsorbed to the surface and reached 97% efficiency by the end of the experiment.

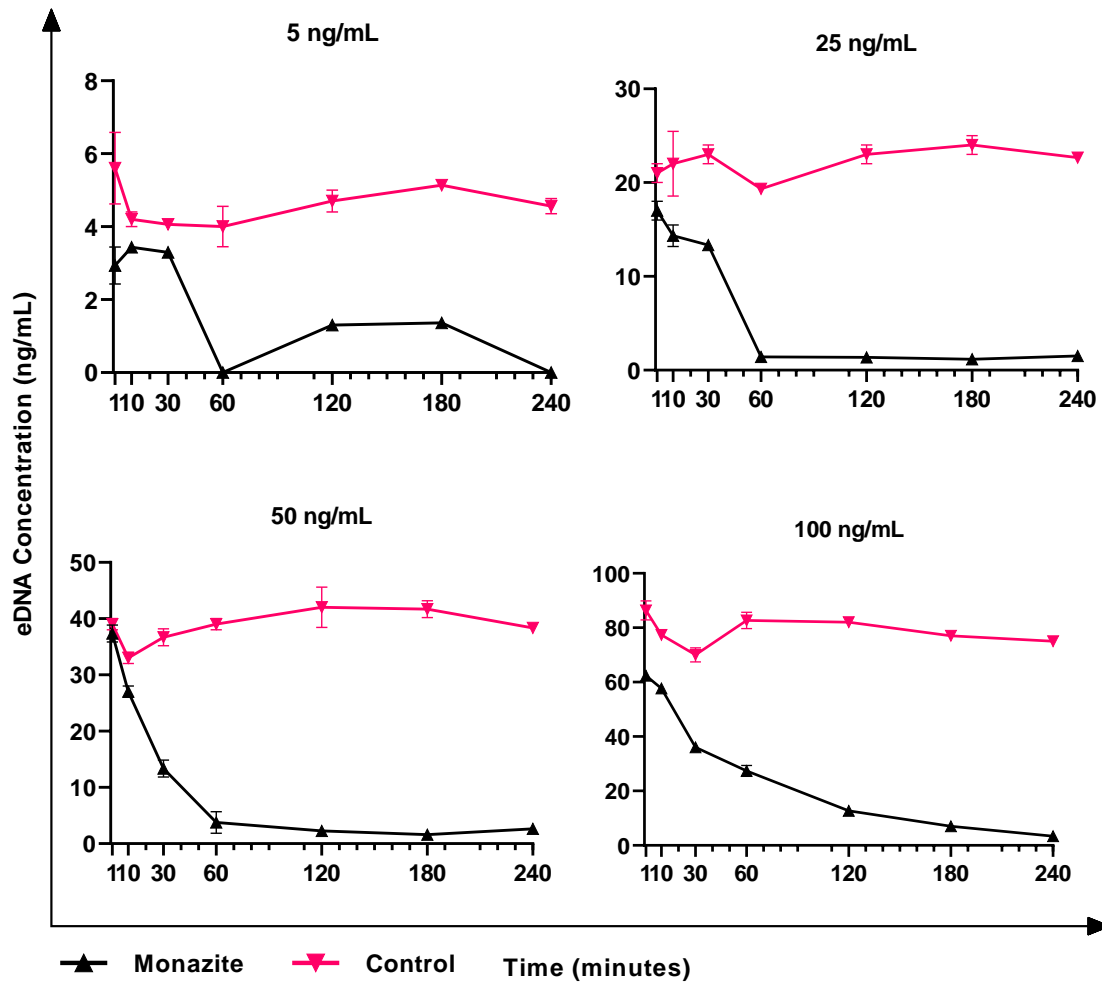


**Figure 6.** The adsorption of pure eDNA of *Klebsiella aerogenes* to glass (marked as control), and monazite and glass (marked as monazite), in the absence of microbial cells. The attachment efficiency is represented by the eDNA concentration remaining in NBRIP medium.

### 3.7. Effects of the Surface Preconditioning with eDNA on Attachment of *K. aerogenes* Cells

To understand the role of eDNA in *K. aerogenes* attachment to the surface, monazite grains were preconditioned with eDNA prior to bacterial inoculation. The pretreatment of the monazite surface with eDNA drastically changed the attachment efficiency of *K. aerogenes* (Figure 7). In the control sample (absence of eDNA at an initial cell concentration of  $1 \times 10^7$  cell mL<sup>-1</sup> and 1% slurry monazite), cells continually attached to the surface over the four hours of the test period. During the first 10 min of inoculation, regardless of the amount of eDNA used for preconditioning, all of the preconditioned samples showed a higher attachment of *K. aerogenes* compared to the control flask. In the control flask, *K. aerogenes* attachment efficiency increased steadily over the course of the experiment. However, looking at the general pattern, the preconditioning of the surface with eDNA reduced the attachment efficiency from 30 min onward (Figure 7, green, black, blue, and purple lines). Preconditioning showed an inhibitory effect on the attachment efficiency, with a noticeable difference in the measured cell numbers between the three biological replicas at each time point and inconsistent attachment efficiency between different time points. This signifies a larger adsorption/detachment dynamic in preconditioned samples, therefore resulting in significant fluctuations in attachment efficacy within and between each sampling time point.



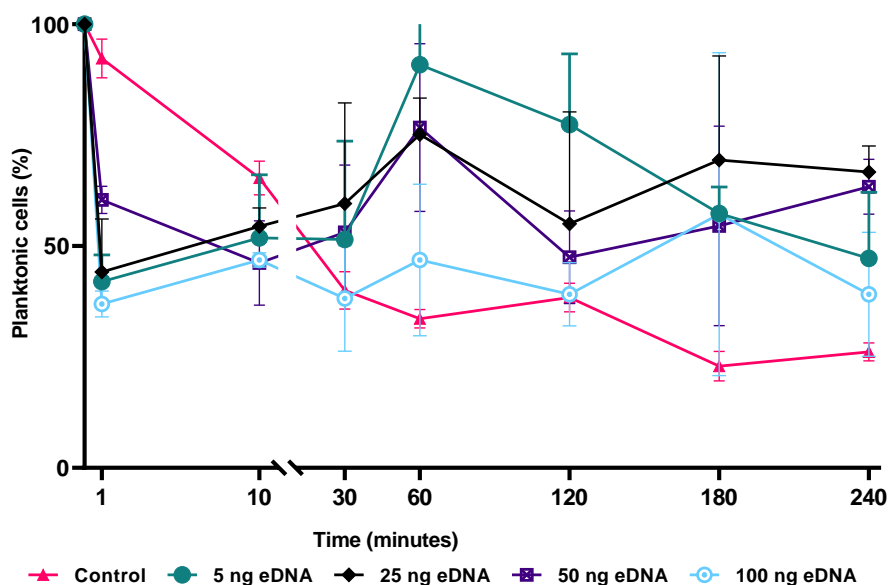


**Figure 7.** The effect of surface preconditioning with eDNA on the early attachment of *Klebsiella aerogenes* to monazite. The experiment was conducted in NBRIP media with 1% slurry of high-grade monazite ore. Bacterial cells were enumerated using flow cytometry.

#### 4. Discussion

In our previous study, it was shown that *K. aerogenes* biofilm formation on phosphate minerals (monazite and xenotime) occurred in three distinctive stages<sup>14</sup>. The formation of mature biofilm has biotechnological advantages in industries such as bioleaching. As attachment to the surface and biofilm formation are the most important prerequisites of contact bioleaching<sup>12</sup>, it is, therefore, important to understand this process to further improve and advance bioleaching systems.

The attachment efficiency of *K. aerogenes* to monazite ore surfaces was affected by several factors such as particle size, eDNA attachment, initial cell number, and total available area for attachment (Figures 1, 2, and 7), as has been seen in other systems<sup>2,33</sup>. In general, extrinsic



factors, such as nutrient availability in the liquid environment, particle size, which can directly affect nutrient accessibility from an ore, flow and shear forces, pH, ionic strength, physical properties of the surface such as topological imperfections, and chemical properties or mineralogy of the surface, play a role in microbial attachment.

In this study, *K. aerogenes* attachment to monazite occurred immediately after inoculation. However, the attachment behaviour was different in response to the particle size of monazite. For larger particles of monazite ( $\geq 50 \mu\text{m}$ ) a notable number of bacteria were attached to the surface over the first minutes of microbial inoculation, whereas for medium-sized ( $\sim 10\text{--}20 \mu\text{m}$ ) and particularly small particles ( $\leq 10 \mu\text{m}$ ) bacteria preferred to gather around the particles (Figure 1). Due to their small size, the microscopic particles offer a rapid dissolution rate compared to larger ore particles, thus providing easier access to the nutrient content of the ore, such as phosphate and trace elements<sup>33</sup>.

During the early attachment stage of the biofilm formation, a greater proportion of cells remained in the planktonic state in the absence of monazite, either with or without soluble phosphate, as compared to that observed in the presence of monazite without phosphate amendment. The adsorption-detachment dynamics of the *K. aerogenes* to and from the glass surface were maintained significantly ( $p \leq 0.05$ ) in favour of the planktonic subpopulation (40% attachment) with and without phosphate in the media. In contrast, the attachment efficiency of *K. aerogenes* was significantly ( $p \leq 0.05$ ) enhanced when cells were exposed to monazite, and by the end of the experiment, the attachment/detachment dynamic stabilised in favour of the sessile subpopulation (75% attachment). Therefore, the surface monazite significantly promoted the sessile subpopulation of *K. aerogenes* compared to a glass surface ( $p \leq 0.05$ ). Adding monazite to the system provided the cells with a source of phosphate, which could attract bacterial cells to the surface through chemotaxis<sup>2</sup>. In addition, higher attachment

efficiency could be due to the nature of the physical surface properties of the glass and monazite. A glass surface provides a fairly smooth interface, while the surface of the high-grade monazite ore is rough and rich in imperfections (Figure S1). The attachment and colonisation of *K. aerogenes*<sup>14</sup> were more favourable in the presence of surface physical imperfections, such as cracks or grooves. Similar results have been reported for *Acidithiobacillus ferrooxidans* attachment to pyrite<sup>19</sup>. Therefore, a surface with more physical irregularities can attract more planktonic cells to attach to and colonise it.

In addition to the physical or chemical quality of a surface, the total available area on the surface altered the attachment efficiency and behaviour of *K. aerogenes*. A planktonic lifestyle is favoured by a higher cell number or a smaller available area. By halving the available space for attachment (decrease from 1% to 0.5% slurry), a lower attachment efficiency was observed. However, using more monazite (2, 5, and 10% slurry) in the system led to a significantly higher ( $p \leq 0.05$ ) rate of attachment in a shorter time. Moreover, altering the rate of inoculation changed the attachment behaviour when the available area remained unchanged. By varying cell numbers, significant ( $p \leq 0.05$ ) changes in the efficiency and/or the attachment behaviour of *K. aerogenes* were recorded. Although, by lowering the inoculum size, the attachment efficiency decreased, the general pattern was that of promoting higher attachment over time. In contrast, using higher cell density reversed the attachment behaviour in favour of a planktonic lifestyle.

Regardless of the initial cell numbers or the available area for attachment, the planktonic and sessile subpopulations will reach equilibrium. At a lower available area or a higher cell density (inoculum size), the equilibrium of planktonic vs. sessile subpopulations shifted towards higher attachment, whereas using a smaller initial inoculum size or providing a higher available area for attachment and colonisation shifted the equilibrium towards the sessile

lifestyle. Nevertheless, a portion of the cells remained in the planktonic state even in a very high available area for attachment (10% monazite slurry). In brief, factors such as competition for space, nutrients, and safety from environmental stresses contribute to the switch from a planktonic lifestyle to a sessile lifestyle and vice versa. For bioleaching activities, biofilm formation (i.e., sessile lifestyle) is more favourable, as it results in higher dissolution rates of rare earths from monazite ore <sup>12</sup>. Therefore, changes in the P:S ratio and resulting attachment behaviours affect the microbial stability and bioleaching performance. While a higher attachment efficiency can result in timely and optimal biofilm formation, it has been demonstrated that a sharp decrease in planktonic cell number or removal of this population can significantly ( $p \leq 0.05$ ) change the bioleaching efficiency <sup>34</sup>. Therefore, considering the higher efficiencies reported for contact bioleaching of monazite using *K. aerogenes* <sup>12</sup>, this case study indicates that using relatively larger particle sizes with rough surfaces, a higher slurry concentration, or an optimised microbial inoculum size to prompt biofilm formation, promotes contact leaching.

In addition to the chemo-physical conditions of the surface and the environmental conditions, intrinsic microbial properties such as their extracellular appendages and the composition of their EPS can affect attachment efficiency <sup>2,6,35</sup>. The CLSM images (Figure 3) clearly showed that *K. aerogenes* cells produced a significant amount of extracellular DNA, with production detected in all three stages of biofilm formation. Further examination of the eDNA production using a reconstructed 3D model (Figure 4) of the ore grains demonstrated that while the monazite particle in the middle harboured a population of *K. aerogenes* with the majority of the cells producing eDNA, only a small proportion of the attached cells on the other grains produced eDNA. Therefore, eDNA production can vary between individual grains, which could be due to differences in the chemical or mineralogical composition of a mineral surface. To

explore this hypothesis, *K. aerogenes* biofilm formation was examined on xenotime. Lower amounts of eDNA were detected in the biofilm of *K. aerogenes* on xenotime, with fewer bacterial cells producing eDNA (Figure 5) in comparison to that produced on monazite (Figure 4). It has been demonstrated that the chemical composition of the mineral surface can affect the attachment behaviour of micro-organisms. *A. ferrooxidans* showed lower attachment affinity to pyrite when grown on elemental sulfur <sup>19</sup>, However, our previous study demonstrated that, *K. aerogenes* showed no selectivity in attachment based on chemical composition or mineralogy on the surface <sup>12,14</sup>. This is in contrast to the current study, which demonstrated that surface mineralogy changed the composition of *K. aerogenes* EPS (Figures 4 and 5) by producing differing amounts of eDNA when grown on xenotime and monazite. According to the observed general patterns based on the CLSM study (Figure S2), when *K. aerogenes* was exposed to light rare earth metals, such as lanthanum, cerium, neodymium, and samarium in monazite ore, it produced a high amount of eDNA. However, using Xenotime ore, which contains heavy rare earth metals, such as dysprosium, yttrium, and ytterbium, exposed this bacterium to a different chemical condition and resulted in remarkably lower eDNA production.

Furthermore, as eDNA is known to play a critical role in initiating or mediating the attachment of planktonic cells to a surface <sup>17</sup>, the cell-surface interactions (both attractive and repulsive) were examined as a way to explain the changes in bioleaching efficiencies. Extracted DNA of *K. aerogenes* was used as the eDNA source, and in the absence of bacteria, the eDNA partially attached to the glass; however, it was almost fully attached to the high-grade monazite ore surface at all of the tested concentrations. This demonstrates that eDNA can facilitate *K. aerogenes* attachment to the surface, as it has been shown for some other microorganisms such as *Pseudomonas*, *Sulfobacillus*, and *Shewanella* <sup>17,25,26</sup>. Tuck et al. (2022) suggested that

preconditioning a metal (steel) surface with eDNA layer promoted *Shewanella chilikensis* attachment; however, preconditioning of a monazite surface with an eDNA layer hindered *K. aerogenes* attachment (Figure 7). The effect of surface preconditioning with an eDNA on the early attachment of *Klebsiella aerogenes* to monazite. The experiment was conducted in NBRIP media with a 1% slurry of high-grade monazite ore. Bacterial cells were enumerated using flow cytometry. The measured electrical potential of each particle (monazite, *K. aerogenes*, and preconditioned monazite with eDNA) showed that the preconditioning of monazite with the eDNA layer resulted in a more negatively charged surface, from -10 mV to -15 mV. On the other hand, *K. aerogenes* has a very negative surface charge (measured at -15 mV). Therefore, bacterial cells were constantly repulsed from the surface of the eDNA-preconditioned monazite (Figure S3) and were incapable of retaining a strong attachment. High variation was observed between the 3 biological replicates of each sample at each time point (Figure 7). Therefore, although Figure 6 clearly shows that eDNA facilitates *K. aerogenes* attachment to the monazite surface, releasing eDNA in a liquid environment to form an eDNA layer on the surface is not a valid mechanism of action. In contrast to Tuck et al. (2022), who showed that released eDNA by *Shewanella* assisted attachment of this micro-organism to the surface by forming an eDNA layer on the surface, forming such a layer by *K. aerogenes* resulted in repulsion of the cells from the monazite surface. Hence, another mechanism involving eDNA allows for the initial attachment. The most potential mechanism could be the production of eDNA alongside other extracellular polymers, such as polysaccharides and proteins, which assists *K. aerogenes* adherence to the surface<sup>17,20,25</sup>.

## 5. Conclusion

The initial attachment stage of *K. aerogenes* to the monazite surface can affect colonisation of the surface. Larger particle sizes with more physical imperfections attract more planktonic cells to the surface of monazite compared to small particles. The attachment behaviour analysis examined in terms of the dynamics of planktonic and sessile equilibrium showed a higher attachment to monazite compared to the control glass surface, in which lowering the initial cell concentration shifted the equilibrium of the two subpopulations towards a sessile lifestyle, as did increasing the total available area. eDNA is an important part of the EPS of the *Klebsiella aerogenes* biofilm matrix. While no difference was recorded in the eDNA production of *K. aerogenes* in response to physical properties of the surface, such as physical imperfections, it responded to changes in the chemical properties of the surface (surface mineralogy). *K. aerogenes* produced more eDNA on monazite, which contains light rare earth metals, compared to that produced when exposed to the heavy rare earth content of Xenotime. Analysing eDNA adherence to glass and monazite showed a significantly improved attachment to monazite, implying that eDNA can assist bacterial attachment to the surface during the initial attachment stage of biofilm formation on monazite. Preconditioning the monazite surface with pure eDNA extracted from *K. aerogenes* repulsed bacterial attachment to the surface, suggesting that eDNA assists bacterial attachment as part of the EPS but not by forming an eDNA layer masking the mineral surface.

### Supplementary Materials:

The following supporting information can be downloaded at: [www.mdpi.com/xxx/s1](http://www.mdpi.com/xxx/s1), Figure S1. Scanning electron microscopy (SEM) image of the smooth surface of glass (a) vs the rough surface of the high-grade monazite ore (b); Figure S2. The general pattern of eDNA production

on monazite (a) and xenotime (b) based on confocal laser scanning microscopy (CLSM). The green fluorescent represents eDNA (eDNA) and blue represent genomic DNA (gDNA). More eDNA was produced using monazite. Yellow circle marks the xenotime grain used for 3D reconstruction in Figure 5; Figure S3. The interaction of *Klebsiella aerogenes* cells with surface pre-conditioned with Edna. Table S1: the XRD and phase identification of the high-grade monazite ore conducted by John de Laeter Centre, Curtin University. The COD ID refers to the phase's identification number in the COD database (<http://www.crystallography.net/>, access date: 28 Sep. 2021); Table S2. The inductively coupled plasma mass spectrometry (ICP-MS) analysis of high-grade monazite ore conducted by Bureau Veritas, Perth, Australia; Table S3. The XRF (X-ray fluorescence) and ICP-MS composition of xenotime beneficiation concentrate (reported by the provider, Northern Minerals), Statistical data.

#### **Author Contributions:**

A.V.A., designed and conducted the experiments, acquired, analysed and interpreted the data, and original draft preparation. E.W., M.K.C., A.H.K., A.P., J.E. and H.F. were involved in the research's conceptualisation and design, critical review of the data analysis and interpretation, and substantial review of the draft. E.W., A.P. and J.E. were involved in funding acquisition. E.W., A.P., J.E., A.H.K. and M.K.C. supervised the project. A.V.A. and M.C.T. developed the flow cytometry methodology and data analysis. All authors were involved in review & editing. All authors have read and agreed to the published version of the manuscript.

#### **Funding**

A.V.A. acknowledges support through a Parker CRC for Integrated Hydrometallurgy Solutions (established and supported under the Australian Government's Cooperative Research



Centres Program). The authors acknowledge the Australian Research Council (ARC) for grant DP200103243. The authors acknowledge the Curtin Health Innovation Research Institute (CHIRI), Bentley, Western Australia, for providing the confocal microscopy and flow cytometry facilities, and the John de Laeter Centre for providing of the X-ray diffraction. The authors acknowledge the Institute for Geoscience Research for financial support through TIGeR Small Grants. The authors would like to acknowledge Jeanne Edmands (CHIRI), Michael Nesbit (CHIRI), and Elaine Miller (JDLC) for their technical support.

#### **Data Availability Statement**

The authors confirm that the data supporting the findings of this study are available within the article's supplementary materials or from the corresponding author [E.W.] on request.

#### **Conflicts of Interest**

The authors declare no competing financial or nonfinancial interests.

**Disclaimer/Publisher's Note:** The statements, opinions and data contained in all publications are solely those of the individual author(s) and contributor(s) and not of MDPI and/or the editor(s). MDPI and/or the editor(s) disclaim responsibility for any injury to people or property resulting from any ideas, methods, instructions or products referred to in the content.

## References

1. Sauer K, Stoodley P, Goeres DM, et al. The biofilm life cycle: expanding the conceptual model of biofilm formation. *Nature Reviews Microbiology*. 2022;20(10):608-620. doi:10.1038/s41579-022-00767-0
2. Berne C, Ellison CK, Ducret A, Brun YV. Bacterial adhesion at the single-cell level. *Nature Reviews Microbiology*. 2018;16(10):616-627. doi:10.1038/s41579-018-0057-5
3. Sharma D, Misba L, Khan AU. Antibiotics versus biofilm: an emerging battleground in microbial communities. *Antimicrobial Resistance & Infection Control*. 2019;8(1):76. doi:10.1186/s13756-019-0533-3
4. Römling U, Kjelleberg S, Normark S, Nyman L, Uhlin BE, Åkerlund B. Microbial biofilm formation: a need to act. *Journal of Internal Medicine*. 2014;276(2):98-110. doi:<https://doi.org/10.1111/joim.12242>
5. Li Q, Sand W, Zhang R. Enhancement of biofilm formation on pyrite by *Sulfobacillus thermosulfidooxidans*. *Minerals*. 2016;6(3):71.
6. Flemming HC, Wingender J, Szewzyk U, Steinberg P, Rice SA, Kjelleberg S. Biofilms: an emergent form of bacterial life. *Nat Rev Microbiol*. 2016;14(9):563-575. doi:10.1038/nrmicro.2016.94
7. Wille J, Coenye T. Biofilm dispersion: The key to biofilm eradication or opening Pandora's box? *Biofilm*. 2020;2:100027. doi:<https://doi.org/10.1016/j.biofilm.2020.100027>
8. Alhede M, Kragh KN, Qvortrup K, et al. Phenotypes of Non-Attached *Pseudomonas aeruginosa* Aggregates Resemble Surface Attached Biofilm. *PLOS ONE*. 2011;6(11):e27943. doi:10.1371/journal.pone.0027943
9. Cai Y-M. Non-surface Attached Bacterial Aggregates: A Ubiquitous Third Lifestyle. *Frontiers in Microbiology*. 2020;11doi:10.3389/fmicb.2020.557035
10. Moreno-Paz M, Gómez MJ, Arcas A, Parro V. Environmental transcriptome analysis reveals physiological differences between biofilm and planktonic modes of life of the iron oxidizing bacteria *Leptospirillum* spp. in their natural microbial community. *BMC Genomics*. 2010;11(1):404. doi:10.1186/1471-2164-11-404
11. Kaksonen AH, Boxall NJ, Gumulya Y, et al. Recent progress in biohydrometallurgy and microbial characterisation. *Hydrometallurgy*. 2018;180:7-25. doi:10.1016/j.hydromet.2018.06.018
12. Fathollahzadeh H, Becker T, Eksteen JJ, Kaksonen AH, Watkin ELJ. Microbial contact enhances bioleaching of rare earth elements. *Bioresource Technology Reports*. 2018-a;3:102-108. doi:<https://doi.org/10.1016/j.biteb.2018.07.004>
13. Corbett MK, Eksteen JJ, Niu X-Z, Watkin ELJ. Syntrophic effect of indigenous and inoculated microorganisms in the leaching of rare earth elements from Western Australian monazite. *Research in Microbiology*. 2018;169(10):558-568. doi:<https://doi.org/10.1016/j.resmic.2018.05.007>
14. Alin Av, Corbett MK, Fathollahzadeh H, et al. Biofilm formation on the surface of monazite and xenotime during bioleaching. *In press*. 2023,
15. Flemming H-C, van Hullebusch ED, Neu TR, et al. The biofilm matrix: multitasking in a shared space. *Nature Reviews Microbiology*. 2022;doi:10.1038/s41579-022-00791-0
16. Allison DG. The Biofilm Matrix. *Biofouling*. 2003;19(2):139-150. doi:10.1080/0892701031000072190
17. Okshevsky M, Meyer RL. The role of extracellular DNA in the establishment, maintenance and perpetuation of bacterial biofilms. *Critical Reviews in Microbiology*. 2015;41(3):341-352. doi:10.3109/1040841X.2013.841639
18. Wang J, Cui Y, Chu H, et al. Enhanced metal bioleaching mechanisms of extracellular polymeric substance for obsolete  $\text{LiNi}_x\text{Co}_y\text{Mn}_{1-x-y}\text{O}_2$  at high pulp density. *Journal of Environmental Management*. 2022;318:115429. doi:<https://doi.org/10.1016/j.jenvman.2022.115429>
19. Zhang R, Bellenberg S, Neu TR, Sand W, Vera M. The Biofilm Lifestyle of Acidophilic Metal/Sulfur-Oxidizing Microorganisms. In: Rampelotto PH, ed. *Biotechnology of Extremophiles: Advances and Challenges*. Springer International Publishing; 2016:177-213. doi:10.1007/978-3-319-13521-2\_6

20. Sand W, Gehrke T. Extracellular polymeric substances mediate bioleaching/biocorrosion via interfacial processes involving iron(III) ions and acidophilic bacteria. *Research in Microbiology*. 2006;157(1):49-56. doi:10.1016/j.resmic.2005.07.012
21. Kinzler K, Gehrke T, Telegdi J, Sand W. Bioleaching—a result of interfacial processes caused by extracellular polymeric substances (EPS). *Hydrometallurgy*. 2003;71(1):83-88. doi:[https://doi.org/10.1016/S0304-386X\(03\)00176-2](https://doi.org/10.1016/S0304-386X(03)00176-2)
22. Rodriguez-Leiva M, Tributsch H. Morphology of bacterial leaching patterns by Thiobacillus ferrooxidans on synthetic pyrite. *Archives of Microbiology*. 1988;149(5):401-405. doi:10.1007/BF00425578
23. Karygianni L, Ren Z, Koo H, Thurnheer T. Biofilm Matrixome: Extracellular Components in Structured Microbial Communities. *Trends in Microbiology*. 2020;28(8):668-681. doi:<https://doi.org/10.1016/j.tim.2020.03.016>
24. Secchi E, Savorana G, Vitale A, Eberl L, Stocker R, Rusconi R. The structural role of bacterial eDNA in the formation of biofilm streamers. *Proceedings of the National Academy of Sciences*. 2022;119(12):e2113723119. doi:10.1073/pnas.2113723119
25. Yu R, Hou C, Liu A, et al. Extracellular DNA enhances the adsorption of Sulfolobus thermosulfidooxidans strain ST on chalcopyrite surface. *Hydrometallurgy*. 2018;176:97-103. doi:<https://doi.org/10.1016/j.hydromet.2018.01.018>
26. Tuck B, Watkin E, Somers A, Forsyth M, Machuca LL. Conditioning of metal surfaces enhances Shewanella chilikensis adhesion. *Biofouling*. 2022;38(3):207-222. doi:10.1080/08927014.2022.2039349
27. Campoccia D, Montanaro L, Arciola CR. Extracellular DNA (eDNA). A Major Ubiquitous Element of the Bacterial Biofilm Architecture. *International Journal of Molecular Sciences*. 2021;22(16):9100. <https://www.mdpi.com/1422-0067/22/16/9100>
28. Berne C, Kysela DT, Brun YV. A bacterial extracellular DNA inhibits settling of motile progeny cells within a biofilm. *Molecular Microbiology*. 2010;77(4):815-829. doi:<https://doi.org/10.1111/j.1365-2958.2010.07267.x>
29. Fathollahzadeh H, Hackett MJ, Khaleque HN, Eksteen JJ, Kaksonen AH, Watkin ELJ. Better together: Potential of co-culture microorganisms to enhance bioleaching of rare earth elements from monazite. *Bioresource Technology Reports*. 2018-b;3:109-118. doi:<https://doi.org/10.1016/j.biteb.2018.07.003>
30. Corbett MK, Eksteen JJ, Niu X-Z, Croue J-P, Watkin ELJB, Engineering B. Interactions of phosphate solubilising microorganisms with natural rare-earth phosphate minerals: a study utilizing Western Australian monazite. 2017;40(6):929-942. doi:10.1007/s00449-017-1757-3
31. Fathollahzadeh H, Eksteen JJ, Kaksonen AH, Watkin ELJ. Role of microorganisms in bioleaching of rare earth elements from primary and secondary resources. *Applied Microbiology and Biotechnology*. 2019;103(3):1043-1057. doi:10.1007/s00253-018-9526-z
32. Allard S, Gutierrez L, Fontaine C, Croué J-P, Gallard H. Organic matter interactions with natural manganese oxide and synthetic birnessite. *Science of The Total Environment*. 2017;583:487-495. doi:<https://doi.org/10.1016/j.scitotenv.2017.01.120>
33. Rafael RBA, Fernández-Marcos ML, Cocco S, et al. Assessment of Potential Nutrient Release from Phosphate Rock and Dolostone for Application in Acid Soils. *Pedosphere*. 2018;28(1):44-58. doi:[https://doi.org/10.1016/S1002-0160\(17\)60437-5](https://doi.org/10.1016/S1002-0160(17)60437-5)
34. Feng S, Yang H, Wang W. Insights to the effects of free cells on community structure of attached cells and chalcopyrite bioleaching during different stages. *Bioresource Technology*. 2016;200:186-193. doi:<https://doi.org/10.1016/j.biortech.2015.09.054>
35. Flemming HC, Wingender J. The biofilm matrix. *Nat Rev Microbiol*. 2010;8(9):623-633. doi:10.1038/nrmicro2415

## Supplementary Material

**Table S.1** the XRD and phase identification of the high-grade monazite ore conducted by John de Laeter Centre, Curtin University. The COD ID refers to the phase's identification number in the COD database (<http://www.crystallography.net/>).

Phase	Nominal elemental composition
<b>Monazite, Ce</b>	CePO <sub>4</sub>
<b>Monazite, La</b>	LaPO <sub>4</sub>
<b>Quartz</b>	SiO <sub>2</sub>
<b>Goethite</b>	FeOOH
<b>Florencite-Ce</b>	Al <sub>3</sub> (Ce,La,Nd,Sm,Ca)(PO <sub>4</sub> ) <sub>2</sub> (OH) <sub>6</sub>

**Table S.2** The inductively coupled plasma mass spectrometry (ICP-MS) analysis of high-grade monazite ore conducted by Bureau Veritas, Perth, Australia.

Elements (%)	
<b>Al</b>	3.9
<b>Ca</b>	1.8
<b>Fe</b>	1
<b>K</b>	<0.01
<b>Mg</b>	0.1
<b>Mn</b>	0.06
<b>Na</b>	0.1
<b>P</b>	8.5
<b>Si</b>	1.6
<b>Ti</b>	0.4
<b>Y</b>	0.18
<b>La</b>	11
<b>Ce</b>	15
<b>Pr</b>	2.1
<b>Nd</b>	7.2
<b>Sm</b>	0.97
<b>S</b>	0

**Table S.3** The XRF (X-ray fluorescence) and ICP-MS composition of xenotime beneficiation concentrate (reported by the provider, Northern Minerals)

Compound	XRF analysis (Mass %)	ICPMS analysis
SiO <sub>2</sub>	52.5	Not measured
Al <sub>2</sub> O <sub>3</sub>	6.1	7.82
Y <sub>2</sub> O <sub>3</sub>	8.6	5.23
Dy <sub>2</sub> O <sub>3</sub>	1	1.03
Er <sub>2</sub> O <sub>3</sub>	0.7	0.63
Yb <sub>2</sub> O <sub>3</sub>	0.5	0.53
Gd <sub>2</sub> O <sub>3</sub>	0.4	0.47
Sm <sub>2</sub> O <sub>3</sub>	0.2	0.21
Fe <sub>2</sub> O <sub>3</sub>	9.1	11.94
CaO	0.255	1.38
U <sub>3</sub> O <sub>8</sub>	0.055	0.05
P <sub>2</sub> O <sub>3</sub>	Not measured	12.77

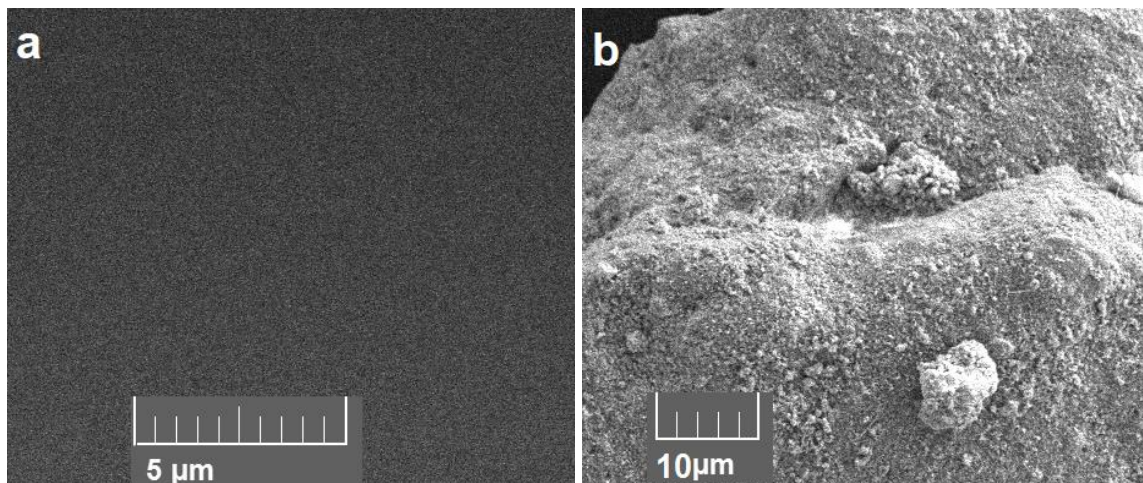


**Figure S-1** Scanning electron microscopy (SEM) image of the smooth surface of glass **(a)** vs the rough surface of the high-grade monazite ore **(b)**.

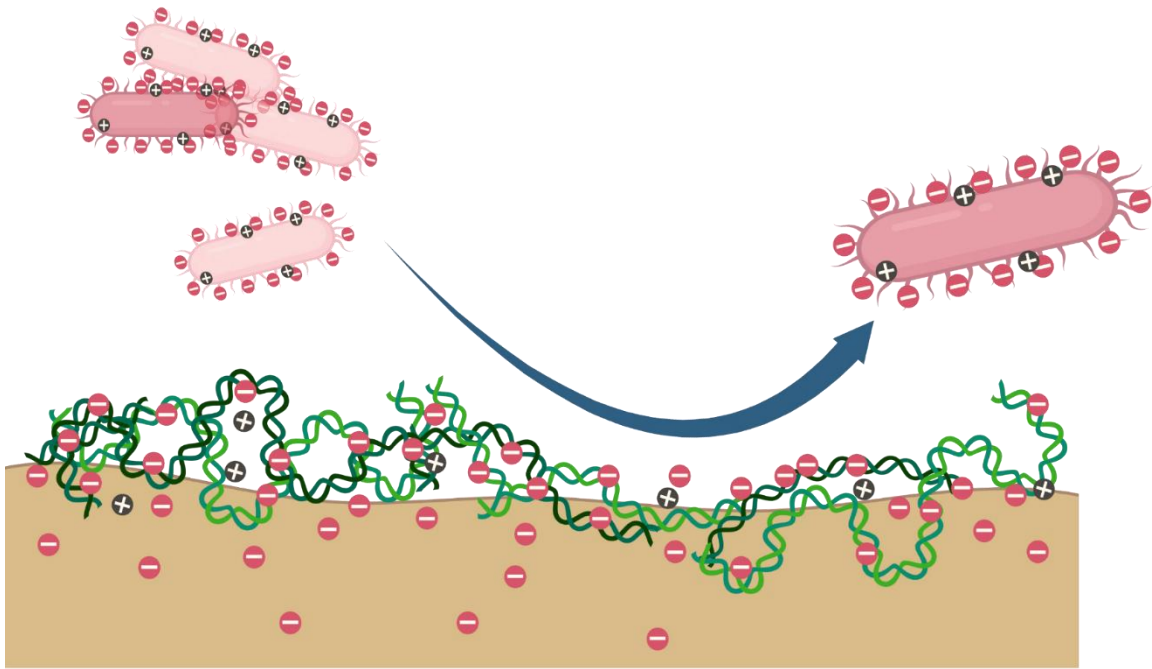


**Figure S-2** The interaction of *Klebsiella aerogenes* cells with surface pre-conditioned with eDNA

## **Chapter Six**

**Complex formation (complexolysis) between rare earth elements and organic acids, a microbial bioleaching mechanism in the extraction of phosphate minerals**



## **Abstract**

Phosphate solubilising microorganisms have been used for bioleaching of rare earth elements (REE) containing phosphate minerals. These microorganisms utilise two main mechanisms for bioleaching of REE from phosphate minerals. One mechanism, known as acidolysis, is to produce organic acids which dissolves the phosphate content of the mineral and as a result release the REE content. The second hypothesised mechanism, known as complexolysis, is potential complex formation between the released organic acids (OA) and REE. While there are many studies demonstrating acidolysis, this study aimed at providing the first empirical evidence on complex formation between REE and the organic acids produced by phosphate solubilising microorganisms. Scanning and transmission electron microscopy (STEM) was used to study chemical changes at the microbe-mineral interface of the attached microorganisms and the mineral surface, the immediate surface and the subsurface of the phosphate mineral. Time of flight secondary ion mass spectrometry (ToF-SIMS) was employed to determine REE-OA complex formation. STEM analysis indicated that there was a strong signal for carbon and nitrogen-based compounds that penetrated the immediate subsurface beneath the microbial cells. ToF-SIMS analysis of this interface revealed there was a sharp signal for REE complexes with formate, acetate, malate, citrate and gluconate on monazite-muscovite samples bioleached for 14 days. The signals for REE-organic acid complexes were significantly higher in both bioleached and abiotic leached minerals, compared to the control samples which did not go through any leaching treatment. Moreover, the acquired signal of REE-OA when the mineral was biotically leached was three times stronger than the acquired signal for minerals with 14 days of abiotic leaching, which could be due to the complexes being trapped inside the biofilm matrix. This result showed that complex formation between REE and organic acids

is possible, hence, complexolysis could be another potential target for further engineering of the bioleaching processes of REE phosphate minerals.

## 1. Introduction

Microbial bioleaching of minerals has gained significant interest in the recent years due to its advantages such as energy efficiency, less harmful chemicals, and lower emission over conventional metal extraction approaches like smelting or chemical extraction with highly concentrated acids<sup>1</sup>. Bioleaching has been mainly used in industrial scale for sulfide minerals giving access to valuable metals including iron, copper, nickel, and gold<sup>1</sup>. It is also becoming a method of interest for bioleaching and biorecovery of metals from electronic wastes<sup>2,3</sup>. Sulfur and iron oxidising microorganisms are the most well-known microbial agents used for bioleaching of these resources<sup>1,4-6</sup>. Some of the general mechanisms used by these microorganisms is to consume the reduced sulfur and iron compounds from the sulfide mineral as a source of energy, produce sulfuric acid and ferric iron, and release the metals from the mineral<sup>6,7</sup>.

In last decades, many studies have further advanced this field by looking into potential application of microorganisms for bioleaching of metals from other resources such as carbonated minerals, oxides such as iron oxides or manganese oxides, and phosphate minerals such as rare earth (REE) phosphate minerals<sup>1</sup>. For the latter, a group of microorganisms called phosphate solubilising microorganisms (PSM) have been used for bioleaching<sup>8</sup>. These microbes are capable of dissolving insoluble phosphate<sup>9</sup> from minerals, hence PSM, and therefore release the metal content<sup>10</sup>. Unlike sulfur- and iron-oxidising microbes, PSM do not use phosphate minerals as an energy source<sup>6</sup>, but they use the phosphate content as source of phosphorus for their metabolism and growth<sup>8-10</sup>.

Regardless of the mineral type, the mechanisms behind bioleaching can be explained through three models, contact, non-contact and cooperative models<sup>6,11</sup>, already discussed in chapter

one. Although these models were previously proposed for bioleaching of phosphate minerals as well<sup>11</sup>, there are some knowledge gap that the current study is aiming to explain.

PSMs are known for their application in bioleaching of REE from phosphate minerals such as monazite<sup>8,10</sup>. Previous studies suggested that these microorganisms employ two main mechanisms to release the REE content of these mineral. One way is by producing organic acids which dissolve the insoluble phosphate<sup>9</sup> from the minerals and release their REE content<sup>8</sup>. Previous studies on PSMs have proven they are capable of producing organic acids, for example *Klebsiella aerogenes* as one of the tested PSMs with a high bioleaching efficiency produced formic acid, acetic acid, oxalic acid, gluconic acid<sup>12</sup> citric acid and malic acid<sup>10</sup>. Previous studies on abiotic leaching by a mixed organic acid solution at the same concentrations produced by *K. aerogenes* showed the organic acid solution alone can dissolve phosphate and release the REE cations from phosphate minerals but to a much lesser extent than in the presence of the microbe<sup>10,11</sup>. Acidolysis using organic acid has been suggested as a green alternative method for leaching of phosphate minerals or biorecovery of valuable metals such as REE from electronic wastes<sup>13</sup>.

The second suggested mechanism is through forming complexes between organic acids anions and the released REE cations (REE-OA complexes)<sup>11</sup> known as complexolysis. Fathollahzadeh et al (2018) reported that although the organic acids concentrations in their abiotic leaching was similar to that of the bioleaching with *K. aerogenes*, the REE dissolution efficiency was higher in bioleaching, suggesting there are other mechanisms employed by PSMs<sup>11</sup>. The released REE are in cationic form, and the produced organic acids are in the anionic form when they are in aquatic solutions, therefore it is hypothesised that there could

be complex formation between these anions and cations <sup>8,11</sup>. Complex formation between some of these organic acids such as acetate and REE has been shown for decades <sup>14,15</sup>.

While previous studies <sup>8,13</sup> provided enough empirical evidence on organic acid production and its capacity to release REE from phosphate minerals, there has not been enough empirical evidence of REE-OA complex formation in bioleaching systems. To the best of our knowledge, the previous studies on REE-OA complex formation is restricted to purely chemical studies to determine the species and stability of potential complexes <sup>16</sup>. One potential reason could be that REE complex formation with organic acids is pH dependent, with a higher chance of complex formation at alkaline and neutral pH compared to lower pH <sup>17</sup> making it difficult to produce high quantity of REE-OA complex, under the acidic pH of bioleaching systems <sup>8,11</sup>, therefore lowering the potential detections of such complexes. This study aimed at providing evidence on complex formation between organic acids and REE under abiotic and biotic leaching conditions.

## **2. Methods**

### **2.1 Microorganism**

*Klebsiella aerogenes* ATCC 13048 was cultivated on National Botanical Research Institute's Phosphate medium (NBRIP)<sup>18</sup>. Cell numbers were quantified with flow cytometry using an Attune NxT flow cytometer as described elsewhere <sup>19</sup>.

### **2.2 Minerals**

Two monazite samples were used in this study. A high-grade monazite ore (HGMO, Lynas Corp, WA, Australia) was used as the sample with complex mineralogy. Mineralogy analysis showed this ore consisted mainly of monazite (~65%) with general chemical formula of (La, Ce, Ne)PO<sub>4</sub>

and florencite with general chemical formula of (La-Ce)-Al<sub>3</sub>(PO<sub>4</sub>)<sub>2</sub> but had several other minerals mainly from crandallite, alunite and magnetite/hematite groups (~33%).

A monazite-muscovite crystal was used as a sample with less complex mineralogy. It was a REE-phosphate crystal with high purity, mainly consisting of monazite (~85-95%) and an aluminium silicate mineral (~4-10%).

## **2.3 Chemical and biological leaching**

### **2.3.1 Chemical leaching**

For chemical leaching a mix of the following organic acids was prepared: formic acid, acetic acid, citric acid, malic acid and gluconic acid in equal proportions of 0.1 mM. These acids have previously been reported to be produced by *K. aerogenes*<sup>10-12</sup>. For abiotic leaching, the organic acid mix was filter sterilised (0.2 µm, Millipore) and added to sterile NBRIP to a final pH of 4.

### **2.3.2 Bioleaching**

The cell numbers used for all inoculations and subcultures in this study was at  $1 \times 10^7$  cell mL<sup>-1</sup>. For scanning transmission electron microscopy super-X energy dispersive spectrometry (STEM-XEDS) analysis, both monazite-muscovite and HGMO samples were bioleached for 14 days<sup>18</sup>. The transmission electron microscope (TEM) samples were prepared from day 3-8 which represent the mature biofilm stage and day 14 which was the end date for bioleaching experiment. For REE-OA complex formation, thick TEM foils were prepared from monazite-muscovite crystals. The TEM foils were UV-sterilised under a biological laminar flow hood. The foils were aseptically transferred to a small beaker containing 10 mL phosphate deficient NBRIP. Then 10 mL of an overnight culture of *K. aerogenes* were centrifuged at 10,000 rcf, the

supernatant discarded with the pellet resuspended in 1 mL of fresh phosphate deficient NBRIP by vortexing. This process was repeated three times to ensure no carry over of phosphate to the bioleaching experiment. The bacterial cells were then added to the media to a final cell number of at  $1 \times 10^7$  cell mL<sup>-1</sup>. One set of samples were bioleached for 24 h, and another set for five days. These samples were analysed using time of flight secondary ion mass spectrometry (ToF-SIMS) for evidence of complex formation between bacterial organic acids and REE content of the mineral.

#### **2.4 Mineralogy analysis**

A TESCAN TIMA instrument equipped with four detectors was employed for mineral processing and mineralogy analyses. TIMA was conducted at 25 kV accelerating voltage, in dot mapping mode at an analytical resolution of 3 microns for Back-scattered Electron Detector (BSE) acquisition and 9 microns for Energy-dispersive X-ray spectroscopy (EDS) point spectroscopy analyses. The SEM micrograph of all samples was also recorded in the TIMA data. Processing of the acquired data was performed using TIMA software v. 2.1.1 (TESCAN, Czech Republic). Only polished sample were analysed on TIMA.

#### **2.5 Scanning Electron Microscopy**

Scanning Electron Microscopy (SEM) imaging was conducted with a TESCAN Clara FESEM microscope using TESCAN Essence software (John de Laeter Centre, Curtin University) at 5 kV operating voltage and 300 pA beam intensity.

#### **2.6 Preparation of TEM foils**

TESCAN LYRA3 GM (TESCAN instruments, JDLC, Curtin University) instrument was used to produce transmission electron microscope foils using focused ion beam (FIB) technology. A 1-



$\mu\text{m}$  thick platinum layer was deposited on the region of interest before FIB. The thick platinum layer acts as a protective barrier against the high energy ion beams and minimises curtaining effect <sup>20</sup>. For abiotic leached samples a protective 5 nm carbon was coated on the sample. This was necessary to protect the very top layer of the surface against FIB as well as making the surface conductive. High current (10 nA) focused ion beam was employed to prepare STEM foils by milling a double-trench at the region of interest. To prepare the TEM foil from any regions of interest, a thin (<100 nm) foil was extracted from the sample and mounted on a TEM grid, using conventional FIB lift-out method <sup>21</sup>. The TEM foils have a typical size of 10  $\mu\text{m}$   $\times$  10  $\mu\text{m}$ , and thickness of <100 nm for TEM analysis. High resolution (nm scale) images acquired with tilt corrected SEM ensure measurements were in the direction orthogonal to sample surface. The same methodology was employed to prepare thicker (1 micron) TEM foils. Trenches were made with high current (10 nA) focused ion beam, and a subsequently low currents (1 nA, 300 pA) ion beams were used to polish the cross-section and minimize the surface damage and roughness.

## **2.7 Scanning transmission electron microscope**

Scanning transmission electron microscopy (STEM) equipped with high resolution super-X energy dispersive spectrometry (XEDS) was used on previously bioleached samples to determine the microbe-mineral interface. The high resolution capacity of STEM-XEDS is at sub-nano meter scale and allows studying if there are any chemical changes <sup>22,23</sup> at the interface or the immediate surface and subsurface of the mineral underneath the microbial cells. A FEI Talos F200X field emission gun STEM equipped with highly sensitive X-EDS detectors was used to study both physical and chemical changes at the interface, immediate surface, and subsurface of the microbe-mineral surface interaction. TEM foils were prepared

using focused ion beam (FIB). The TEM was operated with an accelerating voltage of 200 kV with the samples loaded in a double-tilt low background holder. The Velox software package (version, company) was used to capture and analyse the imaging, diffraction, and x-ray spectroscopy data. Low and High resolution (HRTEM) imaging, and selected area diffraction (SAED) were used to study microbial biofilm thickness and detailed analysis of the physical changes at the minerals immediate subsurface. Elemental mapping by STEM-EDX was used for detailed analysis of chemical changes on the samples through high-resolution (~5 nm) distribution analysis of the elements.

### **2.8 FIB- Time-of-Flight Secondary Ion Mass Spectrometer microanalysis**

ToF-SIMS was used as the main approach to study potential REE-OA formation. ToF-SIMS can detect many organic compounds including organic acids <sup>24,25</sup>. This analytic methodology has been paired with advance microscopy analysis such as focused ion beam (FIB) for analysis of biological samples <sup>26</sup>. The lateral distribution of inorganic matter including REE on the sample surface was analysed using TOFWERK Time-of-Flight Secondary Ion Mass Spectrometer. Prior to any FIB-ToF-SIMS samples were coated with ~20 nm carbon layer to make the sample surface conductive. The lateral resolution for ToF-SIMS analysis was ~10 nm. A minimum of 500 frames and a maximum of 3000 frames were acquired from regions of interest at a minimum 5 µm × 5 µm area. Samples were analysed from top to the bottom in which each 500 frames is equal to approximately 100 nm depth.

### **2.9 IONTOF-ToF-SIMS microanalysis settings**

The elemental distribution on the samples was measured using an IONTOF M6 ToF-SIMS instrument (IONTOF, Germany). This instrument is more sensitive in detection of organic material and unlike, FIB-ToF-SIMS, ION-ToF-SIMS does not require coating. Data was collected

in 'Delayed Extraction' mode for high lateral resolution of  $\sim 100$  nm and a mass resolution  $M/\Delta M$  of  $\sim 1.5 \times 10^3$ . Sample surfaces were precleaned using a 1 kV  $O_2$  sputter source and 1 kV Ar1600 cluster sputter source, to remove contamination and minimize the damage to large particles. Imaging was performed using a 60 keV  $Bi^{3++}$  primary ion source delivering  $\sim 0.1$  pA of target current over a  $30 \times 30 \mu m^2$  area. Both positive and negative secondary ions were used to analyse and map the distribution of various elements and compounds. For monazite-muscovite samples, the biofilm was first polished by FIB in which the bacterial cells in the biofilm were thinned by finely grinding away the bacterial body. The biofilm was thinned to approximately  $< 50$  nm, giving it a thickness close to that of the EPS matrix of the biofilm. For ToF-SIMS data, the signal quality was checked by evaluating signals for double carbon ( $C_2$ , molecular weight = 24), aluminium (Al = 27), Iron (Fe = 56), gallium (Ga = 70) and rare earth elements including lanthanum (La=139), cerium (Ce=140), praseodymium (Pr=141), and neodymium (Nd=142). Rare earth oxide signals were also considered as another set of control signals, including LaO (155), CeO (156), PrO (157), NdO (158, 160), LaO<sub>2</sub> (171), CeO<sub>2</sub> (172), PrO<sub>2</sub> (173) and NdO<sub>2</sub> (174). When required the recorded ToF-SIMS were corrected through "correct shift" options in the software using these control signals.

The acquired mass spectrum was then searched for the molecular weight of the anionic forms of the organic acids produced by *K. aerogenes* (Table 1) as well as potential REE-OA complexes with these organic acids. For example,  $CH_3COO^-$  and  $CeCH_3COO$  (cerium acetate) chemical formulas were looked up in the recorded ToF-SIMS data for acetate and its complex with cerium, cerium acetate, respectively.

For quantitative analysis of the ToF-SIMS data, it was important to provide a normalised means to compare REE-OA complexes in control (no leaching), abiotic leaching and biotic

leaching samples. After collecting the mass count per each element or compound of interest, the recorded REE-OA mass counts of all REE and OA were normalised against the total mass count acquired for the sum of REE and REE oxides. The normalised data were reported as percentage of the total signal for REE content of the samples.

Table 1- List of the elements and compounds analysed using ION-ToF-SIMS

	<b>Name</b>	<b>Formula</b>	<b>Molecular weight</b>
1	Double carbon	C <sub>2</sub>	24
2	Aluminium	Al	27
3	Iron	Fe	56
4	Gallium	Ga	70
5	Lanthanum	La	139
6	Cerium	Ce	140
7	Praseodymium	Pr	141
8	Neodymium	Nd	142
9	Lanthanum oxide	LaO	155
10	Cerium oxide	CeO	156
11	Praseodymium oxide	PrO	157
12	Neodymium oxide	NdO	158
13	Lanthanum oxide	LaO <sub>2</sub>	171
1	Cerium oxide	CeO <sub>2</sub>	172
4	Praseodymium oxide	PrO <sub>2</sub>	173
15	Neodymium oxide	NdO <sub>2</sub>	174
16	Carboxyl group	COO	44
17	monocarboxylic acid anion (Formate)	HCOO	45
18	Acetate	C <sub>2</sub> H <sub>3</sub> O <sub>2</sub>	59
19	Malate	C <sub>4</sub> H <sub>4</sub> O <sub>5</sub>	132
20	Citrate	C <sub>6</sub> H <sub>5</sub> O <sub>7</sub>	189
21	Gluconate	C <sub>6</sub> H <sub>11</sub> O <sub>7</sub>	195

### 3. Results and discussion

#### 3.1 STEM XEDS capacity to analyse chemical changes at the immediate surface and subsurface

The depth analyses of the 3 regions of interest on abiotic leached samples showed that STEM-XEDS can detect changes in the chemical composition of a sample at a nanometre resolution.

The high-angle annular dark-field scanning transmission electron microscopy (HADDF) (Figure 1-A) shows there are two mineral plates, shown in dark and light colour. The EDX spectrum and elemental distribution map showed there were signals for REE (monazite plane) as well as Aluminium (Al) or Silicon (Si) which corresponds to the muscovite plane (Figure 1, B, C and D). Depth analysis of the monazite plate of the region of interest number 1 (ROI-I) (Figure 1-B and E) showed there was a very low signal for Lanthanum (La) and Cerium (Ce) where the protective carbon was located (Figure 1-B). But right below the carbon coating, the signal intensity increased for both La and Ce, but not for Al or Silicon Si. This part of the sample is the monazite plate of the monazite-muscovite crystal. Analysis of ROI-III (Figure 1-G) showed an opposite pattern, with a strong signal for Al and Si below the carbon coating and a very weak signal for La and Ce, indication that this plate is muscovite. For ROI-II (Figure 1-F), there was a noticeable change 50-75 nm below the carbon coating, in the signal intensity for La, Ce, Al and Si, where Al and Si signal decreased and CE and La signal increase. This corresponds with the HADDF image and XEDS mineral map (Figures 2-A, B and C) and indicates the location at which the two different mineral planes, namely monazite and muscovite, meet and merge. This confirms that the sub nano meter resolution of the STEM-XEDS is capable of detecting any significant shift in the chemical composition of the immediate surface and subsurface of the minerals. This is a very important application which allows detection of dissolution of an element of interest relative to the mineral surface.

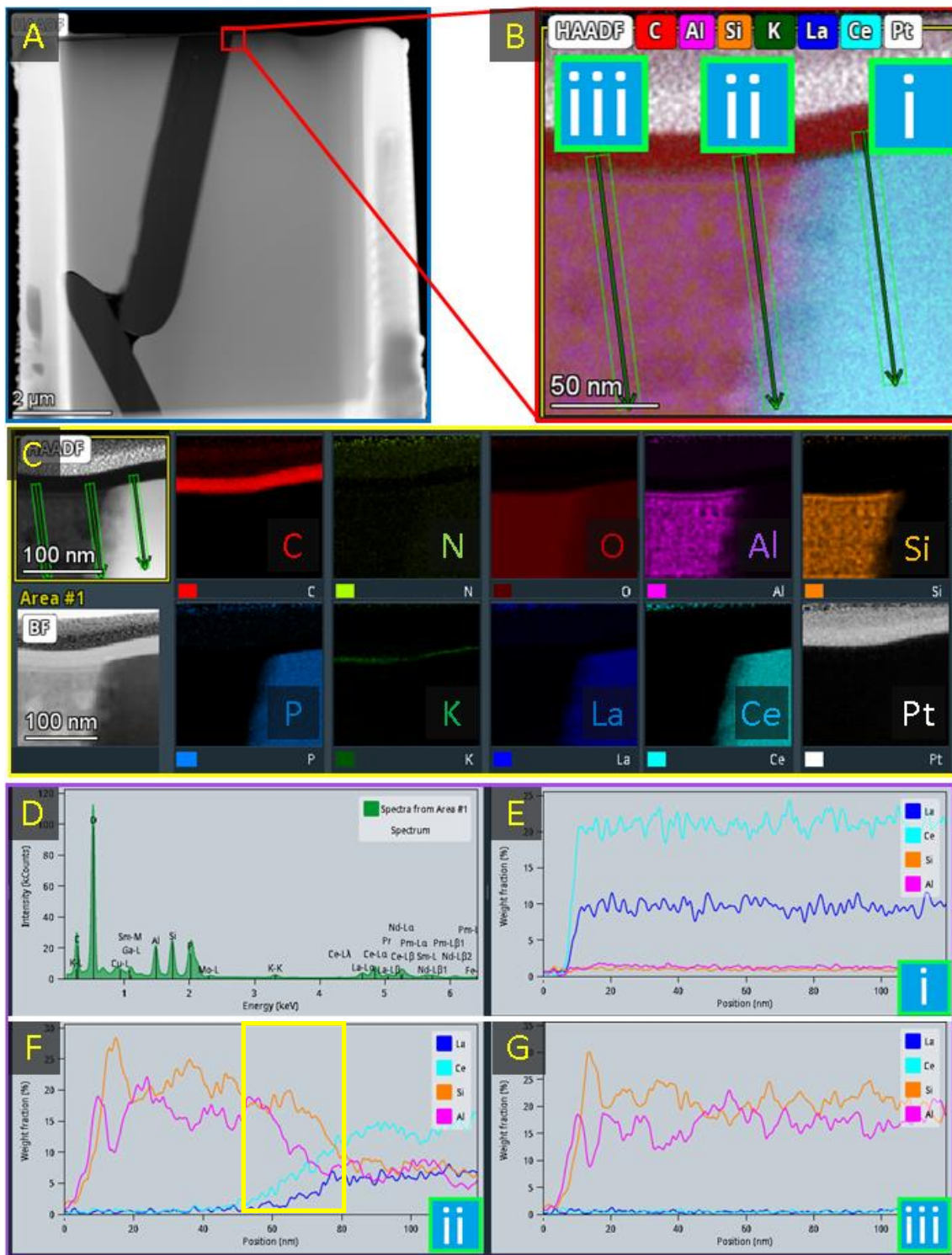


**Figure 1.** Evaluating the resolution and reliability of STEM-XEDS analysis of a monazite-muscovite sample. **A)** High-angle annular dark-field scanning transmission electron microscopy (HAADF-STEM) images of the monazite-muscovite crystal after abiotic leaching. **B)** XEDS elemental distribution map of a region of interest. The three green arrows are the

location and direction of intensity profile analyses, each averaging a 10 nm wide profile, 120 nm deep into the subsurface. **C)** Elemental distribution map of several elements. **D)** XEDS spectra of the entire region. **E)** The depth intensity profile analysis of the REE-phosphate plate. **F)** The depth intensity profile analysis of the aluminium-silicate plate. Yellow box indicates the location at which the two mineral plains meet each other. **G)** The depth intensity profile analysis of the merging region of the two mineral plates. BF=Bright-field; HAADF = High-angle annular dark-field.

For the bioleached samples (Figure 2-A) there was a very high signal for carbon and nitrogen inside the bacterial cell (biofilm). This signal was significantly decreased ( $p < 0.05$ ) at the interface of the bacterial cell and the mineral surface (Figure 2-B, C, F and G). An opposite pattern was recorded for La and Ce, where a very low signal is detected for these REEs inside the bacteria cell, but it significantly shifts at the interface and the subsurface of the mineral (Figure 2-D, E, F and G). Quantitative XEDS analysis (shown as EDS spectrum in Figure 2-G) showed a significant ( $P < 0.5$ ) difference between the intensity of these signals inside bacterial cell (Figure 2-F, area #3), biofilm-mineral interface (Figure 2-F, area#2) and at the subsurface ~80 nm below the interface (Figure 2-F area#1). The signal intensity of carbon, nitrogen, at the interface and immediate subsurface (the first 15 nm below the interface) was approximately half of the signal recorded for the biofilm indicating penetration of a carbon and nitrogen (organic) compound into the immediate subsurface. For abiotic leached samples there was a very low signal for carbon at the top few nanometres of the immediate subsurface of monazite-muscovite samples. This was expected since organic acids have no nitrogen in their structure.



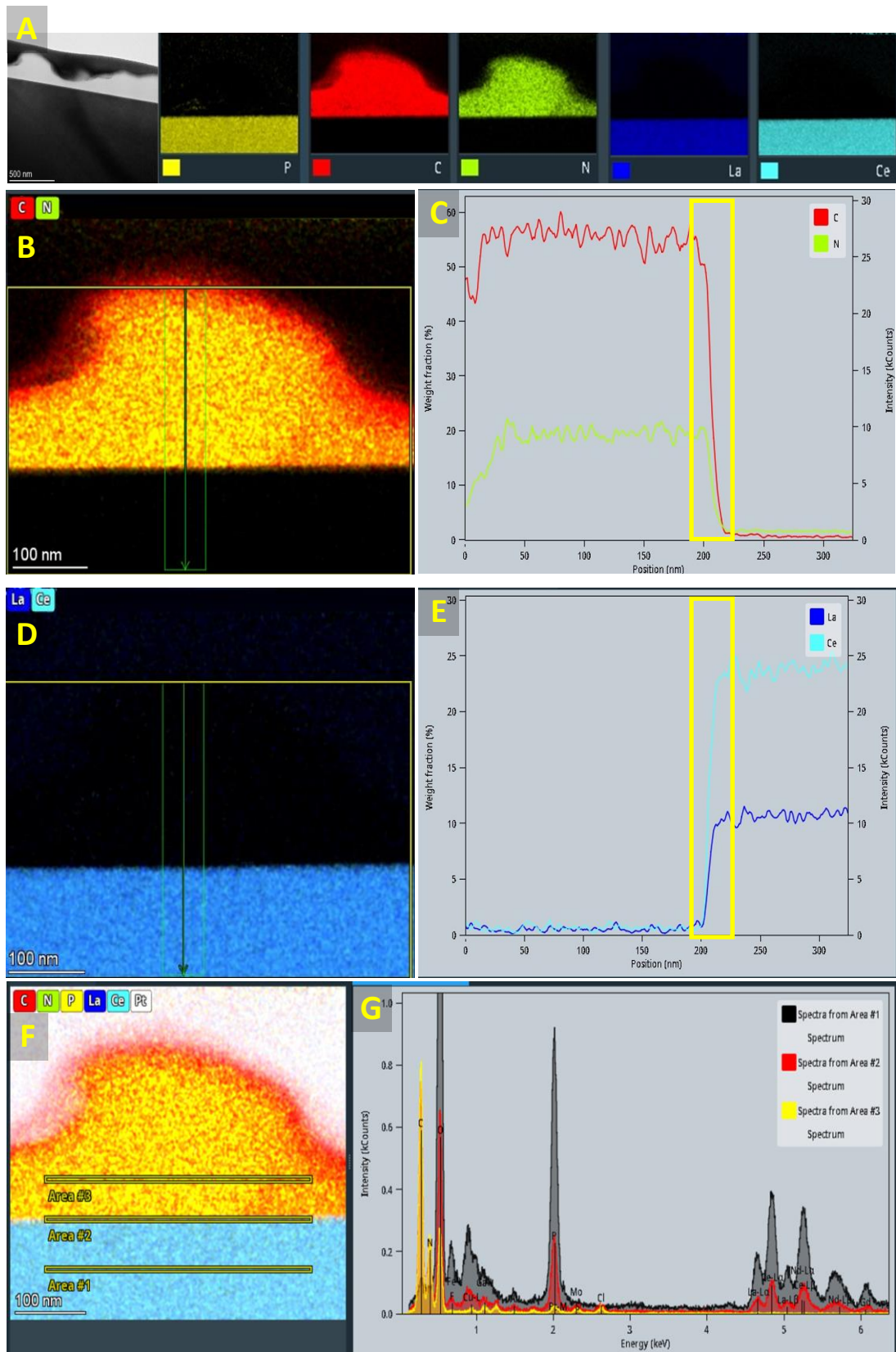


**Figure 2.** STEM-XEDS analysis of a bioleached monazite-muscovite sample. **A)** XEDS elemental map. **B)** Carbon and nitrogen distribution map aligned with bacterial cells. **C)** Depth profile of

carbon and nitrogen signal; the yellow box indicate the location of microbe-mineral interface. **D)** Lanthanum and cerium distribution map aligned with bacterial cells. **E)** Depth profile of lanthanum and cerium signal; the yellow box indicate the location of microbe-mineral interface. **F)** Location of three region of interest, area 1-3, for quantitative XEDS analysis. The volume of all 3 area is 250,000 nm<sup>3</sup>. **G)** Quantitative XEDS spectrum of area#1, #2 and #3 in panel F.

On the other hand, comparing the intensity signal for cerium, lanthanum and phosphate showed the signal at the immediate subsurface was about half of the recorded intensity at deeper subsurface (area#1, 80 nm below the subsurface), signifying potentially higher dissolution of REE-phosphate closer to the mineral surface or the biofilm. This could be due to a high proton content trapped inside microbial biofilms in bioleaching ecosystems <sup>27</sup>.

A relatively similar pattern was recorded for bioleached HGMO samples. The STEM images revealed that, unlike the monazite-muscovite sample which had a very low porosity, HGMO was a very porous mineral. The signal for carbon and nitrogen at the surface of the mineral corresponded well with the biofilm location (Figure 3-A and B). XEDS elemental map (Figure 3, B, C and D) revealed that there was also a very high signal for carbon and nitrogen at the immediate surface below the bacterial cells and even at the deep subsurface (6 μm). The depth analysis was done on several location (one is shown in Figure 3-F and revealed there was a very high intensity signal for carbon and nitrogen even at 6 μm depth from the mineral surface. This indicated penetration of an organic compound into the deep subsurface which could be due to the porous nature of the HGMO ore <sup>28</sup>.

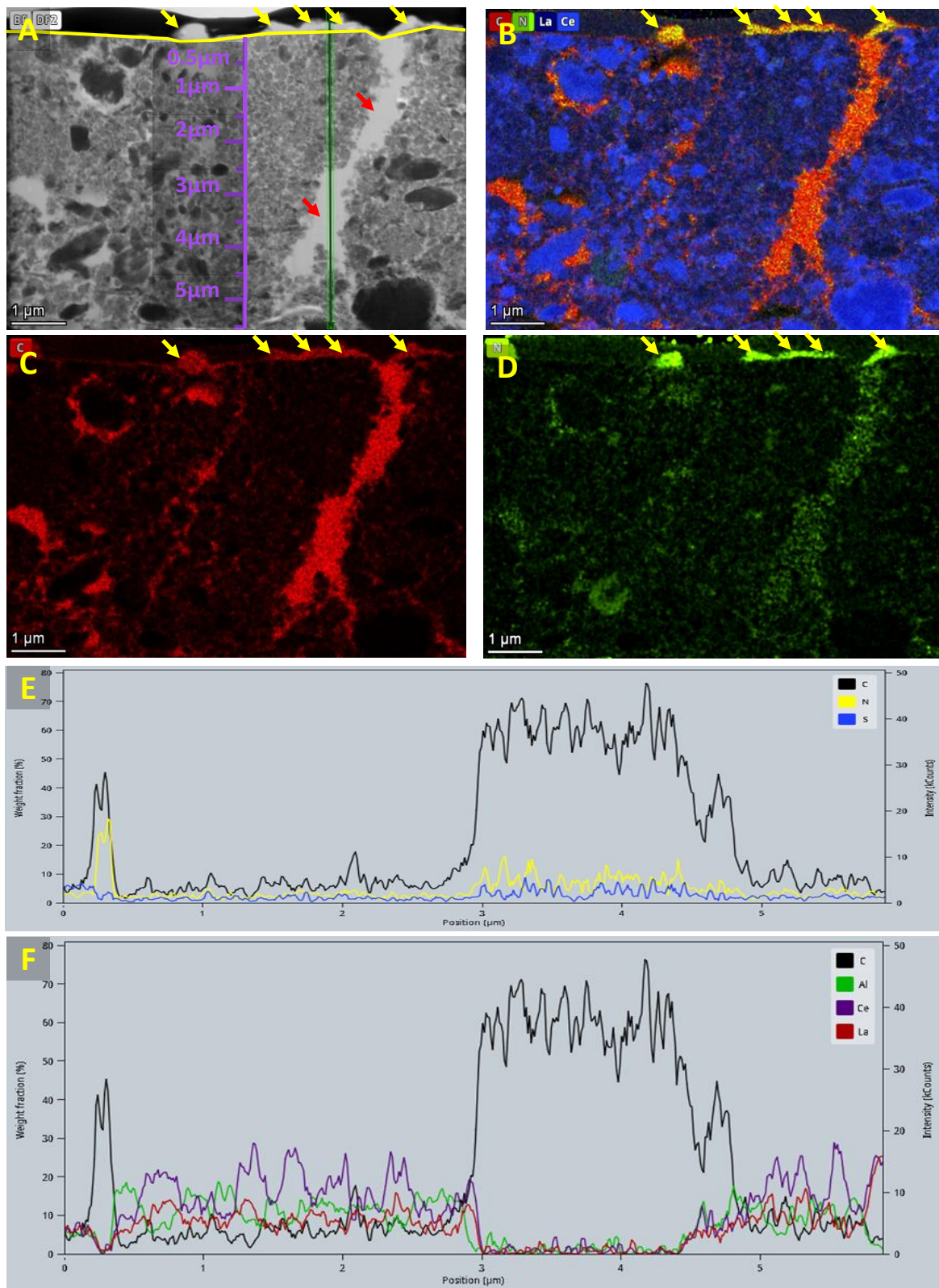


**Figure 3.** Penetration of a carbon- and nitrogen-based compound to deep subsurface in a porous high-grade monazite ore. Purple line indicates the depth from mineral surface **A)** STEM images of the lamella. Yellow line indicates the location of biofilm-mineral interface.

Yellow arrows indicated bacterial cells. Red arrow indicates location of a crack in the mineral. Green line represents the location of the depth analysis with an average width of 100 nm. **B)** Merged XEDS elemental distribution map of lanthanum, cerium, carbon and nitrogen. **C)** XEDS elemental distribution map of carbon and **D)** nitrogen only. **E)** Depth analysis of the signal intensity of carbon, nitrogen and sulfur representing organic compounds. **F)** Depth analysis of the signal intensity of carbon representing organic compounds versus lanthanum, cerium, and aluminium representing the mineral.

In comparison with bioleached samples, control samples (no leaching) and abiotic leached samples (Figure S-1 and S.2) showed a significantly lower ( $p < 0.05$ ) signal for carbon in the deep subsurface of the ore, loss of signal or negligible signal for nitrogen in these samples suggested that the carbon and nitrogen-based compound signal in bioleached samples was potentially produced by microorganisms, potential originated from the EPS matrix of the biofilm which contains polysaccharides, proteins, and extracellular nucleic acids which all contain carbon and nitrogen based monomers <sup>29</sup>.

To further investigate REE dissolution at different depth, three regions of an HGMO with an average volume of  $0.25 \mu\text{m}^3$  were analysed using quantitative XEDS. The surface of this sample was fully covered by bacterial biofilm; hence a very high signal intensity was recorded for carbon and nitrogen inside the biofilm (Figure 4. A, C, and F, area #1). There was a very low signal intensity for the REE such as cerium and lanthanum (Figure 4. F). For area#2 (the immediate subsurface- $0.5 \mu\text{m}$  deep in the subsurface) the signals intensity of phosphorus, cerium and lanthanum was higher than area#1. On the other hand, it showed an average of 4-12.5% decrease compared to the recorded signal for area#3 ( $1 \mu\text{m}$  deep subsurface), indicating a higher dissolution of REE-phosphate closer to the microbe-mineral interface.



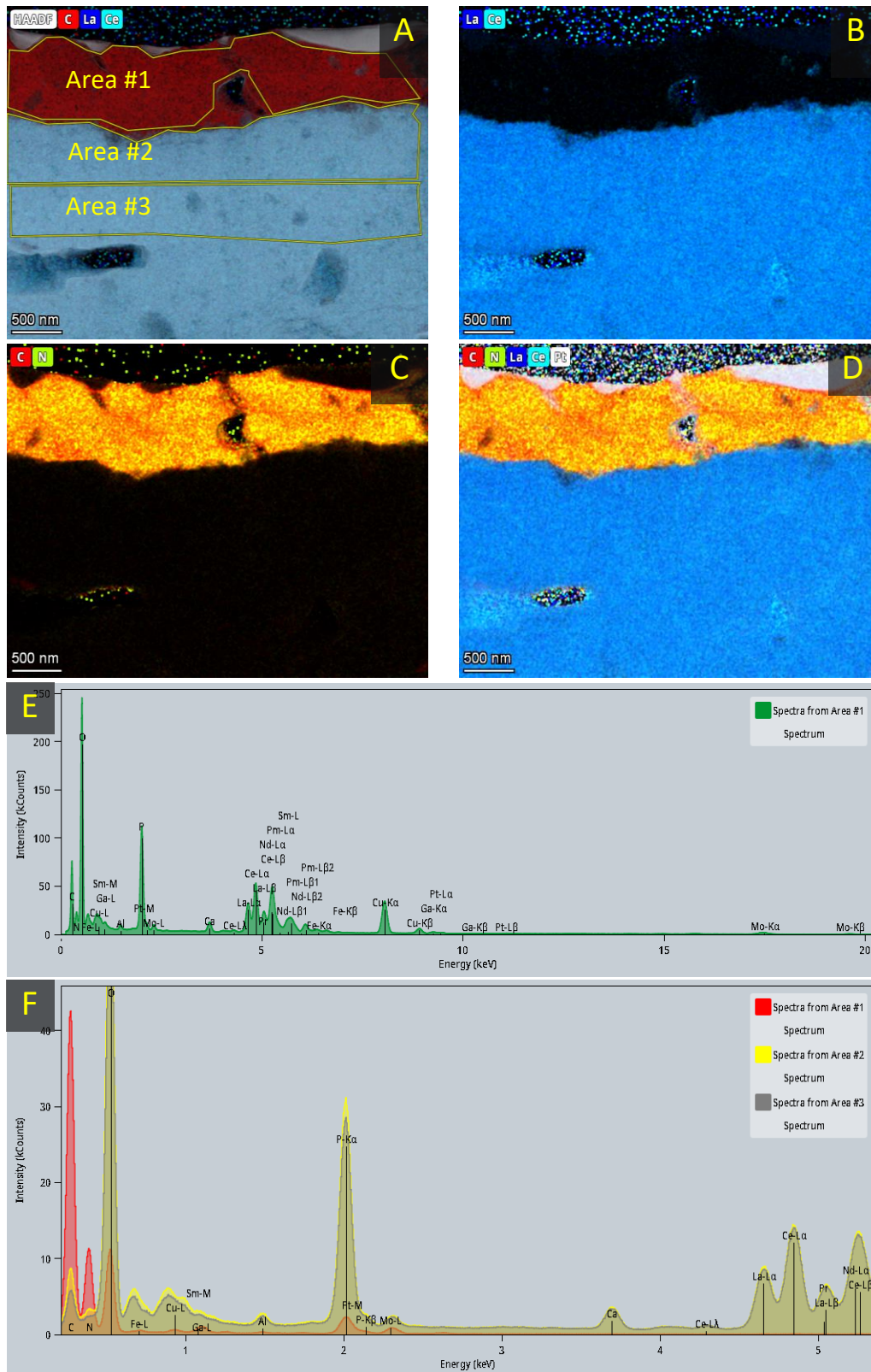


**Figure 4.** STEM-XEDS analysis of a HGMO bioleached sample. **A)** Elemental distribution map of C and REE on the sample marked with three different areas with an average volumetric size of  $0.25 \mu\text{m}^3$ : area #1- biofilm, area #2- immediate surface and subsurface, 500 nm underneath

the biofilm, and area #3) 500-1000 nm deep subsurface. **B)** XEDS elemental distribution map of cerium and lanthanum represent the REE-phosphate mineral. **C)** Elemental map of carbon and nitrogen represents the biofilm. **D)** Merged elemental distribution map. **E)** XEDS spectra of the whole region. **F)** XEDS spectra of the three areas marked in panel A.

The STEM-XEDS analysis of the bioleached minerals indicated that an organic compound can penetrate the deep subsurface of the mineral, which could contribute to higher dissolution of phosphate and as a result the REE content of the mineral closer to the microbe-mineral interface. The origin of this compound was most likely the microbial EPS since it contained both carbon and nitrogen <sup>29</sup>, hence signifying the previous observation on the role of microorganism in contact leaching. Fathollahzadeh et al showed that when there was microbial attachment to the mineral (contact bioleaching) the REE dissolution was higher than both non-contact bioleaching and abiotic leaching <sup>8,11</sup>. Therefore, enhancing biofilm formation can be employed as a strategy to improve bioleaching efficiency <sup>18</sup>. Although STEM is very strong in determining changes in the chemical composition of a region of interest, it is not capable of detecting compounds such as REE complexes with organic acids. The depth analysis using STEM-XEDS (Figure 2) showed the thickness of the biofilm-mineral interface is between 20-50 nm. This area is where XEDS detected signal for both REE and organic compounds (carbon and nitrogen). Therefore, to study the potential complex formation between REE and organic acids, this region was considered as region of interest and was studied using ToF-SIMS instruments which are capable of detecting both elements and compounds.

### **3.2 FIB-ToF-SIMS analysis of the surface and interface**

ToF-SIMS was used as the main approach for detection of REE-OA complexes. Due to highly sensitive nature yet lower energy requirement of ToF-SIMS analysis compared to other SIMS

analyses such as nanoscale secondary ion mass spectrometry (NANO-SIMS)<sup>24</sup>, the chance of producing artifact during analyses is significantly less, hence lowering the potential of false positive signals.

Analysis of the mineral samples using FIB-ToF-SIMS showed that its accuracy and resolution is highly affected by surface charge. For example, analysing an abiotic leached monazite-muscovite crystal using FIB-ToF-SIMS (Figure S-3) showed a conductivity issue in the top 20 nm of the surface. Having no ToF-SIMS signals at this region may be due to dust covering the surface. The signals increased at 20 nm from the surface and reached its maximum at 40-50 nm distance from the surface, this 20-25 nm region with highest conductivity (yellow box) aligns with the carbon coating protective layer applied on FIB-ToF-SIMS samples (Figure S3-C), explaining the highest conductivity acquired from this region. However, there was a significant signal loss (~50% decrease,  $p < 0.05$ ) after this implying a conductivity issue<sup>30,31</sup>. At the area where there was no issue with conductivity (Figure S3-C, frames 400-700, yellow box), the distribution map and intensity profiling for element or compounds of interest produces a clear and accurate map (Figure S3-E) compared the areas with low conductivity (Figure S3-D).

To further investigated this possible conductivity issue, the coating layer of a bioleached sample was removed using FIB (Figure 5). The signal intensity of uncoated samples was immediately lost within the first few nanometres (Figure 5-C), confirming conductivity issue. Therefore, FIB-ToF-SIMS was not a reliable tool to measure the chemical changes of REE-phosphate minerals after bioleaching or abiotic leaching. As a result, ION-ToF-SIMS was used instead of FIB-ToF-SIMS because it does not need require coating and conductive surfaces.



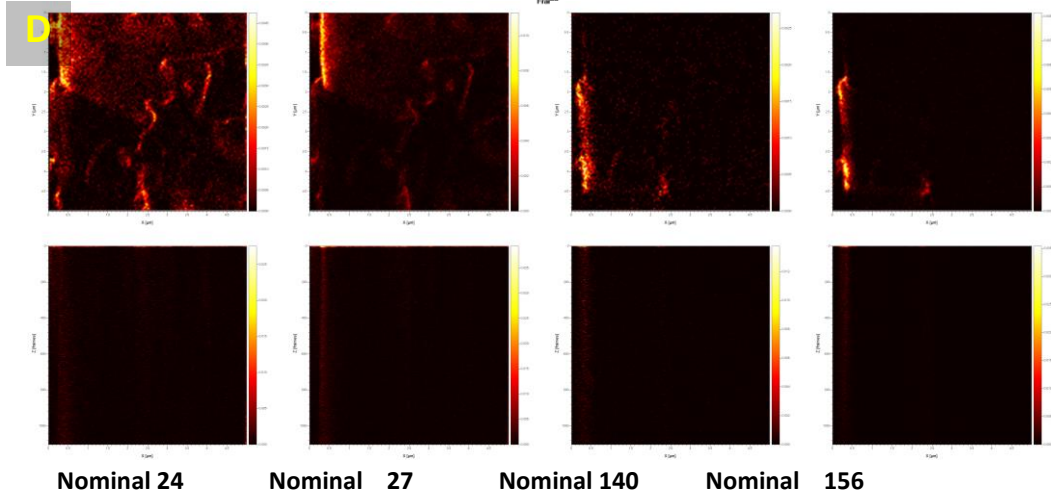
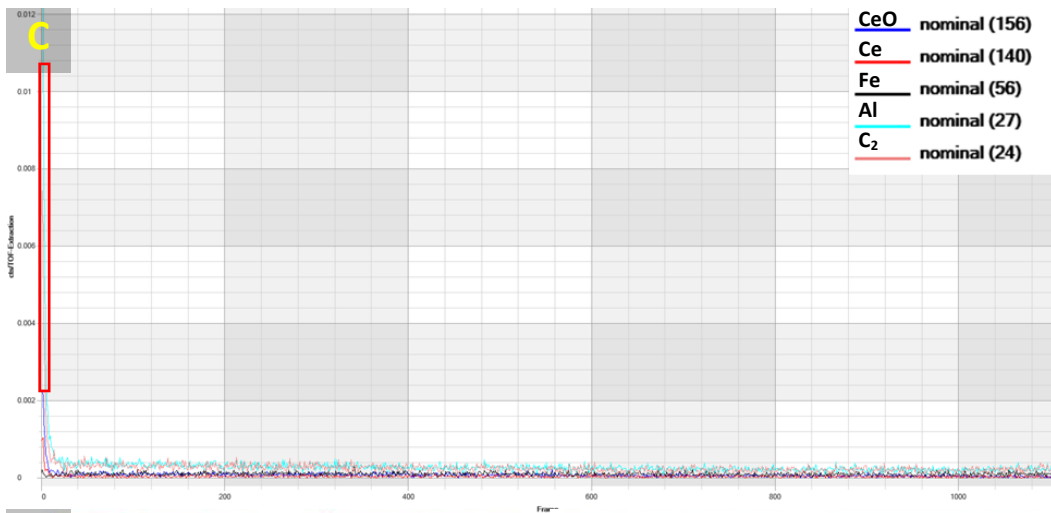
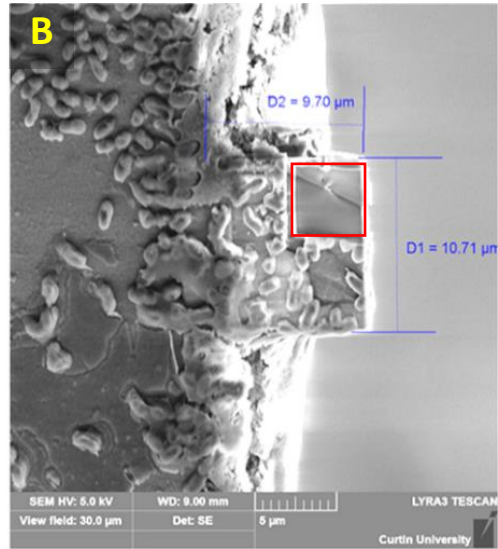
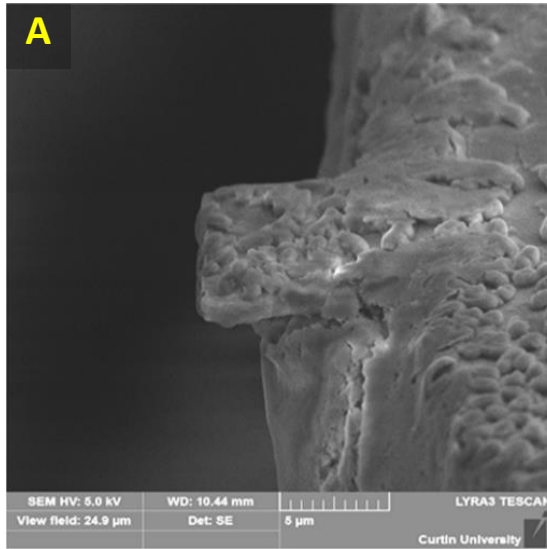


**Figure 5.** FIB-ToF-SIMS of a bioleached HGMO sample. The region of interest was a 5×5 μm area. **A)** The region of interest after FIB-ToF-SIMS analysis. **B)** Analysis area on the sample is shown by a red box. **C)** ToF-SIMS spectrum of the intensity count. The depth is shown as frame in which each five frames is equal to one nanometre per nanometre. The nominal line represent the TOF-SIMS signal intensity acquired for two element and two compound ( $C_2=24$ ,  $Al=27$ ,  $Ce = 140$ , and  $CeO=156$ ). The image shows immediate loss of the signal due to conductivity issue starting just few nm from the surface, the region with significant shift in conductivity is indicated by a red box. **D)** ToF-SIMS distribution heat map of the four elements and compounds

### **3.3 ION-ToF-SIMS analysis of the surface and interface**

Unlike FIB-ToF-SIMS, ION-ToF-SIMS does not require a coating, hence no conductivity issues would arise. The intensity signal for control elements and compounds shows accurate mass detection on the spectrum. The mass assignment accuracy was tested for carbon ( $C = 12$ ) or double carbon ( $C_2= 24$ ), aluminium ( $Al=27$ ), potassium ( $K=39$ ), rare earth elements including lanthanum ( $La=139$ ), cerium ( $Ce=140$ ), praseodymium ( $Pr=141$ ) and neodymium ( $Nd=142$ ) and their oxides (Figure S-4 A and B) as quality control check.

#### **3.2.1 ION-TOF-SIMS analysis of the control sample**

Analysis of monazite-muscovite before any leaching treatment showed that there was no to negligible signal for organic material, particularly organic acids (Figure 6). Both ToF-SIMS distribution heatmap (Figure 6, panels C-I) and mass spectrum plots (Figure S-5) showed that there was very low signal for double carbon, carboxyl group, monocarboxylic acid anion (formate), acetate, propionate, lactate, oxalate, citrate or gluconate, all representative of organic compounds. While there was a very strong signal for rare earths and their oxides

(Figure 6 panels J-Q and Figure S-6) accounting for ~75% of the total mass count, the normalised ToF-SIMS mass count recorded for organic compounds was less than 0.005% of the total acquired counts. Moreover, there was no or negligible signal for REE complexes with any of the organic acids (~0.001% of the normalised mass count, Figure S-6). Although this sample was used as untreated control, the small counts recorded for C2 and organic compounds such as organic acids was expected since monazite-muscovite was not a synthetic mineral, but rather it was a naturally formed mineral. Therefore, it is highly likely that it had been exposed to abiotic or even biotic leaching.

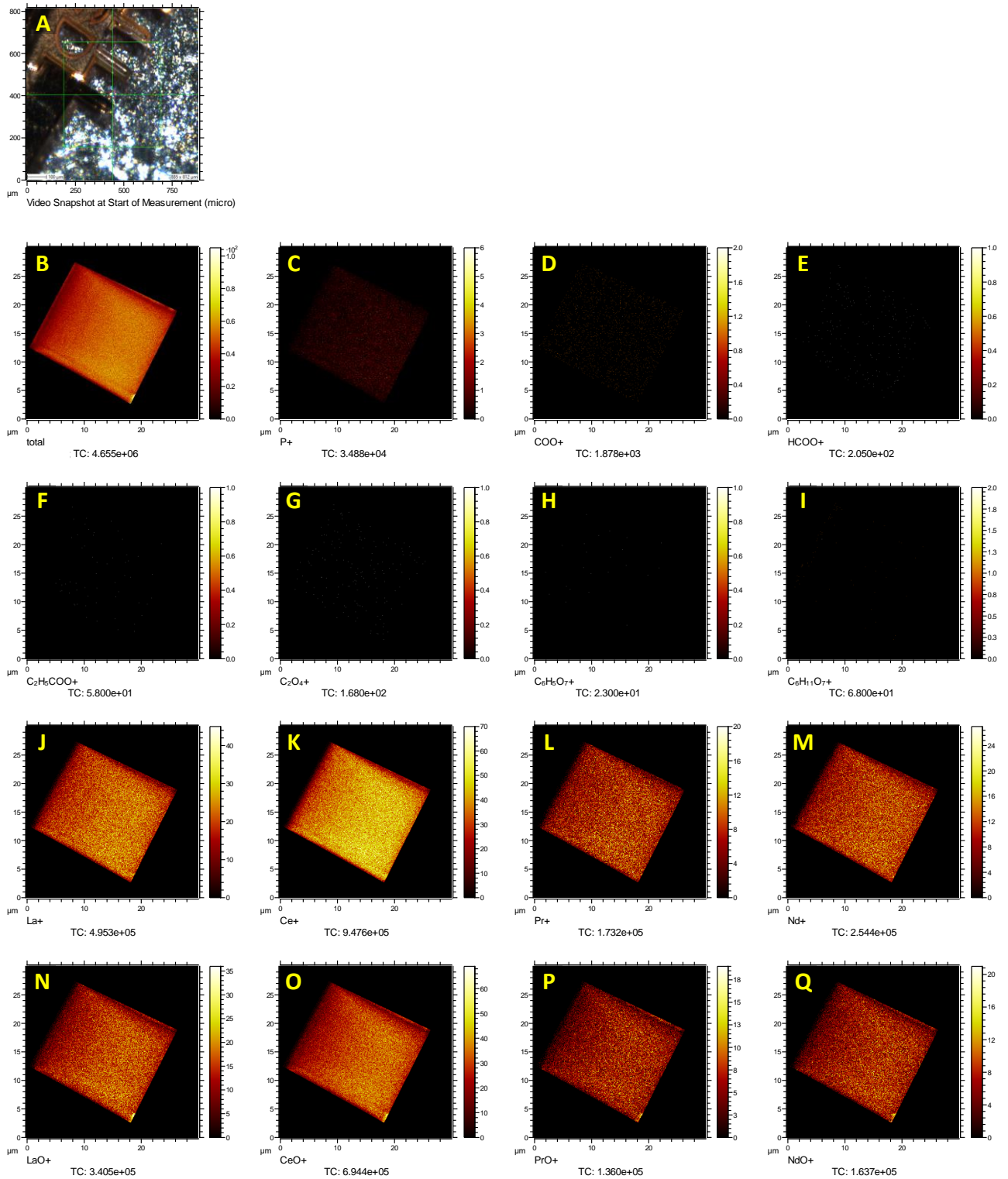


**Figure 6.** The quantitative distribution map of different compounds and elements in the control mineral, a monazite-muscovite sample without any treatment. **A)** The TEM grid that holds the sample. **B)** The total mass count acquired for this sample. The ToF-SIMS distribution

heatmap map of: **C**) phosphorus, **D**) carboxyl group (COO), **E**) monocarboxylic anion (formate), **F**) acetate (CH<sub>3</sub>COO), **G**) oxalate (C<sub>2</sub>O<sub>4</sub>), **H**) citrate (C<sub>6</sub>H<sub>5</sub>O<sub>7</sub>), **I**) gluconate (C<sub>6</sub>H<sub>11</sub>O<sub>7</sub>), **J**) lanthanum, **K**) cerium, **L**) praseodymium, **M**) neodymium, **N**) lanthanum oxide (LaO), **O**) cerium oxide (CeO), **P**) praseodymium oxide (PrO), and **Q**) neodymium oxide (NdO). The X and Y axis are representing the sample size in μm. The heat map colour on the right side of the panel represents the intensity of the mass count. The scale of maximum count for the heat map is different per each panel and is shown as the TC (total count) below the panel.

### 3.2.2 ION-TOF-SIMS analysis of the chemical leaching sample

For the monazite-muscovite samples that were chemically leached using a mix of several organic acids known to be produced by *K. aerogenes*, there was a signal for the REE-OA complexes (Figure 7) which was significantly higher compared to that of the control samples, on average 20-30 times increase. While there was no or negligible signal for REE-OA complexes in the control samples, the normalised mass count of these complexes in abiotic leached samples were at  $\sim 0.25 \pm 0.6$  % of the sum recorded signal for REE and REE-oxides. This was about 200 times stronger than the recorded signal for the untreated control.

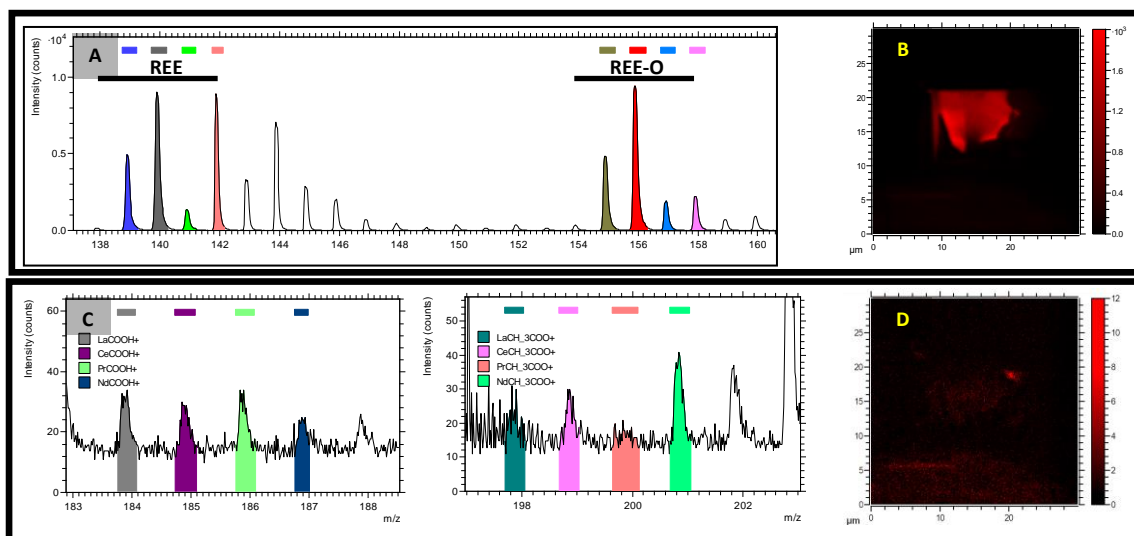


**Figure 7.** ION-ToF-SIMS signals for REE-organic acids complexes after 5 days of abiotic leaching of a monazite-muscovite sample. **A)** ToF-SIMS mass spectrum and **B)** ToF-SIMS distribution heatmap map of the rare earth (REE) and their oxides (REE-O). **C)** Mass spectrum and **D)** the chemical distribution heat map of REE complexes with formate and acetate.

### 3.2.3 ION-TOF-SIMS analysis of the bioleached samples

Analysis of monazite-muscovite after 24 hours of bioleaching showed a significantly stronger signal for organic acids ( $p < 0.05$ , Figure 8). The normalised mass count of the REE-OA complex after only one day of bioleaching was at  $\sim 0.32 \pm 0.5$  % of the recorded signal of the sum of REE and REE-oxides, a 20 % increase compared to the normalised signal for abiotic leached samples for 14 days. The normalised mass count signals for formate and acetate were the strongest in these samples. This could be due to high production and secretion of these acids by *K. aerogenes*<sup>10,12</sup>. Also, acetate is produced through acetate metabolism pathways or assimilates into other microbial biomass via glyoxylate cycle and tricarboxylic acid cycle<sup>32</sup>. Therefore, it was readily available in microbial cells and was expected to collect high ToF-SIMS mass count for acetate explaining why the strongest signal for REE-OA complex was recorded for acetate (Figure 8-D) on a monazite-muscovite samples bioleached for 24 h.

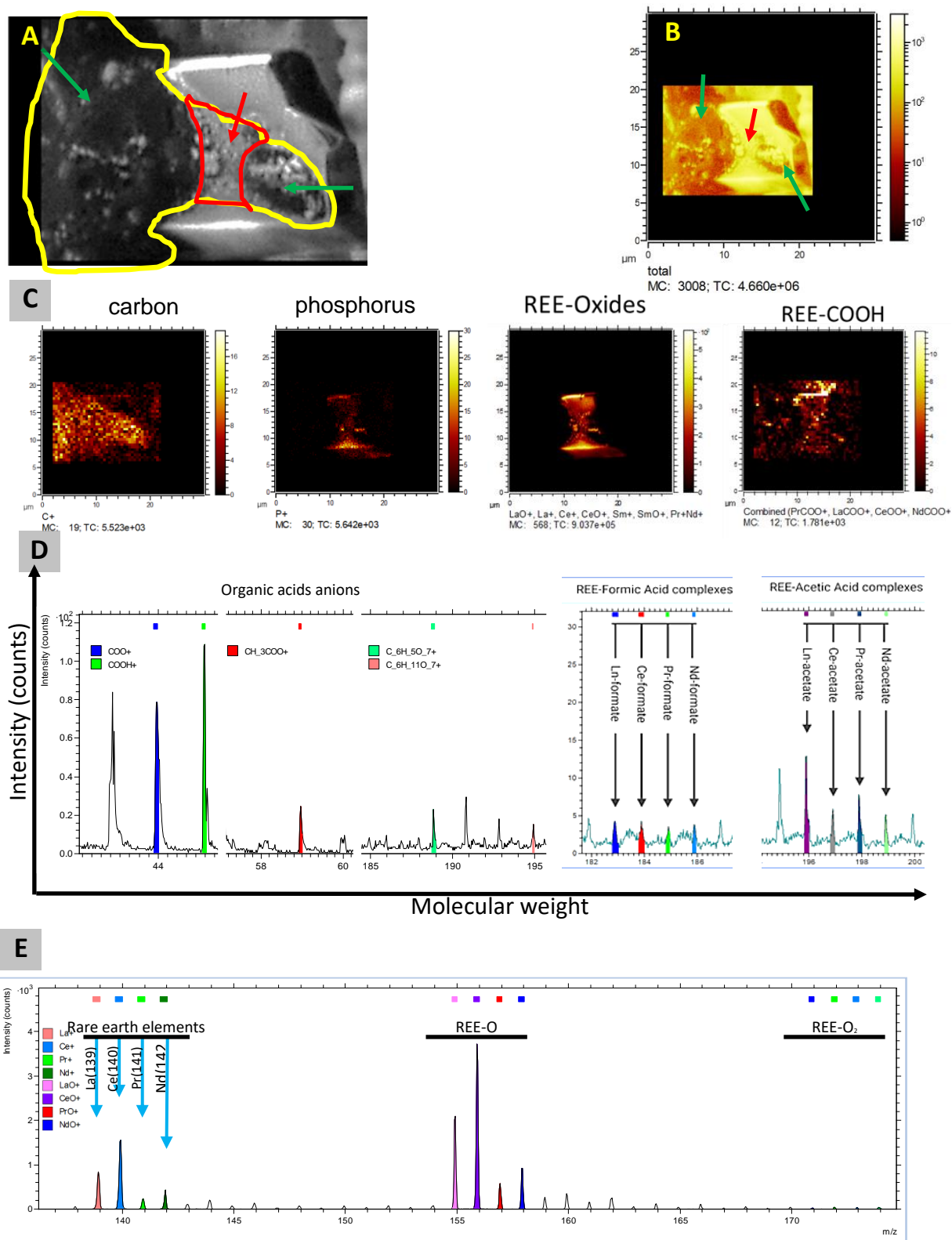


**Figure 8.** ION-ToF-SIMS signals for REE-organic acids complexes on a bioleached monazite-muscovite. **A)** Biofilm border is shown with yellow line, green arrows indicate bacterial cells and red enclosed shape, and arrows are indicating the extracellular polymeric substances (EPS)



of the biofilm matrix. **B)** Location of the bacteria, EPS, and mineral on the ToF-SIMS chemical distribution heatmap map. The image is made from the total mass count acquired from ToF-SIMS. **C)** ToF-SIMS distribution heat map of the carbon, phosphorus, rare earth oxides (REE-O) and rare earth complex with mono carboxylic acid group (REE-COOH). **D)** IONToF-SIMS mass spectrum of the organic acid residues and the REE complexes with formate and acetate. **E)** IONToF-SIMS mass spectrum of the REE and REE-O.

Analysis of the bioleached samples for five days showed a significantly stronger normalised mass count for organic acids and their complexes with REE (Figure 9). The organic acid ToF-SIMS mass count signal acquired from these samples showed a  $75\pm 12\%$  increase in the ToF-SIMS mass signal compared to samples bioleached for only one day. There were also very sharp signals for complexes between formate, acetate, malate, citrate and gluconate with REE (Figure 9- C and D). The normalised mass count of the REE-OA complex was at  $0.9\pm 0.3\%$  of the recorded signal of the sum of REE and REE-oxides, a significant increase compared to the one-day bioleaching (300% increase) and abiotic leached (360% increase) samples.

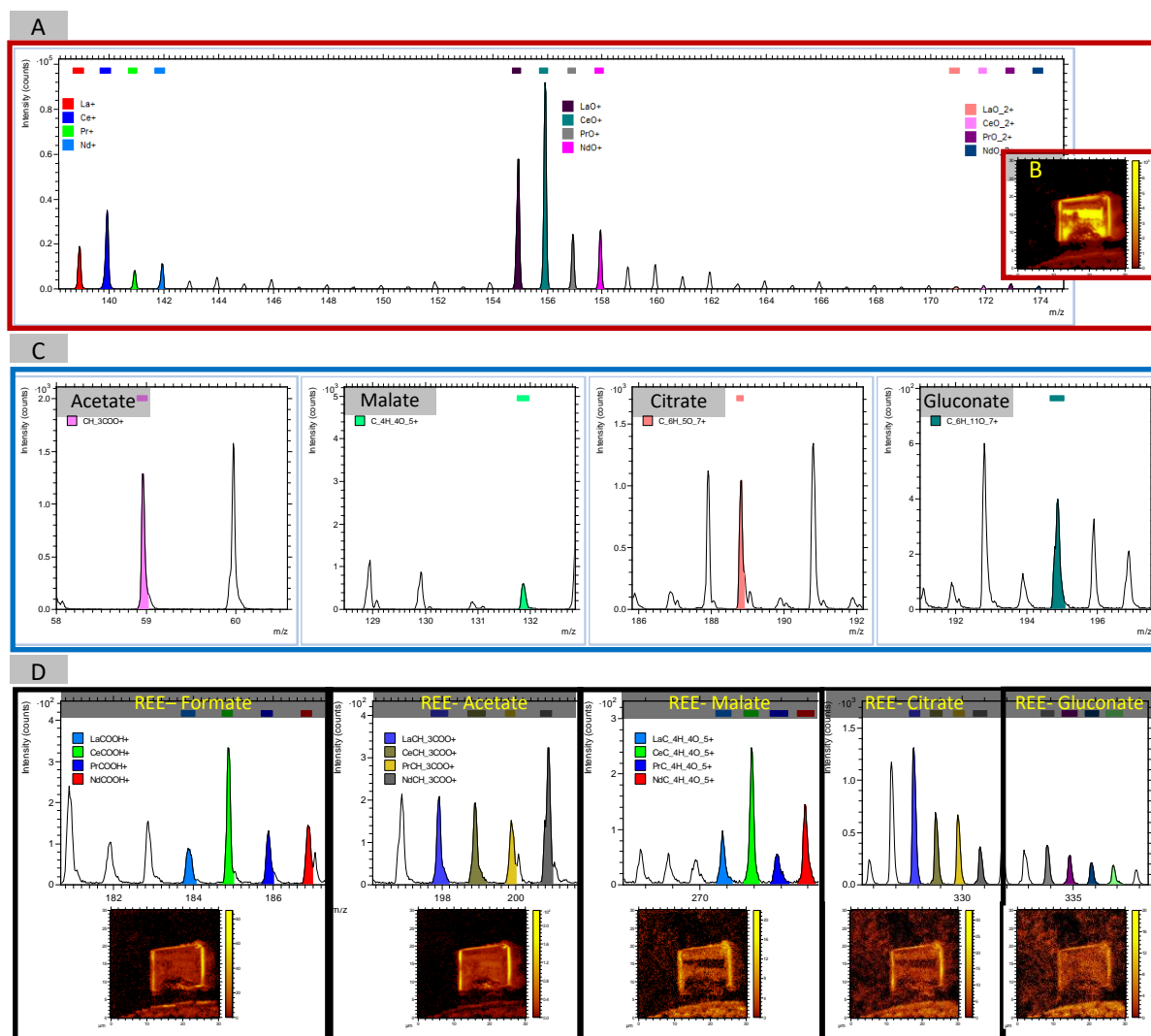


**Figure 9.** ION-ToF-SIMS signals for REE-organic acids complexes on a monazite-muscovite sample bioleached for 14 days. **A)** ToF-SIMS mass spectrum and **B)** ToF-SIMS distribution heat map of the rare earth (REE) and their oxides (REE-O and REE-O<sub>2</sub>). **C)** ToF-SIMS mass spectrum of five organic acid anions produced by *Klebsiella aerogenes*. **D)** ToF-SIMS mass spectrum and the ToF-SIMS distribution heat map of the REE-OA complexes between those five organic acid anions and REE after.

Although further investigation is needed to understand the dissolution process and the stability of REE complexes in the presence of different ligands<sup>33</sup>, the results of this study

provided the first empirical evidence of complex formation between organic acids and REE in REE-phosphate leached samples. Moreover, this study showed that not only the REE-OA complexes were formed under both abiotic and biotic leaching, but the presence of microbial biofilm also significantly enhanced formation of such complexes. The proposed contact bioleaching model suggested that the microbial community attached to the surface of phosphate minerals produced and released organic acids into their EPS matrix<sup>8,11</sup>. The protons attacked the mineral surface and dissolved the phosphate, simultaneously releasing the REE cations. These cations could then form complexes with the organic acids anions<sup>8</sup> entrapped within the biofilm matrix. EPS matrix can contain higher concentrations of organic acids and protons within the biofilm, therefore increasing the dissolution of phosphate<sup>18</sup>. It can also adsorb and entrap the cations into the biofilm matrix<sup>34</sup>. EPS components including polysaccharides, proteins and nucleic acid polymers are capable of interaction with cations. eDNA for example can form strong bonds with divalent cations such as  $\text{Ca}^{2+}$  or  $\text{Mg}^{2+}$ <sup>35</sup>. This can lead to higher concentration of REE cations within the biofilm matrix therefore increasing the potential complex formation with the organic acid anions released to the biofilm matrix of PSMs<sup>8,11,33</sup>. This reconfirms the role and significance of microbial attachment to the mineral surface<sup>8,11,18</sup> leading to an increase in bioleaching efficiency.

#### **4. Conclusion**

The capacity of phosphate solubilising microorganisms to produce high concentrations of organic acids not only contributes to leaching rare earth elements cations from phosphate minerals, but also enhances potential complex formation between organic acids and rare earth cations. The IONToF-SIMS analysis of the mineral surface of abiotic leached monazite-

muscovite samples as well as the microbe-mineral interface of the bioleached minerals showed a substantial increase in the REE-OA signal, compared to untreated samples. The signal intensity of REE-OA complex formation was significantly amplified in the presence of microbial biofilm. In terms of the bioleaching ecosystem, these findings suggested that microbial biofilms play a crucial role in enhancing the formation of OA-REE complexes. The EPS matrix of the microbial biofilm not only act as an adsorbent for a higher concentration of REE cation but also entraps the REE cation complex with OA acids within the confines of the biofilm, thereby intensifying its concentration. These findings imply that fostering conditions that promote microbial biofilm formation could be a potential strategy to improve bioleaching efficiency. By doing so, the biofilm's ability to trap and concentrate REE cation complexes could be leveraged, potentially leading to more efficient bioleaching processes. This strategy could be further optimised by exploring different types of organic acids and their effects on REE complex formation and stability.

## References

1. Kaksonen AH, Boxall NJ, Gumulya Y, et al. Recent progress in biohydrometallurgy and microbial characterisation. *Hydrometallurgy*. 2018;180:7-25. doi:10.1016/j.hydromet.2018.06.018
2. Xia MC, Bao P, Liu AJ, et al. Bioleaching of low-grade waste printed circuit boards by mixed fungal culture and its community structure analysis. *Resources Conservation and Recycling*. 2018;136:267-275. doi:10.1016/j.resconrec.2018.05.001
3. Auerbach R, Bokelmann K, Stauber R, et al. Bioleaching for the Recycling of Secondary Raw Materials. *Chemie in Unserer Zeit*. 2018;52(5):330-340. doi:10.1002/ciuz.201800829
4. Gumulya Y, Boxall NJ, Khaleque HN, Santala V, Carlson RP, Kaksonen AH. In a Quest for Engineering Acidophiles for Biomining Applications: Challenges and Opportunities. *Genes*. 2018;9(2)doi:ARTN 116 10.3390/genes9020116
5. Abdollahi H, Shafaei SZ, Gharabaghi M, Jafari H, Akcil A, Panda S. Acidophilic bioleaching: a review on the process and effect of organic–inorganic reagents and materials on its efficiency AU - Jafari, Mohammad. *Mineral Processing and Extractive Metallurgy Review*. 2018:1-21. doi:10.1080/08827508.2018.1481063
6. Natarajan KA. Chapter 4 - Bioleaching Mechanisms. In: Natarajan KA, ed. *Biotechnology of Metals*. Elsevier; 2018:49-80. doi:<https://doi.org/10.1016/B978-0-12-804022-5.00004-9>
7. Natarajan KA. Chapter 3 - Microbiological Aspects of Leaching Microorganisms. In: Natarajan KA, ed. *Biotechnology of Metals*. Elsevier; 2018:29-47. doi:<https://doi.org/10.1016/B978-0-12-804022-5.00003-7>
8. Fathollahzadeh H, Eksteen JJ, Kaksonen AH, Watkin ELJ. Role of microorganisms in bioleaching of rare earth elements from primary and secondary resources. *Applied Microbiology and Biotechnology*. 2019;103(3):1043-1057. doi:10.1007/s00253-018-9526-z
9. Kishore N, Pindi PK, Ram Reddy S. Phosphate-Solubilizing Microorganisms: A Critical Review. In: Bahadur B, Venkat Rajam M, Sahijram L, Krishnamurthy KV, eds. *Plant Biology and Biotechnology: Volume I: Plant Diversity, Organization, Function and Improvement*. Springer India; 2015:307-333. doi:10.1007/978-81-322-2286-6\_12
10. Corbett MK, Eksteen JJ, Niu X-Z, Croue J-P, Watkin ELJB, Engineering B. Interactions of phosphate solubilising microorganisms with natural rare-earth phosphate minerals: a study utilizing Western Australian monazite. 2017;40(6):929-942. doi:10.1007/s00449-017-1757-3
11. Fathollahzadeh H, Becker T, Eksteen JJ, Kaksonen AH, Watkin ELJ. Microbial contact enhances bioleaching of rare earth elements. *Bioresource Technology Reports*. 2018-a;3:102-108. doi:<https://doi.org/10.1016/j.biteb.2018.07.004>
12. Corbett MK, Eksteen JJ, Niu X-Z, Watkin ELJ. Syntrophic effect of indigenous and inoculated microorganisms in the leaching of rare earth elements from Western Australian monazite. *Research in Microbiology*. 2018;169(10):558-568. doi:<https://doi.org/10.1016/j.resmic.2018.05.007>
13. Banerjee R, Chakladar S, Mohanty A, Chakravarty S, Chattopadhyay SK, Jha MK. Review on the environment friendly leaching of rare earth elements from the secondary resources using organic acids. *Geosystem Engineering*. 2022;25(3-4):95-115. doi:10.1080/12269328.2022.2135139
14. Wood SA. The aqueous geochemistry of the rare-earth elements: Critical stability constants for complexes with simple carboxylic acids at 25°C and 1 bar and their application to nuclear waste management. *Engineering Geology*. 1993;34(3):229-259. doi:[https://doi.org/10.1016/0013-7952\(93\)90092-Q](https://doi.org/10.1016/0013-7952(93)90092-Q)
15. Kolat RS, Powell JE. Acetate Complexes of the Rare Earth and Several Transition Metal Ions. *Inorganic Chemistry*. 1962;1(2):293-296. doi:10.1021/ic50002a019
16. Janicki R, Mondry A, Starynowicz P. Carboxylates of rare earth elements. *Coordination Chemistry Reviews*. 2017;340:98-133. doi:<https://doi.org/10.1016/j.ccr.2016.12.001>
17. Pourret O, Davranche M, Gruau G, Dia A. Rare earth elements complexation with humic acid. *Chemical Geology*. 2007;243(1):128-141. doi:<https://doi.org/10.1016/j.chemgeo.2007.05.018>

18. van Alin A, Corbett MK, Fathollahzadeh H, et al. Biofilm formation on the surface of monazite and xenotime during bioleaching. *Microbial Biotechnology*. 2023;16(9):1790-1802. doi:<https://doi.org/10.1111/1751-7915.14260>
19. Van Alin A, Corbett MK, Fathollahzadeh H, et al. Klebsiella aerogenes Adhesion Behaviour during Biofilm Formation on Monazite. *Microorganisms*. 2023;11(5). doi:10.3390/microorganisms11051331
20. Fager C, Röding M, Olsson A, et al. Optimization of FIB–SEM Tomography and Reconstruction for Soft, Porous, and Poorly Conducting Materials. *Microscopy and Microanalysis*. 2020;26(4):837-845. doi:10.1017/S1431927620001592
21. Wirth R. Focused Ion Beam (FIB) combined with SEM and TEM: Advanced analytical tools for studies of chemical composition, microstructure and crystal structure in geomaterials on a nanometre scale. *Chemical Geology*. 2009;261(3):217-229. doi:<https://doi.org/10.1016/j.chemgeo.2008.05.019>
22. Kosasih FU, Cacovich S, Divitini G, Ducati C. Nanometric Chemical Analysis of Beam-Sensitive Materials: A Case Study of STEM-EDX on Perovskite Solar Cells. *Small Methods*. 2021;5(2):2000835. doi:<https://doi.org/10.1002/smt.202000835>
23. Batista AH, Melo VF, Gilkes R. Scanning and transmission analytical electron microscopy (STEM-EDX) identifies minor minerals and the location of minor elements in the clay fraction of soils. *Applied Clay Science*. 2017;135:447-456. doi:<https://doi.org/10.1016/j.clay.2016.10.032>
24. Jia F, Zhao X, Zhao Y. Advancements in ToF-SIMS imaging for life sciences. *Front Chem*. 2023;11:1237408. doi:10.3389/fchem.2023.1237408
25. Rellán-Álvarez R, López-Gomollón S, Abadía J, Álvarez-Fernández A. Development of a New High-Performance Liquid Chromatography–Electrospray Ionization Time-of-Flight Mass Spectrometry Method for the Determination of Low Molecular Mass Organic Acids in Plant Tissue Extracts. *Journal of Agricultural and Food Chemistry*. 2011;59(13):6864-6870. doi:10.1021/jf200482a
26. Kim Y, Morita Y, Owari M. Three-Dimensional Analysis of Biological Samples using Dual FIB ToF-SIMS. *Journal of Surface Analysis*. 2011;17(3):337-340. doi:10.1384/jsa.17.337
27. Zhang R, Neu TR, Blanchard V, Vera M, Sand W. Biofilm dynamics and EPS production of a thermoacidophilic bioleaching archaeon. *New Biotechnology*. 2019;51:21-30. doi:<https://doi.org/10.1016/j.nbt.2019.02.002>
28. Kumar PS, Yaashikaa PR. Chapter 20 - Recent trends and challenges in bioleaching technologies. In: Krishnaraj Rathinam N, Sani RK, eds. *Biovalorisation of Wastes to Renewable Chemicals and Biofuels*. Elsevier; 2020:373-388. doi:<https://doi.org/10.1016/B978-0-12-817951-2.00020-1>
29. Karygianni L, Ren Z, Koo H, Thurnheer T. Biofilm Matrixome: Extracellular Components in Structured Microbial Communities. *Trends in Microbiology*. 2020;28(8):668-681. doi:<https://doi.org/10.1016/j.tim.2020.03.016>
30. Pillatsch L, Östlund F, Michler J. FIBSIMS: A review of secondary ion mass spectrometry for analytical dual beam focussed ion beam instruments. *Progress in Crystal Growth and Characterization of Materials*. 2019;65(1):1-19. doi:<https://doi.org/10.1016/j.pcrysgrow.2018.10.001>
31. Stegmann H, Schulz H, Whitby J. FIB-SIMS in FIB-SEMs—Practical Aspects for Physical Failure Analysis. ISTFA 2022; 2022; Accessed 7/1/2024. doi:10.31399/asm.cp.istfa2022p0257
32. Hosmer J, McEwan AG, Kappler U. Bacterial acetate metabolism and its influence on human epithelia. *Emerging Topics in Life Sciences*. 2023;8(1):1-13. doi:10.1042/ETLS20220092
33. Fathollahzadeh H, Khaleque HN, Eksteen J, Kaksonen AH, Watkin ELJ. Effect of glycine on bioleaching of rare earth elements from Western Australian monazite by heterotrophic and autotrophic microorganisms. *Hydrometallurgy*. 2019;189:105137. doi:<https://doi.org/10.1016/j.hydromet.2019.105137>
34. Wang J, Tian B, Bao Y, et al. Functional exploration of extracellular polymeric substances (EPS) in the bioleaching of obsolete electric vehicle LiNi<sub>x</sub>CoyMn<sub>1-x-y</sub>O<sub>2</sub> Li-ion batteries. *Journal of Hazardous Materials*. 2018;354:250-257. doi:<https://doi.org/10.1016/j.jhazmat.2018.05.009>
35. Okshevsky M, Meyer RL. The role of extracellular DNA in the establishment, maintenance and perpetuation of bacterial biofilms. *Critical Reviews in Microbiology*. 2015;41(3):341-352. doi:10.3109/1040841X.2013.841639

## Supplementary

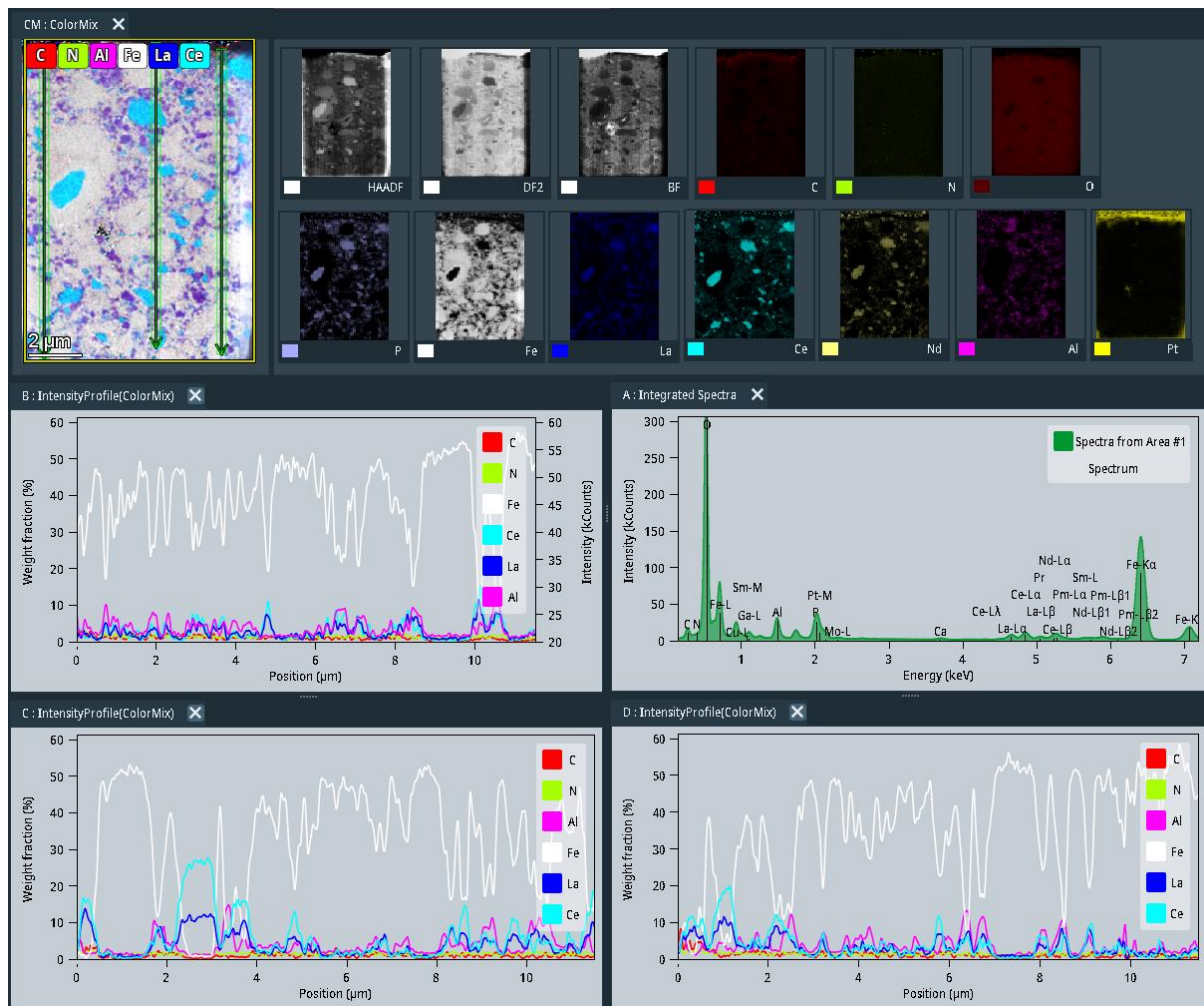


**Figure S-1** Depth profile analysis of abiotic leaching of HGMO sample.



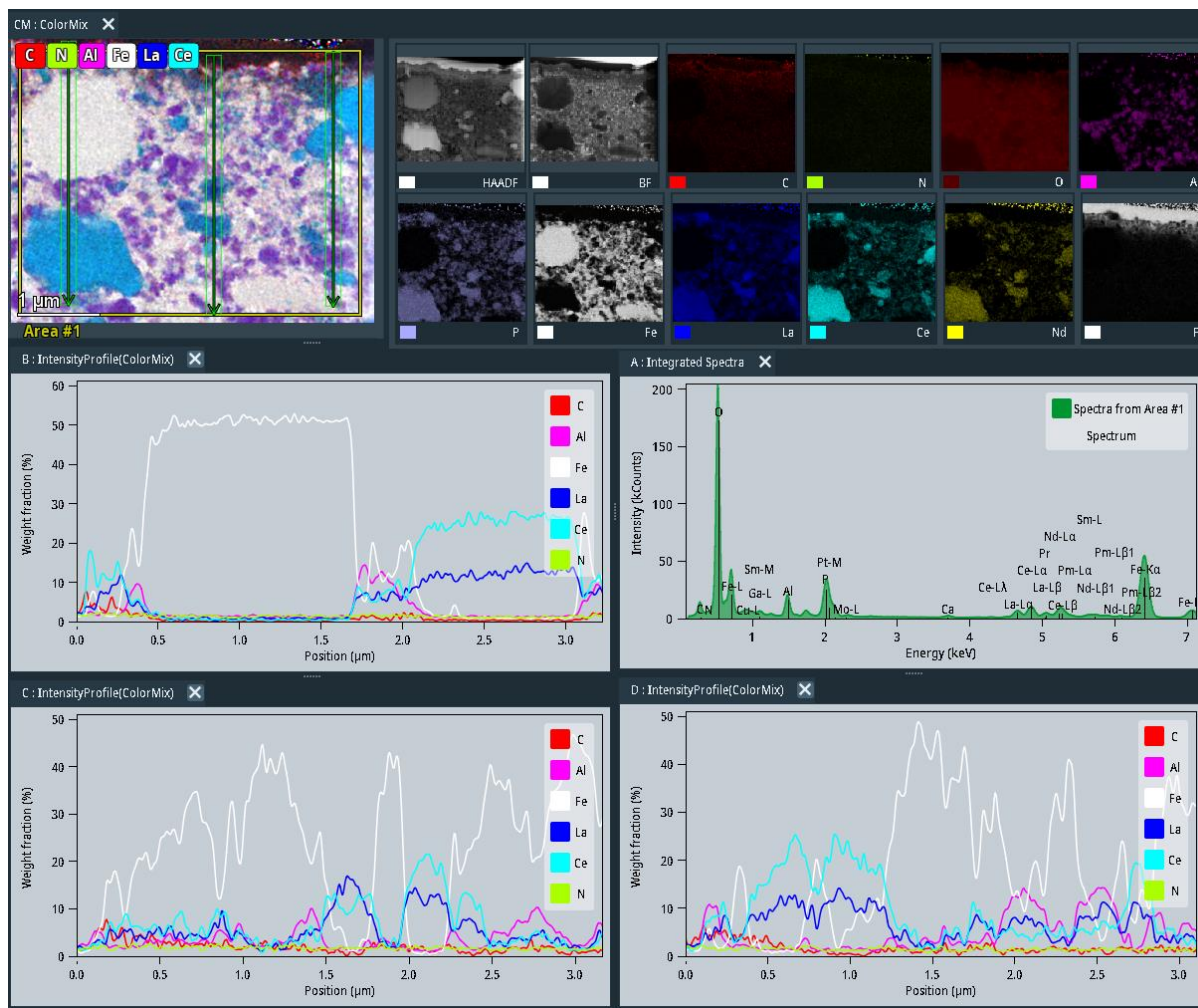
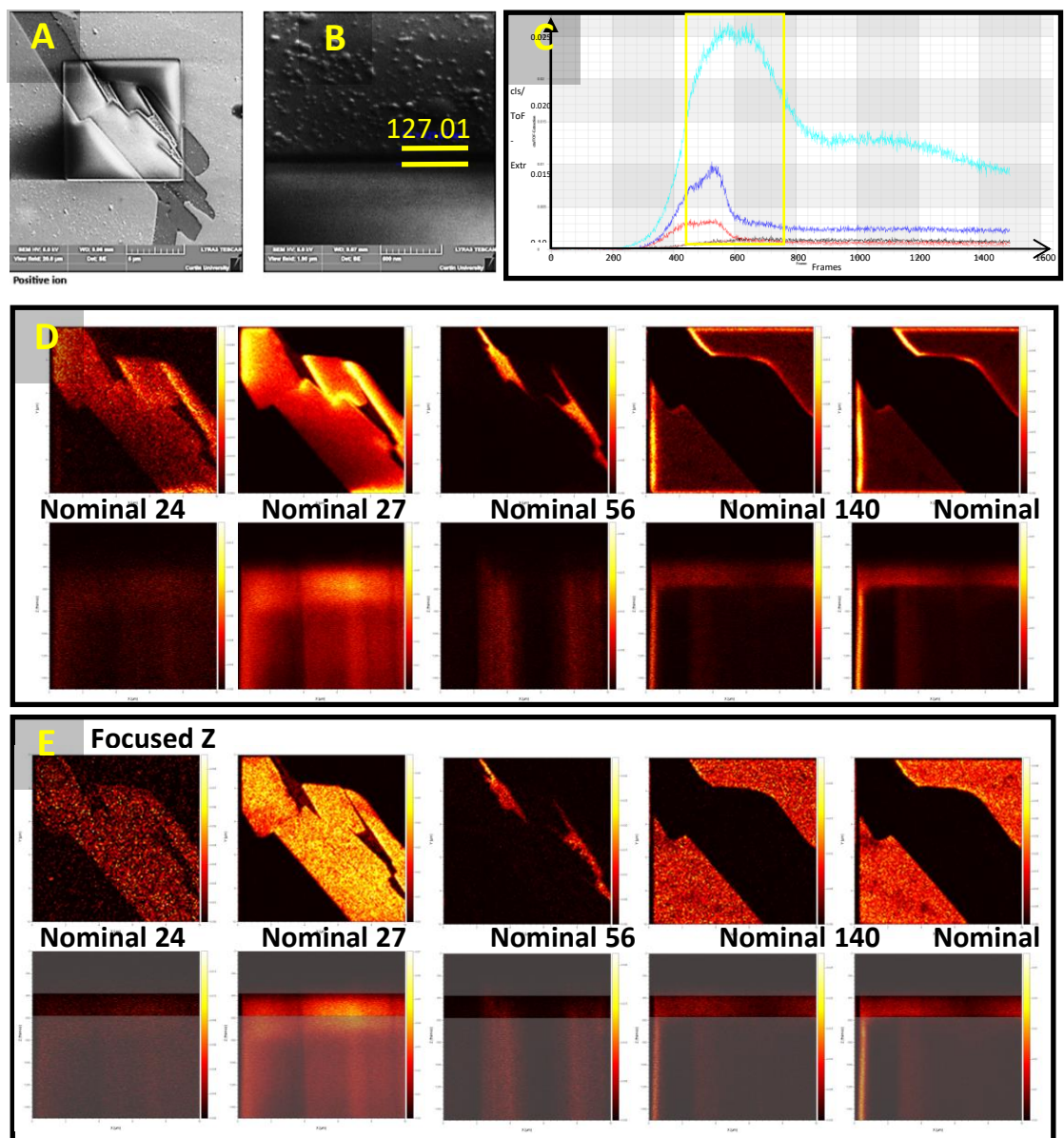


Figure S-2 Depth profile analysis of abiotic leaching of HGMO sample.



**Figure S-3.** FIB-ToF-SIMS of an abiotically bioleached monazite-muscovite sample. The region of interest was a 10×10 μm area. **A)** The region of interest after FIB-ToF-SIMS analysis. **B)** The thickness of the analysed area was 127 nm. **C)** ToF-SIMS spectrum of intensity count per nanometre distance from the mineral surface. Each nm is equal to 12 frames. The nominal line represent the TOF-SIMS signal intensity acquired for three element and two compound (C<sub>2</sub>=24, Al=27, Fe = 56, Ce = 140, and CeO=156). ToF-SIMS distribution heat map of the 5 elements and compounds **D)** before **E)** and after focussing the signal on the conductive region (focused Z).

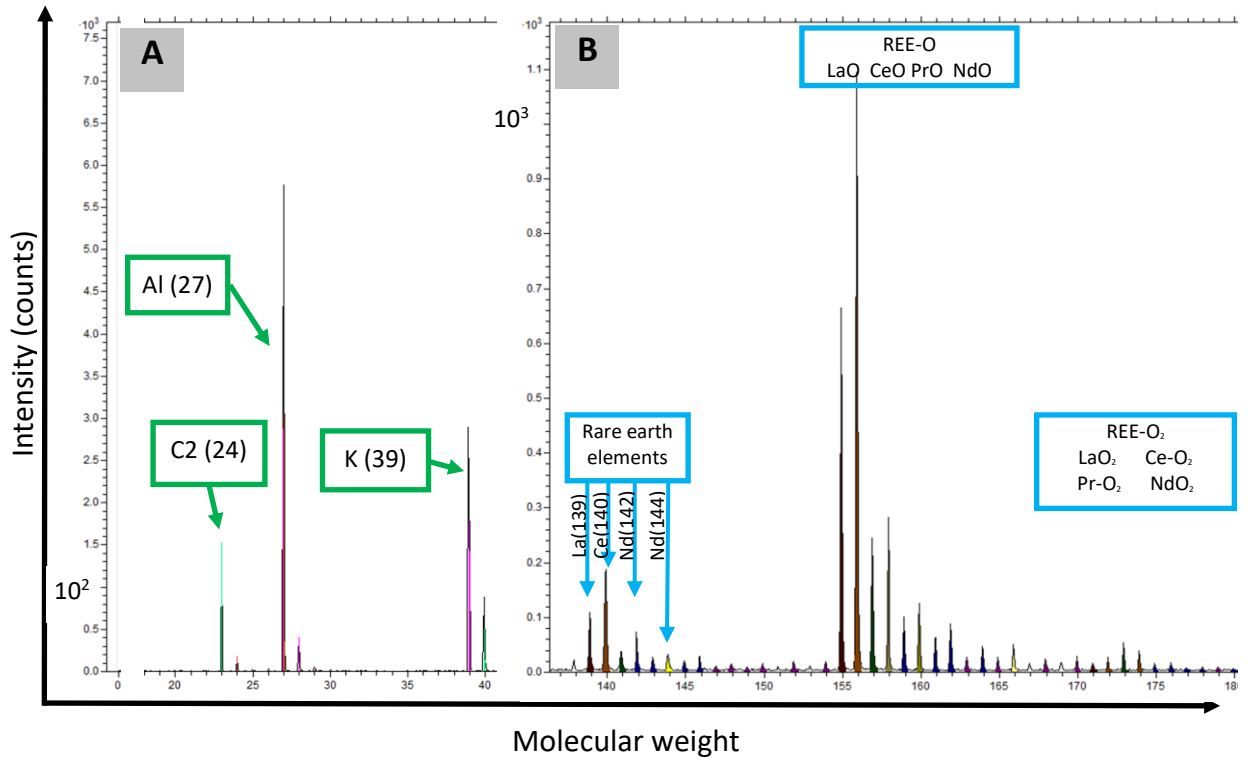
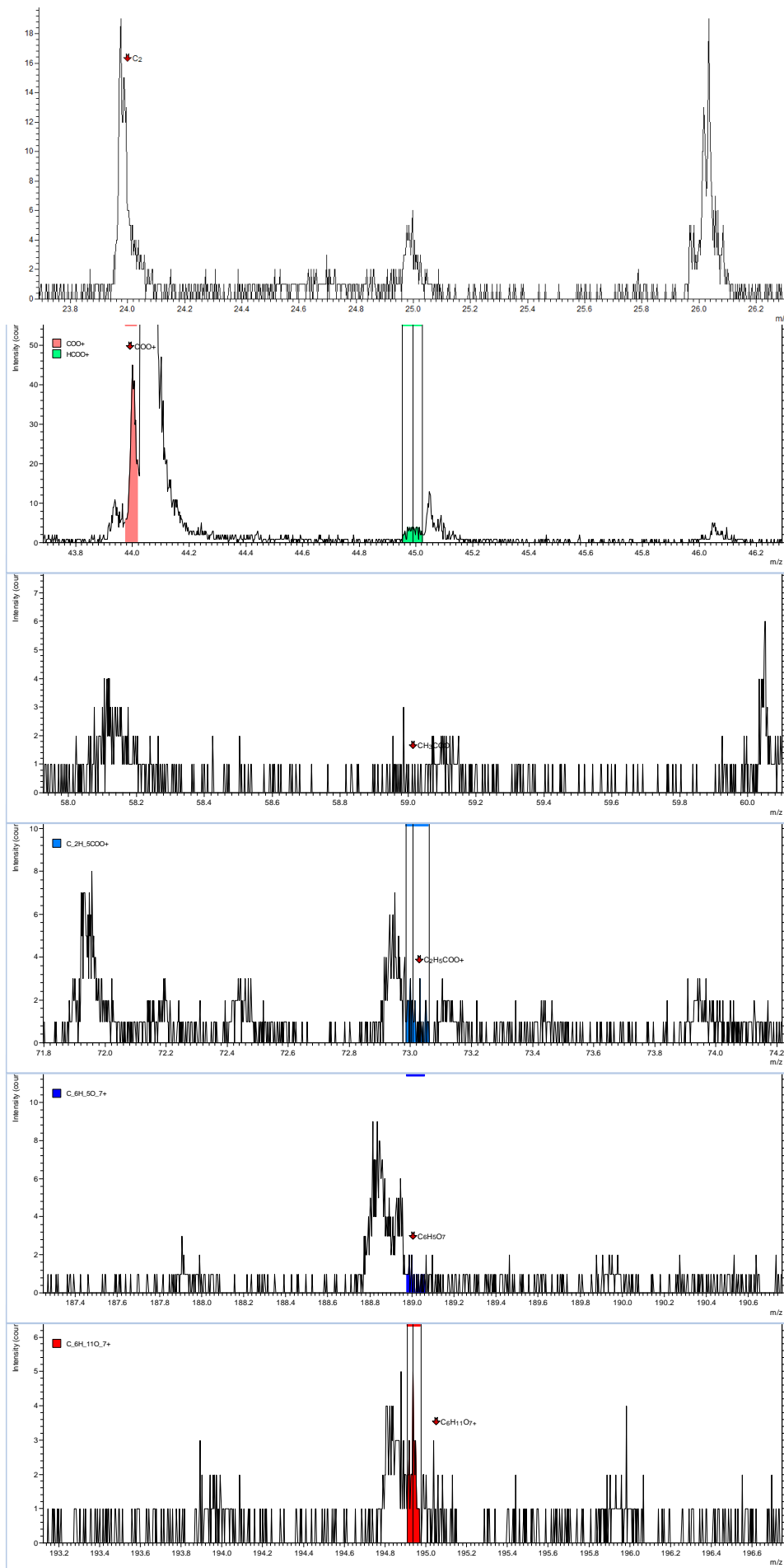
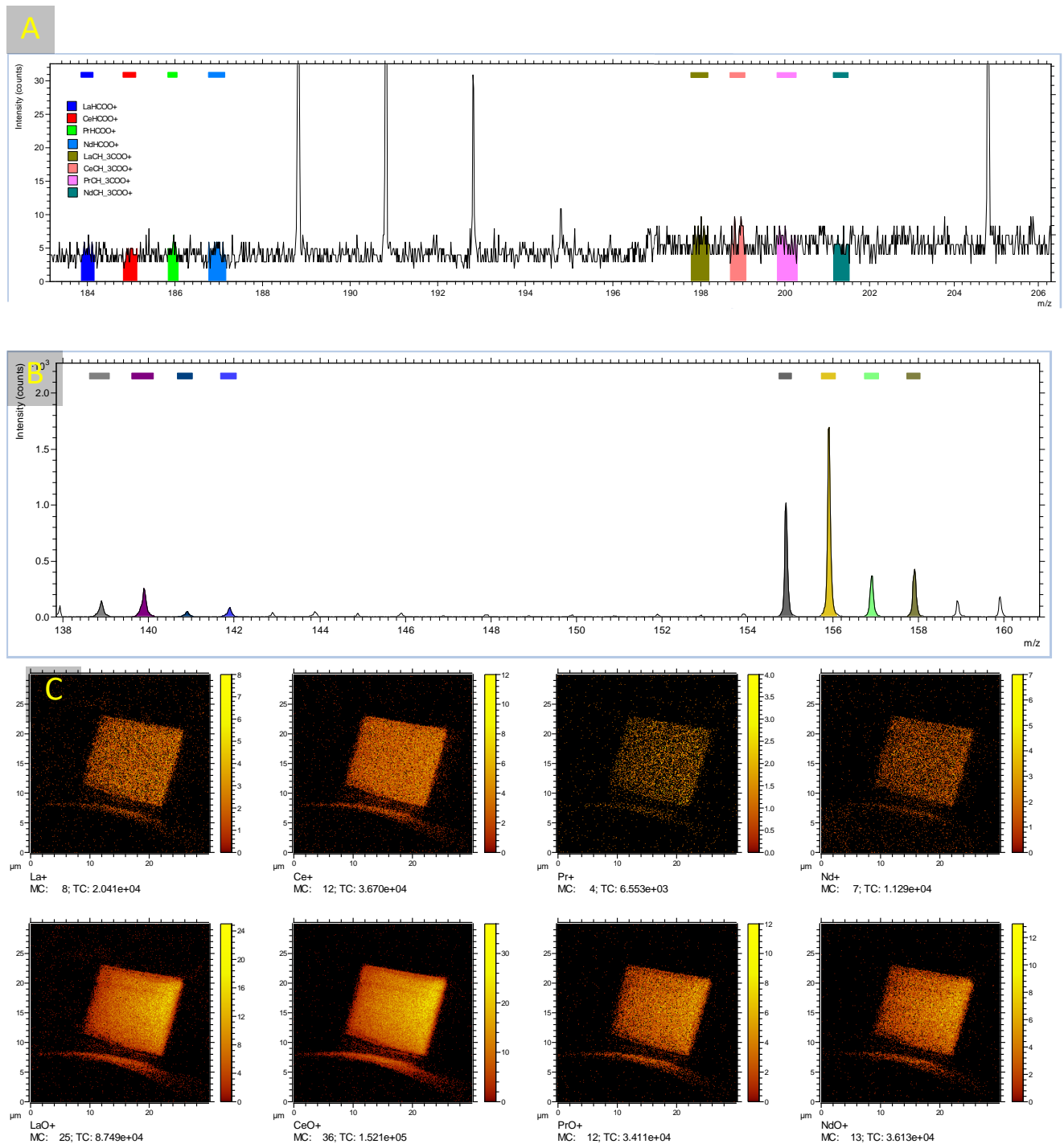


Figure S-4 ION-ToF-SIMS signal of the control elements and compounds



**Figure S-5** ION-ToF-SIMS mass spectrum of the organic compounds in control monazite-muscovite sample before any leaching. In all panels X-axis is the molecular weight, and Y-axis is the mass count. The colours, red arrows or 3-lined box shows where the mass spectra for the compound of interest is expected.



**Figure S-6 A)** ION-ToF-SIMS mass spectrum) of the organic compounds in control monazite-muscovite sample (sample 2) before any leaching. X-axis = molecular mass, Y-axis = mass count. The colours, Coloured area indicates the location of these organic acid on the mass spectrum plots. **B)** Mass spectrum plot and **C)** distribution map of the rear earth elements and their oxides.

# **Chapter Seven**

## **General Discussion**



Biofilm is a universal attribute and the prevalent form of microbial life in natural ecosystems for most microorganisms, if not all<sup>1</sup>. Previous studies have shown that microbial attachment to phosphate minerals significantly increased bioleaching efficiency<sup>2,3</sup>. However, there was not enough empirical evidence demonstrating how phosphate solubilising microorganisms (PSM) attach to these minerals and develop a biofilm. To study biofilm development on phosphate minerals, *Klebsiella aerogenes* was used as the model PSM, due to its performance in previous studies<sup>2,4,5</sup>. Among the tested microorganisms, *K. aerogenes* had the highest bioleaching yield. Results of this study showed that *K. aerogenes* attached and formed a thin biofilm on the surface of the phosphate minerals tested. Three distinctive stages of biofilm formation were observed. The first was the initial attachment, followed by the second stage, colonisation of the surface and development of mature biofilm and finally, the majority of the microbial cells detached from the surface in the third stage, known as dispersion.

Initial attachment of *K. aerogenes* started early as exposure to the high-grade monazite ore. This stage is a dynamic and reversible process in response to changes in environmental conditions<sup>6</sup>. In general, extrinsic factors such as nutrient availability in the aquatic environment, particle size affecting nutrient accessibility from an ore, flow and shear forces, pH, ionic strength, physical properties of the surface such as topological imperfections, and chemical properties or mineralogy of the surface all affect microbial attachment. During initial attachment of *K. aerogenes* to the monazite surface, bacterial population showed a significant shift from planktonic lifestyle to a sessile (attached to a surface) lifestyle. This could be due to the fact that monazite was providing the cells with a source of phosphate, therefore attracting more bacteria to the surface through chemotaxis<sup>7</sup>. Larger particle sizes with more physical imperfections attracted more planktonic cells to the surface of the monazite compared to smaller particles. Moreover, smaller initial inoculum size, or the provision of a

larger surface for attachment and colonisation shifted the equilibrium towards the sessile lifestyle. In addition to the chemo-physical conditions of the surface and the environmental conditions, intrinsic microbial properties such as extracellular appendages and the composition of the extracellular polymeric substances (EPS) can affect microbial attachment efficiency <sup>7-9</sup>. Attachment behaviour analysis showed eDNA, a key component of the *K. aerogenes* EPS, played a crucial role by assisting bacterial cells in initiating or mediating attachment to the mineral surface, therefore promoting biofilm formation <sup>10</sup>. The initial attachment stage and its intrinsic or extrinsic influencing factors could be future targets for engineering of bioleaching processes. This can be achieved by providing conditions that promote microbial attachment such as optimal grain and microbial inoculum size, or by ensuring that conditions for high eDNA production are established.

After initial attachment, *K. aerogenes* cells colonised the surface and developed a mature biofilm. The formation of a mature biofilm has biotechnological advantages in many industries including biomining. In bioleaching systems, attachment to the mineral surface and the development of a biofilm are important prerequisites of contact bioleaching <sup>2</sup>. Although the *K. aerogenes* biofilm on the monazite surface was thin with minimum structural complexity, it covered more than 80% of the total available surface on the ore grains. Moreover, approximately ~80% of *K. aerogenes* cells on HGMO produced eDNA at this stage of the biofilm development, twice of what was measured for the initial attachment stage. The twofold increase in eDNA content indicated that in addition to aiding *K. aerogenes* attachment to the surface, eDNA had other significant roles in biofilm formation on monazite, such as providing mechanical stability for the biofilm structure <sup>11,12</sup>. Moreover, biofilm development was not a random process, rather it was formed on and around the physical imperfections. Easier attachment was attributed to more favourable surface properties such

as energy, charge imbalance, hydrophobicity-hydrophilicity<sup>13</sup>, and degree of crystallinity<sup>14</sup> and have been suggested as reasons for selective attachment and biofilm formation on and around the topographical and physical imperfections by some microorganisms. The physical imperfection sites also provide a higher nutrient availability since these regions are known as potential active dissolution locals on the mineral surface<sup>15</sup>. Chemotactic attraction of microbial cells toward dissolution sites can also produce localised anode and cathode regions on mineral surfaces, consequently driving the dissolution process further. In such a system, the EPS of a biofilm fills the space between the microbial cells and the surface of the mineral as the matrix interface of the leaching reaction<sup>13</sup>. Therefore, biofilm and in particular the EPS matrix can also enhance bioleaching. These physical imperfection sites also provide safety from the sheer fluid force<sup>16</sup> providing protection against passive detachment due to weaker impacts of fluid shear forces or collisions with mineral particles floating around<sup>16,17</sup>, hence preventing early dispersion. Although no selectivity was observed toward certain mineralogy or chemical composition of the surface, the composition of biofilm matrix, in particular eDNA content, was significantly ( $P < 0.05$ ) affected by variation in surface mineralogy. Less eDNA was produced on xenotime compared to monazite, which could be a general physiological response to exposure to surfaces with different chemical composition (mineralogy)<sup>13</sup> or in response to potential toxicity of the REE metals<sup>18,19</sup> of xenotime<sup>20,21</sup>. Further analysis is required to determine the role of EPS in general and eDNA in bioleaching systems, nevertheless, promoting biofilm and EPS production can enhance bioleaching efficiency. eDNA content of EPS with a net negative charge can adsorb and capture the released cations from mineral. Therefore, enhancing biofilm formation or prolonging the biofilm life in bioleaching system can be used as another strategy to improve bioleaching efficiency of REE-phosphate minerals. Moreover, production, release and concentrating organic acids within

the biofilm matrix could be a contributing factor for such enhancement. The proton ions released from the organic acids attack the mineral surface and dissolve the phosphate content, consequently releasing the REE cations<sup>3</sup>. These organic acids can form complexes with the released REE from the mineral<sup>3</sup>. Scanning and transmission electron microscopy equipped with high resolution energy dispersive X-ray spectroscopy (STEM-EDX) detected traces of a carbon and nitrogen-based compound at the interface, immediate subsurface and even deep subsurface of the bioleached monazite. This, implied penetration of some organic compounds produced and released from the biofilm which is most likely the EPS. Time of flight secondary ion mass spectrometry (ToF-SIMS) analysis of the microbe-mineral interface of *K. aerogenes* biofilm on monazite detected a high concentration of organic acids. Moreover, ToF-SIMS analysis showed a significantly high concentration of REE-OA complex formation at the microbe-mineral interface. The ToF-SIMS analysis showed that there was a 300% increase in the REE-OA complex signal in the bioleached samples compared to abiotic leached samples. This could also explain the previously reported higher leaching efficiency when microorganisms were attached to the surface of REE-phosphate minerals<sup>2</sup>. Therefore, promoting biofilm formation can also enhance the bioleaching efficiency through improvement of both acidolysis and complexolysis. Further investigation is required to understand the stability of such complexes and how to be utilised for enhanced bioleaching yield.

Eventually dispersion of biofilm occurs. At this stage, microorganisms detach from the mineral surface leading to changes in the physical characteristics of the mineral surface such as erosion, or even formation of cracks on the mineral surface. How and why this process occurs is not well understood in bioleaching systems. This could be another topic for future research

to further promote bioleaching efficiency through understanding the mechanisms to delay this stage, thereby prolonging the mature biofilm stage.

### **Future directions**

Although the results of this study shed light on how biofilms develop on the surface of the REE-phosphate minerals, the significance of the sessile subpopulation is not clear. This could be explored by comparing the transcriptome and metabolome of the planktonic and sessile subpopulations of a PSM like *K. aerogenes*. Such analyses can provide more information regarding potential genes or their products that promote biofilm formation, prolong the mature biofilm stage, or delay dispersion. It can also shed light on the microbial metabolisms at each stage and provide a ground to optimise and engineer higher organic acid production by either of these subpopulations, or to further promote REE-OA complex formation.

Moreover, because *K. aerogenes* is an opportunistic pathogen, its *in-situ* application would be confined to semi-industrial levels within bioreactors. The reliance on glucose as a carbon source restricts its economical use. Future studies should consider investigating cheaper and more accessible carbon sources including agricultural wastes, whey, winery wastewater, and other carbohydrate- or protein-rich wastes. Additionally, examining the potential use of non-pathogenic microorganisms for bioleaching phosphate minerals is suggested, as this would allow for *in-situ* applications with fewer limitations than those associated with *K. aerogenes*. Another less studied aspect of REE-phosphate bioleaching is the fate of phosphate. PSMs dissolve the phosphate content of the REE-phosphate minerals by producing organic acids. It is not understood how the released phosphate is taken up by the planktonic or sessile subpopulations and how it can affect the bioleaching. A combined approach including single-molecule microscopy

and omics is suggested to explain how the released phosphate is metabolised by either microbial subpopulations. The response to the released phosphate, and its concentrations in terms of regulating the genes activation/deactivation and their respected products, whether being an enzymatic activity or a metabolite is of interest and further investigations are recommended. .

## References

1. Rumbaugh KP, Sauer K. Biofilm dispersion. *Nature Reviews Microbiology*. 2020;doi:10.1038/s41579-020-0385-0
2. Fathollahzadeh H, Becker T, Eksteen JJ, Kaksonen AH, Watkin ELJ. Microbial contact enhances bioleaching of rare earth elements. *Bioresource Technology Reports*. 2018-a;3:102-108. doi:<https://doi.org/10.1016/j.biteb.2018.07.004>
3. Fathollahzadeh H, Eksteen JJ, Kaksonen AH, Watkin ELJ. Role of microorganisms in bioleaching of rare earth elements from primary and secondary resources. *Applied Microbiology and Biotechnology*. 2019;103(3):1043-1057. doi:10.1007/s00253-018-9526-z
4. Fathollahzadeh H, Hackett MJ, Khaleque HN, Eksteen JJ, Kaksonen AH, Watkin ELJ. Better together: Potential of co-culture microorganisms to enhance bioleaching of rare earth elements from monazite. *Bioresource Technology Reports*. 2018-b;3:109-118. doi:<https://doi.org/10.1016/j.biteb.2018.07.003>
5. Corbett MK, Eksteen JJ, Niu X-Z, Croue J-P, Watkin ELJB, Engineering B. Interactions of phosphate solubilising microorganisms with natural rare-earth phosphate minerals: a study utilizing Western Australian monazite. 2017;40(6):929-942. doi:10.1007/s00449-017-1757-3
6. Kostakioti M, Hadjifrangiskou M, Hultgren SJ. Bacterial Biofilms: Development, Dispersal, and Therapeutic Strategies in the Dawn of the Postantibiotic Era. *Cold Spring Harbor Perspectives in Medicine*. 2013;3(4)doi:10.1101/cshperspect.a010306
7. Berne C, Ellison CK, Ducret A, Brun YV. Bacterial adhesion at the single-cell level. *Nature Reviews Microbiology*. 2018;16(10):616-627. doi:10.1038/s41579-018-0057-5
8. Flemming HC, Wingender J. The biofilm matrix. *Nat Rev Microbiol*. 2010;8(9):623-633. doi:10.1038/nrmicro2415
9. Flemming HC, Wingender J, Szewzyk U, Steinberg P, Rice SA, Kjelleberg S. Biofilms: an emergent form of bacterial life. *Nat Rev Microbiol*. 2016;14(9):563-575. doi:10.1038/nrmicro.2016.94
10. Okshevsky M, Meyer RL. The role of extracellular DNA in the establishment, maintenance and perpetuation of bacterial biofilms. *Critical Reviews in Microbiology*. 2015;41(3):341-352. doi:10.3109/1040841X.2013.841639
11. Panlilio H, Rice CV. The role of extracellular DNA in the formation, architecture, stability, and treatment of bacterial biofilms. *Biotechnology and Bioengineering*. 2021;118(6):2129-2141. doi:<https://doi.org/10.1002/bit.27760>
12. Secchi E, Savorana G, Vitale A, Eberl L, Stocker R, Rusconi R. The structural role of bacterial eDNA in the formation of biofilm streamers. *Proceedings of the National Academy of Sciences*. 2022;119(12):e2113723119. doi:10.1073/pnas.2113723119
13. Zhang R, Bellenberg S, Neu TR, Sand W, Vera M. The Biofilm Lifestyle of Acidophilic Metal/Sulfur-Oxidizing Microorganisms. In: Rampelotto PH, ed. *Biotechnology of Extremophiles: Advances and Challenges*. Springer International Publishing; 2016:177-213. doi:10.1007/978-3-319-13521-2\_6
14. Sanhueza A, Ferrer IJ, Vargas T, Amils R, Sánchez C. Attachment of *Thiobacillus ferrooxidans* on synthetic pyrite of varying structural and electronic properties. *Hydrometallurgy*. 1999;51(1):115-129. doi:[https://doi.org/10.1016/S0304-386X\(98\)00079-6](https://doi.org/10.1016/S0304-386X(98)00079-6)

15. Croizé D, Renard F, Bjørlykke K, Dysthe DK. Experimental calcite dissolution under stress: Evolution of grain contact microstructure during pressure solution creep. *Journal of Geophysical Research: Solid Earth*. 2010;115(B9)doi:<https://doi.org/10.1029/2010JB000869>
16. Bellenberg S, Barthen R, Boretska M, Zhang R, Sand W, Vera M. Manipulation of pyrite colonization and leaching by iron-oxidizing Acidithiobacillus species. *Appl Microbiol Biotechnol*. 2015;99(3):1435-1449. doi:10.1007/s00253-014-6180-y
17. Chiume R, Minnaar SH, Ngoma IE, Bryan CG, Harrison STL. Microbial colonisation in heaps for mineral bioleaching and the influence of irrigation rate. *Minerals Engineering*. 2012;39:156-164. doi:10.1016/j.mineng.2012.07.002
18. Brackman G, Breyne K, De Rycke R, et al. The Quorum Sensing Inhibitor Hamamelitannin Increases Antibiotic Susceptibility of Staphylococcus aureus Biofilms by Affecting Peptidoglycan Biosynthesis and eDNA Release. *Scientific Reports*. 2016;6(1):20321. doi:10.1038/srep20321
19. Cherny KE, Sauer K. Pseudomonas aeruginosa Requires the DNA-Specific Endonuclease EndA To Degrade Extracellular Genomic DNA To Disperse from the Biofilm. *Journal of bacteriology*. 2019;201(18):e00059-00019. doi:10.1128/JB.00059-19
20. Malhotra N, Hsu HS, Liang ST, et al. An Updated Review of Toxicity Effect of the Rare Earth Elements (REEs) on Aquatic Organisms. *Animals (Basel)*. 2020;10(9)doi:10.3390/ani10091663
21. Kurvet I, Juganson K, Vija H, et al. Toxicity of Nine (Doped) Rare Earth Metal Oxides and Respective Individual Metals to Aquatic Microorganisms Vibrio fischeri and Tetrahymena thermophila. *Materials*. 2017;10(7). doi:10.3390/ma10070754



## Appendix

Copyright permission for published chapters

### Chapter 3:

Biofilm formation on the surface of monazite and xenotime during bioleaching



#### Biofilm formation on the surface of monazite and xenotime during bioleaching

**Author:** Elizabeth Watkin, Anna H. Kaksonen, Jacques Eksteen, et al

**Publication:** MICROBIAL BIOTECHNOLOGY

**Publisher:** John Wiley and Sons

**Date:** Jun 8, 2023

© 2023 The Authors. *Microbial Biotechnology* published by Applied Microbiology International and John Wiley & Sons Ltd.

#### Open Access Article

This is an open access article distributed under the terms of the [Creative Commons CC BY](#) license, which permits unrestricted use, distribution, and reproduction in any medium, provided the original work is properly cited.

You are not required to obtain permission to reuse this article.

For an understanding of what is meant by the terms of the Creative Commons License, please refer to [Wiley's Open Access Terms and Conditions](#).

Permission is not required for this type of reuse.

Wiley offers a professional reprint service for high quality reproduction of articles from over 1400 scientific and medical journals. Wiley's reprint service offers:

- Peer reviewed research or reviews
- Tailored collections of articles
- A professional high quality finish
- Glossy journal style color covers
- Company or brand customisation
- Language translations
- Prompt turnaround times and delivery directly to your office, warehouse or congress.


Please contact our Reprints department for a quotation. Email [corporatesaleseurope@wiley.com](mailto:corporatesaleseurope@wiley.com) or [corporatesalesusa@wiley.com](mailto:corporatesalesusa@wiley.com) or [corporatesalesDE@wiley.com](mailto:corporatesalesDE@wiley.com).

## Chapter 5:

### Klebsiella aerogenes Adhesion Behaviour during Biofilm Formation on Monazite



Microorganisms <microorganisms@mdpi.com>

To:  Arya Van Alin (Student)

Dear Arya,

Thank you very much for your email. Please note that Journal Microorganisms is an open access journal and we follow the conditions of the Creative Commons Attribution license (<http://creativecommons.org/licenses/by/4.0/>), which provides that published material can be re-used without obtaining permission as long as a correct citation to the original publication is given.

We hope this offers some clarity. Please feel free to let me know if you have any other questions.

Best,  
Kind Regards,  
/Microorganisms/ Editorial Office

## Appendix B

Coauthors' approval.

All coauthors have digitally approved publication of chapter three and chapter five.